Development of Stimuli-responsive Luminescent Probes and Sensitive Detection of TNT Explosive

THESIS

Submitted in partial fulfillment

of the requirements for the degree of

DOCTOR OF PHILOSOPHY

by

Ram Prasad Bhatta

ID. No. 2019PHXF0430P

Under the supervision of

Prof. Inamur R. Laskar

DEPARTMENT OF CHEMISTRY

BIRLA INSTITUTE OF TECHNOLOGY AND

SCIENCE PILANI (RAJASTHAN) INDIA

2024

Birla Institute of Technology and Science Pilani –
333 031 Rajasthan, INDIA

Dr. Inamur Rahaman Laskar,
Ph.D., Department of Chemistry

Email: ir_laskar@pilani.bits-pilani.ac.in
inamur00@gmail.com
Phone: +91 1596-515675
Mob: +91 9602213001

CERTIFICATE

This is to certify that the thesis entitled **'Development of Stimuli-responsive Luminescent Probes and Sensitive Detection of TNT Explosive'** submitted by **Mr. Ram Prasad Bhatta** ID No **2019PHXF0430P** for the award of Ph. D. Degree of the Institute embodies the original work done by him under my supervision.

Signature in full of the Supervisor

Dr. Inamur R. Laskar
Designation: Professor

Date:

DEDICATED

TO MY PARENTS
AND MY BELOVED FAMILY
MEMBERS

To my mentors who are always
there to support and guide me

To those
who believe in hard work
and never-give-up
on their DREAMS

ACKNOWLEDGMENTS

PhD is a completely different educational journey, where one can explore a basic to advanced level of innovative knowledge in their subject area. My thesis represents not only my work in the laboratory or as a research outcome in the form of a research article or patent, but it is also a milestone achieved in half a decade of work in BITS Pilani, specifically in the laboratory (Lab 3105 and 3159-A). I want to take this opportunity to express my appreciation and thanks to everyone who helped and supported me greatly throughout my educational journey. As a Ph.D. student, I entered an entirely new material world and tried my best to contribute to the field of materials science. My thesis is a significant achievement in the last 5 years of work at BITS Pilani, Pilani campus. The BITS Pilani campus has allowed me to explore and gain incredible experience. I remember enrolling on January 13, 2020, and since then, I have been benefited from the institute's resources and getting special opportunities during the thesis work. I want to thank all the people who assisted me throughout my PhD journey. The thesis is also a result of numerous discussions with the dozens of outstanding professors/Research scholars at BITS Pilani.

I start with humble and special thanks to Professor Inamur Rahaman Laskar, my supervisor, for letting me work with his team at BITS Pilani. Since the beginning of my time working in the lab, he has guided and supported me. I always remember him saying, "There is nothing like a true problem; every problem has its' solution, you need to think differently, and the solution will be at your desk!". These words inspired me to think differently and be involved in many research problems. Thanks to PhD supervisor, I had the opportunity to learn many new things during his supervision. His inspiring hard work and constant motivation have helped me to understand better and remain optimistic during my research journey. Moreover, during the most difficult situation when writing research papers and PhD thesis, my supervisor gave me fruitful support and the freedom to move forward. His in-depth analysis of my technical writing has been really helpful for improving scientific writing skills.

I am hugely thankful to the Vice-Chancellor, Directors, Deputy Directors, and Deans of Birla Institute of Technology and Science (BITS) Pilani for allowing me to pursue my doctoral studies by providing the required resources and financial support. My sincere gratitude to Prof. M. B. Srinivas (Dean, Academic-Graduate Studies and Research Division

ACKNOWLEDGMENTS

ACKNOWLEDGMENTS

ACKNOWLEDGMENTS

vision, ethical principles, and teaching about life I inherited from my father (Shri Chandra Prasad Bhatta) are a constant source of inspiration and always accompany me like a shadow. Words cannot define the love and sacrifice of my mother (Chandra Kumari Bhatta). She has unconditionally given me the support and confidence in everything that I strive for. My parents' vision, ethical principles, moral support, endless patience, and eternal inspiration to face any situation in life have guided me to the successful completion of this work. I would also like to acknowledge my sisters (Ambika and Manjula), Venaju (Shakti Prajwal Ghimire, director of white media Pvt. Ltd.), and My Brothers (Krishna Prasad Bhatta and Shiva Prasad Bhatta) for their patience and courage throughout my journey. I would like to say special thanks to my older brother Krishna, without his vision and support this educational journey would not have been possible. I would like to acknowledge my best friend/member of the family, S.I. Priyanka (detective), for her love, motivation, and support throughout my educational journey. I would like to thank my grandparents (late Shri Mukhtar Masih); he was a person who taught me true life lessons. I was very fortunate to have the Masih family (Dr. R. Masih, and Dr. Suman Masih) as a guardian. I would like to say special thanks to Dr Vijay Sharma for being a college teacher, mentor, and guardian. Also, I'm very thankful to the Sharma family, the New Happy School family, and family members of Darshan Street H.NO-521, 522, and 523.

Thanks to all.
Date: 17th October 2024
Place: Pilani, India   Ram Prasad Bhatta

Table of Contents

Content	Page No.

Table of Contents

Table of Contents

Table of Contents

Table of Contents

Table of Contents

Appendices

[A-1] List of Publications

[A-2] List of Oral/Poster Presented in Conferences and Workshops

[A-3] Brief Biography of the Candidate

[A-4] Brief Biography of the Supervisor

The present thesis, entitled "Development of Stimuli-responsive Luminescent Probes and Sensitive Detection of TNT Explosive," mainly has two perspectives. Firstly, the development of 'Aggregation-induced Emission' (AIE) active stimuli-responsive probes and utilization of selective probe molecules for the sensitive detection of TNT explosives. The two basic frameworks for the stimuli-responsive probes are used: one of them is a cyclometalated iridium(III) complex containing triphenylphosphine unit triggering AIE activity, and the other one is the electron-rich twisted pyrene derivatives containing triazine and thiophene units. All the compounds (M1 = [(ppy-(OMe)$_2$)Ir(PPh$_3$)$_2$(Cl)(H)], M2 = [(ppy-CN)Ir(PPh$_3$)$_2$(Cl)(H)], 2-(pyren-1-yl)-4,6-bis(4-vinylphenyl)-1,3,5-triazine (VinTr), 4-chloro-N,N-diphenyl-6-(pyren-1-yl)-1,3,5-triazin-2-aminetriazine (PyTrDA), (E)-1-(5-(pyren-1-yl) thiophen-2-yl)-3-(thiophen-2-yl) prop-2-en-1-one (PySS) and (E)-1-(5-(pyren-1-yl)thiophen-2-yl)-3-(pyridin-2-yl)prop-2-en-1-one (PySP) have been synthesized, purified, and structurally characterized. The iridium(III) complex (M1 and M2) and the pyrene triazene derivative (PyTr, VinTr, and PyTrDA) have been employed for the selective and sensitive sensing of TNT in contact as well non-contact modes (LOD, ~10 ppb from the vapor phase), extending it to detect TNT from the paper strip based technique and rationalized their mechanism.

In other compounds, the pyrene is directly connected with thiophene, and this unit is further linked terminally to photoactive species (thiophene/pyridine) *via* a four-carbon unit conjugated spacer. These molecules show excellent solvatochromic properties and observed a significant emission response to applying grinding and compressive forces. Moreover, these compounds show 'volatile organic compounds' (VOCs) sensing. The present thesis is divided into six chapters, and the details are given below.

Chapter 1: Introduction

The introduction of the thesis covers a brief overview of literature containing various stimuli-responsive probes used for the detection of nitro-based explosive vapor, solvent polarity, pressure sensing, etc. Additionally, the chapter describes the history of the 'Aggregation-induced Emission' (AIE) property, the development of AIE compounds, and details of their employment in sensing applications and their mechanistic investigation.[1] It covers the background of nitro-based explosive materials and their adverse effects on the environment, human health, and terrorism.[2] Moreover, the conventional techniques for emission tuning and mechanofluorochromic materials are discussed.[3] The research gap has also been clearly identified and described in this chapter.

Chapter 2: The **second chapter** of the thesis provides the details of the materials and instruments and the software used for carrying out the whole experiment and computational support throughout

the Ph.D. work.

Chapter 3: The **third chapter** describes the design strategy for efficient solid-state emitters based on the pyrene-triazine system (2-(pyren-1-yl)-4,6-bis(4-vinylphenyl)-1,3,5-triazine (VinTr) and 4-chloro-N,N-diphenyl-6-(pyren-1-yl)-1,3,5-triazin-2-aminetriazine (PyTrDA) The Pyrene triazine framework was chosen as electron-rich D-A (donor-acceptor) system, and further modulation was done by substituting bulkier phenyl groups. The electron-rich pyrene is connected with nitrogen-rich triazine for better electronic interaction with electron-deficient TNT molecules. Additionally, phenyl rotor groups were introduced to make the molecule highly emissive in the solid state One of the synthesized molecules (PyTrDA) is AIE active with 20.89% quantum yield and 14.01 ns excited state lifetime. This molecule is highly sensitive and selective towards TNT explosives. It detected TNT from the aqueous solution by using the AIE solution (90 % f_w) of PyTrDA up to the level of 0.22 nM; the work has extended to detect TNT particle by paper strips. A cheap and easily available paper strip was utilized to recognize TNT in the vapor phase (7.6 ppb). Among the military explosives (TNT, RDX, HMX, PETN etc.), PyTrDA selectively detects TNT vapor within 10 seconds, and one can clearly observe the emission quenching with the naked eye. Surface morphology of material is one of the important parameters for analyte sensing in vapor phase. The film morphology by FESEM images reported that the aggregated nano-rod type horizontally aligned morphology observed for the cases of PyTr and VinTr, while a vertically grown flowery and highly condensed nano-rod based morphology observed for PyTrDA would be responsible for the excellent results obtained for TNT detection.

Chapter 4: The **fourth chapter** describes the potentiality of 'Aggregation-induced Phosphorescent Emission' (AIPE) active cyclometalated iridium(III) compound for the sensitive and selective sensing of TNT.

Two AIPE active iridium(III) complexes (M1 and M2) have been developed for the sensitive detection of TNT in both contact and non-contact modes. The aggregated solution of both complexes (M1 and M2 in THF/H_2O, 1/9 by volume) detects TNT at the pico-molar (pM) level. These complexes showed a greatly enhanced emission intensity while embedded in the PMMA (polymethyl methacrylate) matrix film. The amplified quantum efficiency, improved phosphorescence lifetime, and an enhanced porous network help to sense TNT from their vapors more effectively. It is interestingly observed that the sensitivity of detection of TNT for M2 complex has been significantly improved by 5-fold in the PMMA incorporated complex (CP) with an observed limit of detection (LOD) of 12.8 ppb. From the BET analysis of CP, it was observed that the mesoporous network of CP has an average pore diameter of 8.52 nm and a surface area of 2.03 m^2/g.

The porous network of CP assists in trapping the TNT vapor in a polymeric network containing an electron-rich probe (iridium(III) complex, M2), which helps to trap TNT effectively, thus enhancing better electronic communication. As a result, significant emission quenching was observed.

Chapter 5, Part A: In this chapter, we report a new organic compound (PyS) containing pyrene and thiophene fragments that shows an extremely rare feature in which tunable solid-state emission is wholly reliant on its particle size and surface morphological evolution, which can be controlled by adjusting the reaction time. This allowed us to obtain compounds of the same material emitting at different regions of the visible spectrum, from blue to orange-red. High-resolution transmission electron microscopy (HRTEM) images and Field emission scanning electron microscopy (FESEM) images of the compounds which were isolated at different reaction times reveal a distinct change in the aggregate size and morphology (1D assembly which is slowly turned into 2D layers, that is further converted to 3D hierarchical flowery architectures) that can be unambiguously associated to an observed gradual red shift in the PL emission. Time-correlated single-photon counting (TCSPC), dynamic light scattering, Raman spectroscopy, powder X-ray diffraction and J-aggregates formation are used to complement the explanation of the observed phenomenon.

Part B: This chapter reports that the pyrene-based twisted donor-acceptor (D–A) dyes (E)-1-(5-(pyren-1-yl) thiophen-2-yl)-3-(thiophen-2-yl) prop-2-en-1-one(PySS) and (E)-1-(5-(pyren-1-yl)thiophen-2-yl)-3-(pyridin-2-yl)prop-2-en-1-one(PySP) have been synthesized and characterized. Here, the pyrene is directly connected with thiophene, and this unit is further linked terminally to photoactive species (thiophene/pyridine) *via* a four-carbon unit conjugated spacer. These molecules show excellent solvatochromic properties, with a substantial shifting of emission wavelength (PySS-147 nm and PySP- 130 nm). The lowest transition state contains a significant contribution from ICT characteristics, as evidenced by spectral analysis and theoretical calculations. Moreover, these are identified as 'Aggregation-induced Enhanced Emission' (AIEE) active compounds and exhibit mechanofluorochromism (MFC). By grinding, PySS and PySP display MFC features with 50 nm and 54 nm red shifting, respectively. Interestingly, PySS shows a gradual emission change from green (510 nm) to orange emission (578 nm) by gradually changing pressure with a hydraulic press (0 to 12.5 tons). The single crystal structure of both compounds was investigated to understand the structure-property relationship for MFC. The crystal packing shows that the twisted molecules (dihedral angle of 59.36° and 56.93° between pyrene and thiophene for PySS and PySP, respectively) are loosely bound with several weak interactions (C-H…π, C-π…H, H…H, C-H…O).

Interestingly, it was observed that two molecules in a unit cell are arranged in an antiparallel fashion; these molecular pairs are linearly connected to another pair, forming a long one-dimensional chain-type arrangement. On applying pressure, these twisted molecular pairs slowly planarize, leading the molecules to come closer; thus, molecular interaction increases, and changes the emission. A feasibility study of the potentiality of using these compounds in data encryption-decryption and security ink has also been demonstrated.

List of abbreviations and symbols

Abbreviation/Symbol	Description
Å	Angstrom
AI	Artificial intelligence
ACN	Acetonitrile
^{13}C	Carbon-13
Conc.	Concentration
cm	Centimeter
CV	Cyclic voltammetry
^{0}C	Degree centigrade
c	velocity of light
δ	Delta
Chloroform-*d*	Deuterated chloroform
d	Doublet
dd	Doublet of doublet
DCM	Dichloromethane
DMF	N,N-Dimethylformamide
DMSO-*d6*	Deuterated dimethylsulfoxide
DFT	Density Functional Theory
EI	Electron ionization
ESI	Electron spray ionization
EtOAc	Ethyl acetate
eV	Electron Volt
Equiv.	Equivalent
e.g.	Exempli gratia
ε	Dielectric constant
ε	Molar extinction coefficient
fw	Water fractions

List of abbreviations and symbols

FTIR	Fourier Transform Infrared Spectroscopy
FESEM	Field Emission Scanning Electron Microscopy
G	Gram
gm	Gram
h	Hours
HRMS	High-resolution mass spectra
HRTEM	High-resolution transmission electron microscopy
IR	Infrared
Ir	Iridium
ILCT	Intra-ligand charge transfer
Hz	Hertz
J	Coupling constant
Kcal	Kilocalories
Kpa	Kilopascal
LED	light-emitting diodes
L	Liter
LLCT	Ligand -to- ligand charge transfer
LMCT	Ligand -to- metal charge transfer
λ	Wavelength
MS	Mass spectrometry
m	Multiplet
mg	Milligram
MHz	Mega hertz
MLCT	Metal -to- Ligand charge transfer
min	Minutes
mL	Milliliter
μM	Micro molar
M	Molar
mmhg	Millimetres of mercury
mmol	Millimole

List of abbreviations and symbols

M_w	weight average molecular weight
$\bar{\upsilon}$	Wave number
μ	dipole moment
N_2	Nitrogen gas
NMR	Nuclear magnetic resonance
nm	Nanometers
OLED	organic light-emitting diodes
PEG	Polyethylene glycol
Pt	Platinum
PXRD	Powder X-ray Diffraction
^{31}P	Phosphorous-31
ϕ	Quantum efficiency
AIEE	Aggregation-induced Enhanced Emission
ppm	Parts per million
ppb	parts per billion
PL	Photoluminescence
ppt	parts per trillion
%	Percentage
rt	Room temperature
η	refractive index
π	Pi
h	Planck's constant
σ	Standard deviation
QY	Quantum yield
Sec	Seconds
τ	Tau
θ	Diffraction angle

List of abbreviations and symbols

THF	Tetrahydrofuran
TLC	Thin layer chromatography
TPE	Tetraphenylethene
VOC	volatile organic compound
μL	Microliter
μM	Micromolar
μs	Microseconds
v	Volume
λ	Wavelength
W	Watt
Sec	Seconds

List of tables

List of tables

List of Schemes

List of Figures

ring indicating mix of local transitions and CT) b) S_2 (72.3 % shows mixed CT and LE state while 27.16% shows purely LE transitions) c) S_3 (high energy transitions shows a mixture of LE and CT)

| 3.12 | AIEE study of PyTr, VinTr, and PyTrDA in THF/water system, taken 10^{-4} M solution of probe molecules in THF and changes the water ratio from 0% to 90 % shown in the upper part of the figure and recorded corresponding PL spectra of probe solution with varying water percentages shown in the downside of the figure | 60 |

| 3.13 | Compounds 1- PyTr and 2- VinTr were taken in THF (10^{-4} M), and 3- PyTrDA was taken in 90% water in THF aggregated solution (considering the maximum PL intensity). The top left side image (three vials) was taken under UV excitation (λ_{exc}, 365 nm), then 1mg TNT power was added into each vial and the emission image was captured under 365 nm UV excitation (top right image). The above figure shows the PL spectra of all the probes with and without TNT. | 61 |

| 3.14 | a) 200 µl of different nitro-based explosive (10^{-4} M solution in THF) added into the probe solution (90% AIE solution, 2ml) and recorded image under UV lamp. b) Bar graph showing the intensity profile of aggregated solution (AIE, 90% f_w) with various nitro-based explosives (the abbreviated names of the nitro compounds are written in Figure, TNT (Tri-nitro toluene), DNP (Di-nitro phenol), 4NT (4-nitro-toluene), 4-NBA (4-nitro-benzoic acid), NB (Nitro-benzene), 3,5 DNB (3,5-di-nitro benzene), ANB (2-Amino 4-nitro benzene), 3NBA (3-nitro-benzoic acid), PA (Picric acid), DNClB (1-chloro 2,4-dinitro benzene), A.Nitrate (Ammonium nitrate), PETN | 62 |

several times (b) Stern-Volmer plot for emission quenching. I_0 represents initial PL intensity in absence of TNT vapor, and I represent the intensity in presence of TNT vapor. The error bars shown at each data point represent the standard deviation obtained from three independent measurements.

emission spectra of M1, similarly (b) (top, right) image shows different PEG fraction under UV excitation of 365 nm and (bottom, right) spectra shows corresponding emission spectra of M2

INTRODUCTION AND RESEARCH GAPS
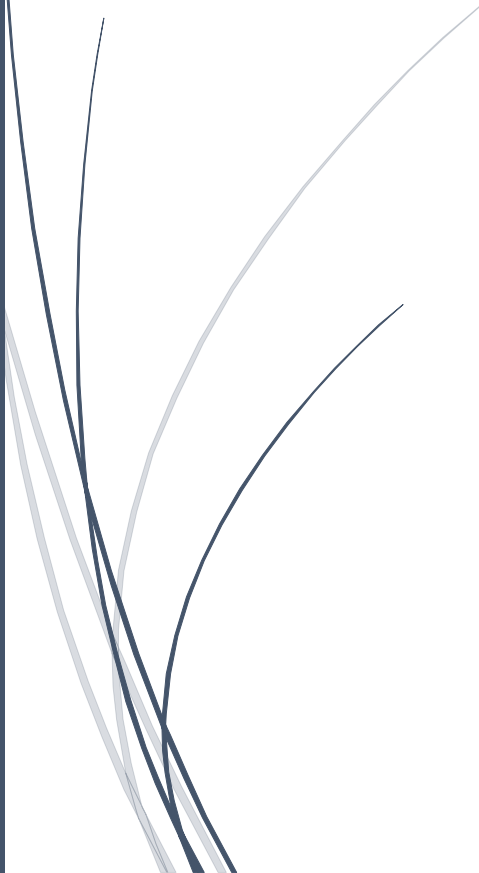
1.1 Luminescent materials

Photoluminescent material can emit light upon UV-VIS light-mediated excitation. The luminescent materials absorb light at a specific wavelength and emit light at a relatively higher wavelength. The kinds of materials that emit light in the solid state are called solid luminescent materials.[1] Photoluminescence is a process where an object emits light (photons) upon excitation. It can be further divided into two types: fluorescence and phosphorescence. In the case of fluorescence, the emission of light occurs immediately after excitation. Think of it as the rapid glow of a fluorescent bulb when you switch it on. In the phosphorescence case, light emission continues even after the excitation source is removed. Imagine the lingering glow of a glow-in-the-dark toy long after it has been exposed to light. The solid luminescent materials are divided into two groups - inorganic luminescent materials and organic luminescent materials. The inorganic luminescent materials are made up of inorganic semiconductors (CdS, ZnS, etc.)[2]. The organic luminescent materials are also divided into two types purely organic materials and materials which consist of metal complexes. The present thesis deals with solid organic luminescent materials. A fluorophore is a material that shows fluorescence properties. Most of the heavy metal-based organometallic complexes (such as iridium(III) and platinum(II)) emit light through phosphorescence, and the lifetime is in the micro- to millisecond range. Further, it can be extended even for hours.[3] Hence, it is gaining massive attention for applications like optoelectronic, metal ions sensing, and explosive sensing,[4-6] as their long luminescence lifetimes (up to µs), high quantum yield, and large stokes shifts (hundreds of nm).[7-9] Solid-state luminescent materials show diverse applications, such as solar cells, organic light-emitting diodes (OLED), sensing, bacterial imaging, stimuli-responsive materials, etc.[10-14] In addition, remarkable progress and exciting discoveries in luminescence-related research originate a new direction for future application through artificial intelligence (AI) techniques.[15]

1.2 Conventional fluorophores and their limitations

Fluorescent probes have been widely explored for their ability to detect various analytes, such as explosives, ions, pH levels, and organic solvents etc. Due to the stronger fluorescence signals produced compared to colorimetric methods, these probes are highly sensitive to the presence of analytes, even at low concentrations. One of the examples is napthalimides-based

frameworks, which have been widely used in the design and synthesis of luminous probes (**1**) among the organic fluorophores developed for fluorescent-based approaches (Fig. 1.1).[16-17]

1
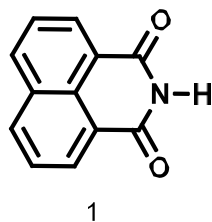
Figure 1.1 Molecular structure of the multi-analyte probe (**1**).

Luminophores are typically utilized in thin films or aggregated forms in applications like organic light-emitting diodes (OLEDs), organic field-effect transistors (OFETs), analyte sensing and so on.[18] Also, the luminescent molecule is used in aqueous medium or physiological conditions for biological applications. With increasing concentration, the emission is quenched in many conventional luminophores; this phenomenon is known as "Aggregation-Caused Quenching" (ACQ). The use of fluorophores in aggregated or solid states in various applications was restricted for many years due to the dominance of ACQ effect.[19]

1.3 Aggregation-caused Quenching

When most of the luminophores exhibit an emission quenching effect, either completely or partially, in their aggregated state or solid state, it leads to an "Aggregation-caused Quenching (ACQ)" effect. As a result, the ACQ effect creates many problems in real-time applications. Most commonly, organic-based conventional luminophores with strong emission in diluted solutions, such as perylene (**2**), pyrene (**3**), naphthalene (**4**), fluorescein (**5**), etc. (Fig. 1.2), have been extensively studied in a variety of fields, including light-emitting diodes (LEDs), chemical sensing, and particularly for bio-imaging. However, ordinary fluorophores (e.g., perylene) often have planar aromatic cores, which favor the occurrence of π-π stacking interactions when they come closer or aggregated. As a result, their emission is decreased or quenched in the concentrated or aggregated state.[20]
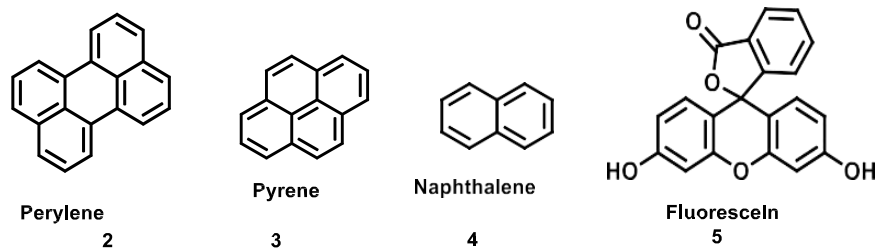
Figure 1.2 Molecular structures for common conventional ACQ fluorophores (**2-5**).

To reverse the ACQ, Tang et al. proposed the concept of "Aggregation-induced Emission (AIE)" in 2001.[21] This concept was based on the fact that luminophores with freely rotating groups were substantially emissive in the aggregated state but non-emissive in a dilute solution.

1.4 Aggregation-induced Emission

Aggregation-induced Emission (AIE) is a fascinating photophysical phenomenon in which non-emissive molecules in solutions are strongly emissive in the aggregated or solid state. AIEgens are luminogens that have the AIE property. When the AIEgens emit stronger in the aggregated state compared to their solution state, it is termed as 'Aggregation-induced Enhanced Emission' (AIEE), in marked contrast to ACQ molecules. Generations of new AIE active compounds have been developed over the past two decades. Some of the core representative AIE molecules are listed as follows- 1-methyl-1,2,3,4,5-pentaphenyl-1H-silole (**6**), 1,1,2,3,4,5-hexaphenyl-1H-silole(HPS) (**7**), 1,1,2,2-tetraphenylethene(TPE) (**8**), 9-(diphenylmethylene)-9H-fluorene (**9**), and monocyclometalated iridium(III) metal complex (**10**) (Fig. 1.3).[22-24]
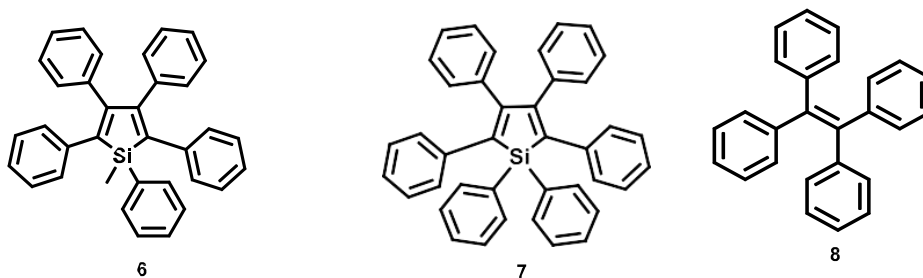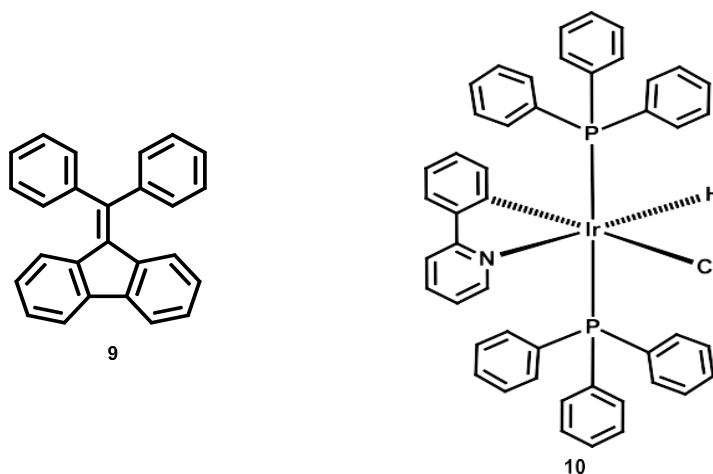
Figure 1.3 Common AIE fluorophores: 1-Methyl-1,2,3,4,5-pentaphenyl-1H-silole (**6**), 1,1,2,3,4,5-hexaphenyl-1H-silole (HPS) (**7**), 1,1,2,2-tetraphenylethene (TPE) (**8**), 9- (diphenylmethylene)-9H-fluorene (**9**), and monocyclometalated iridium metal complex (**10**).

The mechanism involving the emission in the aggregated state must be understood to develop new AIE molecules. The restriction of intramolecular motion (RIM), which includes the rotational and vibrational motion of the molecules, i.e., restriction of intramolecular rotation (RIR) and restriction of intramolecular vibration (RIV) in the aggregated state, is the most widely reported cause in terms of mechanistic studies (Fig. 1.4). If we use the AIE molecule TPE as an example, all four of the phenyl peripheries rotate rapidly in the diluted solution. In a diluted solution, the excitation energy dissipates during the rotation of the rings, which helps to increase the non-radiative decay.[25-26] However, the rotation of the phenyl rings is restricted in the aggregated state, because of a physical constraint. The non-radiative pathway is blocked by restricting rotation, allowing the excitons to decay radiatively.
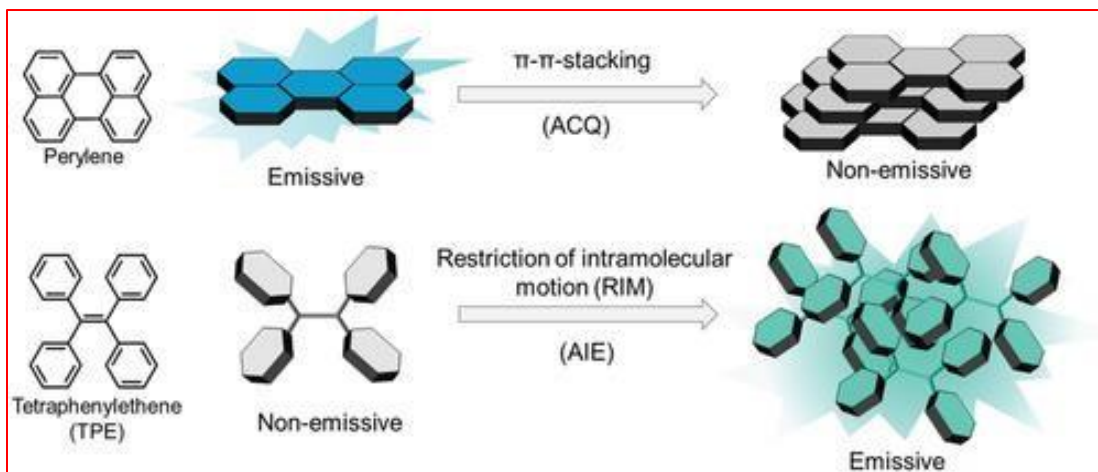
Figure 1.4 Schematic representation of the 'aggregation-caused quenching' (ACQ) mechanism of perylene and the 'aggregation-induced emission' (AIE) phenomena of tetraphenylethene (TPE). Reprinted under the terms and conditions of the Creative Commons Attribution license.[27] Copyright 2021 Wiley-VCH.

1.5 Solvatochromism

Some of the compounds are known to show different responses to light absorption, depending upon the polarity of the medium. These types of compounds are known as solvatochromic probes. The study of polarity around the surrounding medium is important for solute-solvent interactions. Many factors, for example (solute-solvent interaction, hydrogen bonding, Vander Waal interaction, solubility, acid-base equilibria, and keto-enol equilibria etc), play the role of studying the surrounding medium in which the probe is dissolved. The solubility affects the spectroscopic responses due to the environment-induced aggregation.[28] The specific solvent effect, such as hydrogen bonding, not only affects the emission property of the probe but also leads to a significant stoke shift. Knowing the mechanism for the small changes in photophysical properties at the micro-level could help to understand the nature of the living cells.[29] The fluorescence technique is promising for sensing and imaging applications.[30] An organic fluorophore is a highly useful material for sensing, but due to autofluorescence from the background, it interferes with the selectivity of the targeted species. To overcome the problem, materials with high quantum yield in solid state and high Stokes' shifts are necessary.[31] A series of tetraphenyl ethylene-containing BODIPY molecules with excellent solvatochromic properties are reported, their emissions

are tunable from visible to near-IR with large Stokes' shifts up to 142 nm.[32-34] Many AIE active materials have been synthesized, which exhibited large Stokes' shifts.[35-37] The proteins, nucleic acids, and bio-membranes involved in biomolecular interactions can be detected using the solvatochromic probes.[38] Additionally, it can be utilized in chemosensors, bioimaging, mimicking the environment of different organelles, and trace amounts of water detection from solvents.[39-41] Several essential molecular properties, such as degree of polarization, coplanar π-conjugated bridges, and push-pull charge-transfer (CT) character, must be considered to design and synthesize the solvatochromic fluorophore to achieve maximum sensitivity and response to external stimuli.[42-43] High polarization can be attained by introducing polar functionality groups to molecules, such as amino, carbonyl, cyano, nitro, or heteroaryl groups.[44]

1.6 Explosive Sensing

Explosive is a substance or a mechanical or handmade device that can produce the huge volume of rapidly expanding gas in an extremely short span of time.[45] There are three kinds of explosives.

1. Mechanical explosive is one that wholly depends on physical contact or reaction.

2. Chemical explosive is one with continuous rapid reaction producing more and more heat.

3. Nuclear explosives are sustained with nuclear reactions and can be made to take place very rapidly, releasing a large amount of energy.

Recently chemical explosives are used more for terror attacks because these explosives are easy to transport and hide. Chemical explosives are two kinds (1) detonating or high explosives, and (2) deflagrating or low explosives, e.g., propellent and pyrotechnics. Detonating or high explosives are again subdivided into two kinds (a) primary explosives requires a source of fire, spark or enough heat which equals the magnitude of explosives, for example, lead azide and lead styphnate. b) secondary explosive includes the nitroaromatic or nitramines which are much more applied in military sites. Secondary explosives are loosely categorized into melt-pour explosives which are based on nitroaromatics, e.g, trinitrotoluene (TNT), dinitro toluene (DNT) and plastic bonded explosives (PBX) which are based on a binder. Crystalline explosives are a class of secondary explosive such as 1,3,5-Trinitroperhydro-1,3,5-triazine (RDX). Again the nitro explosive can be classified as electron-deficient aromatic like picric acid (PA), 2,4-

dinitrotoluene (DNT), 1,3-dinitrobenzene (m-DNB), 2,4,6-trinitrotoluene (TNT) etc., and electron-deficient aliphatic like 2,3-dimethyl-dinitrobutane (DMNB), trinitroglycerin (TNG), 1,3,5-trinitroperhydro-1,3,5-triazine (RDX), octahydro-1,3,5,7-tetranitro-1,3,5,7-tetrazocine (HMX) etc. (Fig 1.25), RDX, HMX, TNT, TNP, TNG, PA explosives are more hazardous and dangerous. According to the interview by the Institute for Economics and Peace (IEP) from 1970 to 2019, about an average of 15% of deaths are caused by explosives.[46-49]
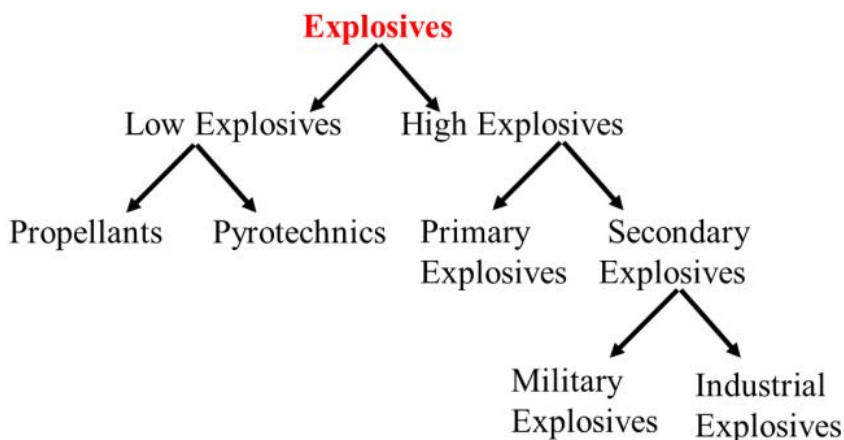
Figure 1.5 Flow chart representing the classification of the Explosive materials.

The measurement of the explosives on contamination sites provides a rapid warning at manufacturing, storage, and demilitarization of the weapons. Not only warning but the identification and quantification of explosives have also become the emerging topic of interest for all the research due to their prominent role in the security threat and increasing terrorism.
The detection of explosives is a critical task in the field of forensic science and global de-mining projects. While the increase in terrorist activities, the demand for reliable and rapid detection of luggage also increases. For counter, the active terrorism scanning of explosives in objects of various sizes, ranging from small rings to large containers, became an important aspect. Furthermore, the other is a significant concern about the health risk when these explosives are released in the environment. Nitro compounds can rapidly penetrate the skin and cause various problems such as liver damage, renal problems, anaemia, etc.[50-51] When these compounds persist in the biosphere, they severely affect the healthy life of humans, fishes, and microorganisms. Therefore, the detection of the explosives as well as tracking and locating the place where the explosive materials are buried or kept is a highly essential task, which could help in reducing the

continued fatalities from the land mines among the civilians. [52-55] Many techniques are available for detecting explosives, such as trained canines, metal detectors, ion mobility spectrometry (IMS), Raman, mass spectrometry, gas chromatography, sensors based on electrochemistry, colorimetry etc.[56-59] While each method provides advantages, their use is not without problems. Many of these devices are very costly and bulkier in size. Fluorescent-based methods provide us with many benefits over common detection techniques, such as low cost, good portability, and high sensitivity.[54] IMS is a commonly used explosive detection system in airports and has sensitivity down to nanogram or picogram for common explosives, but this technique lacks enough sensitivity for a broad range of explosives, such as PETN and RDX, which greatly limits its overall utility.[56] Moreover, IMS requires longer time for calibration and high cost of the devise making it inconvenient for real field applications.[60] Similar limitations also apply to other laboratory explosive detection systems,[61] such as gas chromatography coupled with mass spectrometry (GC-MS),[57] quartz crystal microbalance (QCM), surface plasmon resonance (SPR), electrochemical methods,[62] immunoassay,[63] etc.

Thus, it is a need for the development of innovative detection strategies that are not only low-cost and user-friendly, but also highly sensitive and selective. One particularly attractive and promising method would contain the usage of optical methods, which provide many advantages over different common detection strategies, such as low-cost, portability, sensitivity, and selectivity. Consequently, absorbance (colorimetric) and fluorescence responses are highly important in optical sensors for explosive detection. Typically, fluorescence-based technique has high sensitivity as compared to absorption-based technique. Thus, fluorescence-based sensitive, selective, and ultrafast detection of explosives is highly required.

Photoluminescence response change with nitro-based explosive occurred via different mechanism such as photo-induced electron transfer (PET), intermolecular charge transfer (ICT), electron exchange, resonance energy transfer (RET), and so forth.[64] Nitroaromatic compounds are electron-deficient in nature; they might bind with electron-rich fluorophores as a donor-acceptor (D-A) interaction.[65] The excited state of fluorophores (D) is likely to donate an electron to the ground state of explosive compounds (A) during the PET, as illustrated in Fig. 1.5a.

Explosive sensors have also been developed using the energy transfer mechanism, which can significantly increase the fluorescence-quenching efficiency and improve sensitivity.[66] The extent of overlap between the fluorescence emission spectrum of the donor (the fluorophore) and the absorbance spectrum of the acceptor (an analyte, i.e., nitroaromatics compounds)

determines the amount of resonance energy transfer (RET) (Fig 1.5b).[67-69]
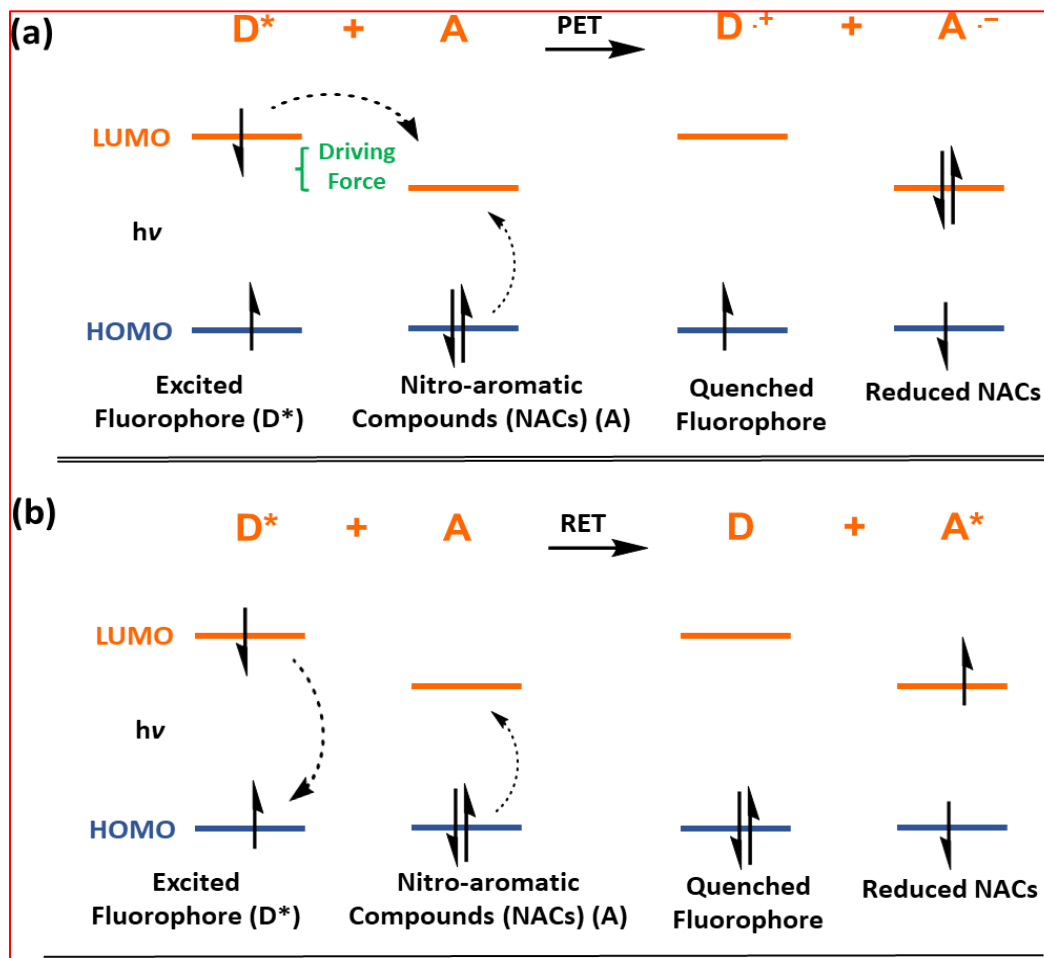
Figure 1.6 Schematic illustration for molecular orbital for different interactions in (**a**) photoinduced electron transfer (PET), (**b**) resonance energy transfer (RET).

Explosive detection systems need to be able to detect a large range of explosive materials, including both traditional high-explosive materials, such as TNT, and chemicals used in IEDs (Improvised Explosive Devices), such as ammonium nitrate.[70-71] Trinitrotoluene (TNT) is the most common explosive, also considered a hazardous waste by the U.S. Environmental Protection Agency (EPA), with a maximum permissible level in drinking water being 2 ppb.[50-51] The increased amount of TNT in water severely affects living organisms. It causes several diseases like headache, anemia, and skin irritation, and the excess amount of TNT results in serious liver, eye, and neurological damage. This calls for developing a rapid and reliable sensor for detecting buried unexploded ordnance and locating underwater mines. Detection of trace amounts of TNT in an aqueous environment and from non-contact mode, i.e., from the

vapor phase, is essential. In this context, several research across the world has significant contributions towards polymeric materials to detect TNT.[68, 72-76] Recent research on dual-state TNT detection using anthracenyl polymeric probes and fluoroarene-based organogelators is inspiring to detect TNT and other nitro-based explosives.[77-78] Several explosive sensors based on small molecules, conjugated polymers, self-assembled organic nanomaterials, and metal− organic frameworks have been studied for both solution and vapor-phase explosives detection up to detection limits of part per trillion (ppt).[79-86]

Mothika et al, reported a tetraphenylene ethylene-based conjugated microporous polymers (PTPETCz) through an electro-polymerization method using tetra(carbazolylphenyl)ethylene monomer (11), which can detect TNT vapor even at a very low concentration of 33 ppb.[87] In that report, the authors used a custom-made set-up with attached heating coils for the probe as well as the analyte and maintained a temperature of 35 °C for generating TNT vapors. Despite these advancements, the selective vapor sensing of TNT under atmospheric conditions, particularly at a detection limit that would be considered satisfactory (lower ppb to ppt), remains a challenging goal. Many other reports are also there but these are solution phase sensing and detection limit in vapor phase is not lowering to ppb range.[88-89] Chakravarty *et al*. reported an anthracene-based small organic AIE probe(12) for TNT, contact mode it is showing excellent results but response time at vapor phase quenching is longer (3 min time was taken to show quenching response on probe coated filter paper under UV excitation).[90]
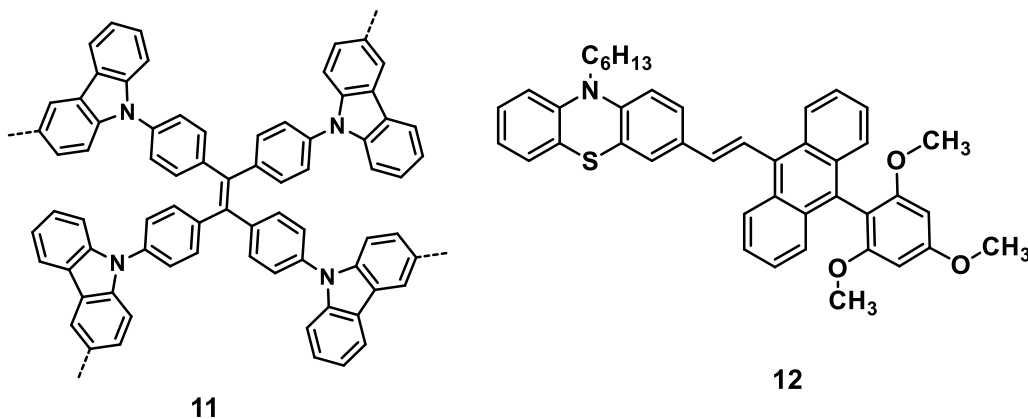
Figure 1.7 Molecular structures for TNT sensing polymer (**11**) and small molecule (E)-10-hexyl-3-(2-(10-(2,4,6-trimethoxyphenyl) anthracen-9-yl) vinyl)-10H-phenothiazine (**12**).

Nitrated explosive TNT detection in an aqueous medium has been effectively carried out using fluorescent conjugated polymers.[91] It has an extended exciton migration pathway than

small molecule fluorophores and more effective electronic communication between quenchers along the polymer backbone. The existence in contact mode sensitive probe molecules is of ppb (parts per billion) to ppt (parts per trillion) level.[53, 68, 72-76, 92-94] Vapor phases sensing of explosives is required for real-time application in military and to reduce mass-destruction from the explosion by detonating explosives in a common people place. It poses a great challenge to design highly sensitive detection of explosives in the non-contact mode because of the inherent lowering of the vapor pressure of nitro based explosives.[54, 64, 95] The use of D-A type highly conjugated materials with high quantum efficiency, phosphorescence lifetime, suitable trapping medium for explosive vapors would be a much better choice for highly sensitive detection of explosive materials.[90, 96-98] It was observed from literature survey that on the designing of small molecules for sensing explosive depends on many factors: probe should have appropriately aligned LUMO levels with the analyte for effective electron transfer, significant extent of overlapping of absorption spectra of analyte and emission spectra of probe molecule for efficient energy transfer, an extended excited state lifetime of the probe to maximize the interaction time with the analyte, a high quantum yield and large surface contact area of the probe. Additionally, fluorophore should be π-electron rich and planar in nature and at the same time to prevent the intermolecular π-π staking interaction and excimers formation bulkier substituent must be present towards the periphery of the chromophore.[54, 99-100]

Phosphorescent transition-metal complexes have been considered to be potential candidates in various fields such as chemosensors[101-105], optoelectronic materials[106-108], biological probe[109-110], etc. The role of heavy metals like osmium(II) (Os), platinum(II) (Pt), and iridium(III) (Ir), etc. as triplet emitters in these probes is highly desirable. Among these metals, iridium(III) complexes shine bright due to their superior emission properties because of strong spin-orbital coupling (3909 cm^{-1}).[111-112]

Photo thermal stabilities and colour tuneability compared to ruthenium(II) and osmium(II) complexes, and their high coordination number relative to platinum(II) complexes, which allows facile structural modifications. Aggregation-induced Phosphorescent Emission (AIPE) active iridium(III) complexes have emerged as a promising avenue in this quest, it

exhibit the desirable photophysical properties, such as large Stokes shift, high emission efficiency, and relatively extended excited state lifetime.[113] [114-115] Their versatility has found applications in diverse fields such as light-emitting diodes, therapy, and sensing. In 2015, our group (Alam *et.al.*) developed mono-cyclometalated AIPE active iridium(III) complexes and studied their potentiality for picric acid detection.[115] Recently, our group (Agarwal *et.al.*) synthesized a series of AIPE active Ir(III) complexes and used them towards sensing of different nitro-based explosives successfully.[116] It was observed that tuning of electronic substituents on phenyl pyridine ligand, modulates their sensitivity and selectivity towards different nitro-based explosives. One of the complexes having moderately electron-withdrawing substituent (COOH) is found to be sensitive towards TNT in contact mode (LOD= 3.6 ppb) based on the PET mechanism.

1.7 Mechanoflorochromism

Mechanoflorochromism (MFC) is the phenomenon by which materials emit light in response to external mechanical stimuli such as pressure, grinding, stress, rubbing, shearing, and crushing.[117] [118-120] The material's response to these stimuli has achieved significant attention from the scientific community because of their potential applications in mechanosensor, optical storage, environmental monitoring, and security papers.[121-122] An intriguing class of materials to enhance the chemistry of MFC compounds would be stimuli-responsive organic materials with aggregation-induced emission (AIE) properties. A tiny device called a diamond anvil cell (DAC) is used to apply high and uniform pressure to materials across a limited space. In mechanical grinding, pressure is not applied isotopically (comparable to shearing force), and it is not sufficient to change complete structural properties by applying anisotropic pressure. In the mechanical grinding process (basically, shear force), the phase transformation of the solid crystals takes place from crystalline to amorphous, and this phase transformation is irreversible. Conversely, high pressure increases intermolecular interactions by decreasing intermolecular distance and can change the molecular arrangements/conformational changes in the crystals reversibly.[123-124]

In the case of twisted molecular structures (such as Tetra phenylethylene and Triphenyl amine, etc.), the twisting ability of the ring, conformational changes, and intermolecular interactions depend on the linker moiety and the position at which it is linked.[125]

In 2012, Tian *et al.*[126] first reported mechanochromic luminescence of a 9,10-distyrylanthracene (DSA) derivative 9,10-bis[(E)-2-(pyridin-2-yl)vinyl]anthracene(BP2VA).

This molecule showed extraordinary luminescence properties: grinding and applying external pressure changing the photoluminescence (PL) of BP2VA powder from green to red color. With the external pressure increasing from 0 to 8 GPa, the emission of BP2VA powder showed a gradual redshift from green (with a maximum at 528 nm) to red (with a maximum at 652 nm) distinctly, which is the greatest shift in mechanochromic effect ever reported at that time. In 2016, Zou *et al.*[127] reported the polymorphs, B-phase and G-phase, prepared from a cyano-substituted distyrylbenzene (CN-DSB), the molecular conformation changes under the hydrostatic pressure of 0.75 GPa from a highly twisted shape to a flat shape under external stimulation (color changes from blue to green). In 2019, Liu *et al.*[128] reported the mechanochromism of the powder and single crystal of two compounds, photoacid-spiropyran(PASP) and tetraphenylethene-decorated photoacid-spiropyran(PASPTPE), under grinding and hydrostatic pressure. Both PASP and PASPTPE exhibited the mechanochromic property under anisotropic grinding and isotropic atmospheric pressure color change from orange to red. Further contribution to MCF materials, including carbon nanodots, metal organic framework (MOF), covalent organic framework (COF) etc.[129-132] Majority of high contrast solid-state MCF materials includes the structures which includes tetraphenyl ethylene(TPE),[125, 133-134] triphenylamine (TPA),[135-137] anthracene,[138-140] carbazole, phenothiazine, stilbene, spiropyrans etc.[141-146]

Polyaromatic compounds (e.g., pyrene, anthracene etc.) containing rigid and planar π-conjugated molecules support excimer emission. But when these are attached to twisted moieties, the twisted ring results in an increased intermolecular distance, which precludes dimer formation. However, at higher pressure, due to the planarization of the rings, dimer formation is allowed, leading to excimer emission creating a distinct response in low and high pressure. Usually, the twisted rings rotate with gradual increasing pressure, which triggers emission property changes through the perturbation of intermolecular forces. These materials' luminous properties are influenced by weak intermolecular interactions, conformational changes, excited state transitions, and molecular rearrangement within the lattice. Therefore, examining how these compounds' luminescence changes with pressure can help us comprehend the excited-state characteristics of different emissive compounds under stress.

It is likely that the development of these materials will encourage the creation of cutting-edge technology around the world.[147] When mechanical stimuli are applied, intermolecular interactions such as hydrogen bonds, dipole-dipole interactions, or π-π interactions can change, causing various morphological changes such as transitions from crystalline to amorphous states,

from a stable to a metastable liquid crystalline phase, between two different crystalline phases, etc.[148] As per the molecular level mechanism, the observation of MFC characteristics is the result of a minor or significant change in the structure of the molecular packing during grinding or pressing. The majority of materials with MFC properties can be quickly reversed by solvent fuming.[149] Numerous AIE luminogens with various characteristics have been designed, and research has been done on the correlation between the molecular structure of AIE luminogens and their photophysical characteristics.[150] Strongly twisted conformations are a common characteristic of AIE-active substances, which facilitate efficient emission in the aggregated state by obstructing tight molecular stacking.[151] Moreover, the highly twisted conformations frequently lead to loss of molecular packing patterns in the crystals, making them responsive to pressure.[152-153] As a result, under a certain stress, compounds having AIE properties are thought to be possible candidates prone to MFC-active materials. Many twisted organic molecules are studied for MCF active probes.[151, 154-157] In 2020, Yang and coworkers combined a π-rich conjugated planar chromophore with a highly twisted molecular rotor. In this case, TPE was conjugated with anthracene, linked at a different position (mTPE-AN-structure 13 and pTPE-AN- structure 14).[158] Upon mechanical grinding, there is no change in the emission observed, indicating a stable crystal state. By applying HP, three steps are observed in mTPE-AN. As pressure increased on mTPE-AN from 1–1.23 GPa, the emission is redshifted, with a decrease in the intensity indicating the formation of AN dimers. When the pressure was increased above 1.23 GPa, a new emission band appeared at 438 nm. The new emission band increases gradually as pressure increases up to 4.28 GPa with a blue shift. This phenomenon is ascribed to the cooperative effect between the aggregation-induced emission of TPE units and energy-transfer (ET) suppression from TPE to an anthracene (AN) excimer.
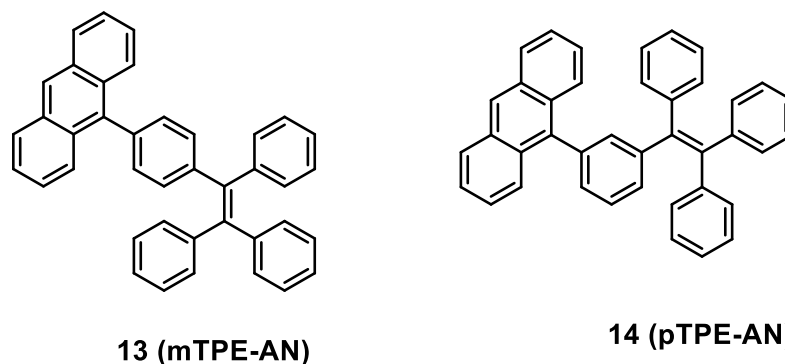
Figure 1.8 Molecular structures for MCF active fluorophore (**13** and **14**).

Chakraborty *et al.* explored the anthracene-based twisted conjugated systems (structures 15 and 16) as a potential reusable MCF material by varying terminal substituents as dicyanovinyl (DCV) and cyanoacryclic acid.[159] These studies clearly stated that the DCV is a unique core that ensures superior solvatochromic and MFC features. Replacing cyano with $-CO_2H$ functionality endows various intermolecular interactions in solution, aggregates, and the solid state. The dimeric tendency of the $-CO_2H$ group creates numerous inter/intramolecular interactions, which is detrimental to both AIE and MFC features. From these study , we could see that supramolecular interactions (C–H···N, C–H···C, π…π, etc.) are very important for controlling the MCF property of materials.[151] [154, 160]

15 (TCN)   **16 (TCNA)**
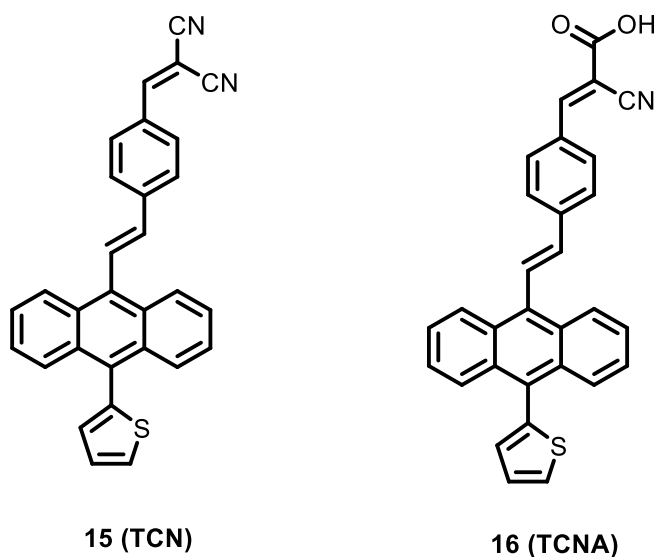
Figure 1.9 Molecular structures for anthracene-based MCF active molecule (**15** and **16**).

1.8 Importance of Molecular Interactions and Self-assembly

In recent decades, a great deal of research in materials sciences has been focused on the preparation of innovative luminescent materials with color-tunable emission, high stability, and ease of preparation. Within the different families of luminescent compounds that have been proposed, purely organic materials in the nanoscale range increase their potential and applicability in numerous fields such as chemical sensing, biological sensing, bioimaging, pharmaceuticals, or organic light-emitting diodes, where the toxicity of other materials including rare earths or heavy metals might become an issue.[161-163] Molecular conformation is a simple, but significant property in organic solid-state chemistry that allows the fine tuning of a material's properties such as the

luminescent emission just by changing the conditions in which a given molecule aggregates to form a solid-state material. Nanoscale control of the supra-molecular architecture is a very relevant topic in the field of nano-chemistry, especially in the case of biological systems where usually a network of non-covalent interactions leads to the formation of a self-assembled system. This approach provides solutions to the fabrication of ordered aggregates from components with sizes from nanometres to micrometers, and in the case of luminescent materials, it may be used for emission tuning.[164-168] The use of thiophene units is well known for the self-assembly of nanostructures and polypyrene has been recently shown to give aggregates with a nano-flower type morphology.[166, 169-170], Achieving a wide range of tunable emission colours, especially in the solid state for single-fluorophore materials, remains a significant challenge[171-172] and in all cases, a certain external stimulus is required to fine-tune this excited state property.

Spontaneous self-association of molecular building units driven by intermolecular interactions can result in diverse nano and microarchitectures.[165-166] Minor modifications can significantly influence the supramolecular self-assembly process in molecular structure.[173-174] Natural macromolecules like peptides and proteins, for instance, are heavily influenced by even the slightest change in amino acid residues, which can regulate their self-assembly and functional diversity.[175] Researchers are inspired by natural systems and exploring the relationship between the shape, size, and properties of artificial self-assembled aggregates. The molecular structures can be strategically perturbed for multifaceted applications, making it an intriguing area of study.[176]

1.9 Research Gap

The present thesis deals with both the development and discovery of stimuli-responsive luminescent materials. We have unearthed the potential of pyrene-based several 'Aggregation-induced Emission' (AIE) active compounds and used them for sensitive and selective detection of TNT vapor, study of their MFC properties, Solvatochromism, and sensing ability towards VOCs. Smart materials are characterized by their smart-responsive behaviour, which is governed by the chemically active functional groups attached to the molecules.

In the field of explosives, onsite detection of nitro explosives in the solid or gaseous state is a significant challenge to addressing anti-terrorism. Vapor phase sensing of explosives is required for real-time application in the military and to reduce mass destruction from the explosion by detonating explosives in a common people place. It poses a great challenge to design highly

sensitive and selective probe molecules for the detection of explosives in the non-contact mode because of the inherent lowering of the vapor pressure of nitro-based explosives.[54, 60] The challenge in the existing research is to obtain the ultra-sensitive (lower ppb to ppt level) probe towards sensing of nitro explosives in the vapor phase. Many research groups have contributed towards the detection of TNT. The macromolecular chemistry group developed a nanometer-thick conjugated microporous polymer film for selective and sensitive detection of TNT vapor. Here, the polymer is showing a good quenching in the case of TNT vapors (response less than 10 ppb of vapors).[177] The problem with the reported polymer is that they have used a custom-made setup to sense TNT vapor at 35°C and electro polymerization technique used for thin film formation, which is tedious and time-consuming. Many other reports are also there but most of these works are solution phase sensing. The limited vapor phase sensing of aromatic explosives is available, but none of them are ppt level sensing.[68, 72-76, 88, 178-180] Chakraborty *et al.* reported an anthracene-containing fluorescence-based AIE probe for TNT detection. It was tested in contact mode (LOD= 39 nM)) but the response time for vapor phase quenching is long (3 min exposure time required to have visibility of the quenching on the probe-coated filter paper).[90] Goudappagouda *et al.* developed a polymeric anthracenyl fluorophore for dual-state selective detection of TNT [181], this approach is very efficient for contact mode selective detection of TNT (LOD not mentioned). Further contributions of Kartha *et al.* for developing fluoroarene-based organogelators were inspiring for identifying TNT in ppq level in contact mode and ppb from vapor phase [78], shows excellent sensitivity for TNT but gel formation of the probe is the prime requirement. The use of D-A type solid state emitters would be a better choice for highly sensitive detection of explosive materials.[96-97] The mechanism underlying to detection of explosive materials using commonly known luminescent materials is mainly operated through photo-induced electron transfer and energy transfer those responsible for quenching of emission intensity.[182] Nitro-based explosives are electron-deficient species and exhibit similar chemical properties. So, selectivity is one of the major challenges in explosive sensing. Very few reports are observed where both selectivity and sensitivity are considered.[88, 183]

Laskar and co-workers developed a series of mono-cyclometalated 'Aggregation-induced Phosphorescent Emission' (AIPE) active iridium(III) complexes.[105, 115-116, 184-185] AIPE active Ir(III) complexes have emerged as a promising material because of their desirable photophysical properties, which include a significant Stokes' shift, high emission efficiency, and relatively

extended excited state lifetime.[24] Phosphorescent emitting mono-cyclometalated Ir(III) complexes have not been explored in vapor phase sensing of explosive.

As sensitivity of probes for the detection of explosives is one of the prime targets, the surface area and morphology of the sensing probe in a thin film/powder can be the important parameters for designing excellent sensors.[186] Reported small D-A type molecules are majorly explored based upon PET/RET mechanism- these processes may be improved if the surface area of the probe is increased so that the adsorption efficiency of the explosives is enhanced. It was not found any reports on organic molecules, that focus on surface morphology for efficient interaction in the vapor phase. So, small AIE molecules with morphology resulting in higher surface area could be the right approach for sensitive vapor phase detection of nitro-explosive.

High-performance organic luminescent materials with full-color tunable emission have attracted great interest owing to their potential applications in many fields, such as chemosensors, fluorescence imaging, full-color displays, and optical devices, as well as message encryption, etc.[187-191] Achieving a wide-range of tunable emission colors from a single fluorophore in the solid phase remains a significant challenge.[192-193]

Based on the literature study of MFC materials,[140, 151, 194] rational molecular design and effective control of solid luminescence with stress are particularly challenging. After applying stress to the compounds, it is hardly possible to get crystals of after-phase compounds. So, it is very challenging to understand structure-property relationships at a molecular level.

Mechanofluorochromic (MFC) compounds are also an interesting luminescent material, that can be used in various applications, such as stress detectors, security encryption devices, deformation detection, fluorescent probes, switches, and optoelectronic.[151] In the MFC materials, there is a significant impact on twisted molecular structure, conformational changes, and intermolecular interactions observed under stress. Many twisted molecules based on TPA, TPE, anthracene, carbazole and phenazine substituted molecules are well explored for MCF properties.[158, 195-198] Pyrene is one of the rigid planar π-conjugated system, thus it suffers from ACQ effect in solid state. Pyrene based molecules are enriched in optical properties because of a highly electron rich polyaromatic system. Very less number of reports are observed where pyrene based solid state emitters exhibiting MCF properties.[199-201] So, MCF properties of pyrene derivatives with twisted structure need to be explored.

1.10 References

1.   Blasse, G.; Grabmaier, B.; Blasse, G.; Grabmaier, B., *A general introduction to luminescent materials*. Springer: 1994.

2.   Kitai, A., *Luminescent materials and applications*. John Wiley & Sons: 2008.

3.   Alam, P.; Climent, C.; Alemany, P.; Laskar, I. R., "Aggregation-induced emission" of transition metal compounds: Design, mechanistic insights, and applications. *Journal of Photochemistry and Photobiology C: Photochemistry Reviews* **2019,** *41*, 100317.

4.   Che, W.; Li, G.; Liu, X.; Shao, K.; Zhu, D.; Su, Z.; Bryce, M. R., Selective sensing of 2, 4, 6-trinitrophenol (TNP) in aqueous media with "aggregation-induced emission enhancement"(AIEE)-active iridium (iii) complexes. *Chemical communications* **2018,** *54* (14), 1730-1733.

5.   Zhang, J.; Wang, Z.; Huo, X.; Meng, X.; Wang, Y.; Suo, H.; Li, P., Anti-Counterfeiting Application of Persistent Luminescence Materials and Its Research Progress. *Laser & Photonics Reviews* **2024,** *18* (3), 2300751.

6.   Cui, F.; Xie, Z.; Yang, R.; Zhang, Y.; Liu, Y.; Zheng, H.; Han, X., Aggregation-induced emission enhancement (AIEE) active bispyrene-based fluorescent probe: "turn-off" fluorescence for the detection of nitroaromatics. *Spectrochimica Acta Part A: Molecular and Biomolecular Spectroscopy* **2024,** *314*, 124222.

7.   Mauro, M.; Cebrián, C., Aggregation-induced Phosphorescence Enhancement in IrIII Complexes. *Israel Journal of Chemistry* **2018,** *58* (8), 901-914.

8.   Zhao, Q.; Huang, C.; Li, F., Phosphorescent heavy-metal complexes for bioimaging. *Chemical Society Reviews* **2011,** *40* (5), 2508-2524.

9.   Ravotto, L.; Ceroni, P., Aggregation induced phosphorescence of metal complexes: From principles to applications. *Coordination Chemistry Reviews* **2017,** *346*, 62-76.

10.   Liu, H.; Bai, Q.; Yao, L.; Zhang, H.; Xu, H.; Zhang, S.; Li, W.; Gao, Y.; Li, J.; Lu, P., Highly efficient near ultraviolet organic light-emitting diode based on a meta-linked donor–acceptor molecule. *Chemical Science* **2015,** *6* (7), 3797-3804.

11.   Kramarenko, M.; Ferreira, C. G.; Martinez-Denegri, G.; Sansierra, C.; Toudert, J.; Martorell, J., Relation between Fluorescence Quantum Yield and Open-Circuit Voltage in Complete Perovskite Solar Cells. *Solar RRL* **2020,** *4* (4), 1900554.

12.   Alam, P.; Leung, N. L.; Zhang, J.; Kwok, R. T.; Lam, J. W.; Tang, B. Z., AIE-based luminescence probes for metal ion detection. *Coordination Chemistry Reviews* **2021,** *429*, 213693.

13.   He, X.; Yang, Y.; Guo, Y.; Lu, S.; Du, Y.; Li, J.-J.; Zhang, X.; Leung, N. L.; Zhao, Z.; Niu, G., Phage-guided targeting, discriminative imaging, and synergistic killing of bacteria by AIE bioconjugates. *Journal of the American Chemical Society* **2020,** *142* (8), 3959-3969.

14.   Alam, P.; Kaur, G.; Chakraborty, S.; Choudhury, A. R.; Laskar, I. R., "Aggregation induced phosphorescence" active "rollover" iridium (iii) complex as a multi-stimuli-responsive luminescence material. *Dalton Transactions* **2015,** *44* (14), 6581-6592.

15.   Zhuo, Y.; Brgoch, J., Opportunities for next-generation luminescent materials through artificial intelligence. *The Journal of Physical Chemistry Letters* **2021,** *12* (2), 764-772.

16.   Niu, C.-G.; Zeng, G.-M.; Chen, L.-X.; Shen, G.-L.; Yu, R.-Q., Proton "off-on" behaviour of methylpiperazinyl derivative of naphthalimide: a pH sensor based on fluorescence enhancement. *Analyst* **2004,** *129* (1), 20-24.

17.   Georgiev, N. I.; Bojinov, V. B.; Nikolov, P. S., The design, synthesis and photophysical properties of two novel 1, 8-naphthalimide fluorescent pH sensors based on PET and ICT. *Dyes and Pigments* **2011,** *88* (3), 350-357.

18.   Mei, J.; Hong, Y.; Lam, J. W.; Qin, A.; Tang, Y.; Tang, B. Z., Aggregation-induced emission: the whole is more brilliant than the parts. *Advanced materials* **2014,** *26* (31), 5429-5479.

19.   Cicoira, F.; Santato, C., Organic light emitting field effect transistors: advances and perspectives. *Advanced Functional Materials* **2007,** *17* (17), 3421-3434.

20.   Huang, Y.; Xing, J.; Gong, Q.; Chen, L.-C.; Liu, G.; Yao, C.; Wang, Z.; Zhang, H.-L.; Chen, Z.; Zhang, Q., Reducing aggregation caused quenching effect through co-assembly of PAH chromophores and molecular barriers. *Nature communications* **2019,** *10* (1), 169.

21.   Luo, J.; Xie, Z.; Lam, J. W.; Cheng, L.; Chen, H.; Qiu, C.; Kwok, H. S.; Zhan, X.; Liu, Y.; Zhu, D., Aggregation-induced emission of 1-methyl-1, 2, 3, 4, 5-pentaphenylsilole. *Chemical communications* **2001,** (18), 1740-1741.

22.   Hong, Y.; Lam, J. W.; Tang, B. Z., Aggregation-induced emission: phenomenon, mechanism and applications. *Chemical communications* **2009,** (29), 4332-4353.

23.   Zhao, Z.; He, B.; Tang, B. Z., Aggregation-induced emission of siloles. *Chemical Science* **2015,** *6* (10), 5347-5365.

24. Alam, P.; Kaur, G.; Kachwal, V.; Gupta, A.; Choudhury, A. R.; Laskar, I. R., Highly sensitive explosive sensing by "aggregation induced phosphorescence" active cyclometalated iridium (iii) complexes. *Journal of Materials Chemistry C* **2015,** *3* (21), 5450-5456.

25. Sengottuvelu, D.; Kachwal, V.; Raichure, P.; Raghav, T.; Laskar, I. R., Aggregation-induced enhanced emission (AIEE)-active conjugated mesoporous oligomers (CMOs) with improved quantum yield and low-cost detection of a trace amount of nitroaromatic explosives. *ACS applied materials & interfaces* **2020,** *12* (28), 31875-31886.

26. Hong, Y.; Lam, J. W.; Tang, B. Z., Aggregation-induced emission. *Chemical Society Reviews* **2011,** *40* (11), 5361-5388.

27. Voskuhl, J.; Giese, M., Mesogens with aggregation-induced emission properties: materials with a bright future. *Aggregate* **2022,** *3* (1), e124.

28. Abramavicius, D.; Mukamel, S., Exciton dynamics in chromophore aggregates with correlated environment fluctuations. *The Journal of chemical physics* **2011,** *134* (17).

29. Rohman, M. A.; Baruah, P.; Yesylevskyy, S. O.; Mitra, S., Specific solvent effect on the photophysical behavior of substituted chromones: A combined fluorescence, DFT and MD study. *Chemical Physics* **2019,** *517*, 67-79.

30. Zarlaida, F.; Adlim, M., Gold and silver nanoparticles and indicator dyes as active agents in colorimetric spot and strip tests for mercury (II) ions: a review. *Microchimica Acta* **2017,** *184*, 45-58.

31. Cho, Y.-J.; Kim, S.-Y.; Cho, M.; Han, W.-S.; Son, H.-J.; Cho, D. W.; Kang, S. O., Aggregation-induced emission of diarylamino-π-carborane triads: effects of charge transfer and π-conjugation. *Physical Chemistry Chemical Physics* **2016,** *18* (14), 9702-9708.

32. Feng, H.-T.; Xiong, J.-B.; Zheng, Y.-S.; Pan, B.; Zhang, C.; Wang, L.; Xie, Y., Multicolor emissions by the synergism of intra/intermolecular slipped π–π stackings of tetraphenylethylene-diBODIPY conjugate. *Chemistry of Materials* **2015,** *27* (22), 7812-7819.

33. Shen, X. Y.; Wang, Y. J.; Zhao, E.; Yuan, W. Z.; Liu, Y.; Lu, P.; Qin, A.; Ma, Y.; Sun, J. Z.; Tang, B. Z., Effects of substitution with donor–acceptor groups on the properties of tetraphenylethene trimer: aggregation-induced emission, solvatochromism, and mechanochromism. *The Journal of Physical Chemistry C* **2013,** *117* (14), 7334-7347.

34. Hu, R.; Lager, E.; Aguilar-Aguilar, A.; Liu, J.; Lam, J.; Sung, H.; Williams, I.; Zhong, Y.; Wong, K. S., E. Peñ a-Cabrera and BZ Tang. *J. Phys. Chem. C* **2009,** *113*, 1845-15853.

35.   Cai, L.; Sun, X.; He, W.; Hu, R.; Liu, B.; Shen, J., A solvatochromic AIE tetrahydro [5] helicene derivative as fluorescent probes for water in organic solvents and highly sensitive sensors for glyceryl monostearate. *Talanta* **2020,** *206*, 120214.

36.   Zhan, Y.; Yang, Z.; Tan, J.; Qiu, Z.; Mao, Y.; He, J.; Yang, Q.; Ji, S.; Cai, N.; Huo, Y., Synthesis, aggregation-induced emission (AIE) and electroluminescence of carbazole-benzoyl substituted tetraphenylethylene derivatives. *Dyes and Pigments* **2020,** *173*, 107898.

37.   Liu, W.; Wang, Y.; Yang, J.; Li, X.; Wang, X.; Ma, L., The abnormal solvatochromism, high-contrast mechanochromism and internal mechanism of two AIEE-active β-diketones. *Dyes and Pigments* **2020,** *175*, 108149.

38.   Bustamante, C.; Alexander, L.; Maciuba, K.; Kaiser, C. M., Single-Molecule Studies of Protein Folding with Optical Tweezers. *Annual Review of Biochemistry* **2020,** *89* (Volume 89, 2020), 443-470.

39.   Klymchenko, A. S., Solvatochromic and fluorogenic dyes as environment-sensitive probes: design and biological applications. *Accounts of chemical research* **2017,** *50* (2), 366-375.

40.   Fegade, U.; Patil, S.; Kaur, R.; Sahoo, S. K.; Singh, N.; Bendre, R.; Kuwar, A., A novel chromogenic and fluorogenic chemosensor for detection of trace water in methanol. *Sensors and Actuators B: Chemical* **2015,** *210*, 324-327.

41.   Grande, V.; Soberats, B.; Herbst, S.; Stepanenko, V.; Würthner, F., Hydrogen-bonded perylene bisimide J-aggregate aqua material. *Chemical science* **2018,** *9* (34), 6904-6911.

42.   Huang, Z.; Tang, F.; Ding, A.; He, F.; Duan, R.-H.; Huang, J.; Kong, L.; Yang, J., D–A–D structured triphenylamine fluorophore with bright dual-state emission for reversible mechanofluorochromism and trace water detection. *Molecular Systems Design & Engineering* **2022,** *7* (8), 963-968.

43.   Niko, Y.; Sasaki, S.; Kawauchi, S.; Tokumaru, K.; Konishi, G. i., Design of Weak-Donor Alkyl-Functionalized Push–Pull Pyrene Dyes Exhibiting Enhanced Fluorescence Quantum Yields and Unique On/Off Switching Properties. *Chemistry–An Asian Journal* **2014,** *9* (7), 1797-1807.

44.   Takagi, K.; Kusafuka, K.; Ito, Y.; Yamauchi, K.; Ito, K.; Fukuda, R.; Ehara, M., Synthesis and optical properties of imidazole-and benzimidazole-based fused π-conjugated compounds: influence of substituent, counteranion, and π-conjugated system. *The Journal of Organic Chemistry* **2015,** *80* (14), 7172-7183.

45.   Armstrong, R.; Elban, W. L., Materials science and technology aspects of energetic (explosive) materials. *Materials Science and Technology* **2006,** *22* (4), 381-395.

46.   Lehnert, A. L.; Kearfott, K. J., The detection of explosive materials: review of considerations and methods. *Nuclear technology* **2010,** *172* (3), 325-334.

47.   Steinfeld, J. I.; Wormhoudt, J., Explosives detection: a challenge for physical chemistry. *Annual review of physical chemistry* **1998,** *49* (1), 203-232.

48.   Cooper, P. W.; Kurowski, S. R., *Introduction to the Technology of Explosives*. John Wiley & Sons: 1997.

49.   Oxley, J. C. In *Explosives detection: potential problems*, Law Enforcement Technologies: Identification Technologies and Traffic Safety, SPIE: 1995; pp 217-226.

50.   Dorsey, A.; Hodes, C. S.; Richter-Torres, P., Toxicological profile for 2, 4, 6-trinitrotoluene. **1995**.

51.   Martel, R.; Mailloux, M.; Gabriel, U.; Lefebvre, R.; Thiboutot, S.; Ampleman, G., Behavior of energetic materials in ground water at an anti-tank range. *Journal of environmental quality* **2009,** *38 1*, 75-92.

52.   Willer, U.; Schade, W., Photonic sensor devices for explosive detection. *Analytical and bioanalytical chemistry* **2009,** *395*, 275-282.

53.   Wu, Y.-w.; Qin, A.-j.; Tang, B. Z., AIE-active polymers for explosive detection. *Chinese Journal of Polymer Science* **2017,** *35* (2), 141-154.

54.   Sun, X.; Wang, Y.; Lei, Y., Fluorescence based explosive detection: from mechanisms to sensory materials. *Chemical Society Reviews* **2015,** *44* (22), 8019-8061.

55.   Jurcic, M.; Peveler, W. J.; Savory, C. N.; Scanlon, D. O.; Kenyon, A. J.; Parkin, I. P., The vapour phase detection of explosive markers and derivatives using two fluorescent metal–organic frameworks. *Journal of Materials Chemistry A* **2015,** *3* (12), 6351-6359.

56.   Hill, H. H.; Simpson, G., Capabilities and limitations of ion mobility spectrometry for field screening applications. *Field Analytical Chemistry & Technology* **1997,** *1* (3), 119-134.

57.   Walsh, M. E., Determination of nitroaromatic, nitramine, and nitrate ester explosives in soil by gas chromatography and an electron capture detector. *Talanta* **2001,** *54* (3), 427-438.

58.   Hu, Z.; Deibert, B. J.; Li, J., Luminescent metal–organic frameworks for chemical sensing and explosive detection. *Chemical Society Reviews* **2014,** *43* (16), 5815-5840.

59.   Kojima, K.; Sakairi, M.; Takada, Y.; NAKAMURA, J., Vapor detection of TNT and RDX using atmospheric pressure chemical ionization mass spectrometry with counter-flow introduction (CFI). *Journal of the Mass Spectrometry Society of Japan* **2000,** *48* (5), 360-362.

60.   Zhou, H.; Chua, M. H.; Tang, B. Z.; Xu, J., Aggregation-induced emission (AIE)-active polymers for explosive detection. *Polymer Chemistry* **2019,** *10* (28), 3822-3840.

61.   Moore, D. S., Instrumentation for trace detection of high explosives. *Review of Scientific Instruments* **2004,** *75* (8), 2499-2512.

62.   Zhang, H.-X.; Hu, J.-S.; Yan, C.-J.; Jiang, L.; Wan, L.-J., Functionalized carbon nanotubes as sensitive materials for electrochemical detection of ultra-trace 2, 4, 6-trinitrotoluene. *Physical Chemistry Chemical Physics* **2006,** *8* (30), 3567-3572.

63.   Goldman, E. R.; Anderson, G. P.; Lebedev, N.; Lingerfelt, B. M.; Winter, P. T.; Patterson, C. H.; Mauro, J. M., Analysis of aqueous 2, 4, 6-trinitrotoluene (TNT) using a fluorescent displacement immunoassay. *Analytical and bioanalytical chemistry* **2003,** *375*, 471-475.

64.   Lefferts, M. J.; Castell, M. R., Vapour sensing of explosive materials. *Analytical Methods* **2015,** *7* (21), 9005-9017.

65.   Lakowicz, J. R., *Principles of fluorescence spectroscopy*. Springer: 2006.

66.   Meaney, M. S.; McGuffin, V. L., Investigation of common fluorophores for the detection of nitrated explosives by fluorescence quenching. *Analytica Chimica Acta* **2008,** *610* (1), 57-67.

67.   Thomas, S. W.; Joly, G. D.; Swager, T. M., Chemical sensors based on amplifying fluorescent conjugated polymers. *Chemical reviews* **2007,** *107* (4), 1339-1386.

68.   Rochat, S.; Swager, T. M., Conjugated amplifying polymers for optical sensing applications. *ACS applied materials & interfaces* **2013,** *5* (11), 4488-4502.

69.   Yang, J.-S.; Swager, T. M., Porous shape persistent fluorescent polymer films: an approach to TNT sensory materials. *Journal of the American Chemical Society* **1998,** *120* (21), 5321-5322.

70.   Kolla, P., The application of analytical methods to the detection of hidden explosives and explosive devices. *Angewandte Chemie International Edition in English* **1997,** *36* (8), 800-811.

71.   Yang, J.-S.; Swager, T. M., Fluorescent porous polymer films as TNT chemosensors: electronic and structural effects. *Journal of the American Chemical Society* **1998,** *120* (46), 11864-11873.

72.   Toal, S. J.; Trogler, W. C., Polymer sensors for nitroaromatic explosives detection. *Journal of Materials Chemistry* **2006,** *16* (28), 2871-2883.

73.   Tanwar, A. S.; Parui, R.; Garai, R.; Chanu, M. A.; Iyer, P. K., Dual "Static and Dynamic" fluorescence quenching mechanisms based detection of TNT via a cationic conjugated polymer. *ACS Measurement Science Au* **2021,** *2* (1), 23-30.

74.   Kumar, V.; Saini, S. K.; Choudhury, N.; Kumar, A.; Maiti, B.; De, P.; Kumar, M.; Satapathi, S., Highly sensitive detection of nitro compounds using a fluorescent copolymer-based FRET system. *ACS Applied Polymer Materials* **2021,** *3* (8), 4017-4026.

75.   Schmidt, J.; Weber, J.; Epping, J. D.; Antonietti, M.; Thomas, A., Microporous conjugated poly (thienylene arylene) networks. *Advanced Materials* **2009,** *21* (6), 702-705.

76.   Zreid, M. S.; Tabasi, Z. A.; Ma, X.; Wang, T.; Almatarneh, M. H.; Zhao, Y., Highly Twisted Aryl-Anthraquinodimethanes: Synthesis, Characterization, and Fluorescence Sensing of TNT. *European Journal of Organic Chemistry* **2020,** *2020* (26), 4031-4041.

77.   Dongre, S. D.; Das, T.; Babu, S. S., Dual mode selective detection and differentiation of TNT from other nitroaromatic compounds. *Journal of Materials Chemistry A* **2020,** *8* (21), 10767-10771.

78.   Kartha, K. K.; Babu, S. S.; Srinivasan, S.; Ajayaghosh, A., Attogram Sensing of Trinitrotoluene with a Self-Assembled Molecular Gelator. *Journal of the American Chemical Society* **2012,** *134* (10), 4834-4841.

79.   Wang, S.; Wang, Q.; Feng, X.; Wang, B.; Yang, L., Explosives in the cage: metal–organic frameworks for high-energy materials sensing and desensitization. *Advanced Materials* **2017,** *29* (36), 1701898.

80.   Xing, S.; Bing, Q.; Qi, H.; Liu, J.; Bai, T.; Li, G.; Shi, Z.; Feng, S.; Xu, R., Rational design and functionalization of a zinc metal–organic framework for highly selective detection of 2, 4, 6-trinitrophenol. *ACS applied materials & interfaces* **2017,** *9* (28), 23828-23835.

81.   Yang, Z.; Dou, X., Emerging and future possible strategies for enhancing 1D inorganic nanomaterials-based electrical sensors towards explosives vapors detection. *Advanced Functional Materials* **2016,** *26* (15), 2406-2425.

82.   Kartha, K. K.; Sandeep, A.; Praveen, V. K.; Ajayaghosh, A., Detection of nitroaromatic explosives with fluorescent molecular assemblies and π-gels. *The Chemical Record* **2015,** *15* (1), 252-265.

83.   Zhang, Y.; Xu, M.; Bunes, B. R.; Wu, N.; Gross, D. E.; Moore, J. S.; Zang, L., Oligomer-coated carbon nanotube chemiresistive sensors for selective detection of nitroaromatic explosives. *ACS Applied Materials & Interfaces* **2015,** *7* (14), 7471-7475.

84.   Zhao, P.; Wu, Y.; Feng, C.; Wang, L.; Ding, Y.; Hu, A., Conjugated polymer nanoparticles based fluorescent electronic nose for the identification of volatile compounds. *Analytical chemistry* **2018,** *90* (7), 4815-4822.

85.   Xu, Y.; Jin, S.; Xu, H.; Nagai, A.; Jiang, D., Conjugated microporous polymers: design, synthesis and application. *Chemical Society Reviews* **2013,** *42* (20), 8012-8031.

86.   Liyanage, T.; Rael, A.; Shaffer, S.; Zaidi, S.; Goodpaster, J. V.; Sardar, R., Fabrication of a self-assembled and flexible SERS nanosensor for explosive detection at parts-per-quadrillion levels from fingerprints. *Analyst* **2018,** *143* (9), 2012-2022.

87.   Mothika, V. S.; Räupke, A.; Brinkmann, K. O.; Riedl, T.; Brunklaus, G.; Scherf, U., Nanometer-thick conjugated microporous polymer films for selective and sensitive vapor-phase TNT detection. *ACS Applied Nano Materials* **2018,** *1* (11), 6483-6492.

88.   Prusti, B.; Chakravarty, M., An electron-rich small AIEgen as a solid platform for the selective and ultrasensitive on-site visual detection of TNT in the solid, solution and vapor states. *Analyst* **2020,** *145* (5), 1687-1694.

89.   Wang, R.; Tavano, E. C. d. R.; Lammers, M.; Martinelli, A. P.; Angenent, G. C.; de Maagd, R. A., Re-evaluation of transcription factor function in tomato fruit development and ripening with CRISPR/Cas9-mutagenesis. *Scientific reports* **2019,** *9* (1), 1696.

90.   Chakraborty, M.; Prusti, B.; Chakravarty, M., Small Electron-Rich Isomeric Solid-State Emitters with Variation in Coplanarity and Molecular Packings: Rapid and Ultralow Recognition of TNT. *ACS Applied Electronic Materials* **2022,** *4* (5), 2481-2489.

91.   Swager, T. M., The molecular wire approach to sensory signal amplification. *Accounts of chemical research* **1998,** *31* (5), 201-207.

92.   Bejoymohandas, K.; George, T.; Bhattacharya, S.; Natarajan, S.; Reddy, M., AIPE-active green phosphorescent iridium (III) complex impregnated test strips for the vapor-phase detection of 2, 4, 6-trinitrotoluene (TNT). *Journal of Materials Chemistry C* **2014,** *2* (3), 515-523.

93.   Malik, A. H.; Hussain, S.; Kalita, A.; Iyer, P. K., Conjugated polymer nanoparticles for the amplified detection of nitro-explosive picric acid on multiple platforms. *ACS Applied Materials & Interfaces* **2015,** *7* (48), 26968-26976.

94.   Boonsri, M.; Vongnam, K.; Namuangruk, S.; Sukwattanasinitt, M.; Rashatasakhon, P., Pyrenyl benzimidazole-isoquinolinones: Aggregation-induced emission enhancement property and application as TNT fluorescent sensor. *Sensors and Actuators B: Chemical* **2017,** *248*, 665-672.

95.   Lee, J. Y.; Root, H. D.; Ali, R.; An, W.; Lynch, V. M.; Bähring, S.; Kim, I. S.; Sessler, J. L.; Park, J. S., Ratiometric Turn-On Fluorophore Displacement Ensembles for Nitroaromatic Explosives Detection. *Journal of the American Chemical Society* **2020,** *142* (46), 19579-19587.

96.   Chen, J.-B.; Li, B.; Xiong, Y.; Sun, J., A novel turn-off fluorescent probe based on TICT for the detection of NO2 and nitramines with high sensitivity and selectivity. *Sensors and Actuators B: Chemical* **2018,** *255*, 275-282.

97.   Islam, M. M.; Hu, Z.; Wang, Q.; Redshaw, C.; Feng, X., Pyrene-based aggregation-induced emission luminogens and their applications. *Materials Chemistry Frontiers* **2019,** *3* (5), 762-781.

98.   Méndez-Gil, N.; Gámez-Valenzuela, S.; Echeverri, M.; Suyo, G. H.; Iglesias, M.; Delgado, M. C. R.; Gómez-Lor, B., Donor-Acceptor Truxene-Based Porous Polymers: Synthesis, Optoelectronic Characterization and Defense-Related Applications. *Advanced Functional Materials* **2024**, 2316754.

99.   Shanmugaraju, S.; Joshi, S. A.; Mukherjee, P. S., Fluorescence and visual sensing of nitroaromatic explosives using electron rich discrete fluorophores. *Journal of Materials Chemistry* **2011,** *21* (25), 9130-9138.

100.   Zhang, R.; Zhang, T.; Xu, L.; Han, F.; Zhao, Y.; Ni, Z., A new series of short axially symmetrically and asymmetrically 1,3,6,8-tetrasubstituted pyrenes with two types of substituents: Syntheses, structures, photophysical properties and electroluminescence. *Journal of Molecular Structure* **2017,** *1127*, 237-246.

101.   Zhao, Q.; Li, F.; Huang, C., Phosphorescent chemosensors based on heavy-metal complexes. *Chemical Society Reviews* **2010,** *39* (8), 3007-3030.

102.   Xu, W.; Liu, S.; Sun, H.; Zhao, X.; Zhao, Q.; Sun, S.; Cheng, S.; Ma, T.; Zhou, L.; Huang, W., FRET-based probe for fluoride based on a phosphorescent iridium(iii) complex containing triarylboron groups. *Journal of Materials Chemistry* **2011,** *21* (21), 7572-7581.

103.   Wong, K. M.-C.; Tang, W.-S.; Lu, X.-X.; Zhu, N.; Yam, V. W.-W., Functionalized Platinum(II) Terpyridyl Alkynyl Complexes as Colorimetric and Luminescence pH Sensors. *Inorganic Chemistry* **2005,** *44* (5), 1492-1498.

104.   Shiu, H.-Y.; Wong, M.-K.; Che, C.-M., "Turn-on" FRET-based luminescent iridium(iii) probes for the detection of cysteine and homocysteine. *Chemical Communications* **2011,** *47* (15), 4367-4369.

105.   Agarwal, A.; Bhatta, R. P.; Kachwal, V.; Laskar, I. R., Controlling the sensitivity and selectivity for the detection of nitro-based explosives by modulating the electronic substituents on the ligand of AIPE-active cyclometalated iridium(iii) complexes. *Dalton Transactions* **2023,** *52* (39), 14182-14193.

106. Ge, G.; He, J.; Guo, H.; Wang, F.; Zou, D., Highly efficient phosphorescent iridium (III) diazine complexes for OLEDs: Different photophysical property between iridium (III) pyrazine complex and iridium (III) pyrimidine complex. *Journal of Organometallic Chemistry* **2009,** *694* (19), 3050-3057.

107. Yang, C.-H.; Cheng, Y.-M.; Chi, Y.; Hsu, C.-J.; Fang, F.-C.; Wong, K.-T.; Chou, P.-T.; Chang, C.-H.; Tsai, M.-H.; Wu, C.-C., Blue-Emitting Heteroleptic Iridium(III) Complexes Suitable for High-Efficiency Phosphorescent OLEDs. *Angewandte Chemie International Edition* **2007,** *46* (14), 2418-2421.

108. Lee, S. J.; Park, K.-M.; Yang, K.; Kang, Y., Blue Phosphorescent Ir(III) Complex with High Color Purity: fac-Tris(2′,6′-difluoro-2,3′-bipyridinato-N,C4′)iridium(III). *Inorganic Chemistry* **2009,** *48* (3), 1030-1037.

109. Ma, D.-L.; Wong, W.-L.; Chung, W.-H.; Chan, F.-Y.; So, P.-K.; Lai, T.-S.; Zhou, Z.-Y.; Leung, Y.-C.; Wong, K.-Y., A Highly Selective Luminescent Switch-On Probe for Histidine/Histidine-Rich Proteins and Its Application in Protein Staining. *Angewandte Chemie International Edition* **2008,** *47* (20), 3735-3739.

110. Lo, K. K.-W.; Zhang, K. Y.; Leung, S.-K.; Tang, M.-C., Exploitation of the Dual-emissive Properties of Cyclometalated Iridium(III)–Polypyridine Complexes in the Development of Luminescent Biological Probes. *Angewandte Chemie International Edition* **2008,** *47* (12), 2213-2216.

111. Sumit; Maravajjala, K. S.; Khanna, S.; Kachwal, V.; Swetha, K. L.; Manabala, S.; Chowdhury, R.; Roy, A.; Laskar, I. R., Rational Molecular Designing of Aggregation-Enhanced Emission (AEE) Active Red-Emitting Iridium(III) Complexes: Effect of Lipophilicity and Nanoparticle Encapsulation on Photodynamic Therapy Efficacy. *ACS Applied Bio Materials* **2023,** *6* (4), 1445-1459.

112. Park, S. W.; Ham, H. W.; Kim, Y. S., Theoretical Studies of Mono-Cyclometalated Ir(III) Complexes with Phenylpyrazole Based Ligands and Phosphines. *Molecular Crystals and Liquid Crystals* **2011,** *551* (1), 24-32.

113. Lowry, M. S.; Bernhard, S., Synthetically Tailored Excited States: Phosphorescent, Cyclometalated Iridium(III) Complexes and Their Applications. *Chemistry – A European Journal* **2006,** *12* (31), 7970-7977.

114. Bejoymohandas, K. S.; George, T. M.; Bhattacharya, S.; Natarajan, S.; Reddy, M. L. P., AIPE-active green phosphorescent iridium(iii) complex impregnated test strips for the vapor-phase detection of 2,4,6-trinitrotoluene (TNT). *Journal of Materials Chemistry C* **2014,** *2* (3), 515-523.

115. Alam, P.; Kaur, G.; Kachwal, V.; Gupta, A.; Roy Choudhury, A.; Laskar, I. R., Highly sensitive explosive sensing by "aggregation induced phosphorescence" active cyclometalated iridium(iii) complexes. *Journal of Materials Chemistry C* **2015,** *3* (21), 5450-5456.

116. Agarwal, A.; Bhatta, R. P.; Kachwal, V.; Laskar, I. R., Controlling the sensitivity and selectivity for the detection of nitro-based explosives by modulating the electronic substituents on the ligand of AIPE-active cyclometalated iridium(iii) complexes. *Dalton Transactions* **2023**.

117. Shen, Y.; Xue, P.; Liu, J.; Ding, J.; Sun, J.; Lu, R., High-contrast mechanofluorochromism and acidochromism of D-π-A type quinoline derivatives. *Dyes and Pigments* **2019,** *163*, 71-77.

118. Zhang, X.; Chi, Z.; Zhang, Y.; Liu, S.; Xu, J., Recent advances in mechanochromic luminescent metal complexes. *Journal of Materials Chemistry C* **2013,** *1* (21), 3376-3390.

119. Sagara, Y.; Kato, T., Stimuli-responsive luminescent liquid crystals: change of photoluminescent colors triggered by a shear-induced phase transition. *Angewandte Chemie* **2008,** *120* (28), 5253-5256.

120. Zhang, X.; Wang, J.-Y.; Ni, J.; Zhang, L.-Y.; Chen, Z.-N., Vapochromic and mechanochromic phosphorescence materials based on a platinum (II) complex with 4-trifluoromethylphenylacetylide. *Inorganic Chemistry* **2012,** *51* (10), 5569-5579.

121. Roberts, D. R.; Holder, S. J., Mechanochromic systems for the detection of stress, strain and deformation in polymeric materials. *Journal of Materials Chemistry* **2011,** *21* (23), 8256-8268.

122. Huang, W.; Feng, S.; Liu, J.; Liang, B.; Zhou, Y.; Yu, M.; Liang, J.; Huang, J.; Lü, X.; Huang, W., Configuration-Induced Multichromism of Phenanthridine Derivatives: A Type of Versatile Fluorescent Probe for Microenvironmental Monitoring. *Angewandte Chemie* **2023,** *135* (9), e202219337.

123. Wang, Y.; Tan, X.; Zhang, Y.-M.; Zhu, S.; Zhang, I.; Yu, B.; Wang, K.; Yang, B.; Li, M.; Zou, B.; Zhang, S. X.-A., Dynamic Behavior of Molecular Switches in Crystal under Pressure and Its Reflection on Tactile Sensing. *Journal of the American Chemical Society* **2015,** *137* (2), 931-939.

124. Xiong, Y.; Huang, J.; Liu, Y.; Xiao, B.; Xu, B.; Zhao, Z.; Tang, B. Z., High-contrast luminescence dependent on polymorphism and mechanochromism of AIE-active (4-

(phenothiazin-10-yl) phenyl)(pyren-1-yl) methanone. *Journal of Materials Chemistry C* **2020,** *8* (7), 2460-2466.

125.   Xiong, J.; Wang, K.; Yao, Z.; Zou, B.; Xu, J.; Bu, X.-H., Multi-Stimuli-Responsive Fluorescence Switching from a Pyridine-Functionalized Tetraphenylethene AIEgen. *ACS Applied Materials & Interfaces* **2018,** *10* (6), 5819-5827.

126.   Dong, Y.; Zhang, J.; Tan, X.; Wang, L.; Chen, J.; Li, B.; Ye, L.; Xu, B.; Zou, B.; Tian, W., Multi-stimuli responsive fluorescence switching: the reversible piezochromism and protonation effect of a divinylanthracene derivative. *Journal of Materials Chemistry C* **2013,** *1* (45), 7554-7559.

127.   Xu, Y.; Wang, K.; Zhang, Y.; Xie, Z.; Zou, B.; Ma, Y., Fluorescence mutation and structural evolution of a π-conjugated molecular crystal during phase transition. *Journal of Materials Chemistry C* **2016,** *4* (6), 1257-1262.

128.   Liu, L.; Su, X.; Yu, Q.; Guo, H.; Wang, K.; Yu, B.; Li, M.; Zou, B.; Liu, Y.; Xiao-An Zhang, S., Photoacid-spiropyran exhibits different mechanofluorochromism before and after modification of tetraphenylethene under grinding and hydrostatic pressure. *The Journal of Physical Chemistry C* **2019,** *123* (41), 25366-25372.

129.   Li, J.; Yuan, S.; Qin, J.-S.; Huang, L.; Bose, R.; Pang, J.; Zhang, P.; Xiao, Z.; Tan, K.; Malko, A. V.; Cagin, T.; Zhou, H.-C., Fluorescence Enhancement in the Solid State by Isolating Perylene Fluorophores in Metal–Organic Frameworks. *ACS Applied Materials & Interfaces* **2020,** *12* (23), 26727-26732.

130.   Li, X.; Gao, Q.; Wang, J.; Chen, Y.; Chen, Z.-H.; Xu, H.-S.; Tang, W.; Leng, K.; Ning, G.-H.; Wu, J.; Xu, Q.-H.; Quek, S. Y.; Lu, Y.; Loh, K. P., Tuneable near white-emissive two-dimensional covalent organic frameworks. *Nature Communications* **2018,** *9* (1), 2335.

131.   Wang, X.; Zhang, J.; Mao, X.; Liu, Y.; Li, R.; Bai, J.; Zhang, J.; Redshaw, C.; Feng, X.; Tang, B. Z., Intermolecular Hydrogen-Bond-Assisted Solid-State Dual-Emission Molecules with Mechanical Force-Induced Enhanced Emission. *The Journal of Organic Chemistry* **2022,** *87* (13), 8503-8514.

132.   Liu, C.; Xiao, G.; Yang, M.; Zou, B.; Zhang, Z.-L.; Pang, D.-W., Mechanofluorochromic Carbon Nanodots: Controllable Pressure-Triggered Blue- and Red-Shifted Photoluminescence. *Angewandte Chemie International Edition* **2018,** *57* (7), 1893-1897.

133. Mei, J.; Hong, Y.; Lam, J. W. Y.; Qin, A.; Tang, Y.; Tang, B. Z., Aggregation-Induced Emission: The Whole Is More Brilliant than the Parts. *Advanced Materials* **2014,** *26* (31), 5429-5479.

134. Valeur, B., Molecular Fluorescence. In *Encyclopedia of Applied Physics*, 2009; pp 477-531.

135. Yang, W.; Li, C.; Zhang, M.; Zhou, W.; Xue, R.; Liu, H.; Li, Y., Aggregation-induced emission and intermolecular charge transfer effect in triphenylamine fluorophores containing diphenylhydrazone structures. *Physical Chemistry Chemical Physics* **2016,** *18* (40), 28052-28060.

136. Jia, J.; Zhao, H., Structure-dependent reversible mechanochromism of D-π-A triphenylamine derivatives. *Tetrahedron Letters* **2019,** *60* (3), 252-259.

137. Fang, M.; Yang, J.; Liao, Q.; Gong, Y.; Xie, Z.; Chi, Z.; Peng, Q.; Li, Q.; Li, Z., Triphenylamine derivatives: different molecular packing and the corresponding mechanoluminescent or mechanochromism property. *Journal of Materials Chemistry C* **2017,** *5* (38), 9879-9885.

138. Yoshizawa, M.; Klosterman, J. K., Molecular architectures of multi-anthracene assemblies. *Chemical Society Reviews* **2014,** *43* (6), 1885-1898.

139. Sun, B.; Yang, X.; Ma, L.; Niu, C.; Wang, F.; Na, N.; Wen, J.; Ouyang, J., Design and Application of Anthracene Derivative with Aggregation-Induced Emission Charateristics for Visualization and Monitoring of Erythropoietin Unfolding. *Langmuir* **2013,** *29* (6), 1956-1962.

140. Zhao, J.; Chi, Z.; Yang, Z.; Mao, Z.; Zhang, Y.; Ubba, E.; Chi, Z., Recent progress in the mechanofluorochromism of distyrylanthracene derivatives with aggregation-induced emission. *Materials Chemistry Frontiers* **2018,** *2* (9), 1595-1608.

141. Gu, Y.; Wang, K.; Dai, Y.; Xiao, G.; Ma, Y.; Qiao, Y.; Zou, B., Pressure-Induced Emission Enhancement of Carbazole: The Restriction of Intramolecular Vibration. *The Journal of Physical Chemistry Letters* **2017,** *8* (17), 4191-4196.

142. Mei, X.; Wei, K.; Wen, G.; Liu, Z.; Lin, Z.; Zhou, Z.; Huang, L.; Yang, E.; Ling, Q., Carbazole-based diphenyl maleimides: Multi-functional smart fluorescent materials for data process and sensing for pressure, explosive and pH. *Dyes and Pigments* **2016,** *133*, 345-353.

143. Takeda, Y.; Mizuno, H.; Okada, Y.; Okazaki, M.; Minakata, S.; Penfold, T.; Fukuhara, G., Hydrostatic Pressure-Controlled Ratiometric Luminescence Responses of a Dibenzo[a,j]phenazine-Cored Mechanoluminophore. *ChemPhotoChem* **2019,** *3* (12), 1203-1211.

144. Yang, Y.; Li, A.; Ma, Z.; Liu, J.; Xu, W.; Ma, Z.; Jia, X., Dibenzo[a,c]phenazine-phenothiazine dyad: AIEE, polymorphism, distinctive mechanochromism, high sensitivity to pressure. *Dyes and Pigments* **2020,** *181*, 108575.

145. Ghosh, S.; Bhambri, H.; Singh, A. K.; Mandal, S. K.; Roy, L.; Addy, P. S., A convenient route to a vinylogous dicyano aryl based AIEgen with switchable mechanochromic luminescence properties. *Chemical Communications* **2023,** *59* (30), 4463-4466.

146. Meng, X.; Qi, G.; Li, X.; Wang, Z.; Wang, K.; Zou, B.; Ma, Y., Spiropyran-based multi-colored switching tuned by pressure and mechanical grinding. *Journal of Materials Chemistry C* **2016,** *4* (32), 7584-7588.

147. Peng, Y.-X.; Feng, F.-D.; Liu, H.-Q.; Zhang, Y.; Hu, B.; Huang, W.; Zheng, W., Switchable mechanoresponsive luminescence from traditional triphenylamine-thiophene carbaldehyde luminogens. *Dyes and Pigments* **2020,** *174*, 108110.

148. Wang, C.; Peng, D.; Pan, C., Mechanoluminescence materials for advanced artificial skin. *Sci. Bull* **2020,** *65* (14), 1147-1149.

149. Shao, Y.; Xiao, Z.; Bi, C.; Yuan, Y.; Huang, J., Origin and elimination of photocurrent hysteresis by fullerene passivation in CH3NH3PbI3 planar heterojunction solar cells. *Nature communications* **2014,** *5* (1), 5784.

150. Zhao, J.; Chi, Z.; Zhang, Y.; Mao, Z.; Yang, Z.; Ubba, E.; Chi, Z., Recent progress in the mechanofluorochromism of cyanoethylene derivatives with aggregation-induced emission. *Journal of Materials Chemistry C* **2018,** *6* (24), 6327-6353.

151. Sun, Y.; Lei, Z.; Ma, H., Twisted aggregation-induced emission luminogens (AIEgens) contribute to mechanochromism materials: a review. *Journal of Materials Chemistry C* **2022,** *10* (40), 14834-14867.

152. Hu, H.; Cheng, X.; Ma, Z.; Sijbesma, R. P.; Ma, Z., Polymer Mechanochromism from Force-Tuned Excited-State Intramolecular Proton Transfer. *Journal of the American Chemical Society* **2022,** *144* (22), 9971-9979.

153. Gong, Y.-B.; Zhang, P.; Gu, Y.-r.; Wang, J.-Q.; Han, M.-M.; Chen, C.; Zhan, X.-J.; Xie, Z.-L.; Zou, B.; Peng, Q.; Chi, Z.-G.; Li, Z., The Influence of Molecular Packing on the Emissive Behavior of Pyrene Derivatives: Mechanoluminescence and Mechanochromism. *Advanced Optical Materials* **2018,** *6* (16), 1800198.

154.   Zhang, G.; Sun, J.; Xue, P.; Zhang, Z.; Gong, P.; Peng, J.; Lu, R., Phenothiazine modified triphenylacrylonitrile derivates: AIE and mechanochromism tuned by molecular conformation. *Journal of Materials Chemistry C* **2015,** *3* (12), 2925-2932.

155.   Revoju, S.; Matuhina, A.; Canil, L.; Salonen, H.; Hiltunen, A.; Abate, A.; Vivo, P., Structure-induced optoelectronic properties of phenothiazine-based materials. *Journal of Materials Chemistry C* **2020,** *8* (44), 15486-15506.

156.   Yu, Z.; Duan, Y.; Cheng, L.; Han, Z.; Zheng, Z.; Zhou, H.; Wu, J.; Tian, Y., Aggregation induced emission in the rotatable molecules: the essential role of molecular interaction. *Journal of Materials Chemistry* **2012,** *22* (33), 16927-16932.

157.   Peng, Y.-X.; Liu, H.-Q.; Huang, W.; Tao, T., Isomeric Pair of E/Z Tetraphenylethene-Cored Luminogens Showing Distinguishing Mechanoresponsive Luminescence Turn-On and Two-Color Behavior. *The Journal of Physical Chemistry C* **2022,** *126* (14), 6491-6498.

158.   Liu, H.; Gu, Y.; Dai, Y.; Wang, K.; Zhang, S.; Chen, G.; Zou, B.; Yang, B., Pressure-Induced Blue-Shifted and Enhanced Emission: A Cooperative Effect between Aggregation-Induced Emission and Energy-Transfer Suppression. *Journal of the American Chemical Society* **2020,** *142* (3), 1153-1158.

159.   Chakraborty, M.; Chakravarty, M., Varied optical features and mechanofluorochromism in dicyanovinyl- vs. cyanoacrylicacid-linked twisted π-conjugates: A potential reusable platform for security applications. *Materials Today Chemistry* **2024,** *35*, 101836.

160.   Wei, J.; Liang, B.; Cheng, X.; Zhang, Z.; Zhang, H.; Wang, Y., High-contrast and reversible mechanochromic luminescence of a D–π–A compound with a twisted molecular conformation. *RSC Advances* **2015,** *5* (88), 71903-71910.

161.   Devi, P.; Thakur, A.; Chopra, S.; Kaur, N.; Kumar, P.; Singh, N.; Kumar, M.; Shivaprasad, S. M.; Nayak, M. K., Ultrasensitive and selective sensing of selenium using nitrogen-rich ligand interfaced carbon quantum dots. *ACS applied materials & interfaces* **2017,** *9* (15), 13448-13456.

162.   Lu, W.; Jiao, Y.; Gao, Y.; Qiao, J.; Mozneb, M.; Shuang, S.; Dong, C.; Li, C.-z., Bright yellow fluorescent carbon dots as a multifunctional sensing platform for the label-free detection of fluoroquinolones and histidine. *ACS Applied Materials & Interfaces* **2018,** *10* (49), 42915-42924.

163.   Wu, D.; Gong, W.; Yao, H.; Huang, L.; Lin, Z.; Ling, Q., Highly efficient solid-state emission of diphenylfumaronitriles with full-color AIE, and application in explosive sensing, data storage and WLEDs. *Dyes and Pigments* **2020,** *172*, 107829.

164.   Saito, D.; Ogawa, T.; Yoshida, M.; Takayama, J.; Hiura, S.; Murayama, A.; Kobayashi, A.; Kato, M., Intense Red-Blue Luminescence Based on Superfine Control of Metal–Metal Interactions for Self-Assembled Platinum (II) Complexes. *Angewandte Chemie International Edition* **2020,** *59* (42), 18723-18730.

165.   Philp, D.; Stoddart, J. F., Self-assembly in natural and unnatural systems. *Angewandte Chemie International Edition in English* **1996,** *35* (11), 1154-1196.

166.   Whitesides, G. M.; Grzybowski, B., Self-assembly at all scales. *Science* **2002,** *295* (5564), 2418-2421.

167.   Nie, F.; Zhou, B.; Wang, K.-Z.; Yan, D., Highly tunable ultralong room-temperature phosphorescence from ionic supramolecular adhesives for multifunctional applications. *Chemical Engineering Journal* **2022,** *430*, 133084.

168.   Yan, D.; Bučar, D.-K.; Delori, A.; Patel, B.; Lloyd, G. O.; Jones, W.; Duan, X., Ultrasound-Assisted Construction of Halogen-Bonded Nanosized Cocrystals That Exhibit Thermosensitive Luminescence. *Chemistry – A European Journal* **2013,** *19* (25), 8213-8219.

169.   Zhong, H.; Li, L.; Zhu, S.; Wang, Y., Controllable self-assembly of thiophene-based π-conjugated molecule and further construction of pillar[5]arene-based host-guest white-light emission system. *Frontiers in Chemistry* **2022,** *10*.

170.   Li, H.; Wu, J.; Li, H.; Xu, Y.; Zheng, J.; Shi, Q.; Kang, H.; Zhao, S.; Zhang, L.; Wang, R., Designing π-conjugated polypyrene nanoflowers formed with meso-and microporous nanosheets for high-performance anode of potassium ion batteries. *Chemical Engineering Journal* **2022,** *430*, 132704.

171.   Huang, R.; Wang, C.; Tan, D.; Wang, K.; Zou, B.; Shao, Y.; Liu, T.; Peng, H.; Liu, X.; Fang, Y., Single-Fluorophore-Based Organic Crystals with Distinct Conformers Enabling Wide-Range Excitation-Dependent Emissions. *Angewandte Chemie International Edition* **2022,** *61* (41), e202211106.

172.   Xu, Z.; Zhang, Z.; Jin, X.; Liao, Q.; Fu, H., Polymorph-Dependent Green, Yellow, and Red Emissions of Organic Crystals for Laser Applications. *Chemistry–An Asian Journal* **2017,** *12* (23), 2985-2990.

173.   Stupp, S. I.; Palmer, L. C., Supramolecular chemistry and self-assembly in organic materials design. *Chemistry of Materials* **2014,** *26* (1), 507-518.

174.   Knaapila, M.; Dias, F.; Garamus, V.; Almásy, L.; Torkkeli, M.; Leppänen, K.; Galbrecht, F.; Preis, E.; Burrows, H.; Scherf, U., Influence of side chain length on the self-assembly of hairy-

rod poly (9, 9-dialkylfluorene) s in the poor solvent methylcyclohexane. *Macromolecules* **2007,** *40* (26), 9398-9405.

175.   Kundu, S.; Chowdhury, A.; Nandi, S.; Bhattacharyya, K.; Patra, A., Deciphering the evolution of supramolecular nanofibers in solution and solid-state: a combined microscopic and spectroscopic approach. *Chemical Science* **2021,** *12* (16), 5874-5882.

176.   Madsen, M.; Gothelf, K. V., Chemistries for DNA nanotechnology. *Chemical reviews* **2019,** *119* (10), 6384-6458.

177.   Mothika, V. S.; Räupke, A.; Brinkmann, K. O.; Riedl, T.; Brunklaus, G.; Scherf, U., Nanometer-Thick Conjugated Microporous Polymer Films for Selective and Sensitive Vapor-Phase TNT Detection. *ACS Applied Nano Materials* **2018**.

178.   Kumar, V.; Maiti, B.; Chini, M. K.; De, P.; Satapathi, S., Multimodal Fluorescent Polymer Sensor for Highly Sensitive Detection of Nitroaromatics. *Scientific Reports* **2019,** *9*.

179.   Chen, L.; Liu, D.; Peng, J.; Du, Q.; He, H., Ratiometric fluorescence sensing of metal-organic frameworks: Tactics and perspectives. *Coordination Chemistry Reviews* **2020,** *404*, 213113.

180.   Xu, B.; Wu, X.; Li, H.; Tong, H.; Wang, L., Selective detection of TNT and picric acid by conjugated polymer film sensors with donor–acceptor architecture. *Macromolecules* **2011,** *44* (13), 5089-5092.

181.   Goudappagouda; Dongre, S. D.; Das, T.; Santhosh Babu, S., Dual mode selective detection and differentiation of TNT from other nitroaromatic compounds. *Journal of Materials Chemistry A* **2020,** *8* (21), 10767-10771.

182.   Giri, D.; Islam, S. N.; Patra, S. K., Synthesis and characterization of 1, 2, 3-triazole appended polythiophene based reusable fluorescent probe for the efficient detection of trace nitroaromatics. *Polymer* **2018,** *134*, 242-253.

183.   Mothika, V. S.; Räupke, A.; Brinkmann, K. O.; Riedl, T.; Brunklaus, G.; Scherf, U., Nanometer-Thick Conjugated Microporous Polymer Films for Selective and Sensitive Vapor-Phase TNT Detection. *ACS Applied Nano Materials* **2018,** *1* (11), 6483-6492.

184.   Alam, P.; Das, P.; Climent, C.; Karanam, M.; Casanova, D.; Choudhury, A.; Alemany, P.; Jana, N. R.; Laskar, I., Facile tuning of the aggregation-induced emission wavelength in a common framework of a cyclometalated iridium (iii) complex: micellar encapsulated probe in cellular imaging. *Journal of Materials Chemistry C* **2014,** *2* (28), 5615-5628.

185. Alam, P.; Karanam, M.; Choudhury, A. R.; Laskar, I. R., One-pot synthesis of strong solid state emitting mono-cyclometalated iridium (iii) complexes: study of their aggregation induced enhanced phosphorescence. *Dalton Transactions* **2012,** *41* (31), 9276-9279.

186. Senthamizhan, A.; Celebioglu, A.; Bayir, S.; Gorur, M.; Doganci, E.; Yilmaz, F.; Uyar, T., Highly Fluorescent Pyrene-Functional Polystyrene Copolymer Nanofibers for Enhanced Sensing Performance of TNT. *ACS Appl Mater Interfaces* **2015,** *7* (38), 21038-46.

187. Li, C.; Chen, G.; Zhang, Y.; Wu, F.; Wang, Q., Advanced fluorescence imaging technology in the near-infrared-II window for biomedical applications. *Journal of the American Chemical Society* **2020,** *142* (35), 14789-14804.

188. Zhang, H.; Li, G.; Guo, X.; Zhang, K.; Zhang, B.; Guo, X.; Li, Y.; Fan, J.; Wang, Z.; Ma, D., High-Performance Ultraviolet Organic Light-Emitting Diode Enabled by High-Lying Reverse Intersystem Crossing. *Angewandte Chemie* **2021,** *133* (41), 22415-22421.

189. Jiang, R.; Wu, X.; Liu, H.; Guo, J.; Zou, D.; Zhao, Z.; Tang, B. Z., High-Performance Orange–Red Organic Light-Emitting Diodes with External Quantum Efficiencies Reaching 33.5% based on Carbonyl-Containing Delayed Fluorescence Molecules. *Advanced Science* **2022,** *9* (3), 2104435.

190. Liu, H.; Ren, D.-D.; Gao, P.-F.; Zhang, K.; Wu, Y.-P.; Fu, H.-R.; Ma, L.-F., Multicolor-tunable room-temperature afterglow and circularly polarized luminescence in chirality-induced coordination assemblies. *Chemical Science* **2022,** *13* (46), 13922-13929.

191. Liu, W.; Li, S.; Xie, Z.; Huang, K.; Yan, K.; Zhao, Y.; Redshaw, C.; Feng, X.; Tang, B. Z., Molecular Engineering toward Broad Color-Tunable Emission of Pyrene-Based Aggregation-Induced Emission Luminogens. *Advanced Optical Materials* **2024**, 2400301.

192. Huang, R.; Wang, C.; Tan, D.; Wang, K.; Zou, B.; Shao, Y.; Liu, T.; Peng, H.; Liu, X.; Fang, Y., Single-Fluorophore-Based Organic Crystals with Distinct Conformers Enabling Wide-Range Excitation-Dependent Emissions. *Angewandte Chemie* **2022,** *134* (41), e202211106.

193. Xu, Z.; Zhang, Z.; Jin, X.; Liao, Q.; Fu, H., Polymorph-Dependent Green, Yellow, and Red Emissions of Organic Crystals for Laser Applications. *Chemistry – An Asian Journal* **2017,** *12* (23), 2985-2990.

194. Fei, G.; Li, S.; Liu, Y.; Carney, J. B.; Chen, T.; Li, Y.; Gao, X.; Chen, J.; Chen, P.; Yue, Y., Structure–activity strategies for mechanically responsive fluorescent materials: a molecular perspective. *Chemical Communications* **2024,** *60* (1), 10-25.

195. Yuan, H.; Wang, K.; Yang, K.; Liu, B.; Zou, B., Luminescence Properties of Compressed Tetraphenylethene: The Role of Intermolecular Interactions. *The Journal of Physical Chemistry Letters* **2014,** *5* (17), 2968-2973.

196. Shi, P.; Duan, Y.; Wei, W.; Xu, Z.; Li, Z.; Han, T., A turn-on type mechanochromic fluorescent material based on defect-induced emission: implication for pressure sensing and mechanical printing. *Journal of Materials Chemistry C* **2018,** *6* (10), 2476-2482.

197. Shao, B.; Jin, R.; Li, A.; Liu, Y.; Li, B.; Xu, S.; Xu, W.; Xu, B.; Tian, W., Luminescent switching and structural transition through multiple external stimuli based on organic molecular polymorphs. *Journal of Materials Chemistry C* **2019,** *7* (11), 3263-3268.

198. Meng, X.; Chen, C.; Qi, G.; Li, X.; Wang, K.; Zou, B.; Ma, Y., From Two, to Three, to Multi-Color Switches: Developing AIEgen-Based Mechanochromic Materials. *ChemNanoMat* **2017,** *3* (8), 569-574.

199. Huang, Z.; Tang, F.; He, F.; Kong, L.; Huang, J.; Yang, J.; Ding, A., Pyrene and triphenylamine substituted cyanostyrene and cyanostilbene derivatives with dual-state emission for high-contrast mechanofluorochromism and cell imaging. *Organic Chemistry Frontiers* **2022,** *9* (19), 5118-5124.

200. Xiong, Y.; Huang, J.; Liu, Y.; Xiao, B.; Xu, B.; Zhao, Z.; Tang, B. Z., High-contrast luminescence dependent on polymorphism and mechanochromism of AIE-active (4-(phenothiazin-10-yl)phenyl)(pyren-1-yl)methanone. *Journal of Materials Chemistry C* **2020,** *8* (7), 2460-2466.

201. Feng, X.; Wang, X.; Redshaw, C.; Tang, B. Z., Aggregation behaviour of pyrene-based luminescent materials, from molecular design and optical properties to application. *Chemical Society Reviews* **2023**.

MATERIALS, METHODS, AND INSTRUMENTATIONS

Chapter 2. Materials, Methods, and Instrumentations

It contains the details of the chemicals used for the synthesis, calculation methods, and instruments for all the experiments included in the thesis.

2.1 Materials

2.1.1   Used Reagents

1-bromopyrene, 5-acetyl thiophene boronic acid, thiophene-2-aldehyde, pyridine-2-aldehyde, 4-vinylphenylboronic acid, tetrakis(triphenylphosphine)palladium(0), 4-(2-Pyridyl) benzaldehyde, and N, N-diphenyl amine was purchased from TCI chemicals. 2-bromopyridine, Cyanuric chloride, and iridium(III) chloride hydrate $IrCl_3.xH_2O$ were purchased from Alfa Aesar company. DNP (2,4-dinitrophenol), 4NT (4-nitro-toluene), 4-NBA (4-nitro-benzoic acid), NB (Nitrobenzene), 3,5 DNB (3,5-di-nitro benzene), 4ANP (4-Amino nitrophenol), 3NBA (3-nitro-benzoic acid), PA (Picric acid) and DNClB (1-chloro 2,4-dinitro benzene) were purchased from Merck company. Higher explosives such as TNT (2,4,6-trinitrotoluene), A. Nitrate (Ammonium nitrate), PETN (Pentaerythritol tetranitrate), HMX (High melting explosive), and RDX (Royal demolition explosive) were used at TBRL DRDO lab through a collaborative project.

Sodium carbonate (Na_2CO_3), potassium carbonate (K_2CO_3), triphenylphosphine (PPh_3), Polyethylene glycol (PEG), anhydrous aluminum chloride ($AlCl_3$), and the UV grades solvents such as THF, ethanol, toluene, hexane, cyclohexane, carbon tetrachloride (CCl_4), acetone, diethyl ether, dichloromethane (DCM), methanol, N, N-dimethylformamide (DMF), and dimethyl sulfoxide (DMSO) procured from Spectrochem. 2-ethoxyethanol, sodium hydroxide (NaOH), ethanol (C_2H_5OH), and sulfuric acid (H_2SO_4) were purchased from Spectrochem and Merck company.

2.2 Methods

2.2.1 Synthesis

In the respective chapters, synthetic methods for each probe and intermediate were included. All the photophysical property studies were performed after the structural characterization of the probe molecules.

2.2.2 Sample preparation to investigate the 'Aggregation-induced Emission (AIE)' property

A set of solutions of AIE compounds was prepared in the range of 10^{-3} to 10^{-5} M. For sample preparations, two solvents were chosen, one in which the AIE compound is soluble and the other, the AIE compounds are insoluble, but the two solvents must be miscible. Then different samples (0-95%) were prepared by adding different volume fractions (f_w) of two solvents in a 5 ml vial. For example, concentration (conc). of 0% water: 10^{-4} M of the compound in 0.5 ml THF (rest is 4.5 mL THF); conc. of 30% water: 10^{-4} M of the compound in 0.5 ml (rest is 3.0 ml THF and 1.5 ml of water), conc. of 60% water: 10^{-4} M of compound in 0.5 ml (rest is 1.5 ml THF and 3 ml water), conc. of 90% water: 10^{-4} M of complex in 0.5 ml (rest is 4.5 ml of water).

2.2.3 Solvatochromism

The solvent effect on the emission spectra of the probe is interpreted in terms of the Lippert-Mataga equation. Lippert Mataga describes the Stoke shifts in terms of the dipole moment in the excited state. The Lippert-Mataga equation describes the energy related to the refractive index (η), and the dielectric constant (ℇ) of the solvent is given by the equation below.

$$(\vartheta_{ab} - \vartheta_{fl}) = \left(\frac{2(\mu_e - \mu_g)^2}{hca^3}\right)\Delta f + constant$$

$$\text{Where } \Delta f = \frac{(\varepsilon - 1)}{(2\varepsilon + 1)} - \frac{(n^2 - 1)}{(2n^2 + 1)}$$

ℇ is the dielectric constant of a particular solvent, n is the refractive index of a specific solvent, h is Planck's constant, c is the velocity of light, 'a' is the Ongsager cavity radius, and μ_G and μ_E is the ground state, and excited state dipole moment of the fluorophore, respectively Δf is the solvent polarity parameters. $\Delta v = v_{abs} - v_{em}$ is the solvatochromic shift (cm^{-1}) between the maxima of absorption and fluorescence emission [$v_{abs} = 1/\lambda_{abs(max)}$, $v_{em} = 1/\lambda_{em(max)}$].

2.2.4 Experimental procedure for detection limit calculations

The emission intensity of the synthesized compounds on thin film and in solution without an analyte was measured 10-12 times, and the standard deviation of blank measurements was calculated to determine the Signal/Noise ratio. The following equation is used to determine the detection limit.

Detection limit = 3σ/m, where 'σ' is the standard deviation of blank measurements, and 'm' is the slope between the plot of PL intensity of the probe in the presence of analyte versus analyte concentration.[1-3]

2.3 Instrumentation

2.3.1 UV-Visible spectrophotometer

It is a spectroscopic tool that measures the amount of radiation that is absorbed in proportion to its frequency or wavelength when it interacts with a sample. The relative energies of the ground and excited states are changed as a result of environmental factors, and this change results in spectrum changes. The absorbance (A) of an absorber (concentration C) having a molar extinction coefficient ε at wavelength λ is given in the following equation.

$$A = \log (I_{o/} I) = \varepsilon \lambda \; cl$$

where 'A' is absorbance (optical density), I_o, and I represent the intensity of the incident and transmitted light, respectively, c is the concentration of the light-absorbing species, and l is the path length of the light-absorbing medium in a decimeter. A matched pair of 10 cm quartz cuvettes (Hellma, 1 cm light path, capacity 3.5 ml, Model: 100-QS) was used for absorption measurements.

The Shimadzu Spectrophotometer (model UV-1800 and 2550) was used to record UV-VIS absorption spectra. The Shimadzu UV-2450 UV-VIS spectrophotometer recorded the solid-state UV-VIS absorption spectra in reflectance mode (using the integrated sphere method) and then converted the reflectance values to absorbance. The block diagram of the instrumentation is shown in Fig. 2.1.
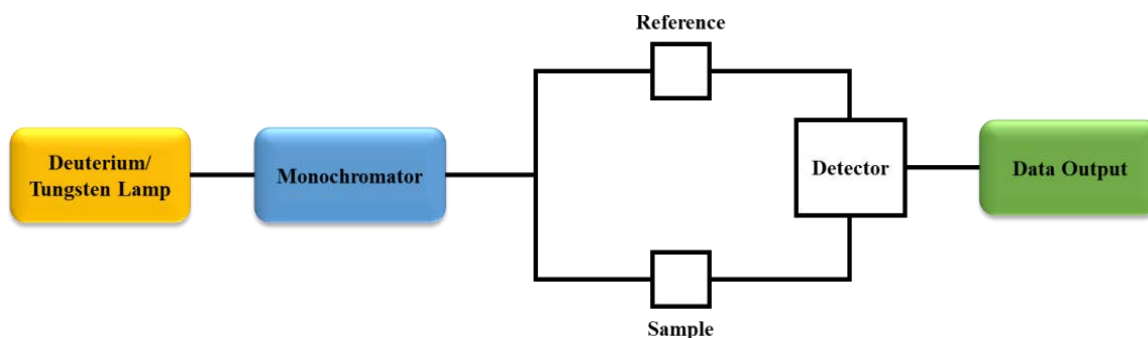
Figure 2.1 Schematic representation of UV-visible spectrometer

2.3.2 Steady-state Spectrofluorometer

In my present thesis, photoluminescence (PL) spectra were recorded on a Horiba Jobin Yvon Spectrofluorometer (FluoroMax-4) and Horiba 'FluoroLog-3' Spectrofluorimeter. To perform a qualitative or quantitative study, the spectrofluorometer irradiates a sample with a suitable excitation light source and detects the fluorescence emitted from the irradiated sample. The block diagram of the instrument is shown in Fig. 2.2. The brief description of its components is given below:
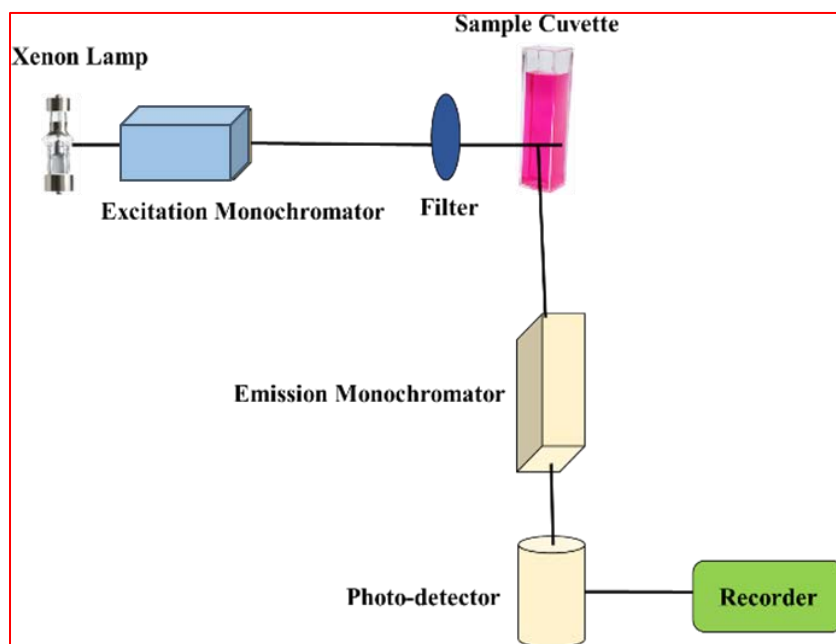
Figure 2.2 Block diagram of a steady-state spectrofluorometer

This instrument is equipped with a light source of 1905-OFR 150-W Xenon lamp. This instrument has a 240-850 nm scan range. A cell containing the sample is kept in the cell holder. The photomultiplier tube (PMT) measures the fluorescence intensity after the emission monochromator receives the fluorescence the sample emits. The photomultiplier tube used in this effective response is the detector for the photometry and monitor sides. This preserves maximum resolution and instant reproducibility. The sample was taken in a Quartz cuvette (Hellma, 1 cm light path, capacity 3.5 ml, Model: 101-QS) with four transparent walls to measure the excitation and emission spectra.

2.3.3 Quantum Yield (QY) Measurement

The quantum yields of solid and liquid forms of the compounds were measured on the Quanta Phi Horiba integrating sphere, which has an accessory of quantum yield (QY) and CIE measurement for the fluorometers. The solid powdered compound was placed in the cups provided. Additionally, it has a bottom-loading drawer for solid/thin film samples that prevents contamination.[4] The lifetime decay [time-correlated single photon counting (TCSPC)] spectra of the iridium(III) complex and organic compounds in different solvents and solids were obtained with a spectrofluorometer HORIBA Jobin Yvon FluoroCube at BITS Pilani, Pilani campus.

2.4 Computational study

The Gaussian 09 and Gaussian 16 software suites were used to perform the Density Functional Theory (DFT) computations.[5] Beckes three-parameter hybrid exchange functional with the Lee-Yang–Parr gradient-corrected correlation (B3LYP functional),[6,7] for larger correlation (CAM-B3LYP), Perdew–Burke-Ernzerhof (PBE functional), and the basis set 6-31G(+), 6- 31G(++)(d,p), LANL2DZ (Los Alamos National Laboratory 2 double-ζ), the level was used in both the DFT and TD-DFT methods. All calculations were performed using the Integral Equation Formalism-Polarizable Continuum Model (IEF-PCM) for the solvents.[8]

2.5 Crystallographic Details

Single crystal X-ray diffraction data was collected on Rigaku XtaLABmini X-ray diffractometer equipped with Mercury CCD detector with graphite monochromatic Mo-Kα radiation ($\lambda = 0.71073$ Å) at 100.0 (2) K using ω scans. The data was reduced using CrysAlisPro 41_64.93a software.[9] The crystal structures were solved using Olex[10] package[11] equipped with XT[12] and were further refined using XL.[13] Crystal packing and interaction diagrams were created using Mercury.[14]

2.6 Ultrafast Transient Absorption Spectroscopy (TAS)

The transient absorption setup has been described elsewhere.[15] An amplified laser (Libra, Coherent, USA) is the primary light source and provides pulses of 75 fs FWHM, with a wavelength of 800 nm and energy of 3.6 mJ at a repetition rate of 1 kHz. About 1.35 mJ of the output is used to pump, an optical parametric amplifier (OPA – TOPAS, Light Conversion, Lithuania) to get tunable pump pulses. For the present experiments, λ_{pump} = 400 nm. A small fraction of the remaining part of the 800 nm light is focused into a CaF_2 crystal to generate a white continuum (WLC) with a range of 280–950 nm, which is used as a probe to interrogate the system. The white light is divided into probe and reference beams using a beam splitter. The reference beam is used to correct real-time intensity fluctuation of the white light continuum. The pump pulse is passed through a synchronized mechanical chopper to cut each alternative pump pulse, creating a succession of "pump" and "no pump" situations. Pump pulse (400 nm) and probe pulses are spatially overlapped on the sample solution, kept in a rotating cell with a path length of 1 mm so that an intense pump pulse cannot damage the sample. A variable delay is provided to the probe pulse in order to follow the time evolution of excited state processes. The effect of rotational diffusion was corrected by adjusting the polarization to the magic angle (54.7°). Steady state absorbance of the sample before and after the transient absorption experiment is monitored so as to check the effect of irradiation of pump light on the sample. All the extracted data have chirp corrected for the removal of the group velocity dispersion (GVD) and fitted using IGOR Pro software. Global analysis of the TA data was done using Glotaran 1.5.1 software. Single-value decomposition was done to obtain the evolution-associated spectra (EDS) and their corresponding lifetimes.[16]

2.7 Other instruments

The ^{1}H NMR (400 MHz) and ^{13}C NMR (100 MHz) spectra were recorded on a Bruker Advance 400 spectrometer using CDCl$_3$ (TMS as an internal standard) as the solvent, and ^{31}P spectra were recorded using phosphoric acid as an internal reference.

High-resolution mass spectra (HRMS) were recorded on an Agilent Q-TOF LC-MS spectrometer in positive electrospray ionization (ESI) mode. The variation in particle size in the aggregated state was recorded by dynamic light scattering (DLS) experiment, using Anton Paar Litesizer 500 at 25 °C temperature. Raman analysis was studied by the HORIBASCI Raman instrument (model no. LabRAM HR EVO) using excitation lasers with 833 nm wavelength. A microscope version, XT Platform version, XT UI version, Modal- 'APREO S" FE-SEM were used to investigate the morphology of the synthesized samples. A JEOL JEM2100 PLUS High-resolution Transmission Electron Microscope was used for recording HR-TEM analysis. Thermogravimetric analysis (TGA) was performed by TGA-50, SHIMADZU equipment at 10 °C/min, under a nitrogen atmosphere. The infrared spectrum was recorded on a Shimadzu FTIR spectrophotometer (IRAffinity-1S). Cyclic voltammetry (CV) measurements were carried out for the sample using CH Instruments company's model CHI601E (220V AC 0.4A) at the Chemistry department, BITS Pilani, Pilani Campus. Tetrabutylammonium hexafluorophosphate (NBu$_4$PF$_6$) was used as the electrolyte in acetonitrile solvent at a scan rate of 100 mVs^{-1}. The working electrode-platinum disc, Ag/AgCl as a pseudo reference electrode, and Pt as a counter electrode were used for the experiment. The solutions were prepared in THF, and tetrabutylammonium hexafluorophosphate (0.1 M) was used as a supporting electrolyte. The grinding force or mechanical stress in mechanoflorochromism was recorded using the Rheometer instrument, using Anton Paar MCR-92. Powder X-ray analysis was performed using a Rigaku Mini Flex II diffractometer with incident radiation of Cu-Kα.

2.8 References

1.   M.-H. Yang, P. Thirupathi and K.-H. Lee, *Organic Letters*, 2011, **13**, 5028-5031.

2.   L. N. Neupane, J. M. Kim, C. R. Lohani and K.-H. Lee, *Journal of Materials Chemistry*, 2012, **22**, 4003-4008.

3.   S. Kaur, V. Bhalla, V. Vij and M. Kumar, *Journal of Materials Chemistry C*, 2014, **2**, 3936-3941.

4.   N. Hasebe, K. Suzuki, H. Horiuchi, H. Suzuki, T. Yoshihara, T. Okutsu and S. Tobita, *Analytical Chemistry*, 2015, **87**, 2360-2366.

5.   A. D. Becke, *The Journal of Chemical Physics*, 1993, **98**, 5648-5652.

6.   S. Marković and J. Tošović, *The Journal of Physical Chemistry A*, 2015, **119**, 9352- 9362.

7.   G. M. Morris, R. Huey, W. Lindstrom, M. F. Sanner, R. K. Belew, D. S. Goodsell and A. J. Olson, *Journal of Computational Chemistry*, 2009, **30**, 2785-2791.

8.   H. Li and J. H. Jensen, *Journal of Computational Chemistry*, 2004, **25**, 1449-1462.

9.   Miclaus, M. O.; Kacso, I. E.; Martin, F. A.; David, L.; Pop, M. M.; Filip, C.; Filip, X., *Journal of Pharmaceutical Sciences,* 2015, *104* (11), 3782-3788.

10.   Dolomanov, O. V.; Bourhis, L. J.; Gildea, R. J.; Howard, J. A.; Puschmann, H., *Journal of applied crystallography,* 2009, *42* (2), 339-341.

11.   Sheldrick, G. M., *Structural Chemistry,* 2015**,** *71* (1), 3-8.

12.   Sheldrick, G. M., *Acta Crystallographica Section A: Foundations of Crystallography,* 2008**,** *64* (1), 112-122.

13. Macrae, C. F.; Bruno, I. J.; Chisholm, J. A.; Edgington, P. R.; McCabe, P.; Pidcock, E.; Rodriguez-Monge, L.; Taylor, R.; Streek, J.; Wood, P. A., *Journal of Applied Crystallography*, 2008, *41* (2), 466-470.

14. Das, S.; Rakshit, S.; Datta, A., *The Journal of Physical Chemistry C,* 2020, *124* (51), 28313-28322.

15. 2. Mosca, L.; Khnayzer, R. S.; Lazorski, M. S.; Danilov, E. O.; Castellano, F. N.; Anzenbacher Jr, P., *Chemistry–A European Journal,* 2015, *21* (10), 4056-4064.

PYRENE-BASED AIEE-ACTIVE VERTICALLY GROWN LUMINESCENT MATERIAL FOR SELECTIVE AND SENSITIVE DETECTION OF TNT VAPOR

Chapter 3. Pyrene-based AIEE-active Vertically Grown Luminescent Material for Selective and Sensitive Detection of TNT Vapor

3.1 INTRODUCTION

Real field and reliable detection of explosive substances is critically important. For example, in a civilian context, fixed monitoring stations in airports are used to prevent explosives-based terrorist attacks. Explosive detection systems need to be able to detect a large range of explosive materials, including both traditional high-explosive materials, such as TNT, and chemicals used in IEDs (Improvised Explosive Devices), such as ammonium nitrate etc.[1-2] Trinitrotoluene (TNT) is the most common explosive, also considered a hazardous waste by the U.S. Environmental Protection Agency (EPA), with a maximum permissible level in drinking water being 2 ppb.[3-4] The increased amount of TNT in water severely affects living organisms. It causes several diseases like headache, anemia, and skin irritation, and the excess amount of TNT results in serious liver, eye, and neurological damage. This calls for developing a rapid and reliable sensor for detecting buried unexploded explosives and locating underwater mines.

Detection of trace amounts of TNT in an aqueous medium and the TNT vapor from the atmosphere is essential. It is challenging to detect explosives from the vapor phase as the vapor pressures of nitro-based explosive compounds (e.g., TNT, RDX, PETN, etc) under ambient conditions are very low (10^{-5}-10^{-15} torr).[5] Many techniques are available for detecting explosives, such as trained canines, metal detectors, ion mobility spectrometry (IMS), Raman mass spectrometry, gas chromatography, sensors based on electrochemistry, colorimetry etc.[6-9] While each method has their own advantages, still they are not free from various problems. Many of these equipment is very costly and bulkier in size. Fluorescent-based methods provide us with many benefits over conventional detection techniques, such as low cost, good portability, and high sensitivity.[5] The source and detector of a fluorescence method could be easily incorporated into a

handheld device to detect explosives. It would be one of the important methods for onsite detection of explosive materials. In this context, several research across the world has significant contributions towards polymeric materials to detect TNT.[10-15] Recent research on dual-state TNT detection using anthracenyl polymeric probes and fluoroarene-based organogelators is inspiring to detect TNT and other nitro-based explosives.[16-17] Several explosive sensing materials based on small molecules, conjugated polymers, self-assembled organic nanomaterials, and metal-organic frameworks have been studied for both solution and vapor-phase explosives detection up to detection limits to parts per trillion (ppt).[18-29] Solid state light emitting small organic molecules are preferred for the on-site detection of TNT. Solid-state emitters are well explored for the detection of picric acid may be due to its lower LUMO energy (-4.73 eV) favoring electron transfer. Moreover, the existence of picrate ion in an aqueous medium favours the extent of overlapping of the absorbance of picrate with the emission of the probe, facilitating the energy transfer.[30-31] On the other hand, selective and quick response solid state emitting TNT sensing probes are relatively sparse. [32-33] Some of the small molecules containing π-electron rich fluorophore such as pyrene-based molecules are reported for sensitive detection of nitro-based explosives (TNP and DNP) in solution phase.[34-36].

'Aggregation-induced Emission' (AIE) active compounds are an important class of fluorescent compounds strongly emissive in the solid state as compared to traditional emissive materials. There are several reports found where AIE active compounds have been used for sensing TNT from the solution phase.[37-39] An important parameter for fluorescent sensors is quenching efficiency, which is determined by the Stern-Volmer quenching constant (Ksv).[40] From the literature survey, it was observed that designing small molecules for explosive sensing depends on many factors: the probe should have appropriately aligned LUMO levels with the analyte for the effective electron transfer from the probe to the analyte, the significant extent of overlapping of absorption spectra of analyte and emission spectra of probe molecule for efficient energy transfer, an extended excited state lifetime of the probe to maximize the interaction time with the analyte, a high quantum yield and large surface contact area of the probe [5, 41] Additionally, fluorophore should be π-electron rich and planar in nature, and at the same time to prevent the intermolecular π - π staking interaction and excimer formation, bulkier substituent must be present at the periphery of the chromophore.[5, 42-43]

In one of our previous studies, a push-pull type pyrene substituted with that of nitrogen-containing heterocycles was used for ultrasensitive detection of picric acid.[36] In this work, a pyrene triazine framework was chosen as an electron-rich D-A (donor-acceptor) system, and further modulation was done by substituting bulkier phenyl groups. In the present design strategy, electron-rich pyrene is connected with nitrogen-rich triazine for better electronic interaction with electron-deficient TNT molecules. Additionally, rotor groups were introduced by replacing Cl of the triazine ring[36] to make the molecule highly emissive in the solid state. Initially, with the help of computational calculations, the molecules were optimized, and the LUMO of the probe and the LUMO of the TNT were found in good alignment for efficient Photo-induced Electron Transfer (PET). The designed molecule (PyTrDA) was highly sensitive and selective towards TNT. It was used to recognize the TNT in solution (ppt level) and vapor phase (ppb level) sensing of TNT. Interestingly, it detected the TNT vapor within 10s from the vapor phase with a visible emission quenching response.

3.2 EXPERIMENTAL SECTION

Synthesis of 2,4-dichloro-6-(pyren-1-yl)-1,3,5-triazine (PyTr) was performed using a previously reported procedure.[44] PyTr is a precursor for synthesizing probe molecules (VinTr and PyTrDA) shown in Scheme 3.1. To synthesize VinTr, a Suzuki coupling reaction between PyTr and 4-vinylphenylboronic acid was performed (Scheme 3.1, the procedure given below (a)). PyTrDA was synthesized using C-N coupling using a strong base (n-BuLi) at low temperatures (-60 to 0 °C) and an inert atmosphere. The detailed synthetic procedure (Scheme 3.1, the procedure given below (b)). Synthesized compounds VinTr and PyTrDA were characterized through NMR and HRMS (Fig 3.1 to Fig 3.6).

3.2.1 Synthesis and characterization
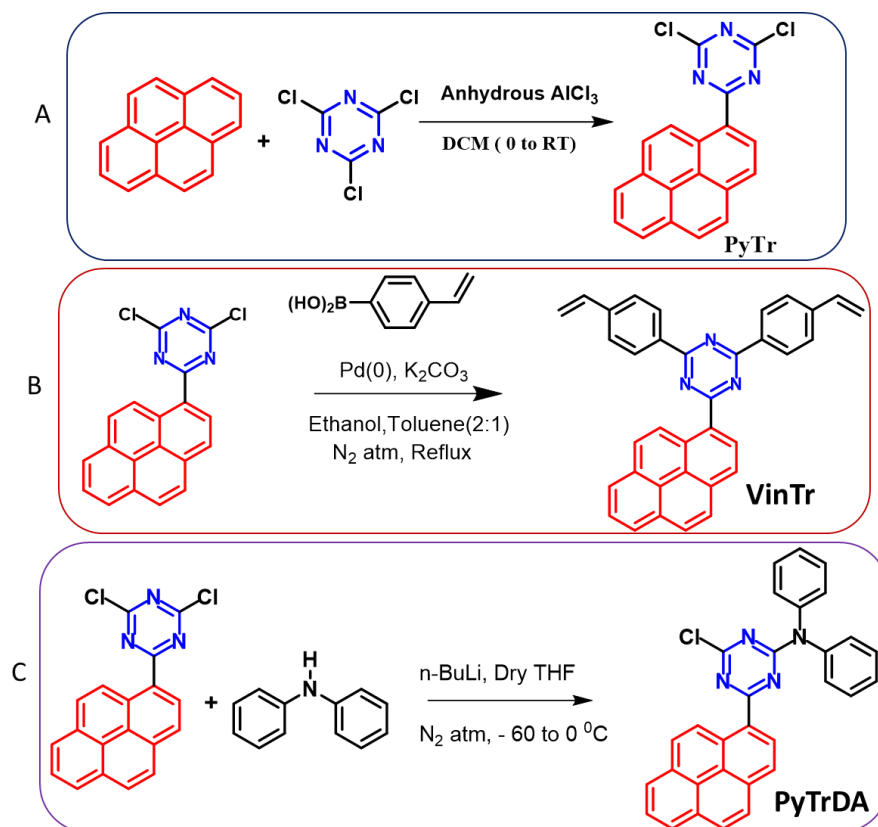
Scheme 3.1 Synthetic route for molecules (PyTr, VinTr and PyTrDA)

(a) Synthesis of 2-(pyren-1-yl)-4,6-bis(4-vinylphenyl)-1,3,5-triazine (VinTr) from PyTr

In a 25 ml round bottom flask, a mixture of 4-vinylphenylboronic acid (88.73 mg, 0.60 mmol) and PyTr (100 mg, 0.23 mmol) in the solvent mixture of toluene/ethanol (2:1, 4ml) stirred with N_2 gas purged for 5 minutes. Then, tetrakis(triphenylphosphine)palladium(0) catalyst (11.5 mg, 0.01 mmol) was added and stirred for 2-3 min, followed by the addition of K_2CO_3 (207.3 mg, 1.5 mmol). It was refluxed for 10-12 h with intermittent TLC observation and then cooled to room temperature. The reaction was quenched with the addition of water, then extracted with ethyl acetate (20ml*2) and washed with brine solution, finally dried with anhydrous Na_2SO_4, and the crude solid product was purified by column chromatography, with Hexane: Ethyl acetate (98:2) as eluent. Yield, 79.4 %. The isolated compound was characterized by NMR and HRMS.

^{1}H NMR (400 MHz, Chloroform-*d*) δ 9.53 (d, *J* = 9.4 Hz, 1H), 9.04 (d, *J* = 8.1 Hz, 1H), 8.88 – 8.73 (m, 4H), 8.35 (d, *J* = 8.1 Hz, 1H), 8.33 – 8.25 (m, 3H), 8.25 – 8.13 (m, 2H), 8.09 (t, *J* = 7.6 Hz, 1H), 7.65 (d, *J* = 8.4 Hz, 4H), 6.88 (dd, *J* = 17.6, 10.9 Hz, 2H), 5.97 (d, *J* = 17.6 Hz, 2H), 5.45 (d, *J* = 10.9 Hz, 2H) (Fig 3.1).

^{13}C NMR (101 MHz, Chloroform-*d*) δ 174.60, 171.12, 141.70, 136.42, 135.65, 133.72, 131.26, 130.89, 130.72, 130.47, 129.35, 129.18, 128.78, 127.43, 126.56, 126.18, 126.00, 125.75, 125.43, 125.28, 124.77, 124.64, 116.01 (Fig 3.2). HRMS: m/z: 486.1958 [M + H] $^+$. Calc.: 485.1892 (Fig 3.3).
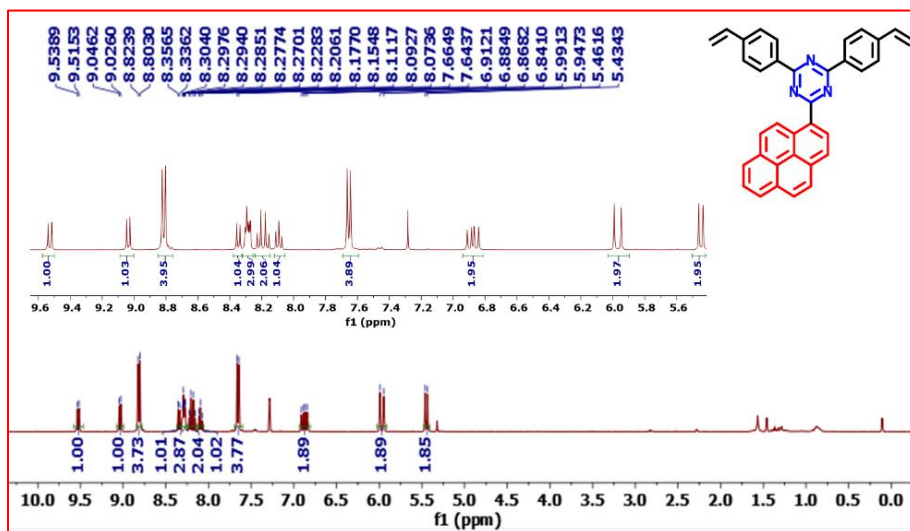
Figure 3.1 ^{1}H NMR of VinTr
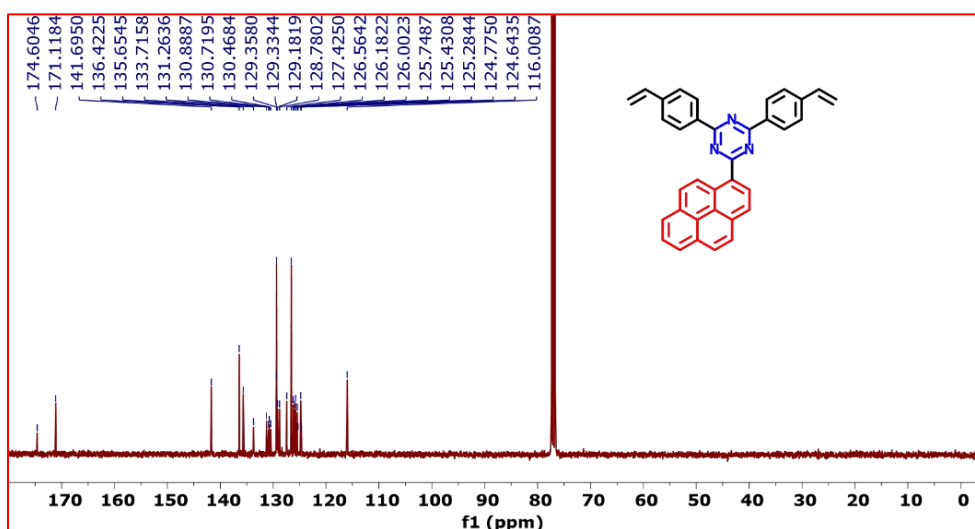
Figure 3.2 ^{13}C NMR of VinTr
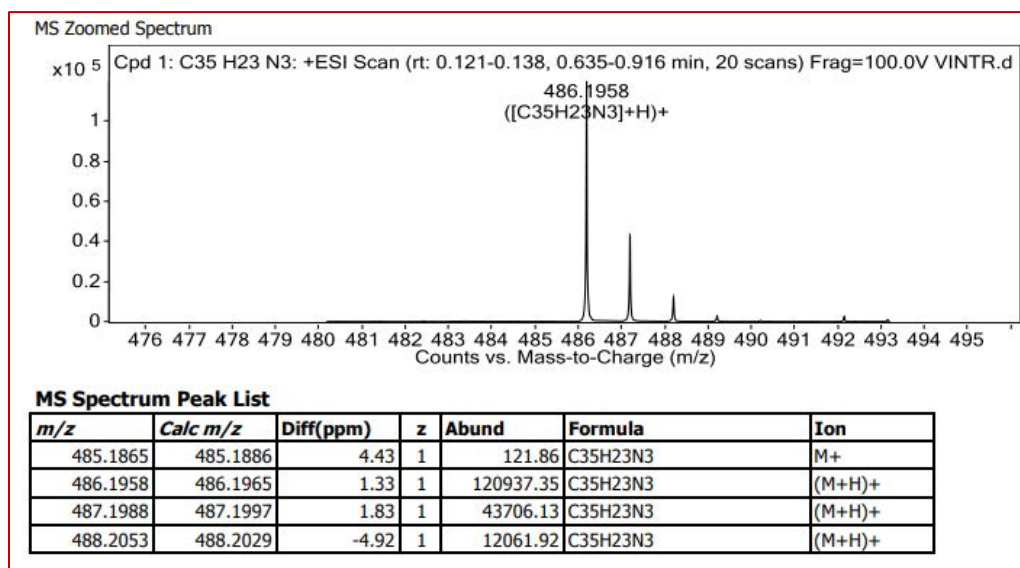
Figure 3.3. HRMS data of VinTr

(b) Synthesis of 4-chloro-N,N-diphenyl-6-(pyren-1-yl)-1,3,5-triazin-2-aminetriazine (PyTrDA)

The clean and dry round bottom flask (RBF) (25 ml) was purged with a constant nitrogen flow. Then, the RBF was charged with freshly dried THF. Then diphenyl amine (100 mg, 0.59 mmol) was added followed by stirring. Then, it was slowly cooled up to the temperature of -60 ^{0} C. n-BuLi (1.6 M in hexane, 0.5 ml) was slowly added into the reaction mass under N_2 atm. Then, the temperature was maintained from -40 to -60 ^{0}C for 2-3 h. PyTr (105 mg, 0.30 dissolved in fresh THF) was added slowly into the reaction mixture at -40 – -60 ^{0}C under N_2 atm. The reaction mixture was kept in stirring for 4-5 h with intermittent TLC observation at -40 to 0 ^{0}C. Then, the reaction mass was quenched with a 10% aq. ammonium chloride solution. It was extracted with ethyl acetate twice, then washed the organic layer with water, evaporated, and purified by column chromatography (2-3 % ethyl acetate in hexane). A solid product with a 69 % yield was observed. The isolated compound was characterized by NMR and HRMS.

^{1}H NMR (400 MHz, Chloroform-*d*) δ 9.20 (d, *J* = 9.5 Hz, 1H), 8.94 (d, *J* = 8.2 Hz, 1H), 8.26 – 8.14 (m, 4H), 8.11 – 8.02 (m, 2H), 7.93 (d, *J* = 9.5 Hz, 1H), 7.58 – 7.45 (m, 8H), 7.41 (d, *J* = 7.3 Hz, 2H) (Fig 3.4).

^{13}C NMR (101 MHz, Chloroform-d) δ 174.68, 170.73, 166.30, 134.36, 131.12, 130.95, 130.39, 129.57 129.44, 128.59, 128.05, 127.68, 127.35, 127.15, 126.14, 125.91, 125.42, 125.10, 124.36 (Fig 3.5). HRMS: m/z: 483.1345 [M + H] [+]. Calc.: 482.1298 (Fig 3.6).
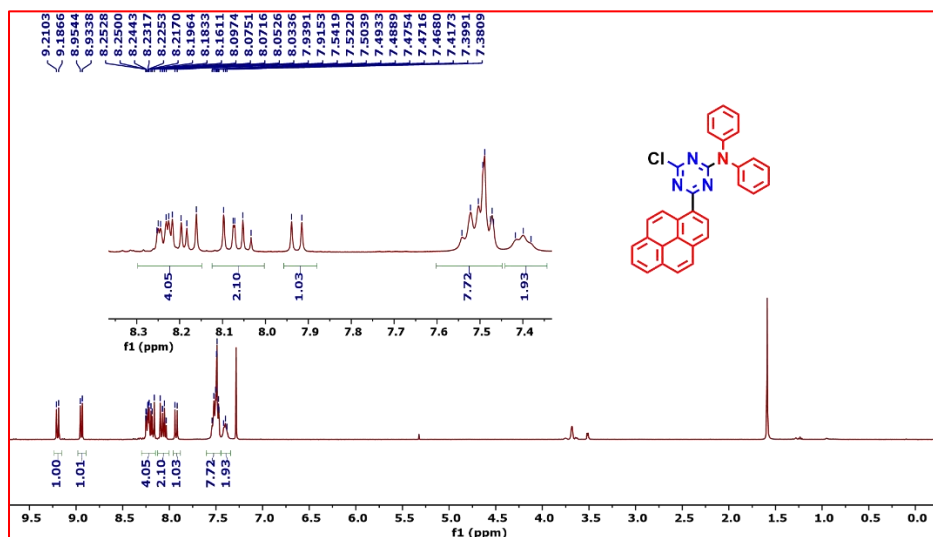
Figure 3.4 ^{1}H NMR of PyTrDA
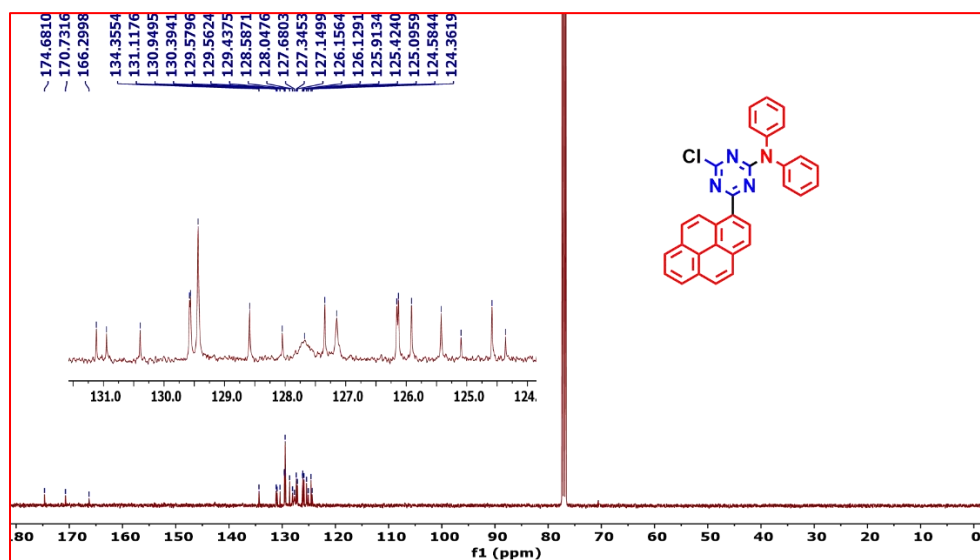
Figure 3.5 ^{13}C NMR of PyTrDA
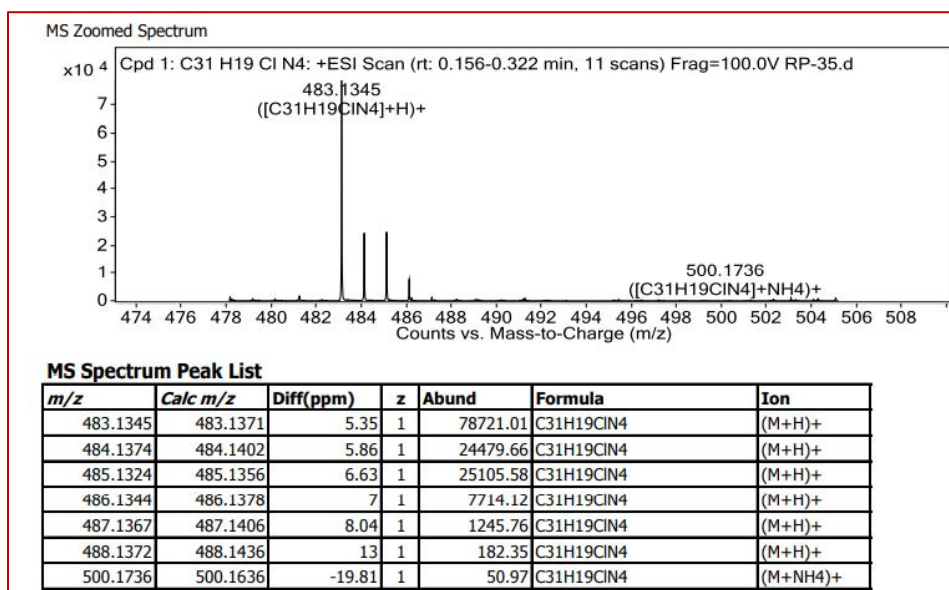
Figure 3.6. HRMS data of PyTrDA

3.3 RESULTS AND DISCUSSION

The synthesized compounds (PyTr, VinTr, and PyTrDA) have good solubility in common organic solvents such as tetrahydrofuran, dichloromethane, etc. The absorption spectra of the synthesized molecules (VinTr and PyTrDA) were recorded in THF (10^{-6} M) solution (Figure-1), showing a similar absorption pattern to PyTr with slight variations of absorption wavelength. A set of transitions corresponds to π-π^* locally excited state transitions ($\sim$ 250-315 nm) and they were assigned to local transitions occurring on the pyrene rings.[45] However, peaks at 350-450 nm are due to charge transfer transitions [46] (Figure-3.7 a). Due to the electron-donating abilities of the diphenyl amine and phenyl vinyl, the absorption bands of VinTr and PyTrDA slightly blue shifted in comparison with those of PyTr. Although the absorption bands of the three compounds were similar, the minor differences in the peak shapes indicated different electronic structures. The TD-DFT and NTO calculations were performed to understand the nature of transitions (*vide infra*). PyTr and VinTr shows emission peaks with maximum wavelength (λ_{max}) at 475 nm and 438 nm, respectively, in a dilute solution of THF, while PyTrDA shows a weakly emissive relatively broader peak at 472 nm (λ_{max}) in a dilute solution of THF (Figure-3.7 b).
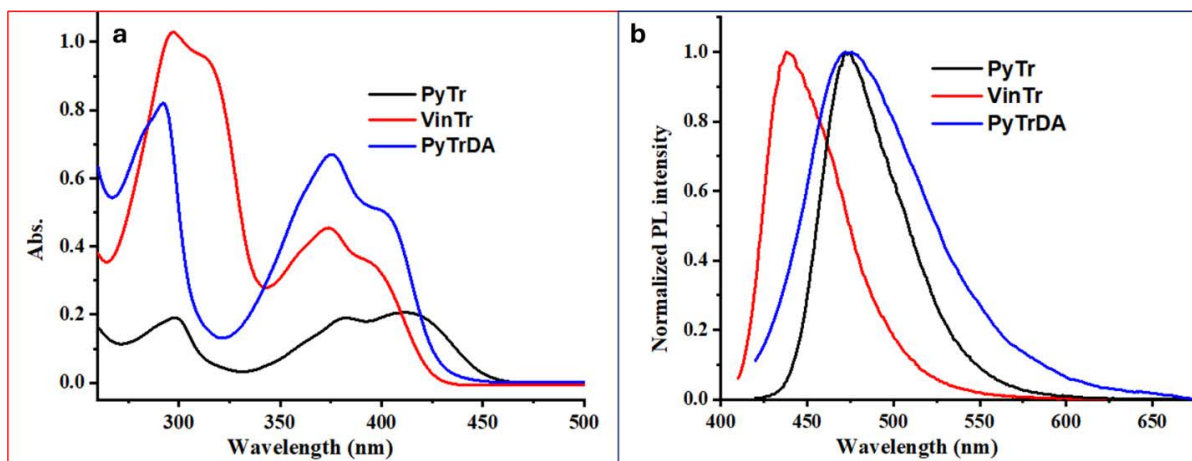
Figure 3.7. (**a**) UV-visible absorption spectra (10^{-6} M in THF) and (**b**) Normalized PL spectra (10^{-4} M in THF) of all the compounds

3.3.1 Computational Study

Computational calculations were performed to validate and understand the photophysical properties of synthesized compounds using the Gaussian-16 package.[47-49] The DFT level of theory using B3LYP hybrid exchange-correlation functional was used to get the correct exchange energy. The 6-311+G (d,p) basis set was employed to consider polarization and diffusion due to electronegative atoms present in the molecules. Firstly, PyTr is optimized, which has already been reported to sense the nitro-based explosives.[36] Then, the rotor phenyl rings were attached without much disturbing the HOMO and LUMO of the moieties to introduce AIE activity. The computationally calculated energies of HOMO and LUMO showed similar trends as obtained by cyclic voltammetry (CV) and UV-VIS study (Table 3.1).

Table 3.1 Experimental and computationally observed HOMO and LUMO energy values are shown in the table below

Molecules	Experimental energy		Theoretical energy			
	HOMO	LUMO	Vapor phase		THF solution	
			HOMO	LUMO	HOMO	LUMO
PyTr	-5.54 eV	-2.92 eV	-6.08 eV	-2.95 eV	-6.02 eV	-2.92 eV
VinTr	-5.05 eV	-2 .21 eV	-5.74 eV	-2.42 eV	-5.83 eV	-2.51 eV
PyTrDA	-4.98 eV	-2.10 eV	-5.21 eV	-2.45 eV	-5.87 eV	-2.52 eV
TNT	-5.25 eV	-2.49 eV	-8.46 eV	-3.49 eV		

The HOMO and LUMO orbitals of all three molecules were mapped, and it was seen that the HOMO is concentrated mainly on pyrene. At the same time, LUMO is spread throughout the pyrene and triazine in the case of PyTr and PyTrDA (Figure 3.8), and the dihedral angle between pyrene (donor) and triazine (acceptor) is 18.10° and 23.97°, respectively (Figure 3.9). In VinTr, some part of the LUMO is additionally extended to one of the phenyl rings of vinyl as these groups are almost in plane with pyrene and triazine (Figure 3.9). The dihedral angle between D and A in the case of VinTr is 34.12° while it is 4.27° and 5.29° between triazine and the two phenyls present in vinyl substituents (Figure 3.9). It was observed that all three compounds sense the TNT, and this fact can be easily understood from the presence of the same basic framework (pyrene-triazene) and the marginal difference in LUMO energy levels (Figure 3.8). Additional phenyl groups attached to the triazine site play a role in making the molecule strongly emissive through AIE activity in the solid state. Thus, these peripheral phenyl groups of VinTr and PyTrDA are significant in improving the detection limit for the detection of TNT. PyTr is nearly a planar molecule, which leads to a close packing in the solid state, where the dihedral angle between D and A is found to be 2.21° in the case of PyTr (Figure 3.10). This closed packing structure of PyTr does not accommodate enough TNT molecules thus resulting in a relatively lesser quenching effect. Meanwhile, in the case of PyTrDA, due to the twisted nature of phenyl rings of diphenylamine (the dihedral angles between triazine and the two phenyl rings are 56.06° and 55.30°, respectively (Figure 3.9), molecules get restricted to approach each other. This provides more room for analyte explosive molecules to access the main detection site, thus it is expected to improve the detection limit.
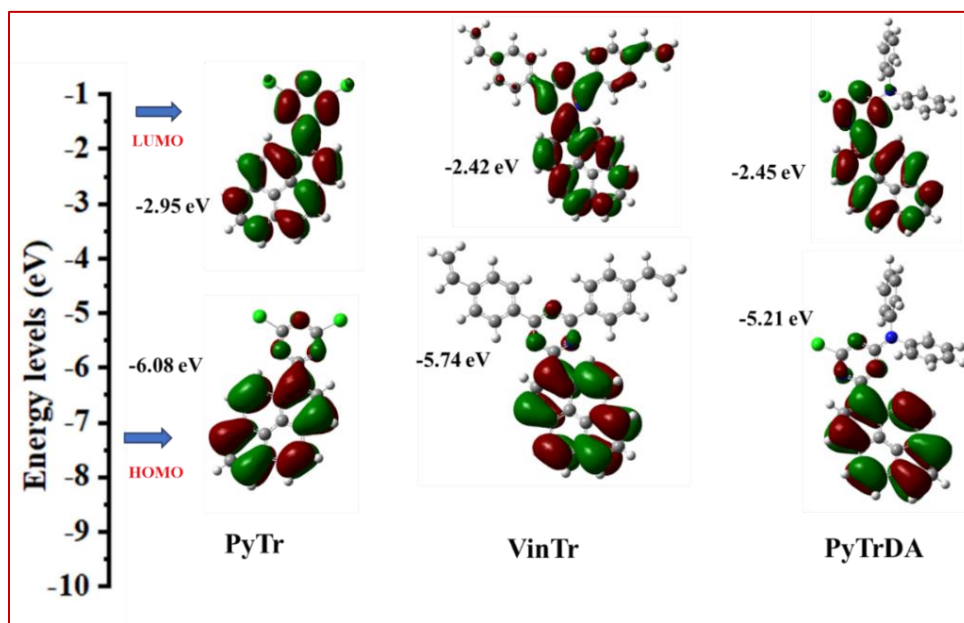
Figure 3.8. Computationally optimized HOMO and LUMO energies of the molecules (PyTr, VinTr, and PyTrDA) by using the Gaussian-16 packages in gas phase
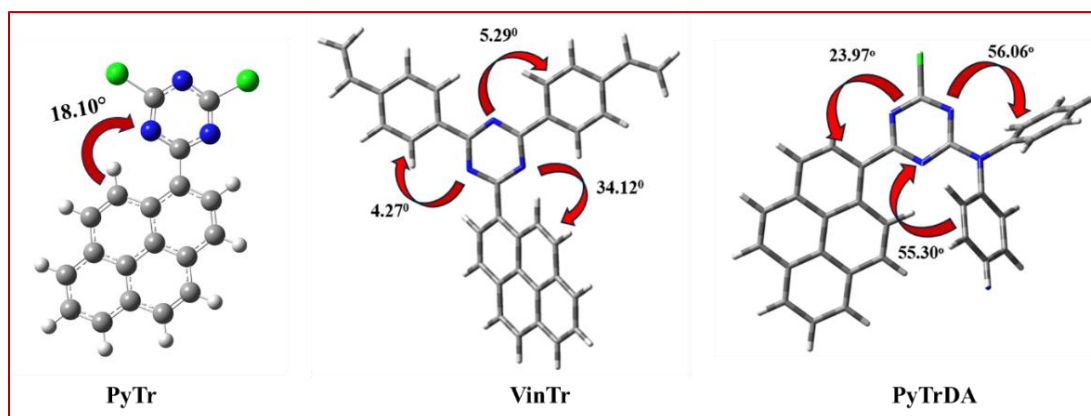
Figure 3.9. Optimized structure of a series of compounds by using DFT (Gaussian-16)
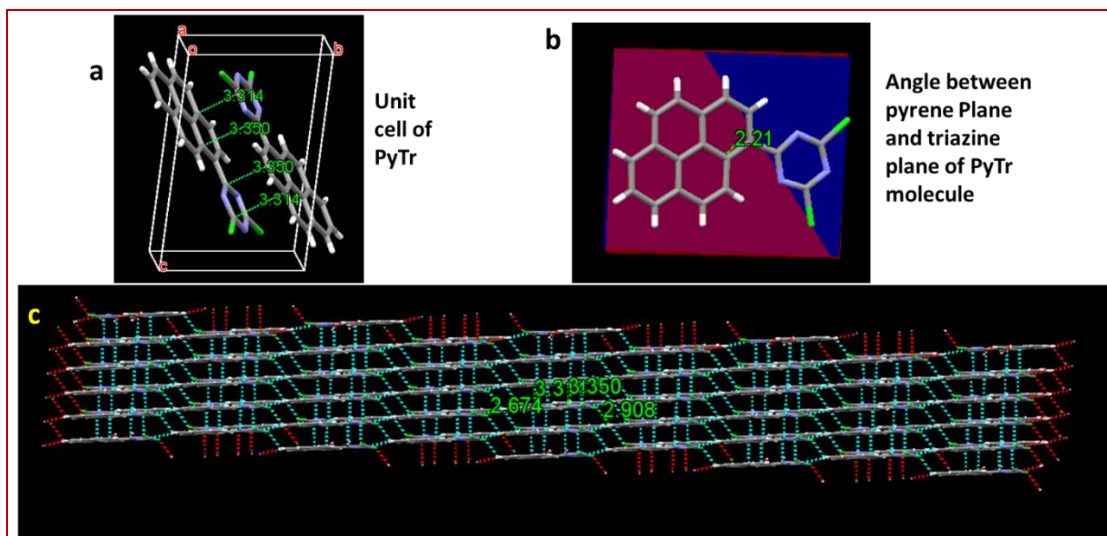
Figure 3.10. a) Packing of PyTr in a unit cell, (b) dihedral angle between a pyrene plane (red) and triazine plane (blue), and (c) long-range packing pattern of PyTr

Table 3.2 Three excited states of PyTrDA along with their oscillator strength and nature of transitions as calculated computationally along with experimental values

State	Experimental value (nm)	Theoretical value (nm)	Oscillator strength (f)	Nature of transition
S_1	400	403	0.4773	Charge transfer
S_2	375	352	0.0507	Charge transfer + π-π^*
S_3	290	298	0.0873	Mixed

Time-dependent density functional theory (TD-DFT) was performed to study the nature of excited states for PyTrDA. The first excited state was found at 403 nm with oscillator strength f=0.4773 (Table 3.2). The NTO analysis showed this to be a HOMO-LUMO transition having charge transfer characteristics with a 96.78% probability of transition (Figure 3.11.a). This transition corresponds to a 400 nm UV-VIS transition. Two more transitions with relatively good oscillator strength were found at 352 nm and 298 nm (f= 0.0507 and 0.0873), which were found at 375 nm and 298 nm, respectively in the experimentally obtained UV-VIS spectra. NTO analysis indicated

that the second state (352 nm) is a mixed transition, having CT (72.3%) and $\pi - \pi^*$ locally excited (LE, 27.16%) state (Figure 3.11.b). The high energy state was found to be a mixed transition state with two different NTOs having transition probability 59.28% and 35.96% (Figure 3.11.c).
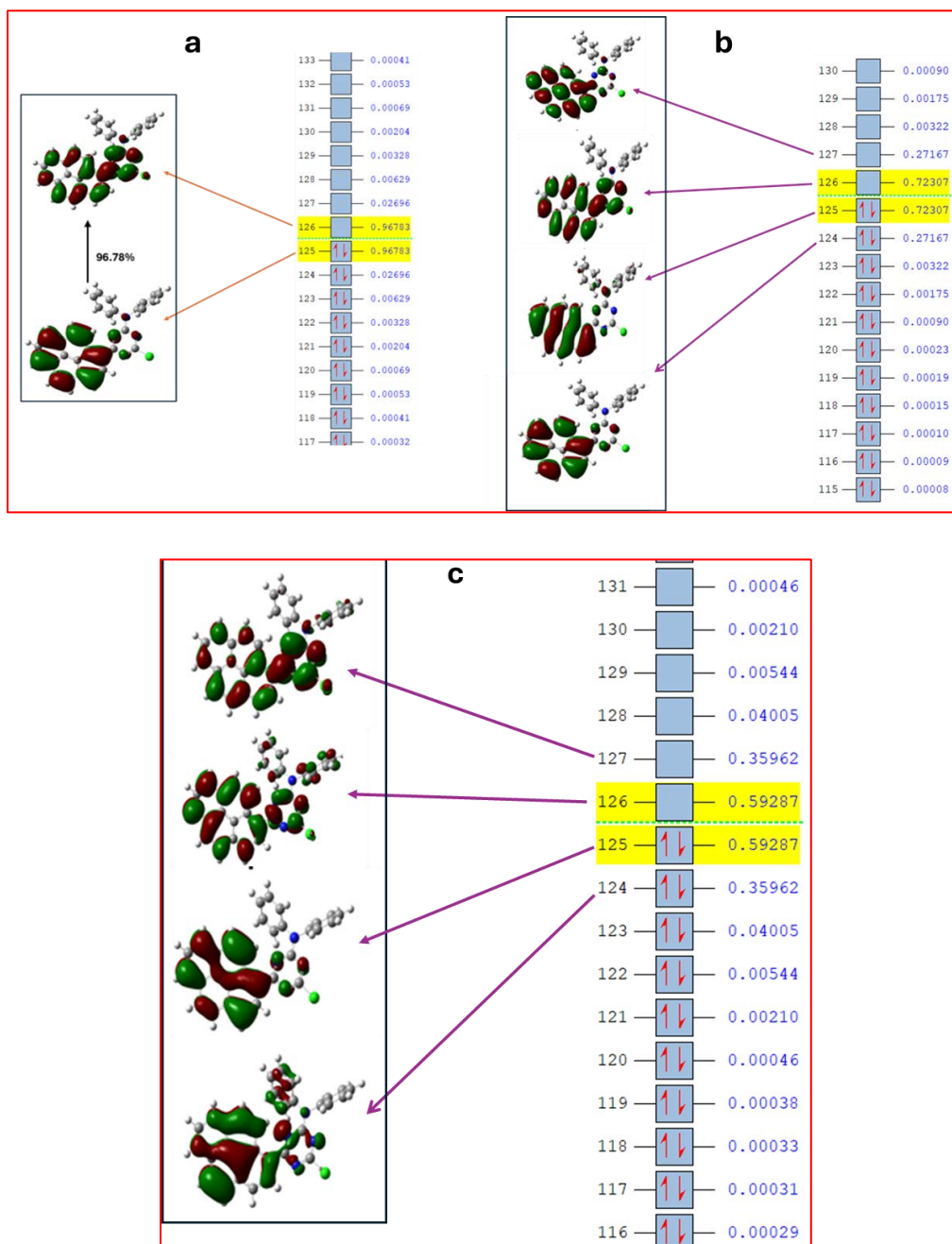
Figure 3.11. Natural Transition Orbitals analysis indicating the transition probability a) S_1 (charge is shifting from pyrene ring to triazine ring indicating mix of local transitions and CT) b) S_2 (72.3 % shows mixed CT and LE state while 27.16% shows purely LE transitions) c) S_3 (high energy transitions shows a mixture of LE and CT)

3.3.2 Explosive Sensing Study

The interest lies in the detection of nitro-based explosives in the vapor phase. So, materials that show AIE (Aggregation -induced Emission) active characteristics with high quantum yield and longer excited state lifetime are potential compounds for sensing. The AIE properties of the synthesized compounds were checked in THF with varying water quantity. It was observed that by increasing the water ratio in a stock solution of THF, PL intensity gradually decreases in the case of PyTr and VinTr, on contrast the PL intensity of PyTrDA is gradually increased (Figure 3.12). This observation reflects the 'Aggregation-induced Enhanced Emission' (AIEE) characteristics of PyTrDA. The recorded solid-state absolute quantum yield of the synthesized compounds VinTr and PyTrDA are 12.17 and 20.89%, respectively. It is clearly observed from the optimized structure (Figure 3.8) that two phenyl rings attached with nitrogen through a triazine ring are highly twisted (the dihedral angles are 56.06° and 55.30°), which makes molecule AIEE active. As observed from the solution phase and AIEE study of all the compounds, it is observed that PyTr and VinTr are highly emissive in solution state, while PyTrDA shows bright emission in aggregated state. All these luminescent probes were tested with TNT.
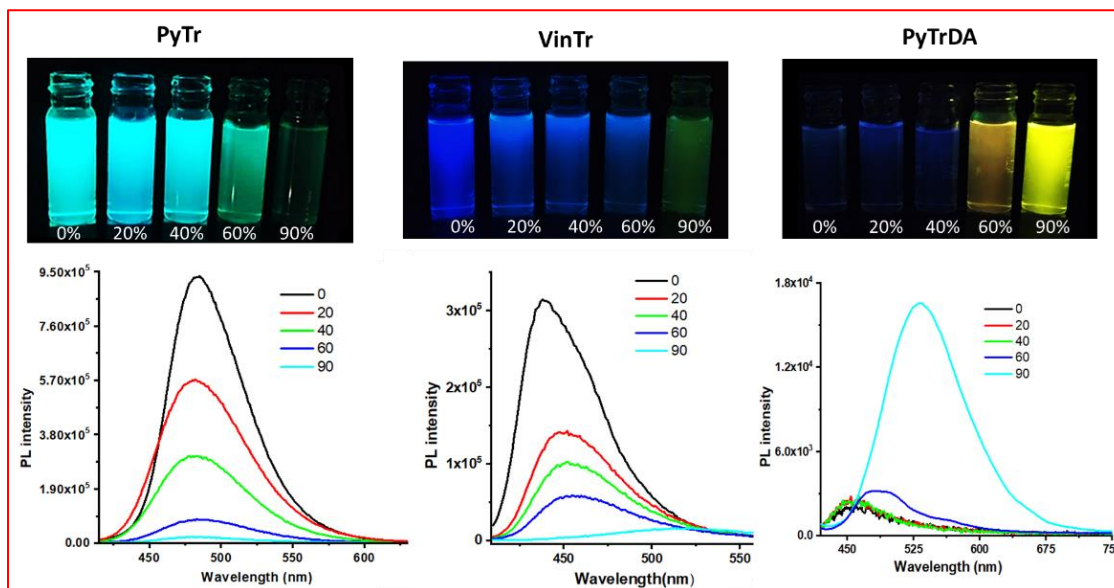
Figure 3.12. AIEE study of PyTr, VinTr, and PyTrDA in THF/water system, taken 10^{-4} M solution of probe molecules in THF and changes the water ratio from 0% to 90 % shown in the upper part of the figure and recorded corresponding PL spectra of probe solution with varying water percentages shown in the downside of the figure

Firstly, the testing was performed in contact mode, where the solid TNT (~1.0 mg) were added into the solutions of probes (PyTr and VinTr) in THF and aggregated solution (90% f$_w$ of PyTrDA) and captured the image under UV light of 365 nm and subsequently, recorded the PL spectra and calculated the percentage quenching of PL intensity in presence of the analyte (Figure 3.13). On comparison, it was observed that aggregated solutions of PyTrDA quenches maximum intensity (97.5%). It concludes that AIEE active PyTrDA is a highly sensitive probe towards TNT analyte.
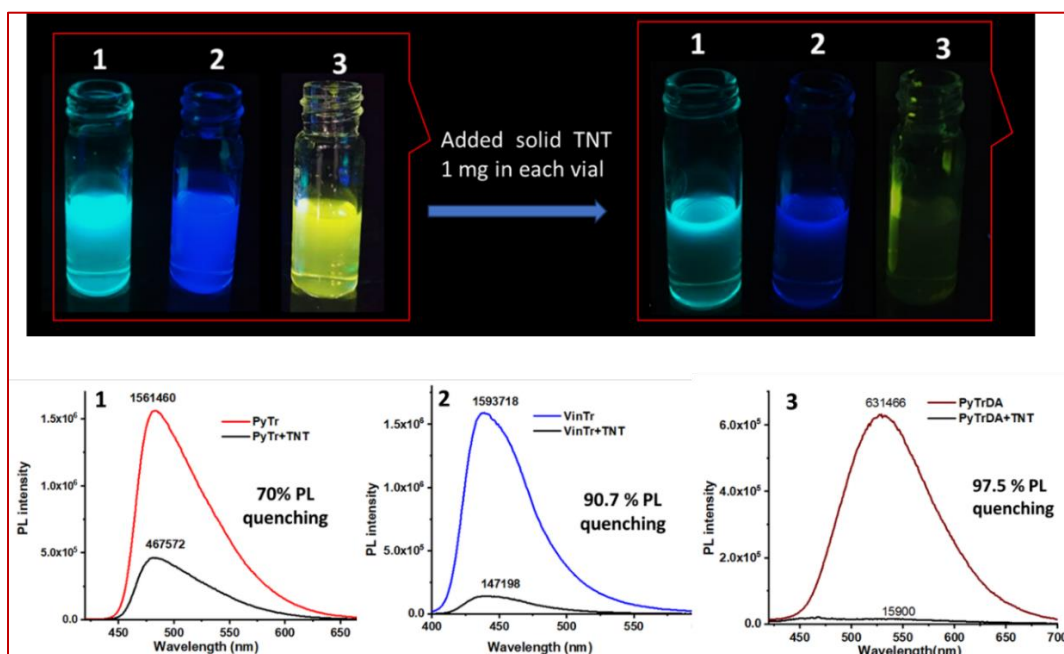
Figure 3.13 Compounds 1- PyTr and 2- VinTr were taken in THF (10^{-4} M), and 3- PyTrDA was taken in 90% water in THF aggregated solution (considering the maximum PL intensity). The top left side image (three vials) was taken under UV excitation (λ_{exc}, 365 nm), then 1mg TNT powder was added into each vial and the emission image was captured under 365 nm UV excitation (top right image). The above figure shows the PL spectra of all the probes with and without TNT

$$\% \text{ PL quenching} = \frac{(\text{Initial intensity - Intensity after adding TNT})}{\text{Initial intensity}} \times 100$$

For PyTr case

PL spectra shown above contain initial intensity (in the absence of TNT) and intensity after adding TNT for the case of PyTr, VinTr, and PyTrDA.

= [(1561460-467572) / 1561460] x 100= 0.7005 x 100

= 70.0 %,

Similarly, the % PL quenching for VinTr and PyTrDA are 90.7 and 97.5 %, respectively.

The selectivity of probe towards different analytes is very important for an efficient sensor. Thus, the selectivity test of probe (PyTrDA) was performed with a wide range of nitro-based explosives (Figure 3.14). It was observed that PyTrDA is selective towards TNT and interestingly found that among the high-explosives[50] used for testing, such as TNT, RDX, HMX, PETN, and ammonium nitrate, this probe responds only to TNT explosives. This observation makes PyTrDA superior to other reported fluorescent sensors.[51]
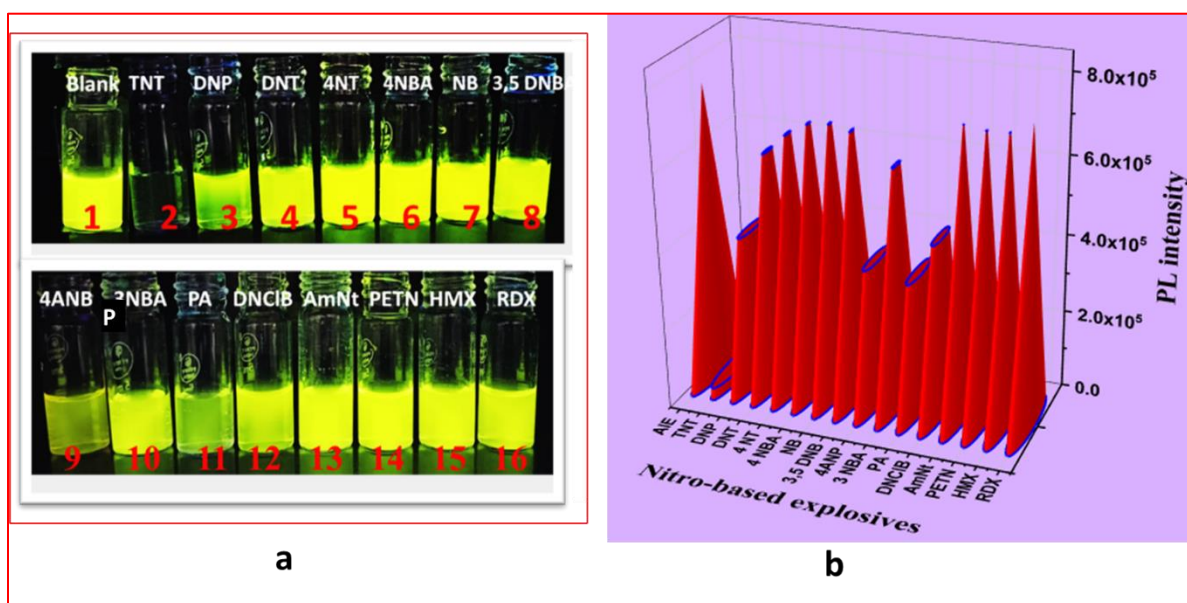
Figure 3.14. a) 200 µl of different nitro-based explosives (10^{-4} M solution in THF) were added into the probe solution (90% AIE solution, 2ml) and recorded image under UV lamp. b) Bar graph showing the intensity profile of aggregated solution (AIE, **90% f_w**) with various nitro-based explosives (the abbreviated names of the nitro compounds are written in Figure, TNT (2,4,6-trinitrotoluene), DNP (2,4-dinitrophenol), 4NT (4-nitrotoluene), 4-NBA (4-nitrobenzoic acid), NB (Nitrobenzene), 3,5 DNB (3,5-dinitro benzene), 4ANP (4-amino nitrophenol), 3NBA (3-nitrobenzoic acid), PA (Picric acid), DNClB (1-chloro-2,4-dinitro benzene), A. Nitrate (Ammonium nitrate), PETN (Pentaerythritol tetranitrate), HMX (High melting explosive), RDX (Royal demolition explosive)

The exciting observation of selective quenching of TNT encourages titrating the analyte with the aggregated solution of the probe molecule. The titration study of AIE solution (f_w=90%) of probe molecule with aqueous TNT (10^{-5} M) was carried out and the limit of detection was found to be 216 ppt (0.22 nM) (Figure 3.15). The Stern–Volmer (SV) plot (Figure 3.16) from this quenching study showed a linear relationship at a lower concentration and the plot was bent upward with a higher concentration. Considering the lower concentration plot, the calculated quenching constant (K_{SV} in M^{-1})) was found to be superior (7.9×10^8 M^{-1}) as compared to the previous reports.[33, 52-53] The S-V plot with deviation from linearity was observed and it indicates that the quenching process is operated through a mixed static/dynamic quenching.[54-55]
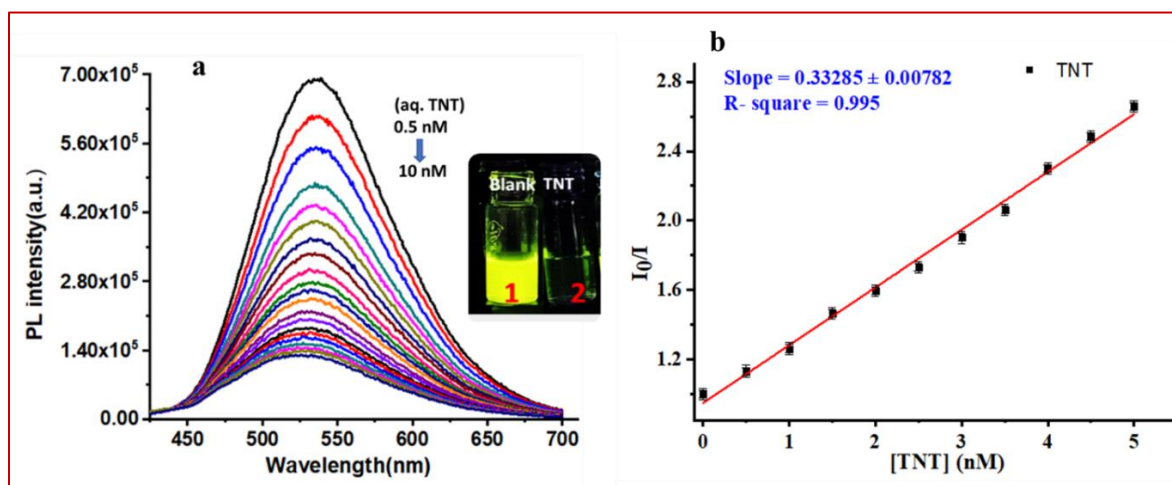
Figure 3.15 (a) Photograph of change in photoluminescence (PL) intensity of AIE solution (10^{-4} M THF (0 %) and water (90 %)) with continuous addition of aq. TNT, 0.5 nM at each time; **(b)** Stern-Volmer plot for emission quenching, I_0 represents the initial PL intensity in the absence of TNT, and I represent the intensity in the presence of TNT. The error bars shown at each data point represent the standard deviation obtained from three independent measurements $= \pm 0.033$
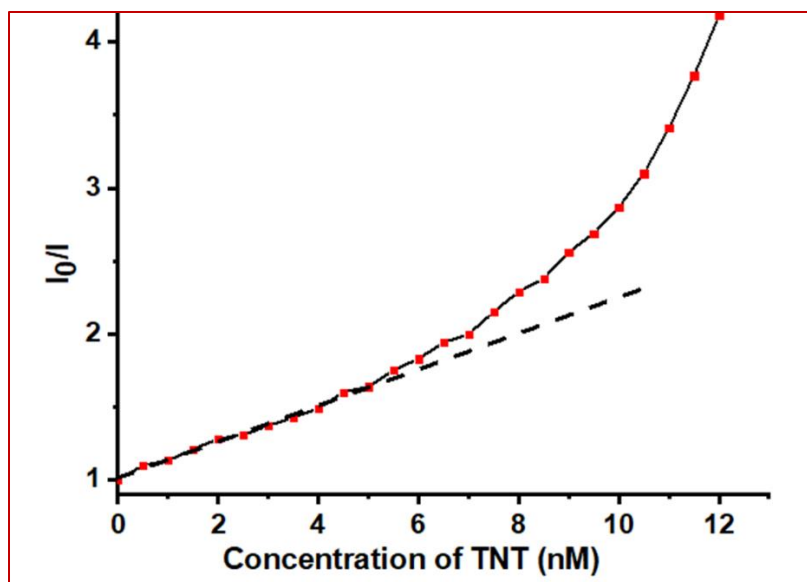
Figure 3.16 Stern–Volmer plot for the PL quenching of the probe upon the gradual addition of TNT, where I_0 represents the PL intensity of the probe (PyTrDA) without TNT, and I indicate the intensity with the gradual addition of TNT

The fluorescence quenching requires molecular contact between the fluorophore and the quencher. This contact can result from complex formation in the ground state, which is static quenching, or from diffusive encounters of the quencher molecules with the excited state fluorophore, which is dynamic quenching in nature. The two quenching processes can be distinguished by time-resolved measurements of the fluorescence decays of the fluorophore with or without a quencher.[56][57]
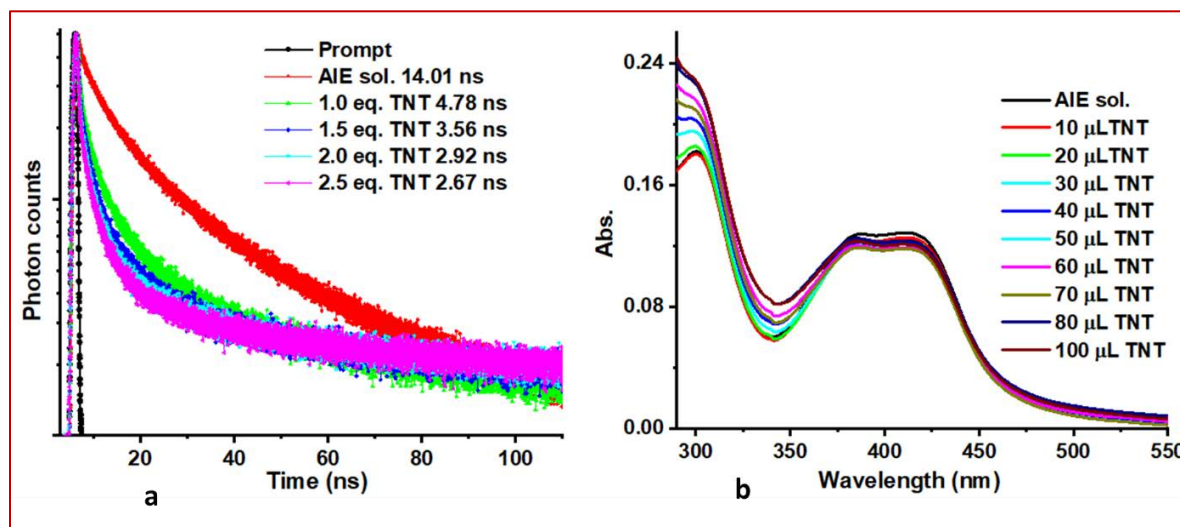
Figure 3.17 (a) Time-resolved photoluminescence studies of PyTrDA at different concentrations of TNT and (b) UV-VIS spectra of probe (AIE solution, 10^{-5} M) with different amounts of TNT (10^{-4} M in water)

Table 3.3 In all the cases, tri-exponential decay fit was observed (components- B1, B2, and B3). The Excited state lifetime with the fitting parameter is shown in the table given below.

Probe		B1	B2	B3	$<\tau>$	$\chi 2$
PyTrDA	Aggregate	27.02	66.09	6.79	14.01	1.38
	1.0 eq. TNT	31.75	56.45	11.81	4.78	1.27
	1.5 eq. TNT	32.12	53.43	13.45	3.56	1.15
	2.0 eq. TNT	33.69	48.91	17.40	2.92	1.28
	2.5 eq. TNT	33.57	47.81	18.63	2.67	1.34

In our study, to examine the nature of the interaction between the fluorophore and quencher at an excited state, time-resolved photoluminescence analysis was performed (Figure 3.17, a). Fluorescence decay is fitted to triple exponential (see components in table 3.3) and checked the average lifetime in AIE solution in the absence and presence of analyte (TNT). In the absence of an analyte, the average lifetime observed for PyTrDA is 14.01 ns. After adding TNT from 1.0 to 2.5 equivalents, lifetime values decrease from 14.01 ns to 2.67 ns (details in table 3.3). The huge drop in lifetime (80.8%) in the presence of a quencher indicates the dynamic quenching between the fluorophore and TNT analyte. The observation of any change of absorption spectra of probe and probe with quencher hints the possibility of static quenching. In our observation, we didn't find any change in UV-VIS spectra (Figure 3.17, b) in the presence of TNT analyte. This observation also neglects the fluorophore (donor) interaction with TNT (acceptor) in the ground state through static quenching. Another quenching phenomenon such as resonance energy transfer (RET) also be possible, but it is ruled out because the overlapping of absorption spectra of TNT and photoluminescence spectra of

probe[5] was not observed (Figure 3.18). The absorption spectra of a list of nitro-based explosives and the emission spectra of the probe molecule were recorded.

It was observed, there is a slight overlapping of UV-VIS absorption spectra of analytes (PA, DNP and 4-ANP) with emission spectra of probe (PyTrDA) (Figure 3.18), which is favorable condition for resonance energy transfer (RET) So, in case of PA, DNP and 4-ANP there is a possibility of fluorescence quenching through RET mechanism.
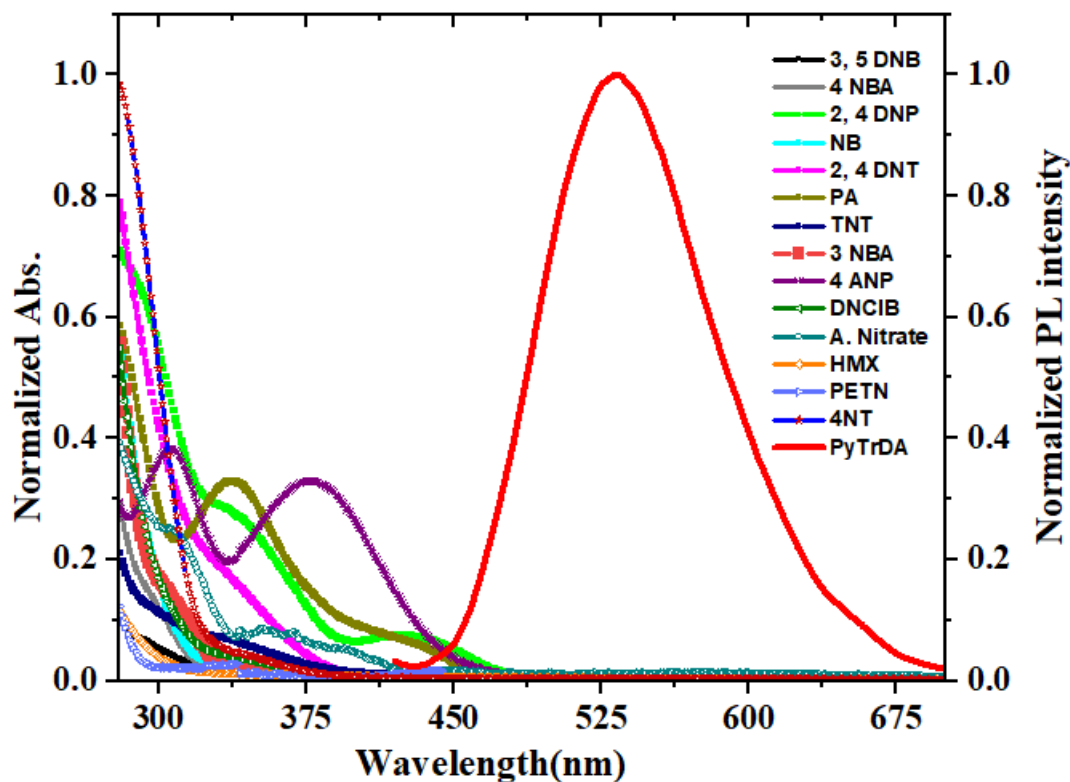
Figure 3.18 The left side Y-axis shows the absorbance of explosives, and the right side of this Y-axis shows the PL intensity of the probe molecule (PyTrDA); the overlapping of absorption of PA and PL spectra of PyTrDA shows the possibility of energy transfer between the probe and explosives

To examine the possibility of photo-induced electron transfer (PET) between the electron-rich (PyTrDA) probe molecule and electron-deficient nitro-based explosive, the alignment of LUMO levels of the probe (PyTrDA) and nitro-based analytes was determined (Figure 3.19). In case of PA, DNP and 4-ANP, we could see their LUMO energy (PA= -3.20 eV, DNP= -2.20 eV and 4ANP= -3.0 eV) are aligned in such a way that photoinduced electron transfer

(PET) is possible with PyTrDA (LUMO= -2.10 eV). It was observed that alignment of LUMO levels of TNT (-2.49 eV) and probe (-2.10 eV), which is appropriate for photo-induced electron transfer from the probe (PyTrDA) to analyte (Figure 3.19). So, PET between the probe and analyte occurs and PL quenching takes place. To get more evidence for PET between the probe and TNT, ultrafast transient absorption (TAS) spectroscopy was performed (vide infra).
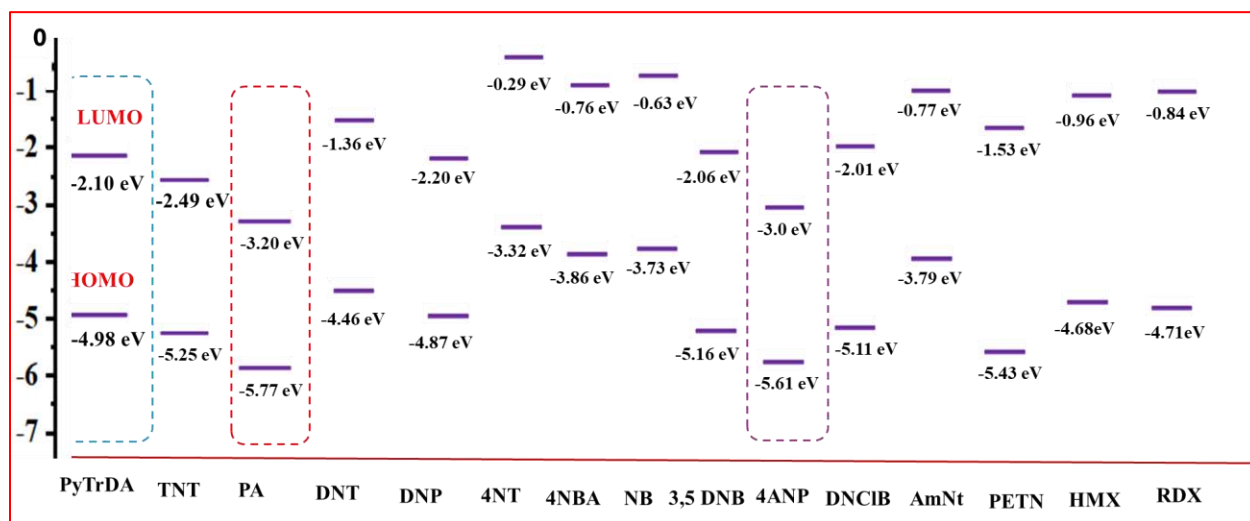
Figure 3.19 Here, on the left side, the Y-axis shows energy levels (eV), and the X-axis contains a probe (PyTrDA) as well as a list of explosives, showing the possibility of electron transfer between the probe and nitro-based explosives

Experimental evidence for PET process (Ultrafast Transient Absorption):

Ultrafast transient absorption spectroscopy experiments have been performed using pump wavelength (λ_{pump}) of 400 nm (Charge transfer characteristics transition) (Figure 3.20).
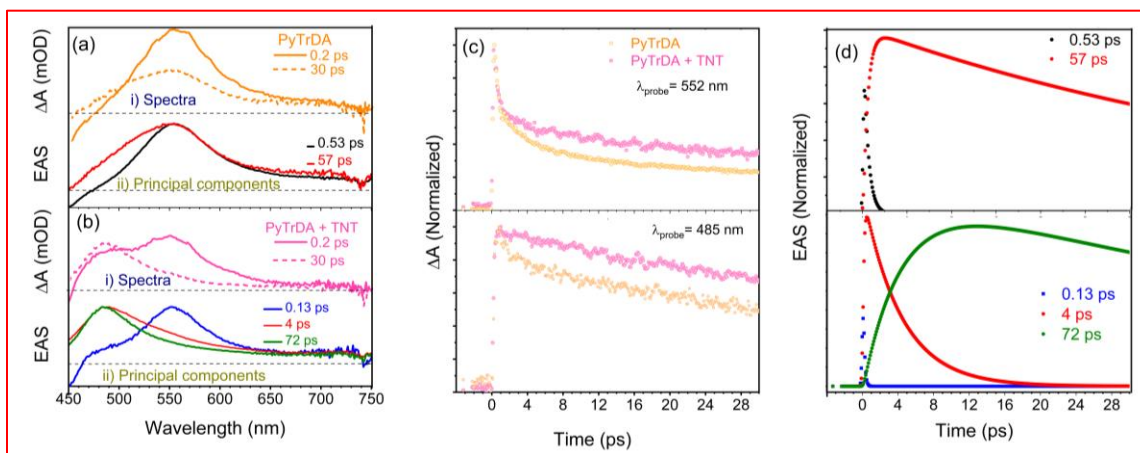
Figure 3.20 (a, b top panels) TA spectra of PyTrDA in (a) absence (orange) and (b) presence (pink) of TNT (125 µM), at 0.2 ps (solid) and 30 ps (dash) after excitation. (c) PIA transients of PyTrDA in the absence (orange) and presence (pink) of TNT (125 µM) at probe wavelengths $(\lambda)_{probe}$ of 552 nm (top) and 485 nm (bottom). Global analysis of the transient absorption spectra yields principal components with time constants of (a, bottom panel) 0.53 ps and 57 ps for PyTrDA without TNT and of (b, bottom panel) 0.13 ps, 4 ps and 72 ps with TNT. (d) Time evolution of the principal components for PyTrDA without (top) and with (bottom) TNT

The TA spectrum of PyTrDA (Figure 5(a) i) solid line) exhibits a prominent, broad photoinduced absorption (PIA) feature with maximum at 552 nm. immediately after excitation by the ultrashort pump pulse. With time, the spectrum decays, with some amount of broadening (Figure 3.21). However, the spectral maximum does not change (Figure 5(a) i) dashed line). Upon the addition of TNT (125 µM), however, the early time spectrum comprises two bands, with maxima at 552 nm and 485 nm (Figure 5(b) i) solid line). At later times, the 552 nm band makes way for the blue shifted spectrum, which evolves over tens of picosecond (Figure 5(b) i) dashed line). The 552 nm band is obviously the characteristic photoinduced absorption spectrum of PyTrDA. The 485 nm feature is attributed to formation of TNT radical anion (TNT·⁻), formed as a result of PET from PyTrDA to TNT. This feature matches the spectrum of the radical anion reported earlier by spectroelectrochemistry.[58] The radical anion appears to be longer lived than the excited state of PyTrDA, as is manifested in the transients of the system in the presence and absence of TNT (Figure 5c). However, a prominent rise is not observed at λ_{probe} = 485 nm. This, along with the fact that the 485 nm feature is observed as early as 0.2 ps after excitation, implies that the PET from PyTrDA to TNT is ultrafast and not resolved very well in the present experiment, with a FWHM of the instrument function of 200 fs. The considerable spectra width of both the species involved renders quantitative analysis of the single wavelength transients difficult and necessitates global analysis of the transient absorption spectra. This has been implemented, using the sequential model.[59] Two principal components, with time constants τ_1= 0.53 ps and τ_2= 57 ps are hence obtained for PyTrDA in the absence of TNT. The evolution associated spectra (EDS) for these two components exhibit practically coincident maxima at 552 nm (Figure 5 (a) ii)), but the 57 ps component exhibits a greater spectral width. Hence, the 0.53 ps component is associated with the vibrational cooling and intramolecular vibrational redistribution (IVR) processes.[60] τ_2= 57 ps can be assigned decay time of excited PyTrDA molecule. In the presence of TNT, three components

are obtained: One with maximum at 552 nm, with $\tau_1 = 0.13$ ps and the other two with maxima at 485 nm and time constants $\tau_2 = 4$ ps and $\tau_3 = 72$ ps (Figure 5 (b ii)). The sub picosecond time constant associated with the component that resembles the excited state spectrum of PyTrDA confirms the ultrafast PET from the molecule to TNT. The 4 ps and the 72 ps components resemble the spectrum of the radical anion of TNT and represent its relaxation, even though the assignment of each of them to specific processes is not achieved in the present experiment.
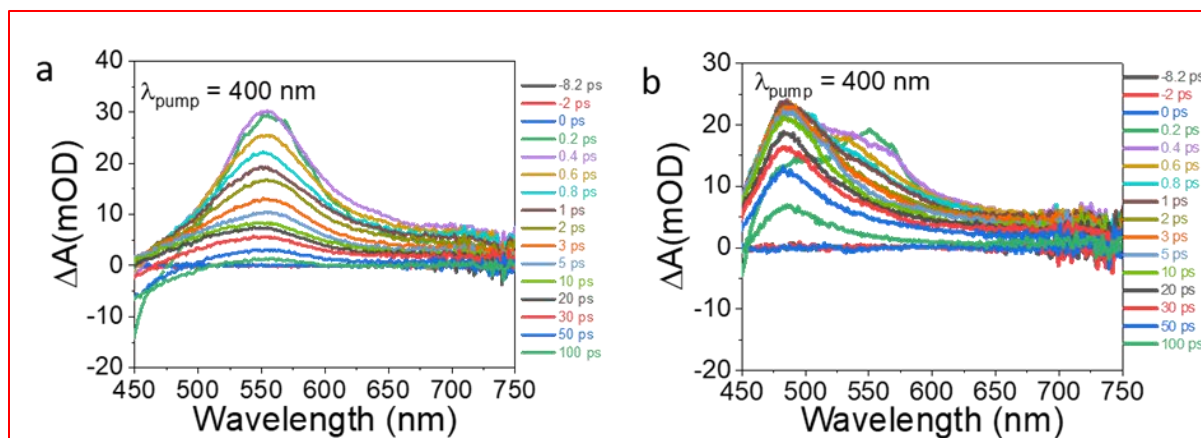
Figure 3.21 TA spectra of (a) PyTrDA, (b) PyTrDA, and TNT in THF solution at different delay times with $\lambda_{ex} = 400$ nm

Surface morphology of the material is one of the important parameters for analyte sensing in vapor phase.[61] PyTr, VinTr, and PyTrDA (10^{-3} M in dichloromethane, 200μL each) was deposited on a glass coverslip, then recorded the FESEM image for all three cases. Aggregated nano-rod type horizontally aligned morphology was observed for the cases of PyTr and VinTr (Figure 3.22). Surprisingly, a vertically grown flowery and highly condensed nano-rod based morphology was observed for PyTrDA (Figure 3.23). Then the same film was exposed to TNT vapor (2.0 min) followed by recording of the FESEM image (Figure 3.22, bottom side image). On comparison of FESEM images before and after TNT vapor exposure, for PyTrDA, it is clearly observed that there is a drastic change of morphology from relatively thinner sized nano-rod to non-uniform thicker heavily aggregated but vertically aligned morphology, under exposure to TNT vapor. On comparing the morphology of PyTr and VinTr before and after exposing them to TNT, there has been a minor change found in morphology, mostly the original nanostructure is retained. This change in morphology on exposure to TNT vapor is

clear evidence that TNT vapor interacts strongly with the vertically grown nanorod i.e., with PyTrDA.
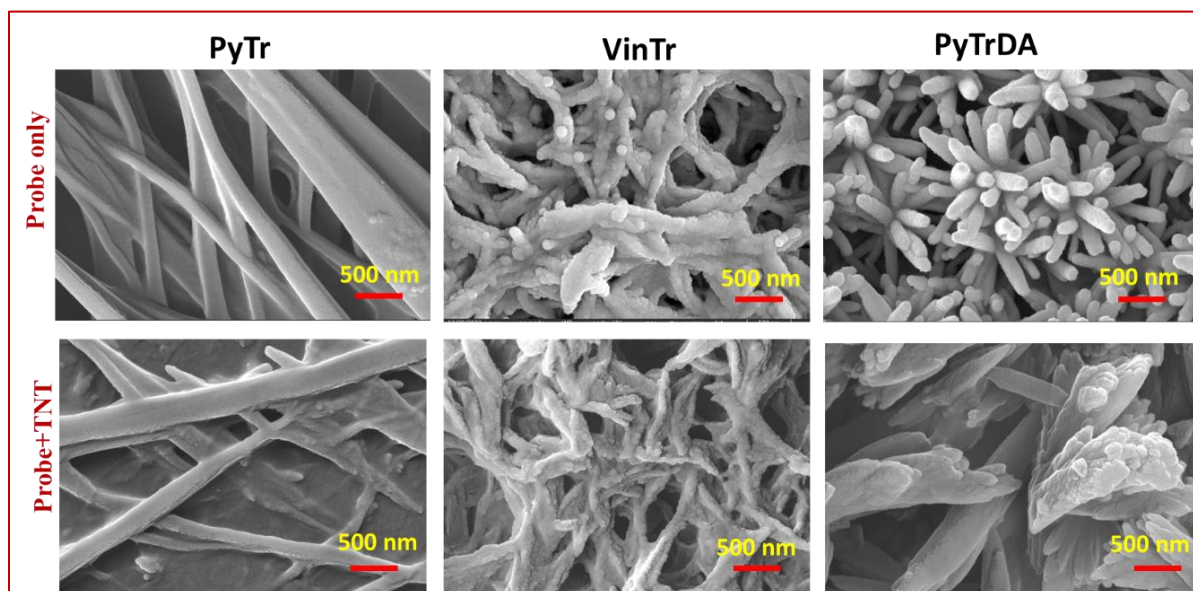
Figure 3.22 FESEM images of PyTr, VinTr and PyTrDA drop cast on glass coverslip (top), and bottom-side images represent corresponding FESEM images after exposure to TNT vapor

From the single crystal XRD structure of PyTr, it was observed that pyrene and triazine fragments in the molecule show co-planarity with an interplanar angle of 2.2°, thus the molecules are closely packed with the range of intermolecular distance, 2.67Å - ~3.50Å (Figure 3.9). This observation hints that the molecules are closely packed and hardly contain any space to accommodate TNT molecules, only surface molecules interact with TNT. From the optimized structure of PyTrDA (Figure 3.8), it is clearly observed that two phenyl rings attached with nitrogen through a triazine ring are highly twisted (the dihedral angles are 58.7^0 and 57.7^0), which makes molecule AIEE active. It is expected that the twisted structure contains interstitial space in their crystal lattices which contains enough free spaces accommodating TNT molecules.[33] In this way, there is a possibility of close contact between the electron-rich probe molecule (Donor) and electron-deficient TNT (acceptor), thus making the PET favorable. Furthermore, vertically grown nano-rod type morphology provides a large surface area for analyte interaction. The vertically grown nano-structural morphology of PyTrDA should properly facilitate the diffusion of TNT molecules and provide a confined

environment, where possible one-to-one host–guest interactions between probe and analytes are possible.
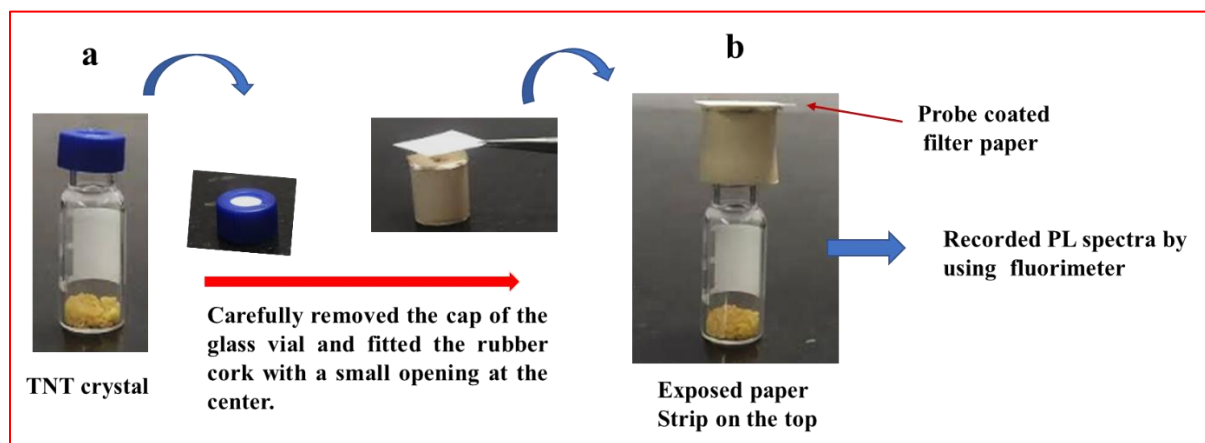
Figure 3.23 (a) Placed 100 mg TNT in a clean and dry glass vial with an airtight lid (2.0 ml capacity) and kept overnight for vapor saturation at 25-30 °C; removed the cap carefully and immediately placed the rubber stopper instead of the cap, then expose with probe coated filter paper from the headspace as shown in above figure **b**. The PL intensity was recorded on the exposed paper strip

Detecting nitro-based explosives in the vapor phase is a difficult task due to their low vapor pressure, which ranges from 10^{-5} to 10^{-15} torr. The ability to detect these explosives from their vapor phase requires the use of a highly sensitive probe molecule. The studied probe (PyTrDA) detects TNT in parts per trillion level from solution. For real time applications, vapor phase detection is highly desirable. It was performed to sense TNT from the vapor phase by using paper strip. The detection of TNT was performed by keeping the substrate (probe impregnated filter paper) horizontally on the top of a glass vial containing TNT vapor (Figure 3.23). The probe coated filter paper was exposed on the top of a glass vial containing TNT vapor and recorded the PL spectra for every minute (Figure 3.24, a). Interestingly, it was observed that the PL intensity continuously decreases with exposure time. The TNT vapor concentration at 25°C (~7.6 ppb) based on reported literature,[62] and plotted the Stern-Volmer plot and calculated LOD in the vapor phase (Figure 3.24, b). The limit of detection observed for TNT vapor is 7.8 ppb.
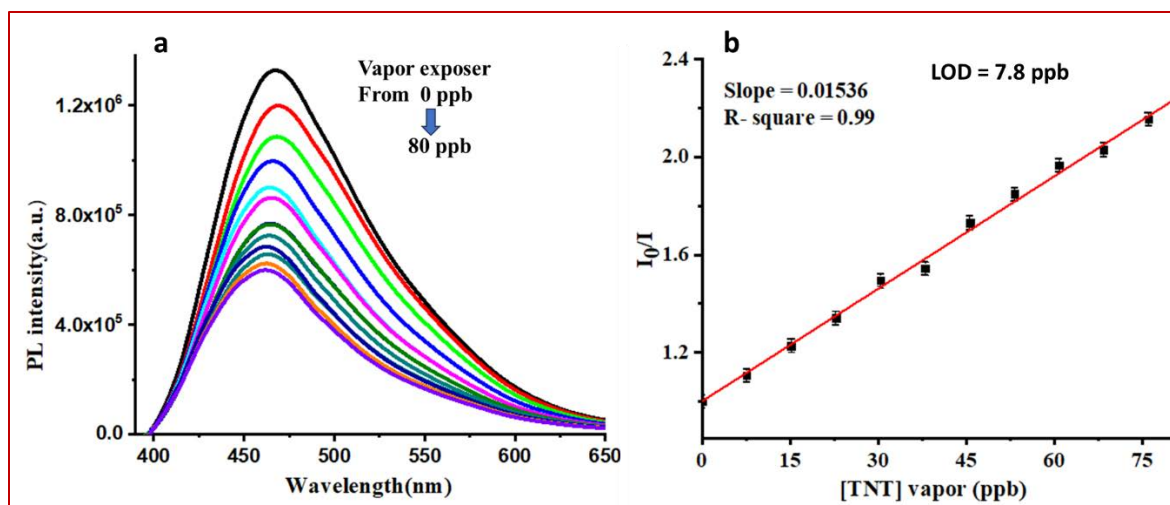
Figure 3.24 (a) Filter paper impregnated with the probe in THF (10^{-5} M, PyTrDA in THF); then the film was exposed to TNT vapors for one minute and recorded the PL spectra; it was repeated several times; **(b)** Stern-Volmer plot for emission quenching. I_0 represents the initial PL intensity in the absence of TNT vapor, and I represent the intensity in the presence of TNT vapor. The error bars shown at each data point represent the standard deviation obtained from three independent measurements $= \pm 0.018$

In view of practicality, the response time and the ease of using the technique for sensing TNT has been estimated. It was observed that synthesized probe can be easily applied on cheaper cellulose substrate (filter paper) which can be used as a paper strip sensor for contact mode and non-contact mode (vapor phase) detection. The paper strip sensor was tested for contact mode by rubbing a crystal of TNT on the paper strip for ~10s and observed the subsequent change of emission just in 30s later under UV lamp (365 nm) as shown in Figure 3.25. In the non-contact mode, the paper strip was exposed to TNT vapor for 10, 20, 40, 60, and 120s and checked the quenching effect on the probe emission under UV excitation (365 nm) as shown in Figure 3.25. The ultrasensitive response time (~ 10s) enables us to observe the visible changes of emission quenching under UV excitation (365 nm), making this probe superior for TNT sensing.
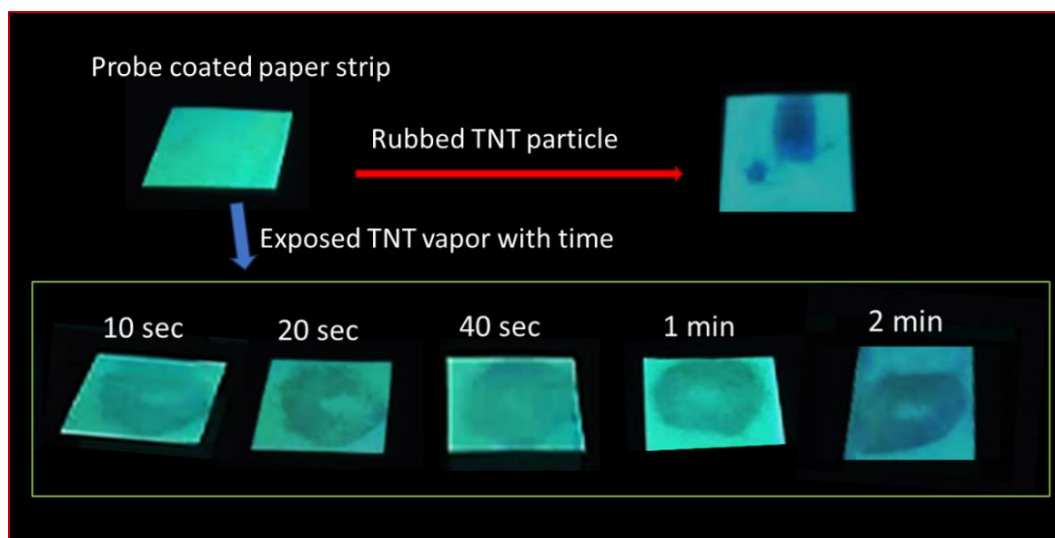
Figure 3.25 Filter paper impregnated with the probe in THF (10^{-5} M, PyTrDA in THF) followed by the exposure in contact (rubbed with TNT particle) and non-contact modes (with vapor phase); then checked the quenching of the visible emission of probe under UV excitation (365 nm)

3.4 CONCLUSION

In this chapter, two pyrene triazine-based probe molecules were synthesized by substituting phenyl-containing rotary groups. One of the synthesized compounds (PyTrDA) is AIE active with 20.9% absolute quantum yield and 14.01 ns excited state lifetime. This molecule is highly sensitive and selective towards TNT explosives. TNT was detected from aqueous solution by using aggregated PyTrDA (90% water-THF) up to 216 ppt. TNT was also detected directly by using paper strips. The cheap and easily available paper strip was utilized to recognize TNT molecules from the vapor phase (7.8 ppb). Among the military explosives (RDX, PETN, HMX, NH_4NO_3), PyTrDA detects TNT vapor within 10 seconds and one can clearly see emission quenching with naked eye. It would be practically a very useful and handy tool for onsite detection of TNT. The twisted nature of diarylamine introduces the AIEE activity and the vertically grown nano-rod type morphology provides more surface area for exposure is the leading cause for the exceptionally sensitive detection of TNT.

3.5 REFERENCES

1. Kolla, P., The application of analytical methods to the detection of hidden explosives and explosive devices. *Angewandte Chemie International Edition in English* **1997,** *36* (8), 800-811.

2. Yang, J.-S.; Swager, T. M., Fluorescent porous polymer films as TNT chemosensors: electronic and structural effects. *Journal of the American Chemical Society* **1998,** *120* (46), 11864-11873.

3. Dorsey, A.; Hodes, C. S.; Richter-Torres, P., Toxicological profile for 2, 4, 6-trinitrotoluene. **1995**.

4. Martel, R.; Mailloux, M.; Gabriel, U.; Lefebvre, R.; Thiboutot, S.; Ampleman, G., Behavior of energetic materials in ground water at an anti-tank range. *Journal of environmental quality* **2009,** *38 1*, 75-92.

5. Sun, X.; Wang, Y.; Lei, Y., Fluorescence based explosive detection: from mechanisms to sensory materials. *Chemical Society Reviews* **2015,** *44* (22), 8019-8061.

6. Hill, H. H.; Simpson, G., Capabilities and limitations of ion mobility spectrometry for field screening applications. *Field Analytical Chemistry & Technology* **1997,** *1* (3), 119-134.

7. Walsh, M. E., Determination of nitroaromatic, nitramine, and nitrate ester explosives in soil by gas chromatography and an electron capture detector. *Talanta* **2001,** *54* (3), 427-438.

8. Hu, Z.; Deibert, B. J.; Li, J., Luminescent metal–organic frameworks for chemical sensing and explosive detection. *Chemical Society Reviews* **2014,** *43* (16), 5815-5840.

9. Kojima, K.; Sakairi, M.; Takada, Y.; NAKAMURA, J., Vapor detection of TNT and RDX using atmospheric pressure chemical ionization mass spectrometry with counter-flow introduction (CFI). *Journal of the Mass Spectrometry Society of Japan* **2000,** *48* (5), 360-362.

10. Toal, S. J.; Trogler, W. C., Polymer sensors for nitroaromatic explosives detection. *Journal of Materials Chemistry* **2006,** *16* (28), 2871-2883.

11. Tanwar, A. S.; Parui, R.; Garai, R.; Chanu, M. A.; Iyer, P. K., Dual "Static and Dynamic" fluorescence quenching mechanisms based detection of TNT via a cationic conjugated polymer. *ACS Measurement Science Au* **2021,** *2* (1), 23-30.

12.   Kumar, V.; Saini, S. K.; Choudhury, N.; Kumar, A.; Maiti, B.; De, P.; Kumar, M.; Satapathi, S., Highly sensitive detection of nitro compounds using a fluorescent copolymer-based FRET system. *ACS Applied Polymer Materials* **2021,** *3* (8), 4017-4026.

13.   Rochat, S.; Swager, T. M., Conjugated amplifying polymers for optical sensing applications. *ACS applied materials & interfaces* **2013,** *5* (11), 4488-4502.

14.   Schmidt, J.; Weber, J.; Epping, J. D.; Antonietti, M.; Thomas, A., Microporous conjugated poly (thienylene arylene) networks. *Advanced Materials* **2009,** *21* (6), 702-705.

15.   Zreid, M. S.; Tabasi, Z. A.; Ma, X.; Wang, T.; Almatarneh, M. H.; Zhao, Y., Highly Twisted Aryl-Anthraquinodimethanes: Synthesis, Characterization, and Fluorescence Sensing of TNT. *European Journal of Organic Chemistry* **2020,** *2020* (26), 4031-4041.

16.   Dongre, S. D.; Das, T.; Babu, S. S., Dual mode selective detection and differentiation of TNT from other nitroaromatic compounds. *Journal of Materials Chemistry A* **2020,** *8* (21), 10767-10771.

17.   Kartha, K. K.; Babu, S. S.; Srinivasan, S.; Ajayaghosh, A., Attogram sensing of trinitrotoluene with a self-assembled molecular gelator. *Journal of the american chemical society* **2012,** *134* (10), 4834-4841.

18.   Wang, S.; Wang, Q.; Feng, X.; Wang, B.; Yang, L., Explosives in the cage: metal–organic frameworks for high-energy materials sensing and desensitization. *Advanced Materials* **2017,** *29* (36), 1701898.

19.   Xing, S.; Bing, Q.; Qi, H.; Liu, J.; Bai, T.; Li, G.; Shi, Z.; Feng, S.; Xu, R., Rational design and functionalization of a zinc metal–organic framework for highly selective detection of 2, 4, 6-trinitrophenol. *ACS applied materials & interfaces* **2017,** *9* (28), 23828-23835.

20.   Yang, Z.; Dou, X., Emerging and future possible strategies for enhancing 1D inorganic nanomaterials-based electrical sensors towards explosives vapors detection. *Advanced Functional Materials* **2016,** *26* (15), 2406-2425.

21.   Kartha, K. K.; Sandeep, A.; Praveen, V. K.; Ajayaghosh, A., Detection of nitroaromatic explosives with fluorescent molecular assemblies and π-gels. *The Chemical Record* **2015,** *15* (1), 252-265.

22.   Zhang, Y.; Xu, M.; Bunes, B. R.; Wu, N.; Gross, D. E.; Moore, J. S.; Zang, L., Oligomer-coated carbon nanotube chemiresistive sensors for selective detection of nitroaromatic explosives. *ACS Applied Materials & Interfaces* **2015,** *7* (14), 7471-7475.

23.   Zhao, P.; Wu, Y.; Feng, C.; Wang, L.; Ding, Y.; Hu, A., Conjugated polymer nanoparticles based fluorescent electronic nose for the identification of volatile compounds. *Analytical chemistry* **2018,** *90* (7), 4815-4822.

24.   Xu, Y.; Jin, S.; Xu, H.; Nagai, A.; Jiang, D., Conjugated microporous polymers: design, synthesis and application. *Chemical Society Reviews* **2013,** *42* (20), 8012-8031.

25.   Liyanage, T.; Rael, A.; Shaffer, S.; Zaidi, S.; Goodpaster, J. V.; Sardar, R., Fabrication of a self-assembled and flexible SERS nanosensor for explosive detection at parts-per-quadrillion levels from fingerprints. *Analyst* **2018,** *143* (9), 2012-2022.

26.   Prusti, B.; Chakravarty, M., An electron-rich small AIEgen as a solid platform for the selective and ultrasensitive on-site visual detection of TNT in the solid, solution and vapor states. *Analyst* **2020,** *145* (5), 1687-1694.

27.   Kumar, V.; Maiti, B.; Chini, M. K.; De, P.; Satapathi, S., Multimodal Fluorescent Polymer Sensor for Highly Sensitive Detection of Nitroaromatics. *Scientific Reports* **2019,** *9*.

28.   Chen, L.; Liu, D.; Peng, J.; Du, Q.; He, H., Ratiometric fluorescence sensing of metal-organic frameworks: Tactics and perspectives. *Coordination Chemistry Reviews* **2020,** *404*, 213113.

29.   Xu, B.; Wu, X.; Li, H.; Tong, H.; Wang, L., Selective detection of TNT and picric acid by conjugated polymer film sensors with donor–acceptor architecture. *Macromolecules* **2011,** *44* (13), 5089-5092.

30.   Gupta, M.; Lee, H.-i., Recyclable polymeric thin films for the selective detection and separation of picric acid. *ACS applied materials & interfaces* **2018,** *10* (48), 41717-41723.

31.   Kalita, A.; Hussain, S.; Malik, A. H.; Barman, U.; Goswami, N.; Iyer, P. K., Anion-exchange induced strong π–π interactions in single crystalline naphthalene diimide for nitroexplosive sensing: An electronic prototype for visual on-site detection. *ACS Applied Materials & Interfaces* **2016,** *8* (38), 25326-25336.

32.   Salinas, Y.; Martínez-Máñez, R.; Marcos, M. D.; Sancenón, F.; Costero, A. M.; Parra, M.; Gil, S., Optical chemosensors and reagents to detect explosives. *Chemical Society Reviews* **2012,** *41* (3), 1261-1296.

33.   Chakraborty, M.; Prusti, B.; Chakravarty, M., Small Electron-Rich Isomeric Solid-State Emitters with Variation in Coplanarity and Molecular Packings: Rapid and Ultralow Recognition of TNT. *ACS Applied Electronic Materials* **2022,** *4* (5), 2481-2489.

34.   Zhang, S.; Lü, F.; Gao, L.; Ding, L.; Fang, Y., Fluorescent sensors for nitroaromatic compounds based on monolayer assembly of polycyclic aromatics. *Langmuir* **2007,** *23* (3), 1584-1590.

35.   Goodpaster, J. V.; McGuffin, V. L., Fluorescence quenching as an indirect detection method for nitrated explosives. *Analytical Chemistry* **2001,** *73* (9), 2004-2011.

36.   Kachwal, V.; Joshi, M.; Mittal, V.; Choudhury, A. R.; Laskar, I. R., Strategic design and synthesis of AIEE (Aggregation Induced Enhanced Emission) active push-pull type pyrene derivatives for the ultrasensitive detection of explosives. *Sensing and Bio-Sensing Research* **2019,** *23*, 100267.

37.   Zhao, D.; Swager, T. M., Sensory responses in solution vs solid state: a fluorescence quenching study of poly (iptycenebutadiynylene) s. *Macromolecules* **2005,** *38* (22), 9377-9384.

38.   Anitha, S.; Brabu, B.; Rajesh, K.; Natarajan, T., Fabrication of UV sensor based on electrospun composite fibers. *Materials Letters* **2013,** *92*, 417-420.

39.   Raichure, P. C.; Bhatt, R.; Kachwal, V.; Sharma, T. C.; Laskar, I. R., Multi-stimuli distinct responsive D–A based fluorogen oligomeric tool and efficient detection of TNT vapor. *New Journal of Chemistry* **2022,** *46* (14), 6560-6569.

40.   Nie, H.; Zhao, Y.; Zhang, M.; Ma, Y.; Baumgarten, M.; Müllen, K., Detection of TNT explosives with a new fluorescent conjugated polycarbazole polymer. *Chemical Communications* **2011,** *47* (4), 1234-1236.

41.   Zhou, H.; Chua, M. H.; Tang, B. Z.; Xu, J., Aggregation-induced emission (AIE)-active polymers for explosive detection. *Polymer Chemistry* **2019,** *10* (28), 3822-3840.

42.   Shanmugaraju, S.; Joshi, S. A.; Mukherjee, P. S., Fluorescence and visual sensing of nitroaromatic explosives using electron rich discrete fluorophores. *Journal of Materials Chemistry* **2011,** *21* (25), 9130-9138.

43.   Zhang, R.; Zhang, T.; Xu, L.; Han, F.; Zhao, Y.; Ni, Z., A new series of short axially symmetrically and asymmetrically 1,3,6,8-tetrasubstituted pyrenes with two types of substituents: Syntheses, structures, photophysical properties and electroluminescence. *Journal of Molecular Structure* **2017,** *1127*, 237-246.

44.   Mosca, L.; Karimi Behzad, S.; Anzenbacher, P., Jr., Small-Molecule Turn-On Fluorescent Probes for RDX. *Journal of the American Chemical Society* **2015,** *137* (25), 7967-7969.

45.   Gong, Y.-B.; Zhang, P.; Gu, Y.-r.; Wang, J.-Q.; Han, M.-M.; Chen, C.; Zhan, X.-J.; Xie, Z.-L.; Zou, B.; Peng, Q.; Chi, Z.-G.; Li, Z., The Influence of Molecular Packing on the Emissive Behavior of Pyrene Derivatives: Mechanoluminescence and Mechanochromism. *Advanced Optical Materials* **2018,** *6* (16), 1800198.

46.   Liu, W.; Li, S.; Xie, Z.; Huang, K.; Yan, K.; Zhao, Y.; Redshaw, C.; Feng, X.; Tang, B. Z., Molecular Engineering toward Broad Color-Tunable Emission of Pyrene-Based Aggregation-Induced Emission Luminogens. *Advanced Optical Materials n/a* (n/a), 2400301.

47.   Gaussian09, R. A., 1, mj frisch, gw trucks, hb schlegel, ge scuseria, ma robb, jr cheeseman, g. Scalmani, v. Barone, b. Mennucci, ga petersson et al., gaussian. *Inc., Wallingford CT* **2009,** *121*, 150-166.

48.   Hehre, W. J.; Ditchfield, R.; Pople, J. A., Self—consistent molecular orbital methods. XII. Further extensions of Gaussian—type basis sets for use in molecular orbital studies of organic molecules. *The Journal of Chemical Physics* **1972,** *56* (5), 2257-2261.

49.   Frisch, M.; Trucks, G.; Schlegel, H. B.; Scuseria, G.; Robb, M.; Cheeseman, J.; Scalmani, G.; Barone, V.; Petersson, G.; Nakatsuji, H., Gaussian 16. Gaussian, Inc. Wallingford, CT: 2016.

50.   Qin, H.; Stewart, M. G., Casualty Risks Induced by Primary Fragmentation Hazards from High-explosive munitions. *Reliability Engineering & System Safety* **2021,** *215*, 107874.

51.   Wang, C.; Tian, L.; Zhu, W.; Wang, S.; Wang, P.; Liang, Y.; Zhang, W.; Zhao, H.; Li, G., Dye@bio-MOF-1 Composite as a Dual-Emitting Platform for Enhanced Detection of a Wide Range of Explosive Molecules. *ACS Applied Materials & Interfaces* **2017,** *9* (23), 20076-20085.

52.   Prusti, B.; Chakravarty, M., An electron-rich small AIEgen as a solid platform for the selective and ultrasensitive on-site visual detection of TNT in the solid, solution and vapor states. *The Analyst* **2020**.

53.   Tanwar, A. S.; Parui, R.; Garai, R.; Chanu, M. A.; Iyer, P. K., Dual "Static and Dynamic" Fluorescence Quenching Mechanisms Based Detection of TNT via a Cationic Conjugated Polymer. *ACS Measurement Science Au* **2022,** *2* (1), 23-30.

54.   Kumar, M.; Vij, V.; Bhalla, V., Vapor-phase detection of trinitrotoluene by AIEE-active hetero-oligophenylene-based carbazole derivatives. *Langmuir* **2012,** *28* (33), 12417-12421.

55.   Bhatta, R. P.; Agarwal, A.; Kachawal, V.; Raichure, P. C.; Laskar, I. R., Enhanced TNT Vapor Sensing Through PMMA-mediated AIPE-Active Monocyclometalated Iridium(III) Complex: A Leap Towards Real-Time Monitoring. *Analyst* **2024**.

56.   Lee, S. H.; Parthasarathy, A.; Schanze, K. S., A Sensitive and Selective Mercury(II) Sensor Based on Amplified Fluorescence Quenching in a Conjugated Polyelectrolyte/Spiro-Cyclic Rhodamine System. *Macromolecular Rapid Communications* **2013,** *34* (9), 791-795.

57.   Kumar, V.; Maiti, B.; Chini, M. K.; De, P.; Satapathi, S., Multimodal Fluorescent Polymer Sensor for Highly Sensitive Detection of Nitroaromatics. *Scientific Reports* **2019,** *9* (1), 7269.

58.   Mosca, L.; Khnayzer, R. S.; Lazorski, M. S.; Danilov, E. O.; Castellano, F. N.; Anzenbacher Jr, P., Sensing of 2, 4, 6-Trinitrotoluene (TNT) and 2, 4-Dinitrotoluene (2, 4-DNT) in the Solid State with Photoluminescent RuII and IrIII Complexes. *Chemistry–A European Journal* **2015,** *21* (10), 4056-4064.

59.   Paul, S.; Kitakado, H.; Suga, K.; Kotani, R.; Dey, N.; Venkatramani, R.; Matito, E.; Saito, S.; Dasgupta, J., Triplet conformation in chromophore-fused cyclooctatetraene dyes. *Journal of Materials Chemistry C* **2023,** *11* (36), 12243-12253.

60.   Yoo, H. S.; DeWitt, M. J.; Pate, B. H., Vibrational Dynamics of Terminal Acetylenes: I. Comparison of the Intramolecular Vibrational Energy Redistribution Rate of Gases and the Total Relaxation Rate of Dilute Solutions at Room Temperature. *The Journal of Physical Chemistry A* **2004,** *108* (8), 1348-1364.

61.   Senthamizhan, A.; Celebioglu, A.; Bayir, S.; Gorur, M.; Doganci, E.; Yilmaz, F.; Uyar, T., Highly Fluorescent Pyrene-Functional Polystyrene Copolymer Nanofibers for Enhanced Sensing Performance of TNT. *ACS Appl Mater Interfaces* **2015,** *7* (38), 21038-46.

62.   Oxley, J. C.; Smith, J. L.; Luo, W.; Brady, J., Determining the Vapor Pressures of Diacetone Diperoxide (DADP) and Hexamethylene Triperoxide Diamine (HMTD). *Propellants, Explosives, Pyrotechnics* **2009,** *34* (6), 539-543.

ENHANCED TNT VAPOR SENSING THROUGH PMMA-MEDIATED AIPE-ACTIVE MONO-CYCLOMETALATED IRIDIUM(III) COMPLEX: A LEAP TOWARDS REAL-TIME MONITORING

Chapter 4. Enhanced TNT Vapor Sensing Through PMMA-mediated AIPE-Active Monocyclometalated Iridium(III) Complex: A Leap Towards Real-Time Monitoring

4.1 INTRODUCTION

In recent years, the convenient way to detect nitro-based explosive compounds with high selectivity and sensitivity has become an area of significant interest, as these compounds pose a potential threat to humanity and the environment. Among these compounds, 2,4,6-trinitrotoluene (TNT) is one of the most extensively utilized in military operations and terrorist attacks due to its stability under ambient conditions.[1-2] Being a low-melting solid (81°C), TNT is widely used to load into an improvised explosive device (IED). These attributes of TNT lead to its easy handling. Thus, it is becoming a handy work of evil people that triggers a severe concern for homeland security. Moreover, it is a contaminant in water bodies, with permissible concentrations in drinking water limited to 2 ppb, beyond which it causes potential risk of liver, eye, and neurological damage.[3] Thus, it is kept under the category of priority pollutants by the United States Environmental Protection Agency (USAEPA).[3-6] So, sensitive detection of TNT from the water bodies and in the vapor phase is highly desirable.

In general, nitro-based explosives have a low vapor pressure (10^{-5}-10^{-15} torr).[7] For the case of TNT, the vapor pressure is 5.8×10^{-6} Torr (~10 ppb) at 25 °C, which makes it challenging to identify it in the vapor phase.[8] Many approaches have been used to detect TNT such as chromatography, mass spectrometry, Raman spectroscopy, X-ray imaging, thermal neutron analysis, electrochemical assay, and ion mobility spectroscopy.[9] The equipment required for these procedures is expensive, heavy in nature and difficult to monitor in real-time applications.[10-11] The fluorescent-based technique has a distinct set of advantages, such as greater sensitivity, low cost, and convenient fabrication with portable devices for onsite and real-time detection. Many fluorescent-based probe molecules have been developed for the detection of TNT in the solution phase, with sensitivity so high that even parts per quadrillion (ppq) level.[12-20] However, vapor phase sensing presents many challenges such as exceptionally low vapor pressure (10^{-5}-10^{-15} torr)[7] and demands of detecting hidden explosives in

transportation hubs and war zones create a complex landscape that is difficult to navigate.[7, 21-24] The scientific community thus finds itself in urgent need of a fluorescent-based probe that is highly sensitive and selective for the detection of TNT in the vapor phase. The key attributes, a robust probe should have appropriately aligned LUMO levels of probe molecule and analyte for effective electron transfer, significant extent of overlapping of absorption spectra of analyte and emission spectra of probe molecule for efficient energy transfer, an extended excited state lifetime of the probe to maximize the interaction time with the analyte, a high quantum yield, and the integration of a porous medium to trap the elusive vapors of the explosives.[7] In the quest to detect nitro-based explosive compounds, various luminescent explosive sensors have been developed, leveraging small molecules, conjugated polymers, self-assembled organic nanomaterials, and metal-organic frameworks.[14-15, 25-34] These have been evaluated for their utility in both solution and vapor-phase sensing, but very few reports for fluorescence-based molecules have been employed to detect TNT vapor.[15, 20, 25, 34-36] Mothika and co-workers reported films of tetraphenylene ethylene-based conjugated microporous polymers (PTPETCz) through an electro-polymerization method using tetra(carbazolylphenyl)ethylene monomer, which can detect TNT vapor even at a very low concentration of 33 ppb. In that work, authors used a custom-made setup with attached heating coils for the probe as well as the analyte and maintained a 35 °C temperature for generating TNT vapors. Despite these advancements, the selective vapor sensing of TNT at atmospheric conditions, particularly at a detection limit that would be considered satisfactory (lower ppb to ppt), remains an elusive goal.

Phosphorescent transition-metal complexes have been considered to be potential candidate in various fields such as chemosensors[37-41], optoelectronic materials[42-44], biological probe[45-46] etc. The role of heavy metals like Osmium(II) (Os), Platinum(II) (Pt), and Iridium(III) (Ir) as triplet emitters in these probes is highly desirable. Among these metals, iridium(III) complexes are highly impactful primarily due to their superior emission properties because of strong spin-orbit coupling (3909 cm^{-1}).[47-48] Moreover, the superior photothermal stabilities and color tuneability as compared to ruthenium(II) and osmium(II) complexes and their high coordination number relative to platinum(II) complexes allow the iridium(III) complexes a better platform for the structural modifications. 'Aggregation-induced Phosphorescent Emission' (AIPE) active iridium(III) complexes have emerged as a promising avenue in this quest, their desirable photophysical properties, which include a significant Stokes shift, high emission efficiency, and relatively extended excited state lifetime.[49-51] Their versatility has found applications in diverse fields such as light-emitting diodes, therapy, and sensing.[50-55]

In 2015, our group (Alam et al.) developed mono-cyclometalated AIPE active iridium(III) complexes and studied their potentiality for picric acid detection.[51] Recently, our group (Agarwal et al.) synthesized a series of AIPE active Ir(III) complexes and used them to sense different nitro-based explosives successfully.[56] It was observed that tuning of electronic substituent on phenyl pyridine ligand modulated their sensitivity and selectivity towards different nitro-based explosives. One of the complexes having a moderately electron-withdrawing substituent, i.e., a carboxyl group (-COOH), was found to be sensitive towards TNT in contact mode (LOD -3.6 ppb) based on the PET mechanism. In our study, we have ventured into this exciting terrain to design and synthesize the two new mono cyclometalated AIPE active iridium(III) complexes (M1 and M2) by using electron-donating -methoxy (-OMe) and highly electron-withdrawing cyano (-CN) substituent on the phenyl ring of phenyl pyridine ligand, to explore their potential in sensing of TNT explosive. Initially, we tested in contact mode sensing of TNT and found the limit of detection in the pM (ppt) range. This impressive sensitivity emboldened us to test our probes for TNT vapor phase sensing. To improve further the sensitivity and stability of the probe, we made the strategic decision to impregnate the probes into a porous PMMA polymer. This decision yielded impressive results, i.e., the post-impregnated probes exhibited a quantum yield and lifetime, which is enhanced as that of the original probe. Then, the preparation of various films from the polymer-impregnated complex (CP) and exposure to nitro-based explosive vapors were carried out. The results were resoundingly positive: the probes demonstrated an uncanny ability to selectively sense TNT vapors with a high level of sensitivity, achieving a detection limit of 12.8 ppb. These findings have affirmed the potential of our approach and laid the foundation for further advancements in the field.

4.2 EXPERIMENTAL SECTION
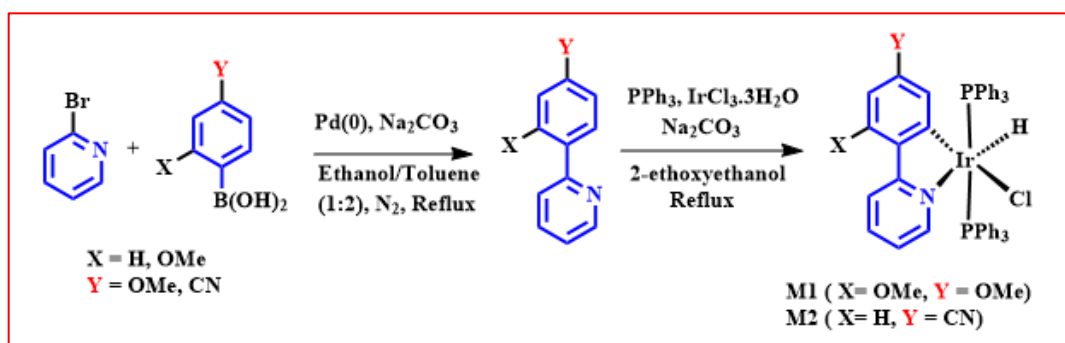
Scheme 4.1 General synthetic route for ligands and their corresponding complexes M1 and M2

4.2.1 Synthesis of ligands: -

L1 (Scheme 4.2): (2,4-dimethoxyphenyl) boronic acid (1.1 mmol) and 2-bromopyridine (1 mmol) were taken in a clean and dry two-neck round bottom flask. A solvent mixture of toluene and ethanol (2:1) was added to a round bottom flask, and the mixture was purged with nitrogen for 5-10 minutes. Tetrakis(triphenylphosphine)palladium(0) (0.0015 mmol) was added in an inert atmosphere under stirring. Sodium bicarbonate (2.1 mmol) in water was added after 10 minutes of catalyst addition. The reaction mixture was refluxed for 15 hours with intermittent TLC observation. After completion of the reaction, the reaction mixture was cooled down to room temperature, water was added, and the compound was extracted in ethyl acetate twice. The organic layer was collected and purified by column chromatography using silica (mesh 60-120) and hexane and ethyl acetate (9:1) as a solvent system. A brownish solid product was obtained with an 80% yield (Scheme- 4.2). The ligand was characterized by NMR (spectra shown in Figure 4.1 and 4.2, respectively).
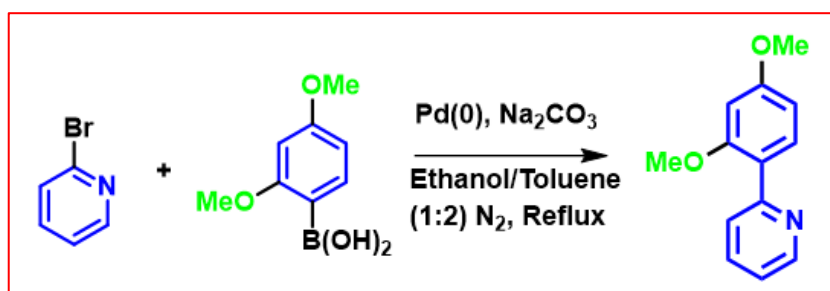
Scheme 4.2 Synthesis of ligand L1

^{1}H NMR (400 MHz, Chloroform-d) δ 8.68 (dd, J = 4.9, 1.9, 1.0 Hz, 1H), 7.86 – 7.75 (m, 2H), 7.69 (dd, J = 8.1, 7.4, 1.9 Hz, 1H), 7.17 (m, J = 7.4, 4.9, 1.2 Hz, 1H), 6.64 (dd, J = 8.5, 2.4 Hz, 1H), 6.58 (d, J = 2.4 Hz, 1H), 3.88 (s, 3H), 3.87 (s, 3H) (Figure 4.1).

^{13}C NMR (101 MHz, Chloroform-d) δ 161.33, 158.11, 155.90, 149.30, 135.61, 131.98, 124.74, 122.11, 121.14, 105.06, 98.89, 55.59, 55.46 (Figure 4.2).

8.6945
8.6920
8.6896
8.6872
8.6823
8.6798
8.6774
8.6750
7.8331
7.8304
7.8276
7.8129
7.8102
7.8075
7.7941
7.7729
7.7097
7.7049
7.6910
7.6995
7.6864
7.6849
7.6710
7.6663
7.1908
7.1877
7.1786
7.1755
7.1722
7.1691
7.1599
7.1569
6.6565
6.6506
6.6352
6.6292
6.5831
6.5772
3.8800
3.8674

1.00
2.10 1.07
1.04
1.13 1.00
2.80 2.95
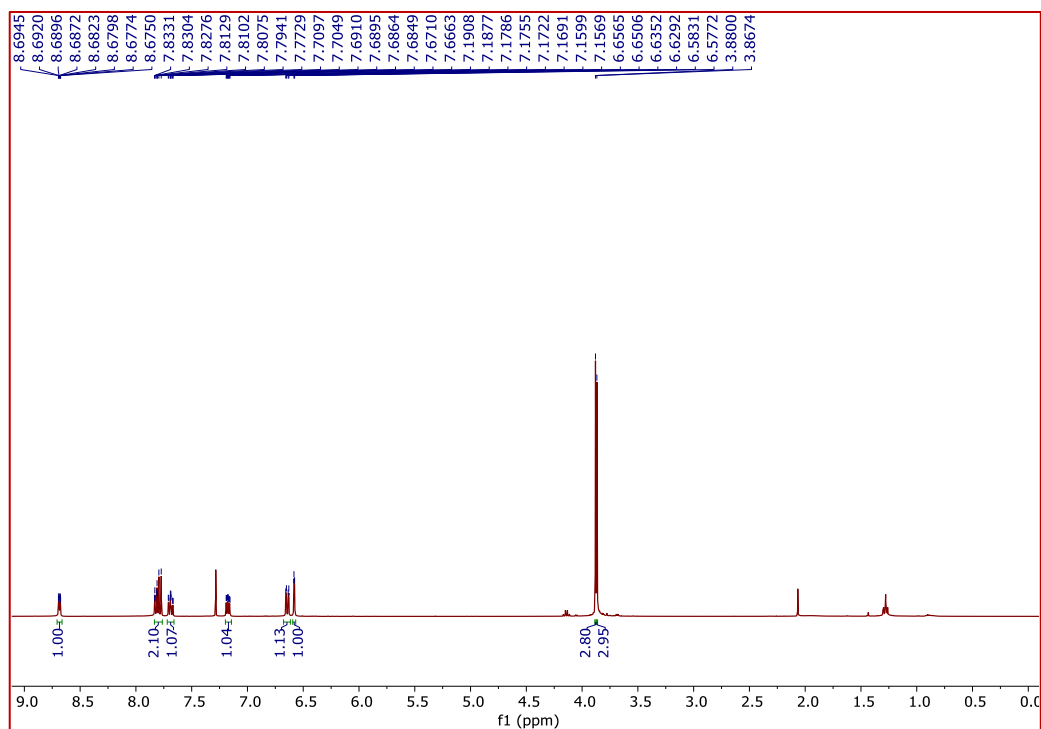
Figure 4.1 ^{1}H NMR spectrum of L1 in Chloroform-*d* solvent

161.3318
158.1140
155.9014
149.3021
135.6132
131.9785
124.7386
122.1084
121.1400
105.0623
98.8907
55.5881
55.4591
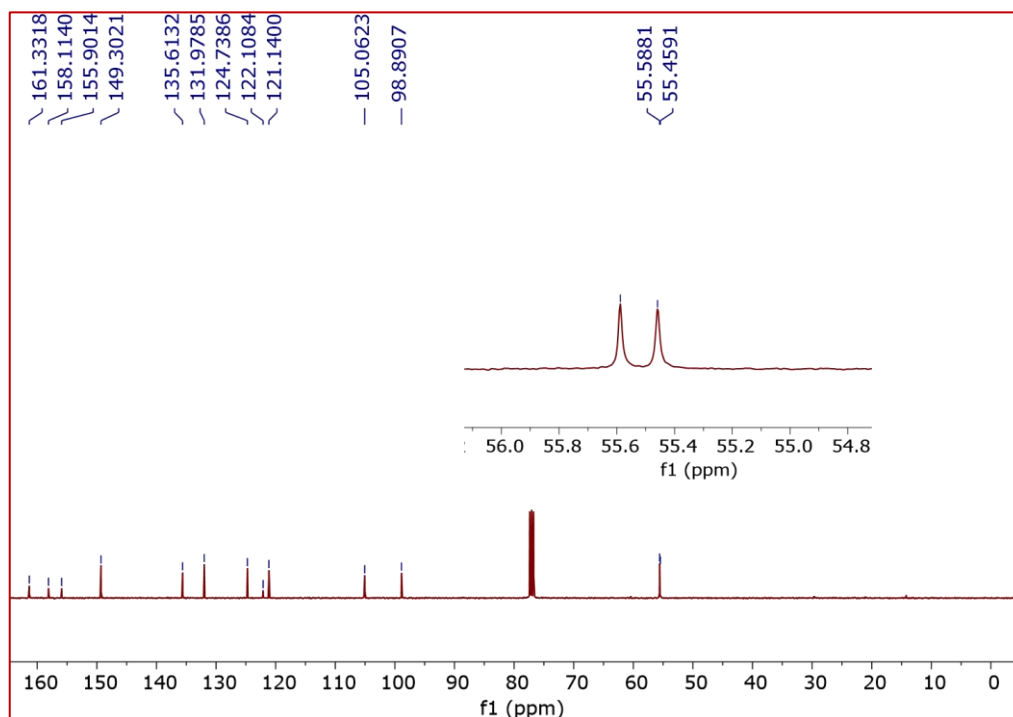
Figure 4.2 ^{13}C NMR spectrum of L1 in Chloroform-*d* solvent

L2 (Scheme 4.3): (4-Cyanophenyl) boronic acid (1.1mmol) and 2-bromopyridine (1mmol)

were taken in a clean and dry two-neck round bottom flask. A solvent mixture of toluene and ethanol (2:1) was added to a round bottom flask, and the mixture was purged with nitrogen gas for 5-10 minutes. Tetrakis(triphenylphosphine)palladium(0) (0.0015 mmol) was added in an inert atmosphere under stirring. Sodium bicarbonate (2.1 mmol) in water was added after 10 minutes of catalyst addition. The reaction mixture was refluxed for 15 hours with intermittent TLC observation. After completion of the reaction, isolation of the product was done by following the same process as for L1, and the solid product was obtained with 85% yield (Scheme-4.3). The ligand was characterized by NMR (spectra shown in Figure 4.3 and 4.4, respectively).
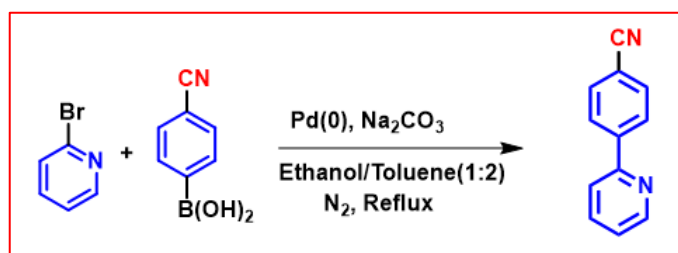
Scheme 4.3 Synthesis of ligand L2

^{1}H NMR (400 MHz, Chloroform-*d*) δ 8.83 – 8.73 (m, 1H), 8.13 (d, *J* = 8.3 Hz, 2H), 7.83 (dd, *J* = 7.4, 1.8 Hz, 1H), 7.83 – 7.72 (m, 3H), 7.39 – 7.31 (m, 1H). (Figure 4.3)

^{13}C NMR (101 MHz, Chloroform-*d*) δ 155.22, 150.06, 143.47, 137.16, 132.59, 127.48, 123.39, 121.04, 118.84, 112.45. (Figure 4.4)
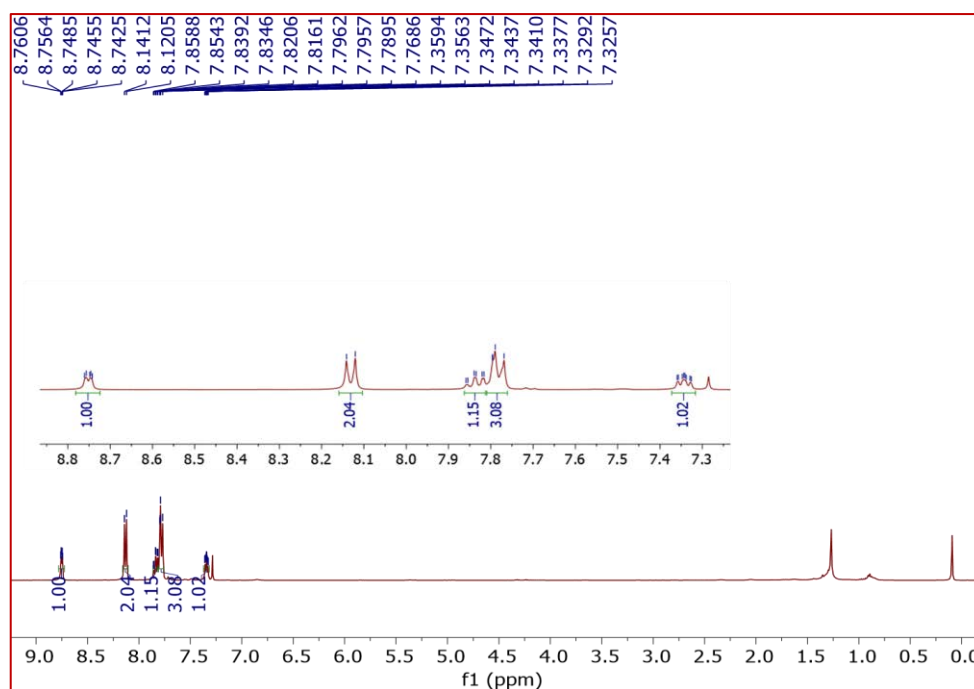
Figure 4.3 ^{1}H NMR spectrum of L2 in Chloroform-*d* solvent
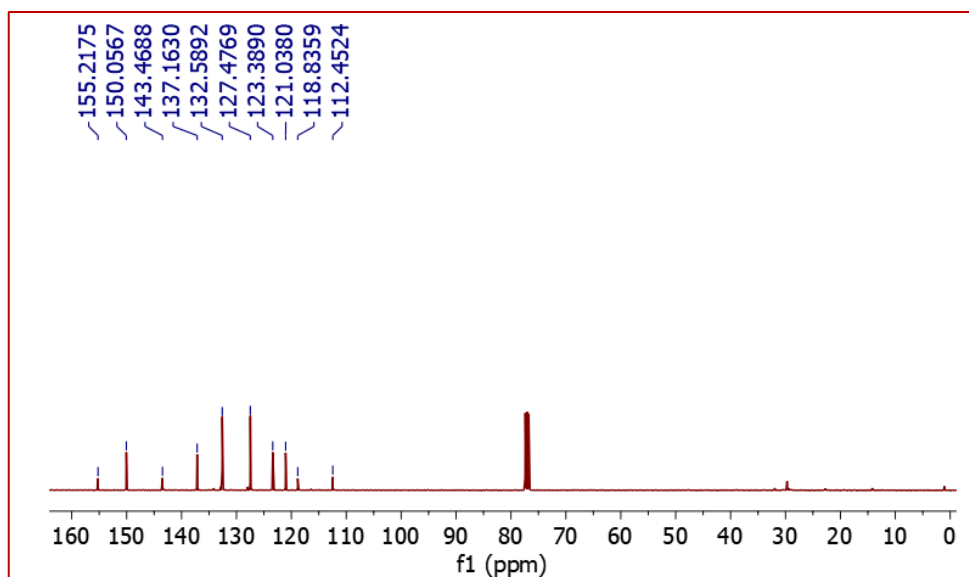
Figure 4.4 ^{13}C NMR spectrum of L2 in Chloroform-*d* solvent

4.2.2 Synthesis of Complexes:

M1 (Scheme 4.4): Iridium(III) salt (IrCl$_3$.3H$_2$O) (1 mmol) and triphenylphosphine (3 mmol) were taken in a 10 ml round bottom flask and refluxed in 2-ethoxyethanol for 4-5 hours. A pale-yellow salt was formed. The addition of L1(1 mmol) was done, followed by sodium bicarbonate (1.1 mmol) as a base, and further refluxed for 1 hour, and the progress of the reaction was monitored by TLC. The reaction mixture was cooled down to room temperature (RT), followed by the addition of hexane, then decanting, the solvent part. The crude complex was washed with hexane and diethyl ether 2-3 times and then dissolved in DCM. The dissolved complex was filtered and then recrystallized in DCM and hexane solvent system. A blue emissive product was obtained with 76% yield. The complex was characterized by NMR, HRMS, and IR (spectra shown in Figures 4.5 to 4.8).

^{1}H NMR *(400 MHz, Chloroform-d)* δ 8.15 (dd, *J* = 8.3, 1.2 Hz, 1H), 7.70 (dd, *J* = 12.0, 8.2, 1.4 Hz, 1H), 7.61 – 7.53 (m, 1H), 7.49 (dd, *J* = 8.4, 6.8, 3.1 Hz, 1H), 7.39 (dd, *J* = 7.2, 6.0, 4.3 Hz, 11H), 7.26 (d, *J* = 7.2 Hz, 1H), 7.21 (t, *J* = 7.3 Hz, 6H), 7.16 – 7.08 (m, 11H), 6.58 (dd, *J* = 7.1, 5.6, 1.4 Hz, 1H), 5.76 (d, *J* = 2.3 Hz, 1H), 5.32 (d, *J* = 2.3 Hz, 1H), 3.83 (s, 3H), 2.92 (s, 3H), -16.45 (t, *J* = 17.1 Hz, 1H). (Figure 4.5)

^{13}C NMR (101 MHz, Chloroform-*d*) δ 164.56, 161.16, 158.52, 154.62, 149.49, 135.20, 134.21 (t, *J* = 5.4 Hz), 132.17, 132.08, 131.98, 131.96, 131.69, 131.43, 128.95, 128.59, 128.47, 127.16 (t, *J* = 4.8 Hz), 124.42, 121.46, 118.66, 92.05, 54.86, 54.20. 79.16. (Figure 4.6)

^{31}P NMR (162 MHz, Chloroform-*d*) δ 10.397 (Figure 4.7), Stretching frequency of Ir-H bond= 2127 cm $^{-1}$. (Figure 4.13)

HRMS calculated: [M+H] $^{+}$: m/z = 967.2087; found: [M+H] $^{+}$: m/z = 969.2034 (Figure 4.8).
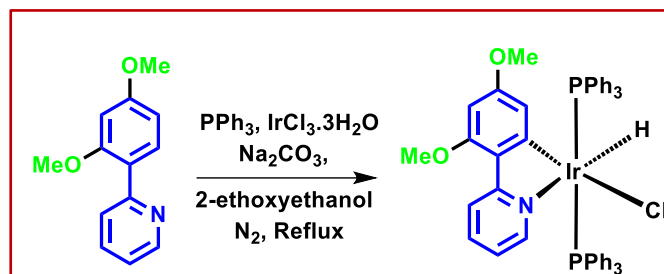
Scheme 4.4 Synthesis of metal complex M1
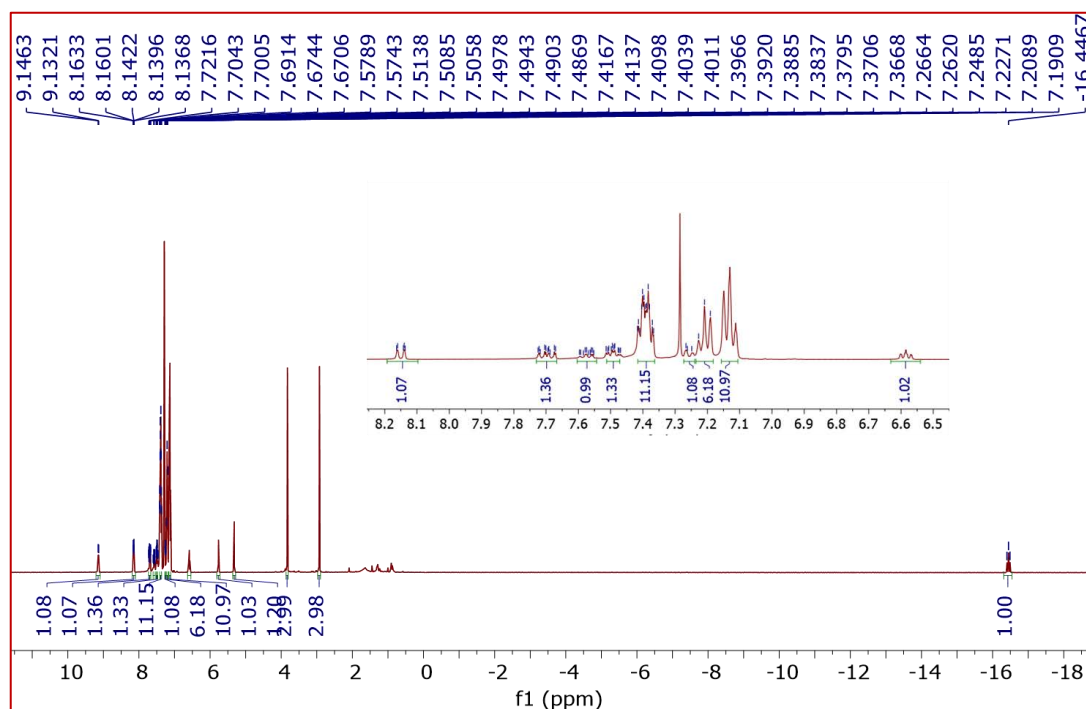
Figure 4.5 ^{1}H NMR spectrum of M1 in Chloroform-*d* solvent
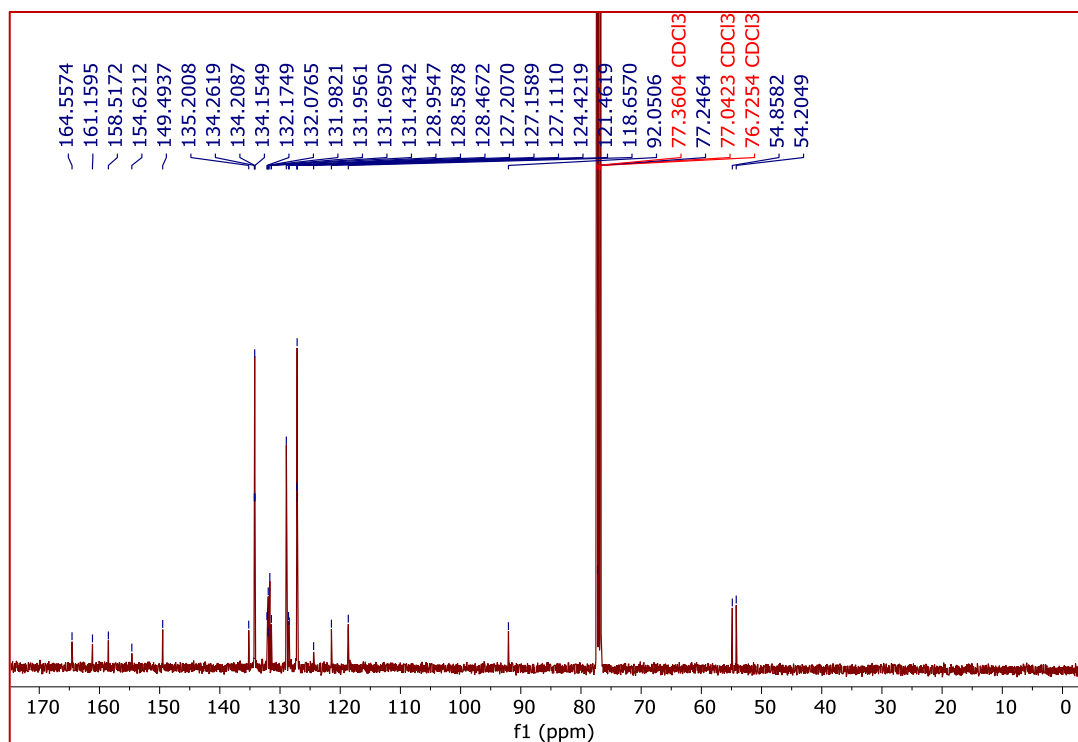
Figure 4.6 ^{13}C NMR spectrum of M1 in Chloroform-*d* solvent
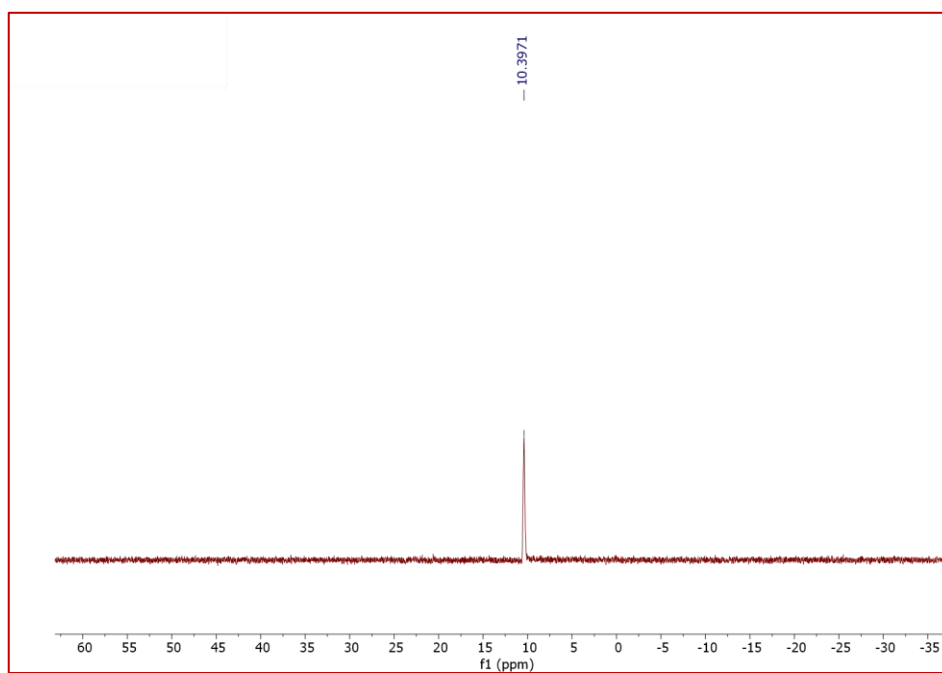
Figure 4.7 ^{31}P NMR spectrum of M1 in Chloroform-*d* solvent
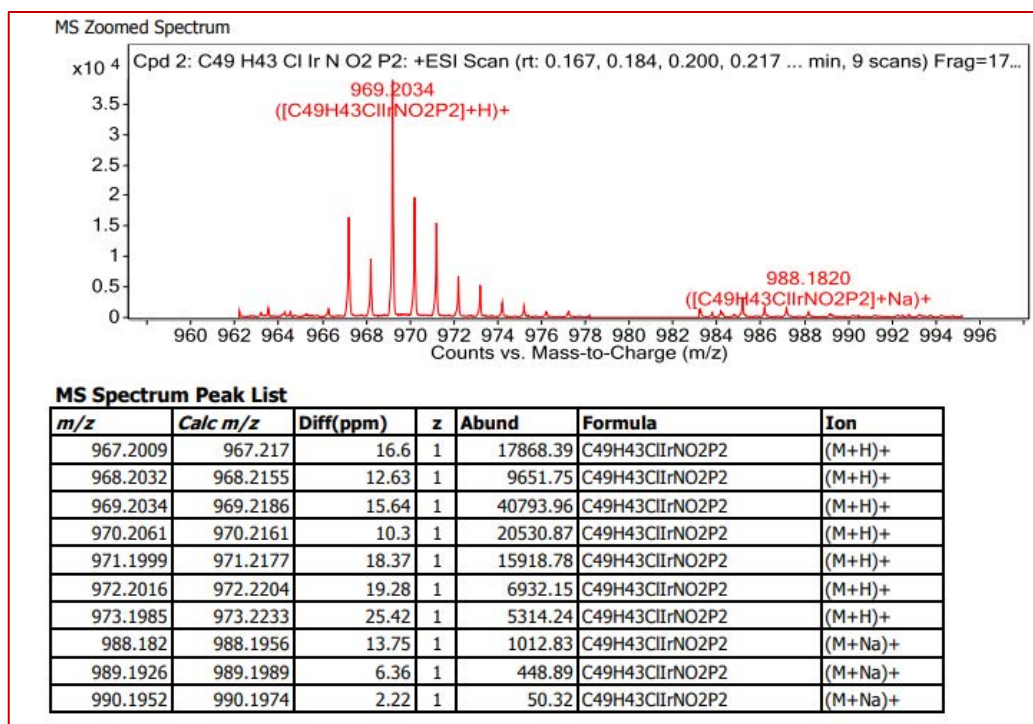
Figure 4.8 Mass spectrum of M1

M2 (Scheme 4.5): Iridium(III) salt (IrCl$_3$.3H$_2$O) (1 mmol) and triphenylphosphine (3 mmol) were taken in a 10 ml round bottom flask and refluxed in 2-ethoxyethanol for 4-5 hours. A pale-yellow salt was formed. L2 (1 mmol) was added, followed by sodium bicarbonate (1.1 mmol) as a base, and refluxed for 1 hour. Then the product was isolated, which followed a similar procedure as M1. A greenish-yellow emissive product was obtained with 78% yield. Then, the structure of the compound was characterized by NMR, HRMS, and IR (spectra shown in Figure 4.9 to 4.13).

^{1}H NMR (400 MHz, Chloroform-*d*) δ 9.08 (d, *J* = 5.6 Hz, 1H), 7.54 (d, *J* = 8.1 Hz, 1H), 7.48 (td, *J* = 7.7, 1.6 Hz, 1H), 7.43 – 7.34 (m, 12H), 7.28 – 7.19 (m, 7H), 7.15 (tt, *J* = 6.9, 1.4 Hz, 12H), 6.86 – 6.76 (m, 2H), 6.40 (d, *J* = 1.6 Hz, 1H), -16.87 (t, *J* = 16.7 Hz, 1H). (Figure 4.9)

^{13}C NMR (101 MHz, Chloroform-*d*) δ 163.70,150.78, 150.38, 146.66, 146.17, 135.99, 133.88 (t, *J* = 5.5 Hz), 131.67, 131.41, 131.14, 129.39, 127.45 (t, *J* = 4.9 Hz), 122.13, 121.68, 119.23, 118.37, 112.37 (Figure 4.10).

^{31}P NMR (162 MHz, Chloroform-*d*) δ 7.118 (Figure 4.11), Stretching frequency of Ir-H bond= 2137 cm^{-1}. (Figure 4.13)

HRMS calculated: [M+H]$^+$: *m/z* = 932.1828; found: [M+H]$^+$: *m/z* = 931.1869. (Figure 4.12)
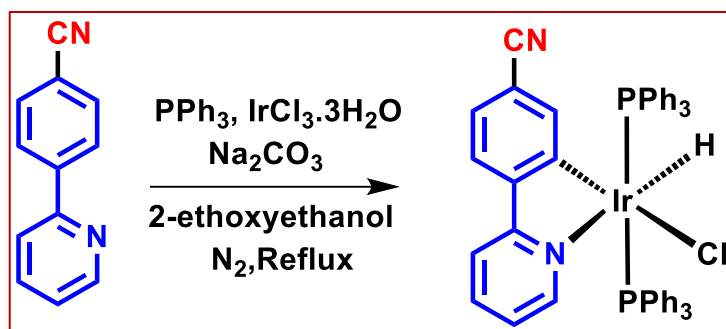
Scheme 4.5 Synthesis of metal complex M2
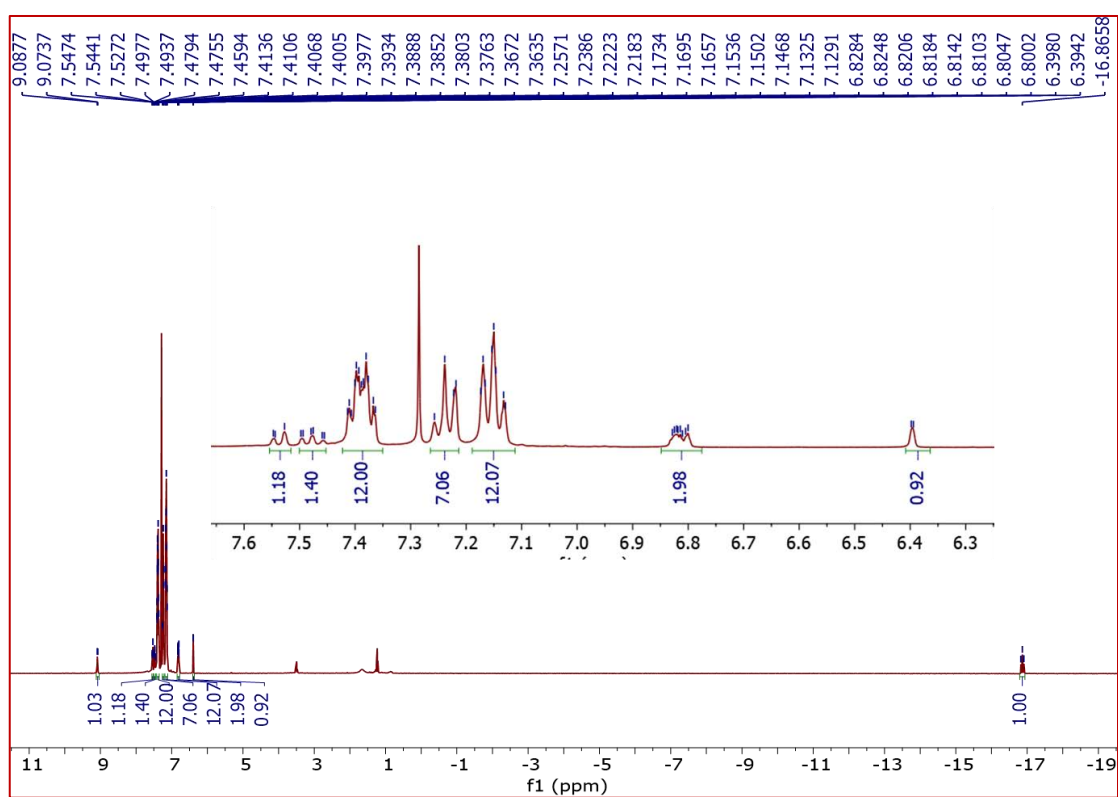
Figure 4.9 ^{1}H NMR spectrum of M2 (IrCN) in Chloroform-*d* solvent
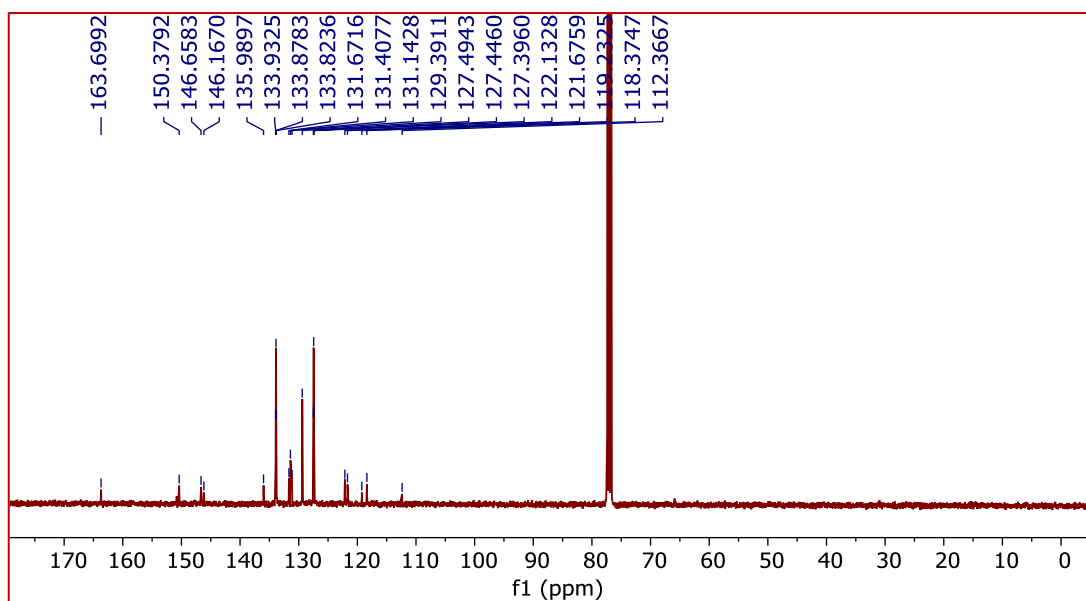
Figure 4.10 ^{13}C NMR spectrum of M2 in Chloroform-*d* solvent
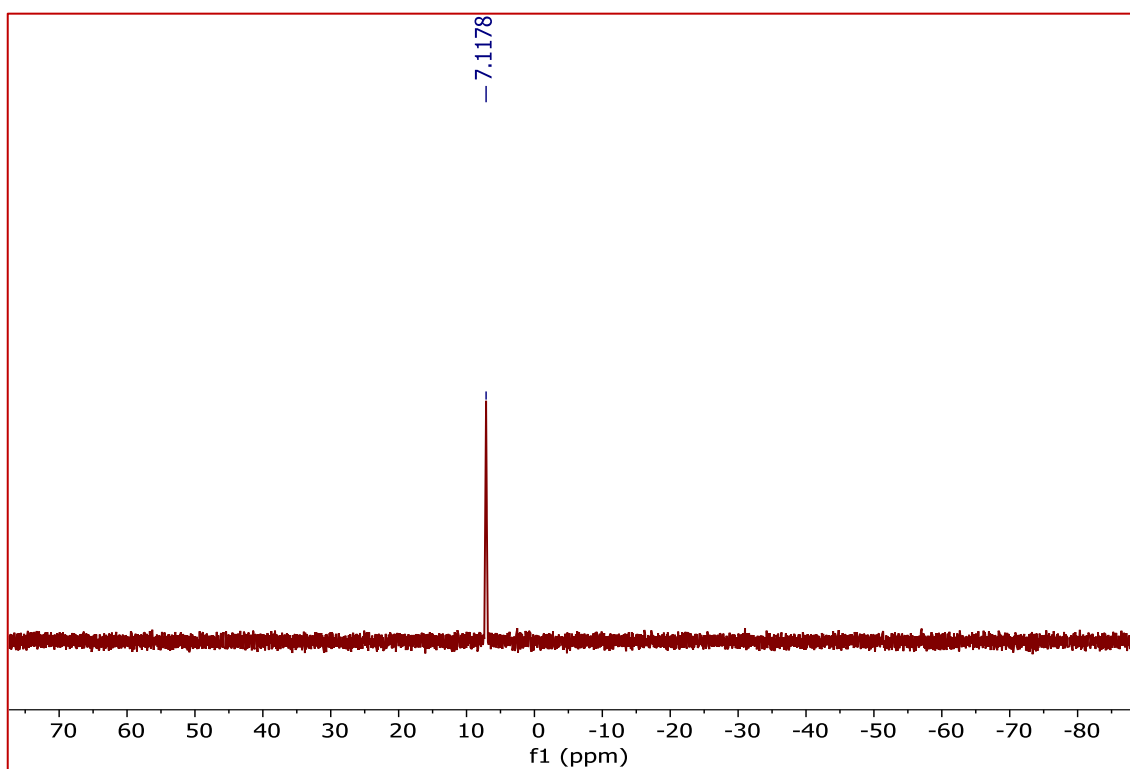
Figure 4.11 ^{31}P NMR (162 MHz, Chloroform-*d*) δ 7.1178 of M2

MS Spectrum Peak List

m/z	Calc m/z	Diff(ppm)	z	Abund	Formula	Ion
931.1869	931.1877	0.88	1	23324.43	C48H38ClIrN2P2	(M+H)+
932.1894	932.191	1.72	1	11677.66	C48H38ClIrN2P2	(M+H)+
933.1874	933.1896	2.33	1	8954.15	C48H38ClIrN2P2	(M+H)+
953.1836	953.1697	-14.57	1	41071.75	C48H38ClIrN2P2	(M+Na)+
954.1867	954.173	-14.4	1	21597.53	C48H38ClIrN2P2	(M+Na)+
955.1859	955.1715	-15.06	1	91164.81	C48H38ClIrN2P2	(M+Na)+
956.1884	956.1746	-14.42	1	43708.67	C48H38ClIrN2P2	(M+Na)+
957.1869	957.1721	-15.54	1	32760.49	C48H38ClIrN2P2	(M+Na)+
958.1885	958.1736	-15.58	1	13658.25	C48H38ClIrN2P2	(M+Na)+
959.1941	959.1763	-18.52	1	4406.58	C48H38ClIrN2P2	(M+Na)+

Figure 4.12 Mass spectrum of M2
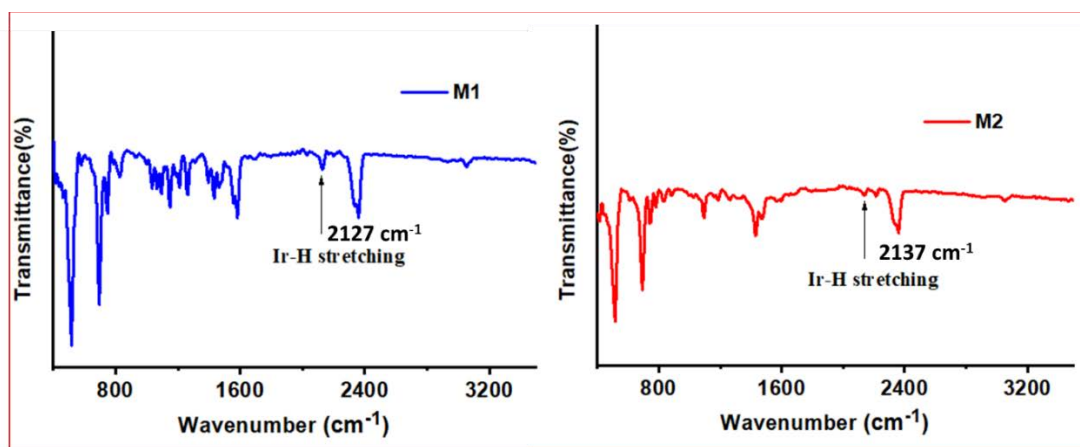
Figure 4.13 IR spectrum of M1 and M2, Ir-H stretching was indicated in the above spectrum.

4.2.3 Sample preparation for sensing

The "Aggregation-induced Phosphorescent Emission" (AIPE) active solution of both the complexes were prepared. A stock solution of M1 and M2 (10^{-3} M in THF) was prepared first, then 0.5 ml of each complex solution was taken in a glass vial of 5 ml volume. For preparing 0% water fraction, 4.5 ml of THF and for making 90% water fraction, 4.5 ml of water was

added. The total volume was made to 5 ml. Then the 90% water (f_w) in the mixed solvent (THF/Water) was directly used for contact mode detection of TNT.

Both the complexes were dissolved in chloroform (10^{-3} M solution), and directly applied to the Whatman filter paper of dimensions 1cm x 2cm by dipping paper strips in complex solution, then the soaked paper was air dried for 12 hr and used to record the PL spectra. Similarly, to prepare PMMA embedded iridium(III) complex, the mixture of 5 mg iridium(III) complex and 95 mg PMMA in 10 ml chloroform was sonicated for 15-20 min, then the filter paper strip was dipped into the iridium complex-PMMA mixture solution. The paper strips were dried for 12 hr and then used for sensing applications.

For TNT vapor saturation, 200 mg of TNT crystal was placed in an airtight glass vial of 5 ml capacity overnight at 25°C to obtain saturated vapors of TNT. Filter paper (FP) is one of the cheaper and easy-to-handle substrates for use as coated probe material. Initially, FP was cut into (1.0 cm × 2.0 cm) pieces and coated the probe material (M1 and M2) by simply dipping the filter paper in a solution of complexes (10^{-3} M solution in chloroform), air dried, and used to record PL spectra. The probes (M1 and M2) coated filter paper was held on the top of a glass vial with saturated TNT vapors (Figure 4.14).
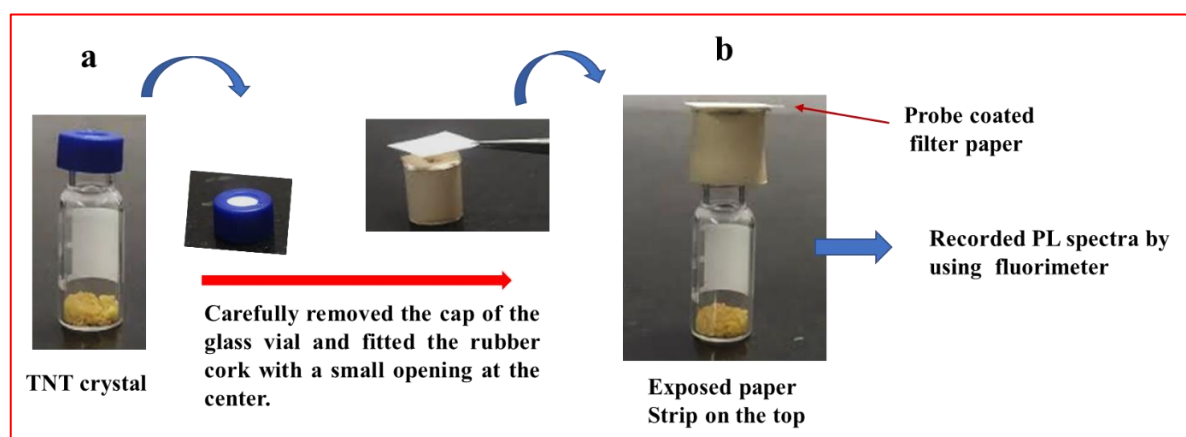
Figure 4.14 (a) Placed 100 mg TNT in a clean and dry glass vial with an airtight lid (2.0 ml capacity) and kept overnight for vapor saturation at 25-30°C; removed the cap carefully and immediately placed the rubber stopper instead of the cap, then expose with probe coated filter paper from the headspace as shown in above figure **b**. The PL intensity was recorded on the exposed paper strip

4.3 RESULTS AND DISCUSSION

Absorption spectra of the complexes were recorded in the THF solvent at room temperature (Figure 4.15, a). Here, three absorption bands were observed for the cyclometalated complexes of iridium(III) (M1 and M2), which are in line with the previous reports.[24][51] The intense lowest

wavelength transition for both the complexes is at 290 nm which is primarily due to $^1\pi$-π^* transitions centred in the cyclometalated ligand as observed in unsubstituted complex (Figure 4.16). The middle-ranged transitions (320-400 nm) are attributed to the mixed $^3\pi$-π^* transitions and spin-allowed ^{1}MLCT (metal-to-ligand charge transfer) transitions, which are centred at ~330 and ~380 nm for M1 and M2, respectively. For M1, these transitions were starting at 374 nm which extended up to 404 nm might be due to mixing of ^{1}MLCT and ^{3}MLCT.[57-58] Similarly, for M2, combined ^{1}MLCT and ^{3}MLCT was probably observed at 413 nm which extended up to 490 nm. The bathochromic shift was observed because of the electron-withdrawing substituent on the phenyl pyridine ligand of M2. It stabilizes the LUMO of M2, which in turn shifts the absorption to longer wavelength as compared to the M1 complex.
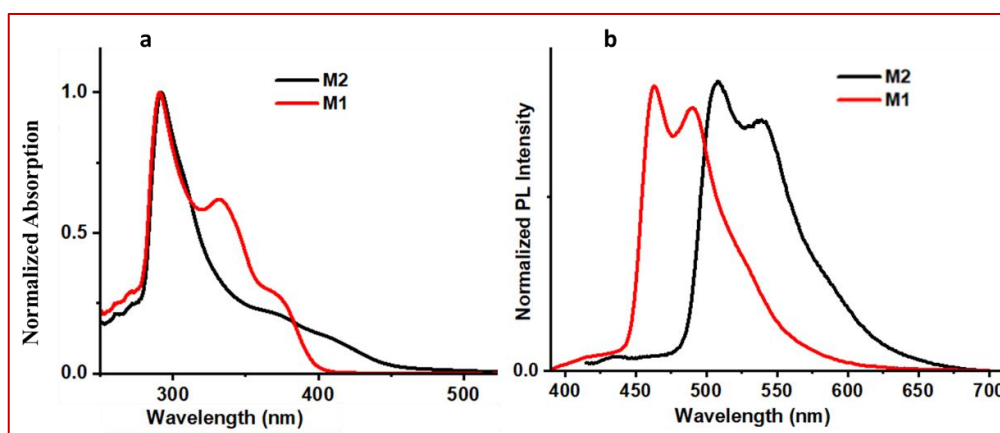
Figure 4.15 (**a**) UV visible spectra (10^{-6} M solution in THF) and (**b**) PL spectra (10^{-3} M solution in THF) of both the complexes in THF solution
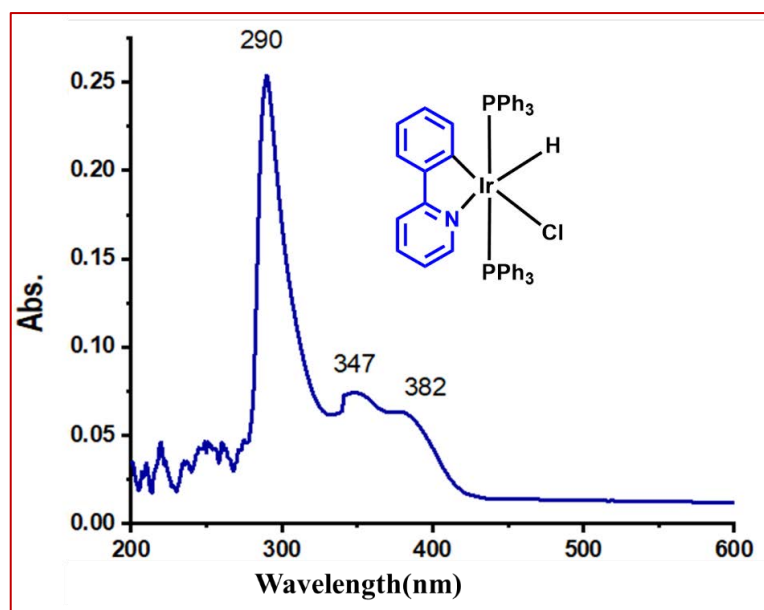
Figure 4.16 UV-VIS spectrum of the unsubstituted complex in THF (10^{-6} M) solution

10^{-3} M solution of iridium(III) complexes were prepared in THF solvent to record the emission spectra (Figure 5.16, b). The observed structured emission suggesting the lowest excited state will have the predominantly ligand centred transition.[58-59] On exciting at 370 nm, Ir 2OMe (M1) results the emission with λ_{max} of 492 nm which is in accordance with its bluish emission colour under UV lamp. On substitution to the phenyl pyridine with electron-withdrawing group (-CN), the value of λ_{max} in emission spectra is shifted bathochromically by 47 nm with respect to M1, which shows a greenish emission ($\lambda_{max} \sim 539$ nm). On recording the excited state lifetime of both the complexes, these are observed in µs range (M1-7.5 µs and M2-8.8), suggesting them as phosphorescence emitting molecules.

We have been able to grow single crystals of one of the complexes (M2) in a DCM/hexane (1:1) mixture through the diffusion technique (M2, **CCDC-2314849**). ORTEP diagram for M2, showing distorted octahedral geometry at the Ir(III) site. An asymmetric unit contains two molecules. Crystal packing with crystal voids present in the crystal lattice is shown in Figure 4.17. The presence of propeller-shaped triphenylphosphine molecules in a crystal packing leads to the void space in the crystal packing.
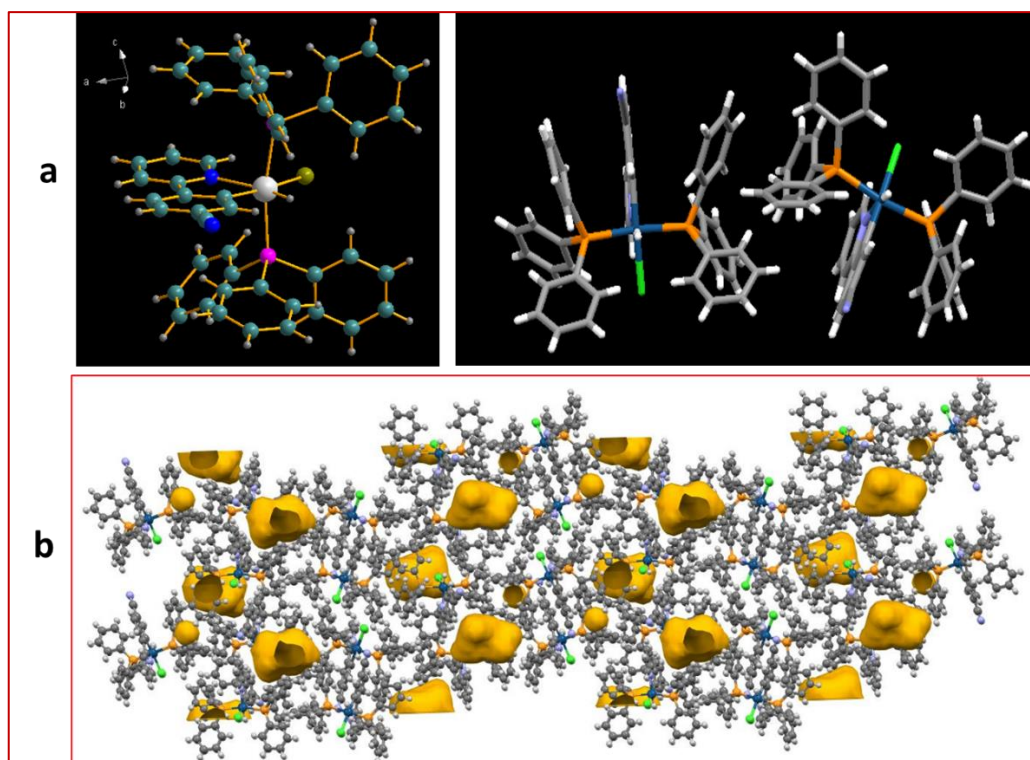
Figure 4.17 (a) ORTEP diagram for M2 (left) and asymmetric unit of complex having two molecules of M2 (right), **(b)** Crystal packing diagram showing crystal voids (filled with yellow colour)

We have investigated the 'Aggregation-induced Phosphorescence Emission' (AIPE) property of both the complexes in the mixed tetrahydrofuran and water solution. In a solution of THF, the complexes show very weak emission. An increase in photoluminescence intensity was observed when water concentration was gradually increased (Figure 4.18). Photographs of the AIPE study under a 365 nm UV excitation and a plot of PL intensity at 0% water to 90% water are shown below (Figure 4.18, inset). Additionally, a PEG and THF experiment was conducted to verify the restricted intramolecular rotations (RIR) of PPh$_3$ units in the complexes (Figure 4.19). The gradual enhancement of emission with increasing PEG concentration supports the RIR effect might be responsible for AIPE. The observation of AIPE occurs because of the limited rotation of phenyls in triphenylphosphines, known as restricted intramolecular rotation (RIR).
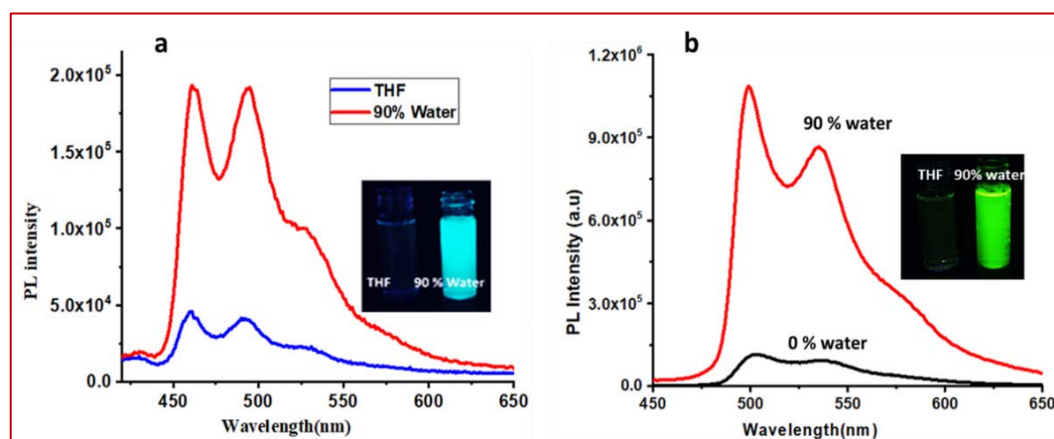
Figure 4.18 Probe in THF (10^{-4}M) and its aggregated solution (90% water), (a) PL spectra of probe in THF (0% water, blue line) and its aggregated solution (90% water, red line) in case of M1 complex and (b) PL spectra of probe in THF (0% water, black line) and its aggregated solution (90% water, red line) in case of M2 complex, inset image represent the emission of respective probe solutions under UV lamp (λ_{ex} = 365 nm)

This phenomenon is evidenced by the crystal packing diagram of M2, which clearly displays C–H···π interactions and several short contacts with distances ranging from 2.35–2.85 Å. The phenyls in triphenylphosphines participate in these short contacts, which restrict the rotation of propeller-shaped triphenylphosphines in the solid state. As a result, non-radiative pathways are blocked, leading to AIPE activity in the solid state. DLS study for particle size analysis was performed for 0% and 90% water of both the complexes (Figure 4.20). For M1, the observed particle size for 0% is 22.3 nm and 90% is 231.9 nm, whereas for M2, 38.9 nm for 0% and 165.8 nm for 90% solution.
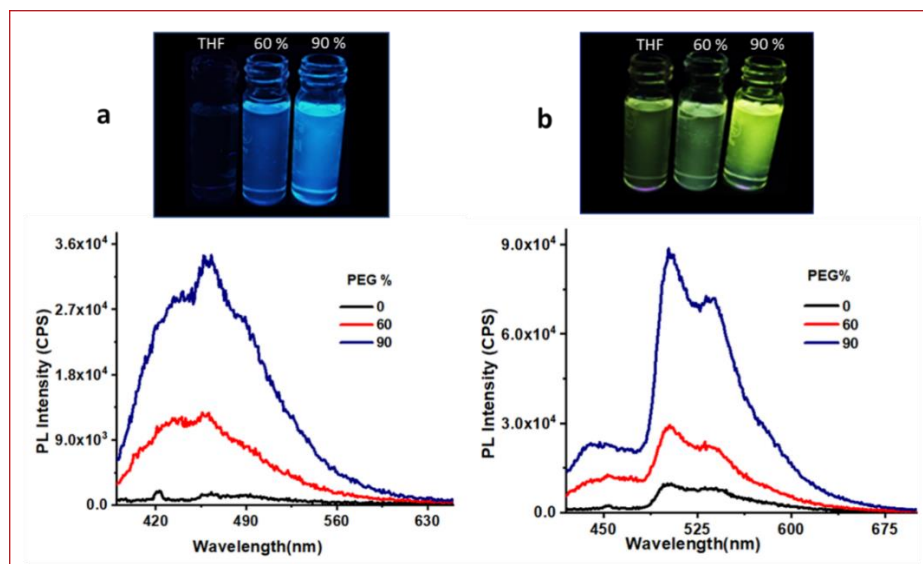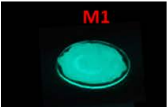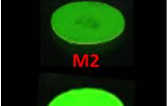
Figure 4.19 M1 and M2 in THF and different fractions of PEG, **(a) (**top, left): image of 0, 60 and 90% PEG fraction under UV excitation (365 nm) for M1; (bottom, left) corresponding emission spectra of M1, similarly **(b)** **(**top, right) image shows different PEG fraction under UV excitation of 365 nm and (bottom, right) spectra shows corresponding emission spectra of M2

Table 4.1 It shows phosphorescent lifetime, quantum yield, and limit of detection (LOD), of sole complexes (M1and M2) and complexes embedded with PMMA polymer (CP)

Complexes	Lifetime, chi-square (μs) (χ^2)	Quantum yield(%)	LOD	
			Solution	**Vapor**
M1	7.5 (χ^2 - 1.20)	27.38	1.09 nM	X
CP	9.4 (χ^2 - 1.10)	71.20		X
M2	8.8 (χ^2 - 0.97)	33.60	450 pM	66.3 ppb
CP	11.3 (χ^2 - 1.02)	97.40		12.8 ppb
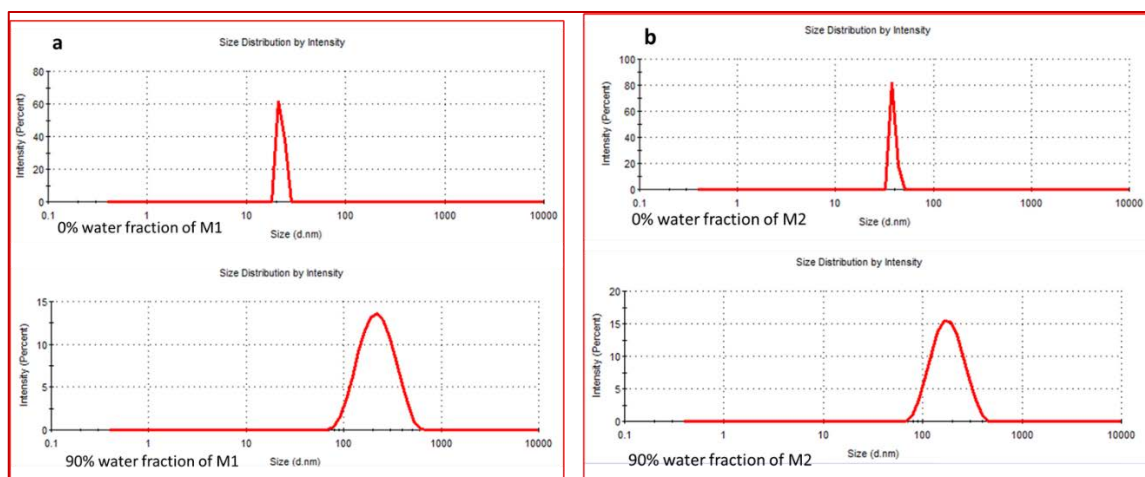
Figure 4.20 DLS study of M1 (a) and M2 (b) in THF solution 0% (top) and 90% water fraction (bottom)

The reported iridium(III) based mono-cyclometalated complexes showed AIPE active properties with high quantum yield and phosphorescence lifetime.[60] Thus, we have analysed excited state lifetime and quantum yield (QY) of both the complexes in solid state (Table 4.1). It was noted that M1 having absolute QY of 23.8% and lifetime of 7.5 µs, while in case of M2, it was observed QY of 33.6 % and lifetime of 8.8 µs. The observed high QY and lifetime data also indicate the potentiality of these complexes towards sensing of analytes. The synthesized complexes M1 and M2 were tested towards the sensing of different nitro-based explosive by using probe coated filter paper strips (Figure 4.21 a and b) which shows that M1 is selective towards both TNP and TNT, while M2 is specific towards TNT. Further, the selectivity of M2 in AIPE active solution was tested (Figure S21 c), It showed selectivity towards TNT analyte. We have also performed the anti-interference study of M2 in the presence of different nitro-based analytes for TNT sensing experiments and shown in a bar graph (Figure 4.21 d). It was found that the quenching performance of M2 was not affected in the presence of various analytes.
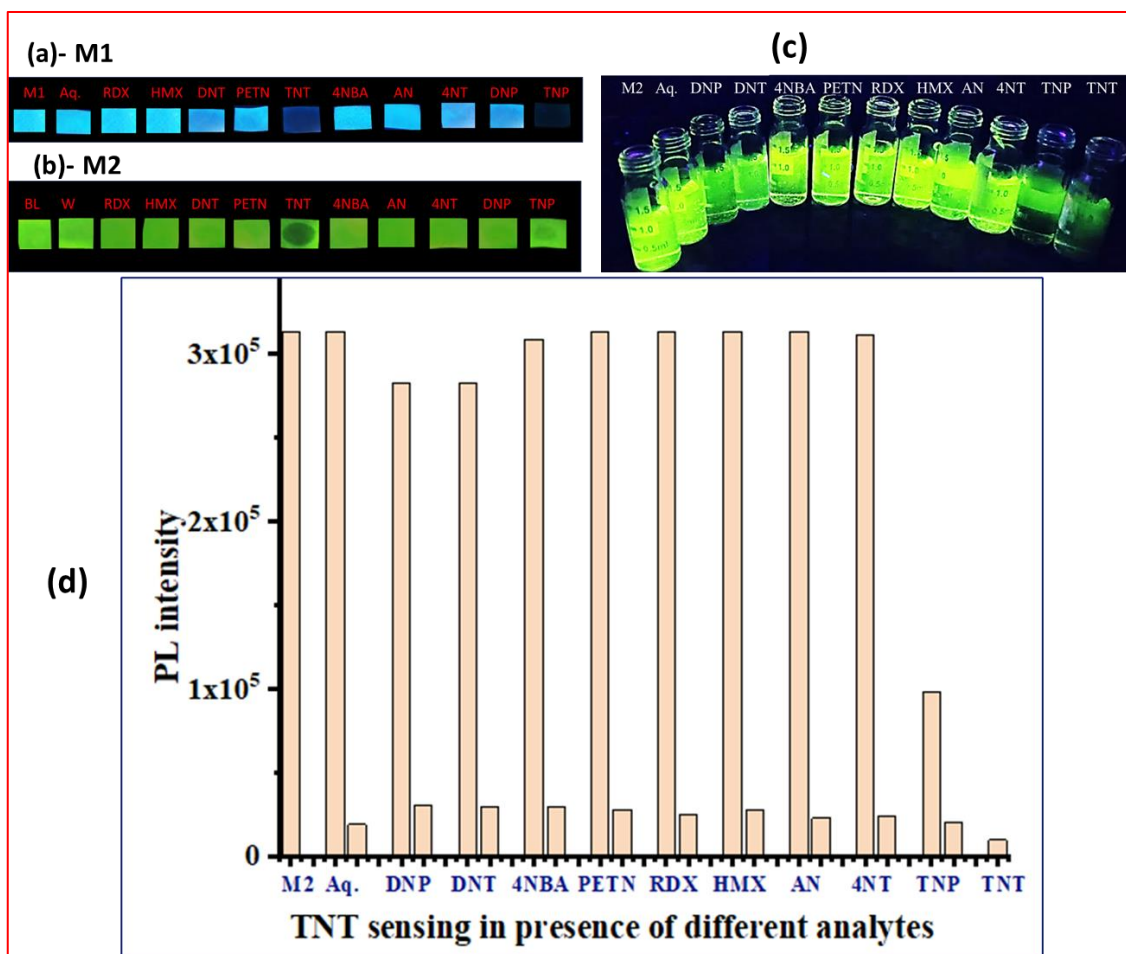
Figure 4.21 Selectivity test of probe M1 **(a)** and M2 **(b)** with different nitro-based explosive materials. Each one of the 10 μL 10^{-4} M aqueous solutions of different nitro-based explosives was added to the probe-coated filter paper, and the resulting image was obtained through excitation by UV ray (365 nm) as shown in the figure. Similarly, **(c)** from the left side, the first one is the PL intensity of the aggregated solution of the probe (THF/90% water), then different nitro-based analyte was added and taken the image under UV excitation (365 nm). (d) representations of the quenching performance of M2 with TNT in the presence of different analytes shown in the bar graph, extreme left represents the AIPE active probe solution, then different analytes as mentioned on the X-axis and adjacent bar corresponding to each analyte showing quenching after adding TNT

Thus, the synthesized complexes have been used for sensing TNT in aqueous medium. An aqueous solution of TNT (10^{-4} M) was added to the aggregated solution (90% water) of M1 (addition: 1.0 nM each time up to 14 nM). The emission spectrum of each solution was recorded (Figure 4.22 for M1). Similarly, the initial emission spectrum of the aggregated solution of M2 was recorded, then titrated with aqueous TNT (10^{-5} M) by gradually adding 0.5 nM at each time and recording the change in emission intensity (Figure 4.23 for M2). It is observed that in case of M1, limit of detection (LOD) is 1091 pM (1.091 ppb) and for the case of M2 LOD is 450 pM (450 ppt). The Stern-Volmer (SV) plot (Figure S22, ESI) showed a linear relationship at a lower concentration. Moreover, it was bent upward with increasing concentrations of TNT (Figure 4.24).
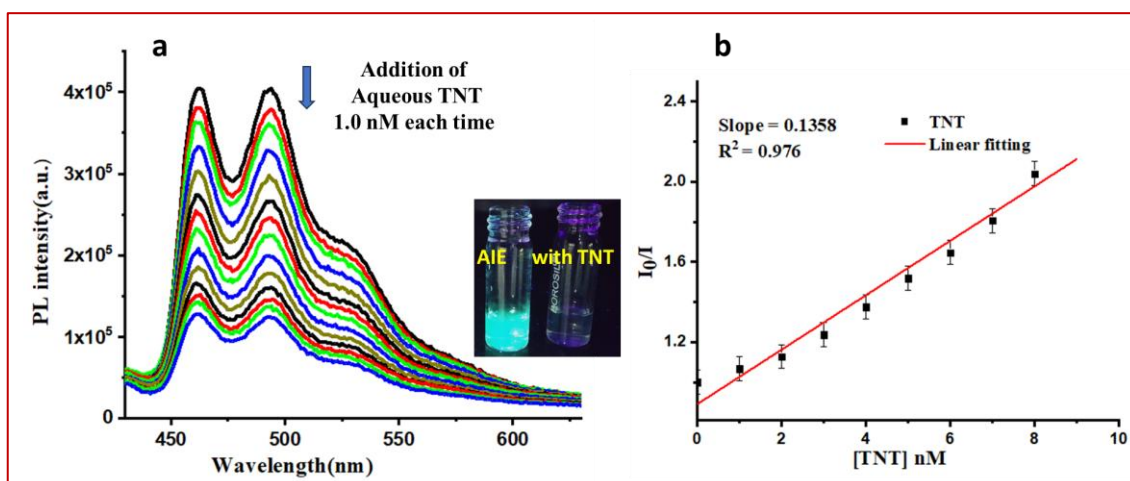
Figure 4.22 (a) PL Spectra shows decrease in photoluminescence (PL) intensity of AIE solution of M1 (10^{-3} M THF (10 %) and water (90 %)) with continuous addition of aq. TNT (1.0 nM) at each time); Inset Figure: 1st vial aggregated (90% water) solution of probe and 2nd vial shows aggregated solution of probe with TNT (b) Stern-Volmer plot of emission quenching for M1, error bars represent the standard deviation obtained from three independent measurements
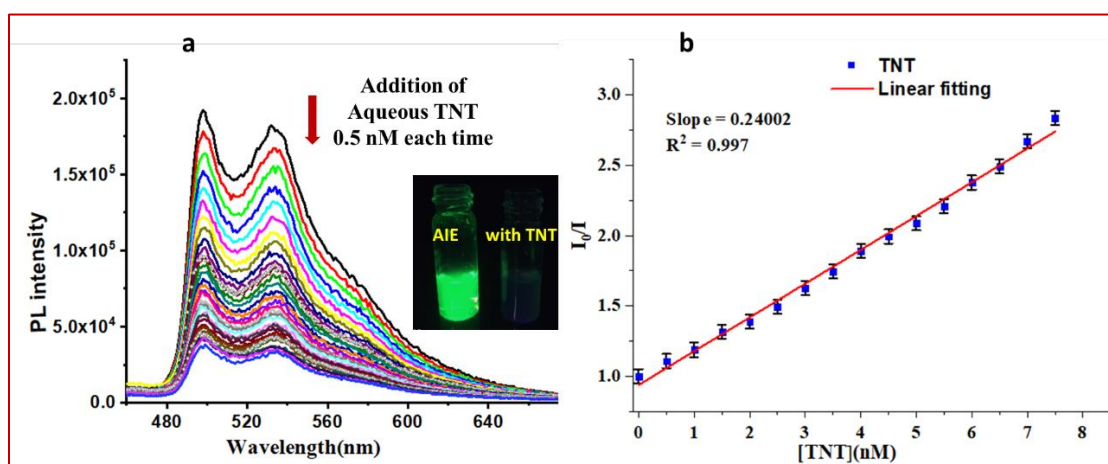
Figure 4.23 (a) PL spectra shows the gradual decrease in photoluminescence (PL) intensity of AIE solution of M2 (10^{-3} M THF (10 %) and water (90 %) with continuous addition of aq. TNT (10^{-5} M) 0.5 nM at each time; Inset figure: 1st vial AIE (90% water) solution of the probe and 2nd vial shows the aggregated solution of the probe with TNT (b) Stern-Volmer plot for emission quenching in case of M2, error bars represent the standard deviation obtained from three independent measurements

Considering the lower concentration plot, the quenching constant (K_{SV} in M^{-1}) was calculated for both the complexes (for M1- 1.49×10^8 M^{-1} and for M2- 2.5×10^8 M^{-1}). The S-V plot with deviation from linearity was observed and it indicates that the quenching process is operated through a mixed static/dynamic quenching[23, 61], (Figure 4.24).
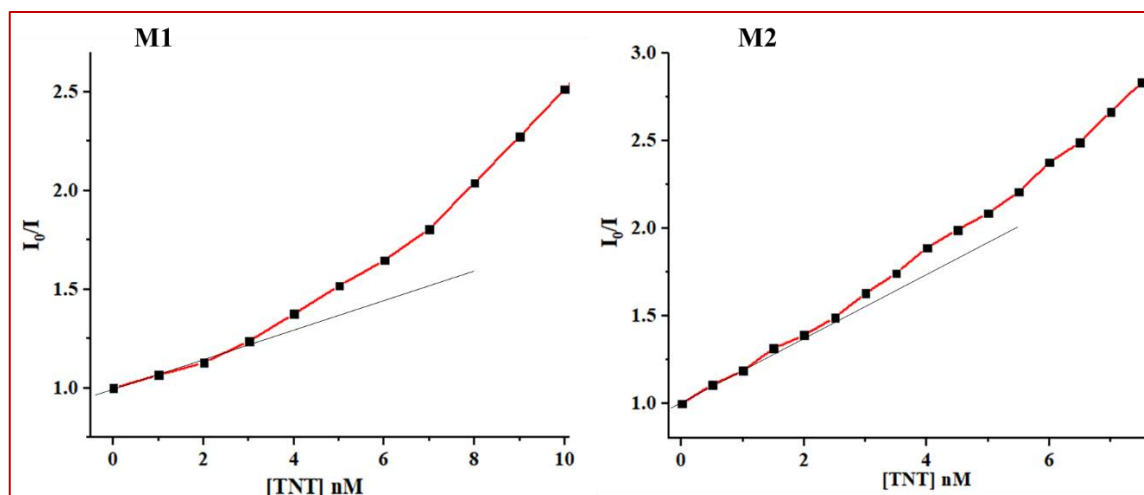
Figure 4.24 Stern–Volmer plot for the PL quenching of the probe upon the gradual addition of TNT, where I_0 represents the PL intensity of the probe in the absence of TNT, and I denote the intensity in the presence of TNT. S-V plot deviates upward with increasing TNT concentration

Furthermore, to confirm the nature of quenching, we have analysed the excited state lifetime study of both the complexes in presence and absence of analyte (Figure 4.25). For both the cases (M1 and M2), the excited state lifetime values decrease in presence of TNT analyte, which excludes the possibility of static quenching. It was not observed a notable difference in UV-VIS absorbance spectra of the probe and TNT with the absorbance of the sole probe molecule (Figure 4.26). This observation also neglects the fluorophore (donor) interaction with TNT (acceptor) in ground state, hence no static quenching could occur.
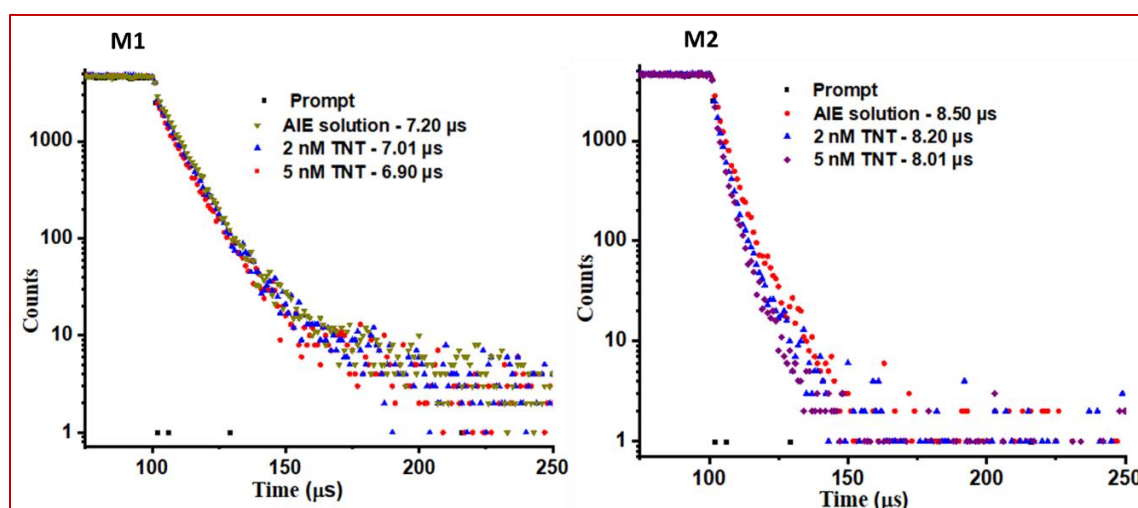
Figure 4.25 Aggregated solution of M1 and M2 in the presence of TNT; the lifetime measurement was done; it was observed that there is a decrease in excited state lifetime of M1 and M2 in the presence of TNT
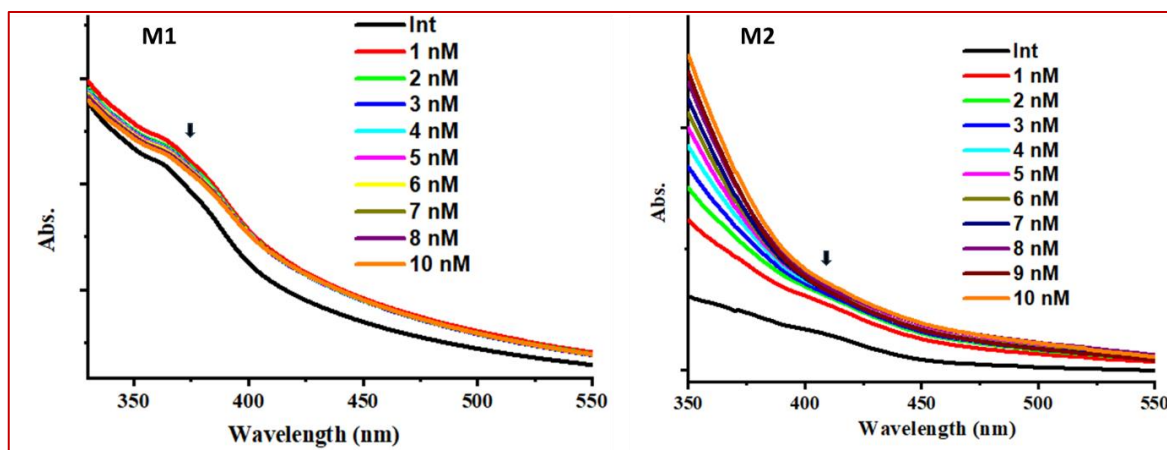
Figure 4.26 UV visible absorption spectra of M1 and M2 in the presence of different amounts of TNT analyte. In the presence of TNT, there is no significant change in the UV-VIS spectra of complexes indicating ground state complex formation is not observed

From these LOD values, we conclude that M2 is more sensitive towards TNT as compared to M1. To investigate the quenching mechanisms, the possibilities of quenching of emission by inner filter effect (IFE), resonance energy transfer (RET), and photo-induced electron transfer (PET) have been studied. It is observed that there is no overlapping of excitation and emission spectra of M1 and M2, which indicates that there is no IFE present in the prepared complexes (Figure 4.27). To investigate the possibility of RET, in the case of M1, we found that there is a slight overlap of absorption of TNT and emission spectra of M1 in the same solvent medium (Figure 4.28, a), indicating a possible quenching mechanism for M1 is RET. The overlapping integral (J) calculated by using the MATLAB program is 3.94×10^{14}.[62] No such overlapping was found in the case of M2 (Figure 4.28, b). The HOMO and LUMO energies of synthesized complexes (Figure 4.30) were determined experimentally to check the possibility of an electron transfer from the electron-rich complexes to the electron-deficient TNT. Further analyzing the PET possibilities, we could observe that the LUMO levels of TNT (-2.49 eV) and, for M1 and M2, LUMO levels are -1.50 eV and -1.91 eV, respectively (Figure 4.31). From this LUMO alignment, it is observed that electron transfer is more favourable from the LUMO of M2 to the LUMO of TNT (Figure 4.31). which leads to the quenching of emission intensity for M2.[63-65]
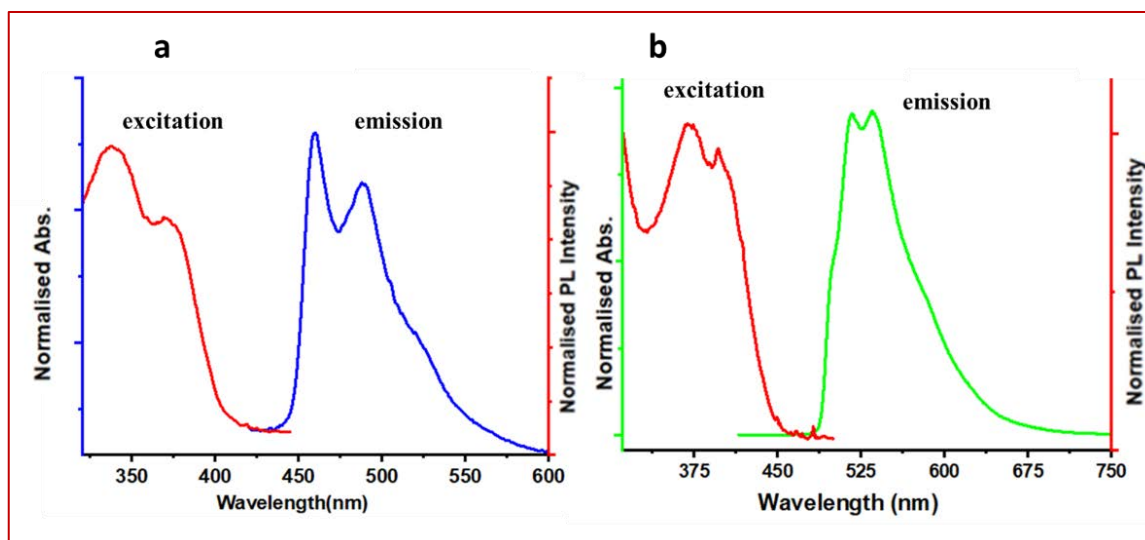
Figure 4.27 (a) Excitation and emission of M1 (**b**) Excitation and emission of M2 to check the possibility of inner filter effect in complexes
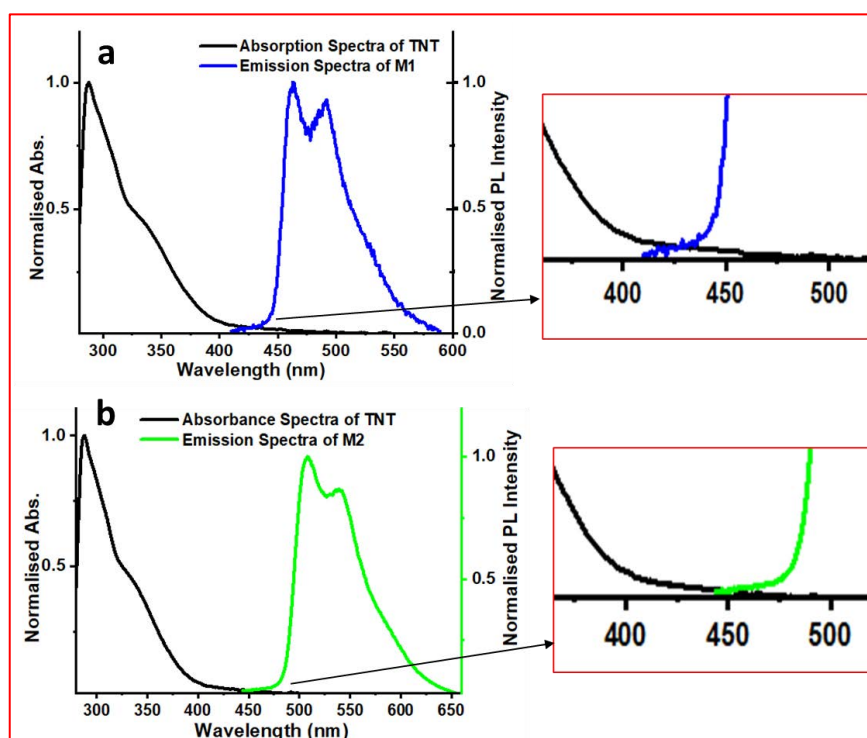
Figure 4.28 Absorption spectra of TNT and emission spectra of M1 and M2 in THF solutions to check the possibilities of spectral overlap between absorption and emission

The vapor phase detection of nitro-based explosives is challenging task as the vapor pressure of nitro-explosive is very low (10^{-5}-10^{-15} torr)[7]. To detect nitro-explosive from their vapor phase, very sensitive probe molecule is desirable. The solution phase sensing performance of complexes (M1 and M2) indicates that M2 was relatively much better sensitive towards TNT

(LOD= 450 ppt). To test the probe molecules with TNT vapors, many aspects need to look such as, TNT vapor saturation, selection of substrate, and experimental setup for sensing. All the experimental set-up for TNT vapor sensing is shown in Figure 4.4. On testing the M1 and M2 complexes towards TNT vapors, there is no observable decrement in PL intensity with TNT vapor is observed in the case of M1. On the other side, M2 shows observable PL intensity quenching in the presence of TNT vapor (Figure 4.29). The limit of detection (LOD) was found to be 66.3 ppb for the case of M2. Although M1 shows a quenching response in contact mode detection of TNT, it is not responding to vapors of TNT, it might be due to the relatively lower quantum yield and excited state lifetime of M1 as compared to M2 (Table 4.1).
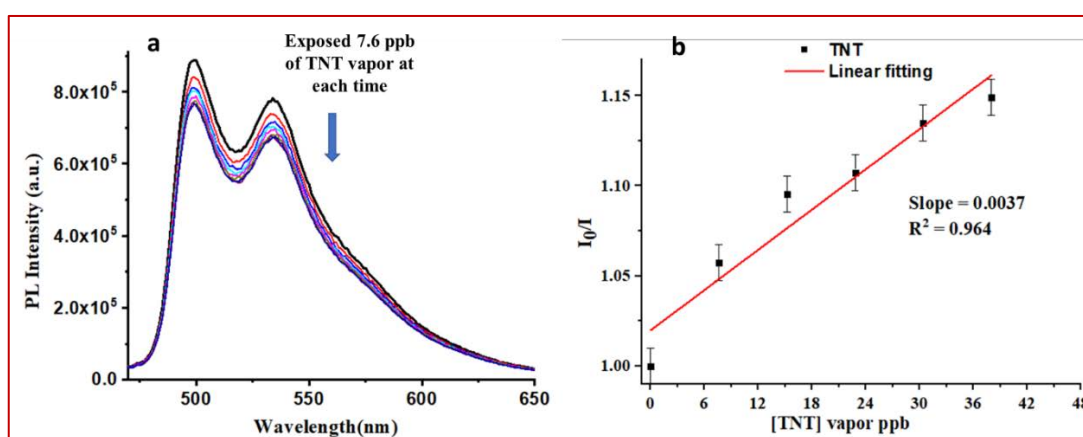
Figure 4.29 (a) PL spectra show change in photoluminescence (PL) intensities of M2 on filter paper upon continuous exposure with TNT vapors for 2 min each time; (b) Stern-Volmer plot for emission quenching in case of M2 (error bars represent the standard deviation obtained from three independent measurements)

$$E_{HOMO} = -(E_{OX} + 4.4) \, eV$$
$$-(0.15 + 4.4)$$
$$-4.55 \, eV$$

$$E_{(gap, \, electronic)} = h \times c/\lambda$$
$$= 1240/407$$
$$= 3.05 \, eV$$

$$E_{LUMO} = E_{HOMO} + E_{(gap, \, electronic)}$$
$$-4.55 + 3.05 \, eV$$
$$E_{LUMO} = -1.50 \, eV$$

$$E_{HOMO} = -(E_{OX} + 4.4) \, eV$$
$$-(0.16 + 4.4)$$
$$-4.56 \, eV$$

$$E_{(gap, \, electronic)} = h \times c/\lambda$$
$$= 1240/467$$
$$= 2.65 \, eV$$

$$E_{LUMO} = E_{HOMO} + E_{(gap, \, electronic)}$$
$$-4.56 + 2.65 \, eV$$
$$E_{LUMO} = -1.91 \, eV$$
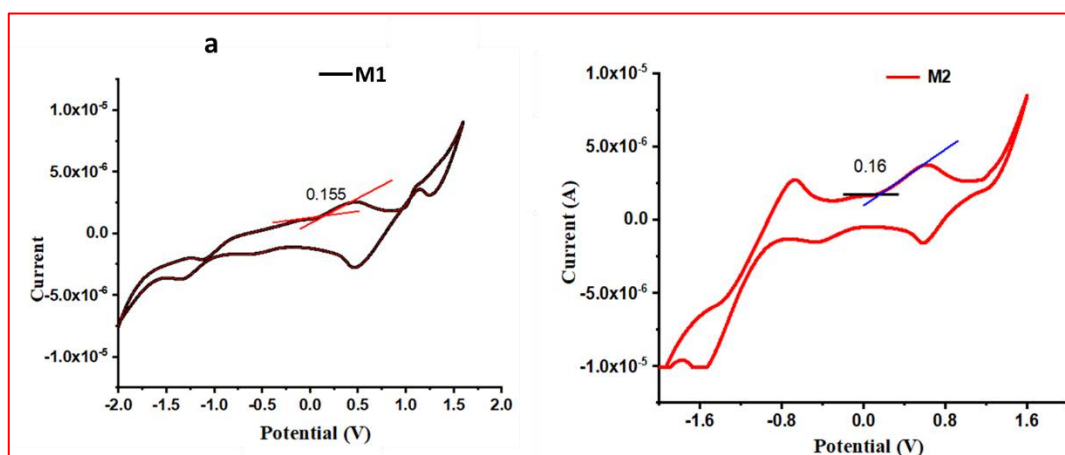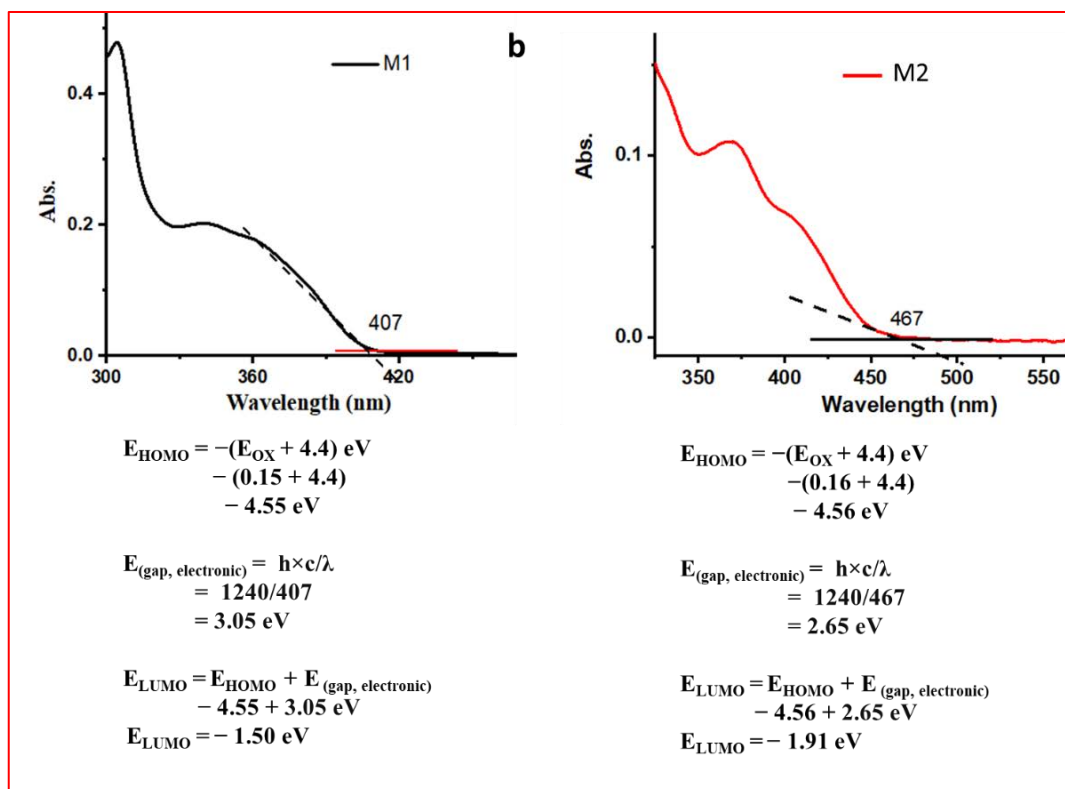
Figure 4.30 (a) Cyclic voltammetry (CV) plots of complexes in THF solvent. 10^{-4} M solution of complexes was prepared in THF solvent followed by the addition of supporting electrolyte, tetrabutylammonium hexafluorophosphate (NBu_4PF_6), and (b) UV-VIS spectra of M1 and M2 in THF solvent along with calculation of $E_{(LUMO)}$ by using oxidation onset potential from CV plot and band edge absorption from UV-VIS absorption spectra
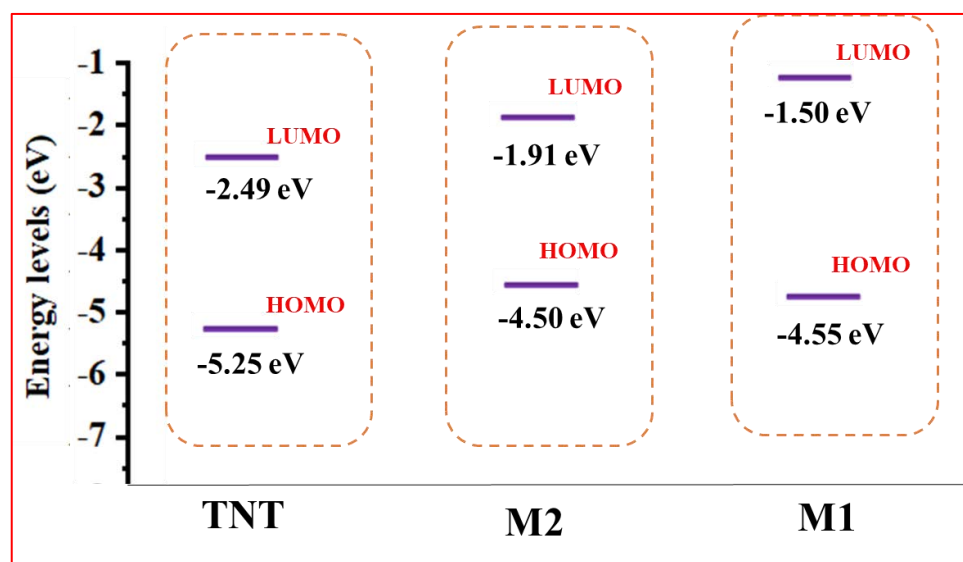
Figure 4.31 Here, on the left side, the Y-axis shows energy levels (eV), and the X-axis contains TNT and Ir(III) complexes (M1 and M2), showing the possibility of electron transfer between probe and TNT

Apart from the mechanism (IFE, RET, and PET) mentioned above, many other factors are responsible for improving the sensitivity for detecting nitro-explosive from vapors such as

quantum efficiency of probe molecule, excited state lifetime of probe and porous substrate for trapping vapors of explosive. On keeping these features in mind, we started searching the literature and found some interesting reports in the years 2007 and 2011, where the utilization of PMMA polymer as a substrate for improving photostability and optical properties of metal complexes (quantum yield and excited state lifetime).[66-68] The work inspired us to proceed further improvement of quantum efficiency of the present probe. Thus, the probe was embedded with PMMA and tested with TNT vapour to improve trapping of TNT molecules. Firstly, the composite materials made of complexes (M1 or M2) and PMMA that was coated on the filter paper (detailed method of preparation described in experimental section).
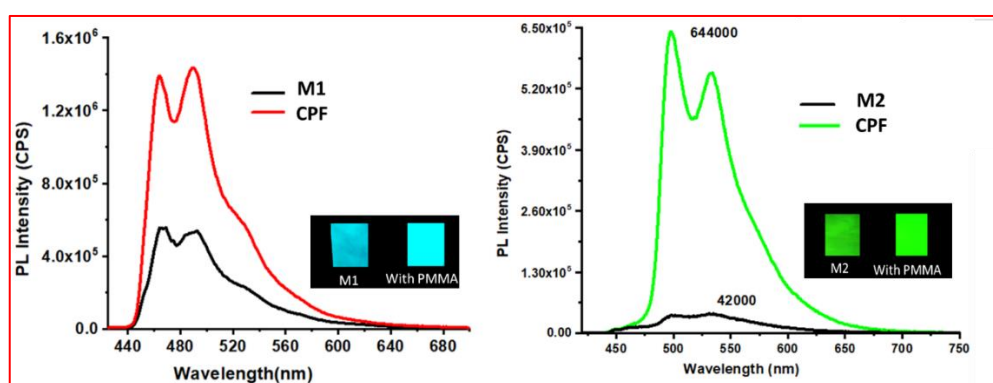
Figure 4.32 The PL intensity of filter paper impregnated complexes and complex with PMMA polymer (CPF), inset figures show image of filter paper after coating complex and complex-PMMA under UV excitation (365 nm)

After fabricating probe-PMMA film on filter paper strips, the emission spectra were recorded. Interestingly, the photoluminescent intensity of the embedded film is drastically increased as compared to the filter paper containing only complex (PL intensity increases up to ~ 4-fold in the case of M1 and ~15-fold in the case of M2 (Figure 4.32). It was recorded the QY and lifetime of Ir(III) complexes with and without incorporating into the PMMA matrix and observed both parameters are enhanced in the complex embedded polymeric matrix (Table-1). To explore the insights for the observed enhanced PL intensity in the presence of PMMA, the study of surface morphology and porosity of the composite material (CP) was determined. Thus, it was recorded the BET of polymer (PMMA) and CP (Figure 4.33). The obtained isotherms of CP belong to type IV with an H2(b)- type hysteresis loop at a higher relative pressure.[69-72] The observed H2(b)- type hysteresis loops indicate that the pores are not uniform and are made up of an interconnected network of different sizes. The pore size and the surface area of PMMA and CP were obtained by the Barrett−Joyner−Halenda (BJH) method.[10, 73-74] The surface area for PMMA was found to be 2.944 m^2g^{-1} with an average pore radius of 2.3407

nm and a total pore volume of 0.0034 cc/g. For CP, the surface area is found to be 2.029 m^2g^{-1} with an average pore radius of 4.259 nm and total pore volume of 0.0043 cc/g.

Sample	S. Area (m²/g)	Pore radius(nm)	Pore volume (cc/g)
PMMA	2.944	2.3407	0.00344
CP	2.029	4.258	0.00432
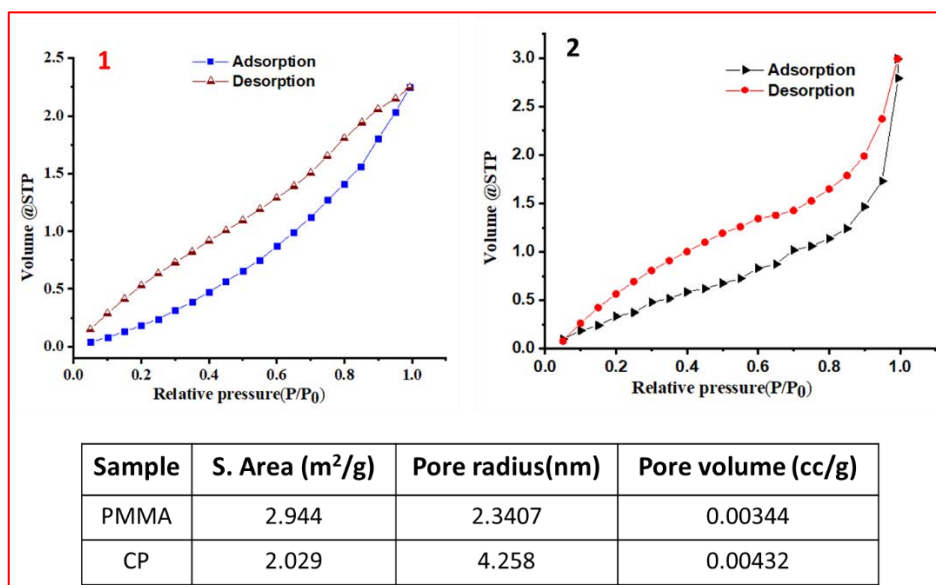
Figure 4.33 Nitrogen adsorption-desorption isotherms of PMMA polymer (**1**) and M2-PMMA composite (CP) (**2**)

After developing CP with high photo-stability, quantum efficiency, improved excited state lifetime and porous polymeric network, we tested CP with TNT vapors and observed exciting results for TNT vapor sensing (Figure 4.34). The CP shows LOD of 12.8 ppb which is ~5 times better quenching efficiency than the sole M2 (66.3 ppb). The FESEM images of PMMA, M2, CP, and TNT-exposed CP are shown in Figure 4.35. The FESEM image shows that the TNT molecules occupy the surfaces as well as the pores of the network in CP. The Ir(III) complexes are, in general highly electron-rich, while trinitrotoluene (TNT) is an electron-deficient molecule. The porous network of CP assists in trapping the TNT vapor in a polymeric network containing an electron-rich probe (iridium(III) complex, M2), which helps to trap TNT effectively, thus enhancing better electronic communication. As a result, significant emission quenching was observed in the case of CP. The essence of the work was to develop a paper strip-based porous polymeric matrix with AIPE active iridium(III) complex which improved the vapor sensing ability of TNT.
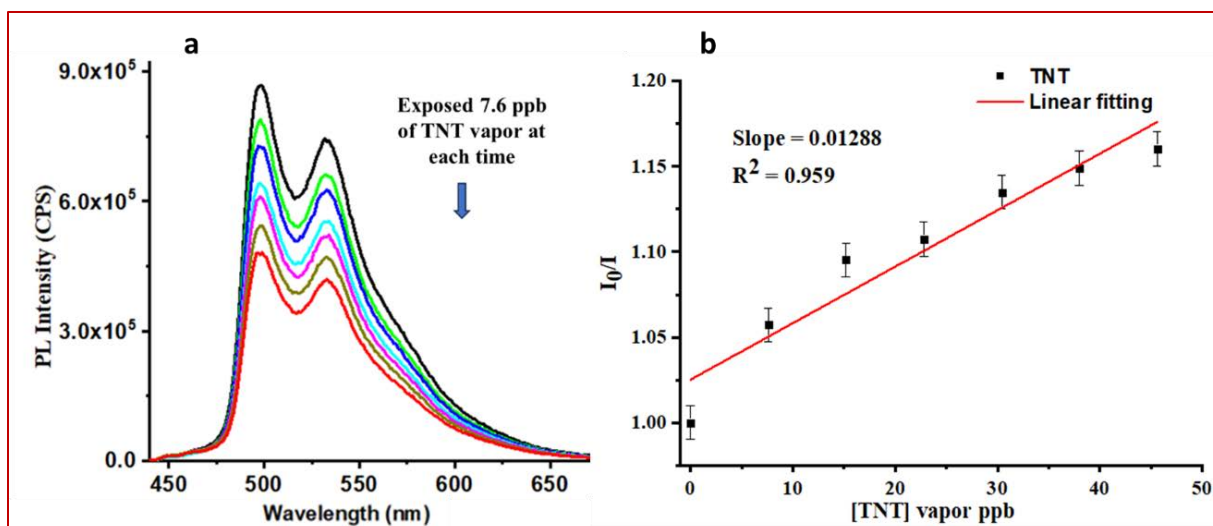
Figure 4.34 (a) Photograph of lowering in photoluminescence (PL) intensities of M2-PMMA on filter paper upon continuous exposure with TNT vapors for 2 min each time; (b) Stern-Volmer plot for emission quenching (error bars represent the standard deviation obtained from three independent measurements)
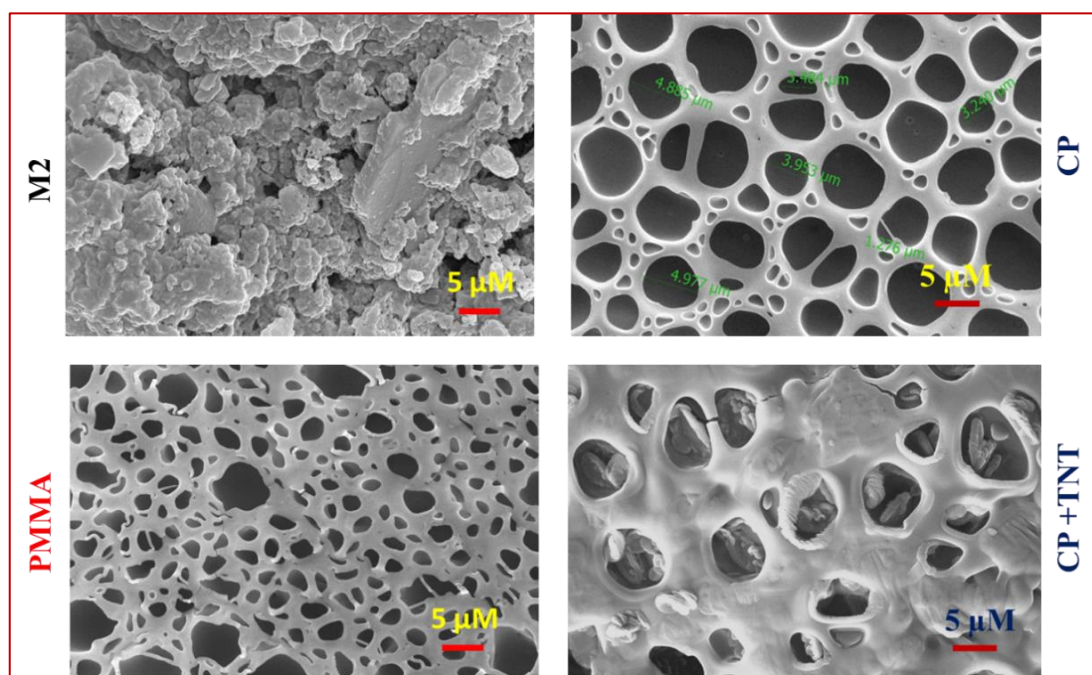

Figure 4.35 FE-SEM images of M2, CP, PMMA, and TNT-exposed CP, we could see that after TNT exposure surface morphology changes

4.4 CONCLUSION

In this chapter, iridium(III)-based monocyclometalated (C^N) phosphorescence sensory materials have been developed from a substituted phenyl pyridine ligand. It was strategically planned to impregnate the probes into a porous polymethylmethacrylate (PMMA) polymer. The M2-impregnated PMMA resulted in a much higher quantum yield and enhanced lifetime as compared to the sole complex (5 times of QY enhancement). PMMA polymer-based films

fabricated from Ir(III) complex have demonstrated compelling efficiency in the detection of explosive vapor. The probe molecule with enhanced quantum efficiency and phosphorescence lifetime are the essential features of fluorescent sensors and the extended porous morphology provides better interaction of the probe with analyte. These findings affirm the potential of the present approach which will be promising for detecting explosives having low vapor pressure in real-time monitoring.

4.5 REFERENCES

1.   Rao, K. S.; Ganesh, D.; Yehya, F.; Chaudhary, A. K., A comparative study of thermal stability of TNT, RDX, CL20 and ANTA explosives using UV 266 nm-time resolved photoacoustic pyrolysis technique. *Spectrochimica Acta Part A: Molecular and Biomolecular Spectroscopy* **2019,** *211*, 212-220.

2.   Dattelbaum, D. M.; Chellappa, R. S.; Bowden, P. R.; Coe, J. D.; Margevicius, M. A., Chemical stability of molten 2,4,6-trinitrotoluene at high pressure. *Applied Physics Letters* **2014,** *104* (2).

3.   Dorsey, A.; Hodes, C. S.; Richter-Torres, P., Toxicological profile for 2, 4, 6-trinitrotoluene. **1995**.

4.   Strehse, J. S.; Appel, D.; Geist, C.; Martin, H.-J.; Maser, E., Biomonitoring of 2, 4, 6-trinitrotoluene and degradation products in the marine environment with transplanted blue mussels (M. edulis). *Toxicology* **2017,** *390*, 117-123.

5.   Chatterjee, S.; Deb, U.; Datta, S.; Walther, C.; Gupta, D. K., Common explosives (TNT, RDX, HMX) and their fate in the environment: Emphasizing bioremediation. *Chemosphere* **2017,** *184*, 438-451.

6.   Singh, S., Sensors—An effective approach for the detection of explosives. *Journal of Hazardous Materials* **2007,** *144* (1), 15-28.

7.   Sun, X.; Wang, Y.; Lei, Y., Fluorescence based explosive detection: from mechanisms to sensory materials. *Chemical Society Reviews* **2015,** *44* (22), 8019-8061.

8.   Lv, Y.-Y.; Xu, W.; Lin, F.-W.; Wu, J.; Xu, Z.-K., Electrospun nanofibers of porphyrinated polyimide for the ultra-sensitive detection of trace TNT. *Sensors and Actuators B: Chemical* **2013,** *184*, 205-211.

9.   Mäkinen, M.; Nousiainen, M.; Sillanpää, M., Ion spectrometric detection technologies for ultra-traces of explosives: A review. *Mass Spectrometry Reviews* **2011,** *30* (5), 940-973.

10.   Sengottuvelu, D.; Kachwal, V.; Raichure, P.; Raghav, T.; Laskar, I. R., Aggregation-

induced enhanced emission (AIEE)-active conjugated mesoporous oligomers (CMOs) with improved quantum yield and low-cost detection of a trace amount of nitroaromatic explosives. *ACS applied materials & interfaces* **2020,** *12* (28), 31875-31886.

11.   Yu, H. A.; Lee, J.; Lewis, S. W.; Silvester, D. S., Detection of 2,4,6-Trinitrotoluene Using a Miniaturized, Disposable Electrochemical Sensor with an Ionic Liquid Gel-Polymer Electrolyte Film. *Analytical Chemistry* **2017,** *89* (8), 4729-4736.

12.   Dongre, S. D.; Das, T.; Babu, S. S., Dual mode selective detection and differentiation of TNT from other nitroaromatic compounds. *Journal of Materials Chemistry A* **2020,** *8* (21), 10767-10771.

13.   Dong, W.; Ma, Z.; Chen, P.; Duan, Q., Carbazole and tetraphenylethylene based AIE-active conjugated polymer for highly sensitive TNT detection. *Materials Letters* **2019,** *236*, 480-482.

14.   Çorman, M.; Ozcelikay, G.; Cetinkaya, A.; Kaya, S.; Armutcu, C.; Özgür, E.; Uzun, L.; Ozkan, S., Metal-organic frameworks as an alternative smart sensing platform for designing molecularly imprinted electrochemical sensors. *TrAC Trends in Analytical Chemistry* **2022**, 116573.

15.   Boonsri, M.; Vongnam, K.; Namuangruk, S.; Sukwattanasinitt, M.; Rashatasakhon, P., Pyrenyl benzimidazole-isoquinolinones: Aggregation-induced emission enhancement property and application as TNT fluorescent sensor. *Sensors and Actuators B: Chemical* **2017,** *248*, 665-672.

16.   Kartha, K. K.; Babu, S. S.; Srinivasan, S.; Ajayaghosh, A., Attogram sensing of trinitrotoluene with a self-assembled molecular gelator. *Journal of the American Chemical Society* **2012,** *134* (10), 4834-4841.

17.   Kim, S.-B.; Lee, E.-B.; Choi, J.-H.; Cho, D.-G., Simple fluorescent chemosensors for TNT: one-step synthesis. *Tetrahedron* **2013,** *69* (23), 4652-4656.

18.   Li, Q.; Guo, Y.-M.; Gao, Y.; Li, G., Polyethyleneimine-protected silver cluster for label-free and highly selective detection of 2, 4, 6-trinitrotoluene. *Spectrochimica Acta Part A: Molecular and Biomolecular Spectroscopy* **2022,** *276*, 121224.

19.   Moon, S.; Yoo, J.; Lee, W.; Lee, K., Enhancement of electrochemical detection performance towards 2, 4, 6-trinitrotoluene by a bottom layer of ZnO nanorod arrays. *Heliyon* **2023,** *9* (5).

20.   Kumar, V.; Maiti, B.; Chini, M. K.; De, P.; Satapathi, S., Multimodal Fluorescent Polymer Sensor for Highly Sensitive Detection of Nitroaromatics. *Scientific Reports* **2019,** *9* (1), 7269.

21.   Lefferts, M. J.; Castell, M. R., Vapour sensing of explosive materials. *Analytical Methods* **2015,** *7* (21), 9005-9017.

22.   Mothika, V. S.; Räupke, A.; Brinkmann, K. O.; Riedl, T.; Brunklaus, G.; Scherf, U., Nanometer-thick conjugated microporous polymer films for selective and sensitive vapor-phase TNT detection. *ACS Applied Nano Materials* **2018,** *1* (11), 6483-6492.

23.   Kumar, M.; Vij, V.; Bhalla, V., Vapor-Phase Detection of Trinitrotoluene by AIEE-Active Hetero-oligophenylene-Based Carbazole Derivatives. *Langmuir* **2012,** *28* (33), 12417-12421.

24.   Steinfeld, J. I.; Wormhoudt, J., Explosives detection: a challenge for physical chemistry. *Annual review of physical chemistry* **1998,** *49* (1), 203-232.

25.   Prusti, B.; Chakravarty, M., An electron-rich small AIEgen as a solid platform for the selective and ultrasensitive on-site visual detection of TNT in the solid, solution and vapor states. *Analyst* **2020,** *145* (5), 1687-1694.

26.   Sarkar, S., Computational design of a nanoconjugate model of pyrene-linked CdTe quantum dot for the detection of trinitrotoluene. *Computational and Theoretical Chemistry* **2022,** *1211*, 113681.

27.   Wang, Z.-J.; Li, Q.; Tan, L.-L.; Liu, C.-G.; Shang, L., Metal–organic frameworks-mediated assembly of gold nanoclusters for sensing applications. *Journal of Analysis and Testing* **2022,** *6* (2), 163-177.

28.   Yildirim, A.; Budunoglu, H.; Deniz, H.; O. Guler, M.; Bayindir, M., Template-free synthesis of organically modified silica mesoporous thin films for TNT sensing. *ACS Applied Materials & Interfaces* **2010,** *2* (10), 2892-2897.

29.   Zreid, M. S.; Tabasi, Z. A.; Ma, X.; Wang, T.; Almatarneh, M. H.; Zhao, Y., Highly Twisted Aryl-Anthraquinodimethanes: Synthesis, Characterization, and Fluorescence Sensing of TNT. *European Journal of Organic Chemistry* **2020,** *2020* (26), 4031-4041.

30.   Huang, G.; Li, Q.; Li, L.; Wang, E., Development of novel polymeric nanoagents and their potential in cancer diagnosis and therapy. *Frontiers in Chemistry* **2022,** *10*, 1569.

31.   Chakraborty, M.; Prusti, B.; Chakravarty, M., Small Electron-Rich Isomeric Solid-State Emitters with Variation in Coplanarity and Molecular Packings: Rapid and Ultralow Recognition of TNT. *ACS Applied Electronic Materials* **2022,** *4* (5), 2481-2489.

32.   Naddo, T.; Che, Y.; Zhang, W.; Balakrishnan, K.; Yang, X.; Yen, M.; Zhao, J.; Moore, J. S.; Zang, L., Detection of explosives with a fluorescent nanofibril film. *Journal of the American Chemical Society* **2007,** *129* (22), 6978-6979.

33.   Xu, B.; Wu, X.; Li, H.; Tong, H.; Wang, L., Selective detection of TNT and picric acid

by conjugated polymer film sensors with donor–acceptor architecture. *Macromolecules* **2011,** *44* (13), 5089-5092.

34.   Raichure, P. C.; Bhatt, R.; Kachwal, V.; Sharma, T. C.; Laskar, I. R., Multi-stimuli distinct responsive D–A based fluorogen oligomeric tool and efficient detection of TNT vapor. *New Journal of Chemistry* **2022,** *46* (14), 6560-6569.

35.   Mothika, V. S.; Räupke, A.; Brinkmann, K. O.; Riedl, T.; Brunklaus, G.; Scherf, U., Nanometer-Thick Conjugated Microporous Polymer Films for Selective and Sensitive Vapor-Phase TNT Detection. *ACS Applied Nano Materials* **2018,** *1* (11), 6483-6492.

36.   Ghorpade, T. K.; Palai, A. K.; Rath, S. K.; Sharma, S. K.; Sudarshan, K.; Pujari, P. K.; Patri, M.; Mishra, S. P., Pentiptycene-tbutylpyrene based poly(arylene-ethynylene)s: Highly sensitive and selective TNT sensor in aqueous as well as vapor phase. *Sensors and Actuators B: Chemical* **2017,** *252*, 901-911.

37.   Zhao, Q.; Li, F.; Huang, C., Phosphorescent chemosensors based on heavy-metal complexes. *Chemical Society Reviews* **2010,** *39* (8), 3007-3030.

38.   Xu, W.; Liu, S.; Sun, H.; Zhao, X.; Zhao, Q.; Sun, S.; Cheng, S.; Ma, T.; Zhou, L.; Huang, W., FRET-based probe for fluoride based on a phosphorescent iridium(iii) complex containing triarylboron groups. *Journal of Materials Chemistry* **2011,** *21* (21), 7572-7581.

39.   Wong, K. M.-C.; Tang, W.-S.; Lu, X.-X.; Zhu, N.; Yam, V. W.-W., Functionalized Platinum(II) Terpyridyl Alkynyl Complexes as Colorimetric and Luminescence pH Sensors. *Inorganic Chemistry* **2005,** *44* (5), 1492-1498.

40.   Shiu, H.-Y.; Wong, M.-K.; Che, C.-M., "Turn-on" FRET-based luminescent iridium(iii) probes for the detection of cysteine and homocysteine. *Chemical Communications* **2011,** *47* (15), 4367-4369.

41.   Agarwal, A.; Bhatta, R. P.; Kachwal, V.; Laskar, I. R., Controlling the sensitivity and selectivity for the detection of nitro-based explosives by modulating the electronic substituents on the ligand of AIPE-active cyclometalated iridium(iii) complexes. *Dalton Transactions* **2023,** *52* (39), 14182-14193.

42.   Ge, G.; He, J.; Guo, H.; Wang, F.; Zou, D., Highly efficient phosphorescent iridium (III) diazine complexes for OLEDs: Different photophysical property between iridium (III) pyrazine complex and iridium (III) pyrimidine complex. *Journal of Organometallic Chemistry* **2009,** *694* (19), 3050-3057.

43.   Yang, C.-H.; Cheng, Y.-M.; Chi, Y.; Hsu, C.-J.; Fang, F.-C.; Wong, K.-T.; Chou, P.-T.; Chang, C.-H.; Tsai, M.-H.; Wu, C.-C., Blue-Emitting Heteroleptic Iridium(III) Complexes Suitable for High-Efficiency Phosphorescent OLEDs. *Angewandte Chemie International*

Edition **2007,** *46* (14), 2418-2421.

44.   Lee, S. J.; Park, K.-M.; Yang, K.; Kang, Y., Blue Phosphorescent Ir(III) Complex with High Color Purity: fac-Tris(2′,6′-difluoro-2,3′-bipyridinato-N,C4′)iridium(III). *Inorganic Chemistry* **2009,** *48* (3), 1030-1037.

45.   Ma, D.-L.; Wong, W.-L.; Chung, W.-H.; Chan, F.-Y.; So, P.-K.; Lai, T.-S.; Zhou, Z.-Y.; Leung, Y.-C.; Wong, K.-Y., A Highly Selective Luminescent Switch-On Probe for Histidine/Histidine-Rich Proteins and Its Application in Protein Staining. *Angewandte Chemie International Edition* **2008,** *47* (20), 3735-3739.

46.   Lo, K. K.-W.; Zhang, K. Y.; Leung, S.-K.; Tang, M.-C., Exploitation of the Dual-emissive Properties of Cyclometalated Iridium(III)–Polypyridine Complexes in the Development of Luminescent Biological Probes. *Angewandte Chemie International Edition* **2008,** *47* (12), 2213-2216.

47.   Sumit; Maravajjala, K. S.; Khanna, S.; Kachwal, V.; Swetha, K. L.; Manabala, S.; Chowdhury, R.; Roy, A.; Laskar, I. R., Rational Molecular Designing of Aggregation-Enhanced Emission (AEE) Active Red-Emitting Iridium(III) Complexes: Effect of Lipophilicity and Nanoparticle Encapsulation on Photodynamic Therapy Efficacy. *ACS Applied Bio Materials* **2023,** *6* (4), 1445-1459.

48.   Park, S. W.; Ham, H. W.; Kim, Y. S., Theoretical Studies of Mono-Cyclometalated Ir(III) Complexes with Phenylpyrazole Based Ligands and Phosphines. *Molecular Crystals and Liquid Crystals* **2011,** *551* (1), 24-32.

49.   Lowry, M. S.; Bernhard, S., Synthetically Tailored Excited States: Phosphorescent, Cyclometalated Iridium(III) Complexes and Their Applications. *Chemistry – A European Journal* **2006,** *12* (31), 7970-7977.

50.   Bejoymohandas, K. S.; George, T. M.; Bhattacharya, S.; Natarajan, S.; Reddy, M. L. P., AIPE-active green phosphorescent iridium(iii) complex impregnated test strips for the vapor-phase detection of 2,4,6-trinitrotoluene (TNT). *Journal of Materials Chemistry C* **2014,** *2* (3), 515-523.

51.   Alam, P.; Kaur, G.; Kachwal, V.; Gupta, A.; Roy Choudhury, A.; Laskar, I. R., Highly sensitive explosive sensing by "aggregation induced phosphorescence" active cyclometalated iridium(iii) complexes. *Journal of Materials Chemistry C* **2015,** *3* (21), 5450-5456.

52.   Alam, P.; Karanam, M.; Roy Choudhury, A.; Rahaman Laskar, I., One-pot synthesis of strong solid state emitting mono-cyclometalated iridium(iii) complexes: study of their aggregation induced enhanced phosphorescence. *Dalton Transactions* **2012,** *41* (31), 9276-9279.

53.   Longhi, E.; De Cola, L., Iridium (III) complexes for OLED application. *Iridium (III) in optoelectronic and photonics applications* **2017**, 205-274.

54.   Li, T.-Y.; Wu, J.; Wu, Z.-G.; Zheng, Y.-X.; Zuo, J.-L.; Pan, Y., Rational design of phosphorescent iridium (III) complexes for emission color tunability and their applications in OLEDs. *Coordination Chemistry Reviews* **2018**, *374*, 55-92.

55.   Lo, K. K.-W.; Zhang, K. Y., Iridium (III) complexes as therapeutic and bioimaging reagents for cellular applications. *RSC advances* **2012**, *2* (32), 12069-12083.

56.   Agarwal, A.; Bhatta, R. P.; Kachwal, V.; Laskar, I. R., Controlling the sensitivity and selectivity for the detection of nitro-based explosives by modulating the electronic substituents on the ligand of AIPE-active cyclometalated iridium(iii) complexes. *Dalton Transactions* **2023**.

57.   Lai, P.-N.; Brysacz, C. H.; Alam, M. K.; Ayoub, N. A.; Gray, T. G.; Bao, J.; Teets, T. S., Highly Efficient Red-Emitting Bis-Cyclometalated Iridium Complexes. *Journal of the American Chemical Society* **2018**, *140* (32), 10198-10207.

58.   Sprouse, S.; King, K. A.; Spellane, P. J.; Watts, R. J., Photophysical effects of metal-carbon .sigma. bonds in ortho-metalated complexes of iridium(III) and rhodium(III). *Journal of the American Chemical Society* **1984**, *106* (22), 6647-6653.

59.   Deaton, J. C.; Taliaferro, C. M.; Pitman, C. L.; Czerwieniec, R.; Jakubikova, E.; Miller, A. J.; Castellano, F. N., Excited-state switching between ligand-centered and charge transfer modulated by metal–carbon bonds in cyclopentadienyl iridium complexes. *Inorganic Chemistry* **2018**, *57* (24), 15445-15461.

60.   Ravotto, L.; Ceroni, P., Aggregation induced phosphorescence of metal complexes: From principles to applications. *Coordination Chemistry Reviews* **2017**, *346*, 62-76.

61.   Bhatta, R. P.; Agarwal, A.; Kachwal, V.; Raichure, P. C.; Laskar, I. R., Enhanced TNT vapor sensing through a PMMA-mediated AIPE-active monocyclometalated iridium(iii) complex: a leap towards real-time monitoring. *Analyst* **2024**, *149* (8), 2445-2458.

62.   Muthusubramanian, S.; Saha, S. K., Exploration of twisted intramolecular charge transfer fluorescence properties of trans-2-[4-(dimethylamino) styryl] benzothiazole to characterize the protein–surfactant aggregates. *Journal of luminescence* **2012**, *132* (8), 2166-2177.

63.   Jiang, N.; Li, G.; Che, W.; Zhu, D.; Su, Z.; Bryce, M. R., Polyurethane derivatives for highly sensitive and selective fluorescence detection of 2,4,6-trinitrophenol (TNP). *Journal of Materials Chemistry C* **2018**, *6* (42), 11287-11291.

64.   Wang, G.; Li, M.; Wei, Q.; Xiong, Y.; Li, J.; Li, Z.; Tang, J.; Wei, F.; Tu, H., Design

of an AIE-Active Flexible Self-Assembled Monolayer Probe for Trace Nitroaromatic Compound Explosive Detection. *ACS Sensors* **2021,** *6* (5), 1849-1856.

65. Bejoymohandas, K.; George, T.; Bhattacharya, S.; Natarajan, S.; Reddy, M., AIPE-active green phosphorescent iridium (III) complex impregnated test strips for the vapor-phase detection of 2, 4, 6-trinitrotoluene (TNT). *Journal of Materials Chemistry C* **2014,** *2* (3), 515-523.

66. Fleming, C. N.; Dattelbaum, D. M.; Thompson, D. W.; Ershov, A. Y.; Meyer, T. J., Excited State Intervalence Transfer in a Rigid Polymeric Film. *Journal of the American Chemical Society* **2007,** *129* (31), 9622-9630.

67. Thompson, D. W.; Fleming, C. N.; Myron, B. D.; Meyer, T. J., Rigid Medium Stabilization of Metal-to-Ligand Charge Transfer Excited States. *The Journal of Physical Chemistry B* **2007,** *111* (24), 6930-6941.

68. Wang, X.; Xu, S.; Xu, W., Luminescent properties of dye-PMMA composite nanospheres. *Physical chemistry chemical physics : PCCP* **2011,** *13* (4), 1560-7.

69. Myilsamy, M.; Mahalakshmi, M.; Subha, N.; Murugesan, V., Mesoporous Ga–TiO2: Role of Oxygen Vacancies for the Photocatalytic Degradation Under Visible Light. *Journal of Nanoscience and Nanotechnology* **2018,** *18* (2), 925-935.

70. Rasines, G.; Macías, C.; Haro, M.; Jagiello, J.; Ania, C. O., Effects of CO2 activation of carbon aerogels leading to ultrahigh micro-meso porosity. *Microporous and Mesoporous Materials* **2015,** *209*, 18-22.

71. Zhou, X.; Cheng, X.; Feng, W.; Qiu, K.; Chen, L.; Nie, W.; Yin, Z.; Mo, X.; Wang, H.; He, C., Synthesis of hollow mesoporous silica nanoparticles with tunable shell thickness and pore size using amphiphilic block copolymers as core templates. *Dalton Transactions* **2014,** *43* (31), 11834-11842.

72. Thommes, M.; Kaneko, K.; Neimark, A. V.; Olivier, J. P.; Rodriguez-Reinoso, F.; Rouquerol, J.; Sing, K. S., Physisorption of gases, with special reference to the evaluation of surface area and pore size distribution (IUPAC Technical Report). *Pure and applied chemistry* **2015,** *87* (9-10), 1051-1069.

73. Rahman, Z. U.; Wei, N.; Li, Z.; Sun, W.; Wang, D., Preparation of hollow mesoporous silica nanospheres: Controllable template synthesis and their application in drug delivery. *New Journal of Chemistry* **2017,** *41* (23), 14122-14129.

74. Jeromenok, J.; Weber, J., Restricted access: on the nature of adsorption/desorption hysteresis in amorphous, microporous polymeric materials. *Langmuir* **2013,** *29* (42), 12982-12989.

PYRENE-THIOPHENE BASED MOLECULES FOR STIMULI-RESPONSIVE PROBES
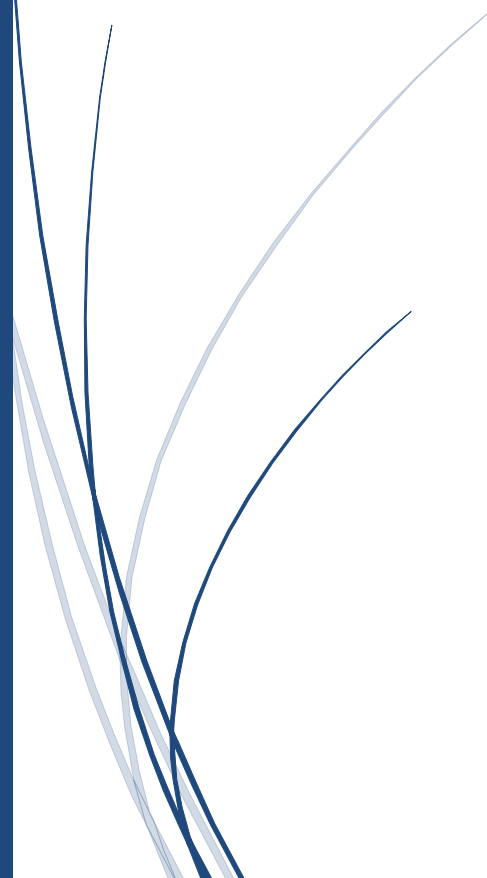
Chapter 5. Pyrene-thiophene Based Molecules for Stimuli-responsive Probes

Part A. 5.1 Tunable Emission in Visible Range from a Single Organic Fluorophore through Time-controlled Morphological Evolution

5.1.1 Introduction

In recent decades, a great deal of research in material sciences has been focused on the preparation of innovative luminescent materials with colour-tunable emission, high stability, and ease of preparation. Within the different families of luminescent compounds that have been proposed, purely organic materials in the nanoscale range increase their potential and applicability in numerous fields such as chemical sensing, biological sensing, bioimaging, pharmaceuticals, or organic light-emitting diodes, where the toxicity of other materials including rare earth or heavy metals might become an issue.[1-3] Molecular conformation is a simple but significant property in organic solid-state chemistry that allows the fine-tuning of the properties of materials. In this respect, polymorphism refers to a compound's ability to exist in different crystal structures that differ in the packing arrangements of its constituent molecules.[4-7] In most cases, the different conformations adopted by a molecule in the crystalline state are forced by the presence of solvent molecules, so-called pseudo-polymorphic phases. Although originating from the same compound, the chemical, physical, and mechanical properties of polymorphic crystals are all different. Polymorphs present not only different melting temperatures and solubilities but may also show different vibrational transitions (i.e., different infrared and Raman spectra), electronic transitions, densities, surface tensions, crystal shapes, kinetic stabilities, crystal hardness, or colours. Because of these differences, controlling the formation of polymorphs is an important aspect in the pharmaceutical industry as well as in the obtention of compounds for agrichemical applications, food additives, pigments, or explosives.[8-13]

If we restrict our scope to luminescent materials, the luminescent properties of most organic crystals are governed mainly by the nature of the emitting states, which depend basically on the chemical nature of the molecule (its main functional groups) and of the molecular structure (the relative disposition of the relevant functional groups in space). Aggregation in the condensed phases may dramatically change this second aspect, and intermolecular interactions resulting in different packing modes may lead to relevant changes in the observed emission, so all these aspects are critical in luminescent organic crystals.[14-19] As an illustration of this situation, we may refer to a recent report on the properties of organic compounds containing a pyrene unit where the importance of exploring various crystallization conditions is highlighted, showing that the relative orientation of the individual molecules plays a crucial role in modulating the excited-state properties of the pyrene excimer.[5] This example shows how obtaining different crystal structures by varying the solvent system allows colour tuning in a relatively narrow range (from blue to green). Other ways to induce different emission colours in crystals involve co-crystallization techniques.[20-22] Although these few examples show that modulating the luminescent properties of a given compound by forcing it to crystallize in different polymorphs is feasible, experience demonstrates that it is a complex and unpredictable process and it is desirable to explore other more simple ways of influencing the structure-properties relations for organic luminescent materials.

Nanoscale control of the supra-molecular architecture is a very relevant topic in the field of nano-chemistry, especially in the case of biological systems where usually a network of non-covalent interactions leads to the formation of a self-assembled system. This approach provides solutions to the fabrication of ordered aggregates from components with sizes from nanometres to micrometres, and in the case of luminescent materials, it may be used for emission tuning.[23-27] The use of thiophene units is well known for the self-assembly of nanostructures and polypyrene has been recently shown to give aggregates with a nano-flower type morphology.[25, 28-29] In 2002 Tang et al., reported the formation of nanostructures of hexaphenylsilole with enhanced colour-tunable emissions due to the formation of nanoflowers, nano-globules, and micro-globules, depending on the water fraction added to a THF solution of hexaphenylsilole.[30] It has also been shown that alkyl chain-dependent microstructures and self-assembled aggregates produce various emission colours in solution.[31-37] The fabrication of luminescent materials with adjustable emission color by self-assembly of π-conjugated molecules has attracted particular attention. In the literature,[38] a

thiophene-based α-cyanostyrene derivative was observed to form nanoparticles with a bright fluorescence when self-assembled by adding water to an organic solution (THF or DMSO). With the increase of the water ratio, a sharp decrease in the fluorescence intensity was observed, together with a red shift as the morphology of the assemblies changed from nanoparticles to nanofibers. As illustrated by the examples above, achieving a wide range of tunable emission colours, especially in the solid state for single-fluorophore materials, remains a significant challenge[16, 39] and in all cases, a certain external stimulus is required to fine-tune of excited state property.

Since colour tuning of organic solid-state luminescent materials remains difficult and time-consuming in the case of organic fluorophores,[27,40] many research groups have switched to luminescent inorganic quantum dots instead.[41-42] Quantum dots have also been used in a variety of applications such as bio-imaging, solar cells, or display technologies. In this case, emission colour is tuned simply by varying size in the nano range.[43-44] From the experimental point of view, the emission from quantum dots is tuned by doping the material and one of the major challenges of this method is to fully determine the internal structure of the material.[45] Most of the available quantum dots are metal-based, so their toxicity to cells is a major issue in biological imaging applications.[46] For this reason, highly efficient organic solid-state luminescent materials (OSSLMs) are currently being investigated for use in a variety of applications, including luminescent sensors, bio-labelling and imaging agents, as well as in organic light-emitting diodes (OLEDs). The π-conjugated structures, molecular conformations, and intermolecular packing modes are three key factors that determine the optoelectronic properties of OSSLMs. Thiophene-based conjugated materials have been used in organic photovoltaics (OPVs), organic field-effect transistors (OFETs), and OLEDs.[47]

In this article, we describe a straightforward method for obtaining the entire visible spectrum from a single organic molecule without any structural modification. In this new material, pyrene and thiophene derivatives are reacted through the Suzuki coupling reaction to produce PyS (1-(5-(Pyren-1-yl) thiazol-2-yl) ethan-1-one). On monitoring the reaction, we found that the gradually increasing size and evolution of surface morphology with allowing the reaction for a longer time, leading to significant changes in the emission colour of the aggregates. HRTEM analysis reveals that as the synthetic time increases, the size of the nanoaggregates increases, together with the gradual evolution of morphology resulting in the emission tuning from blue to red. Experiments

such as HRTEM, FESEM, dynamic light scattering, Raman spectroscopy, powder X-ray diffraction, and computational DFT-based tools have been employed to gain a fundamental understanding of this phenomenon. To the best of our knowledge, this is the first report of a material based on a single organic fluorophore that emits the whole visible range in the same chemical entity.

5.1.2 EXPERIMENTAL SECTION

5.1.2.1 Synthesis and Characterization of PyS

1-(5-(Pyren-1-yl) thiazol-2-yl) ethan-1-one (PyS) was synthesized by Suzuki coupling of 1-bromo pyrene (0.300 gm, 1.067 mmol) and 5-acetyl thiophene-2-boronic acid (0.199 gm, 1.174mmol) with ethanol (1ml) and toluene (2 ml) as a solvent, palladium(0) as the catalyst (0.0181 mmol), and sodium carbonate (0.295 mg 2.134 mmol) as a base. The whole reaction was carried out under a nitrogen atmosphere. The reaction mixture was heated at reflux temperature (90-100 °C) and was monitored by TLC for time intervals of 6-8 hr., 12-14 hr., 20-24 hr. and more than 40 hr. After completion of the reaction within the stipulated time, the reaction mass was cooled down followed by addition of water, and then extracted with a minimum amount of ethyl acetate (3 ml each time) for two times. The organic layer was collected and evaporated by rotary evaporator at 40-45°C and purified by column chromatography by using silica gel (60-120 mesh size) as a stationary phase and a mixture of ethyl acetate (5%) and hexane as an eluent. As the product was well separated on TLC plate from the starting material, around 1hr. is enough for isolating the pure product from the column. After isolating the pure compound through column chromatography, the solvent was removed by a rotatory evaporator (40-45°C bath temperature). Solid products were isolated, and then dried the product at vacuum oven for 8-10h at 50°C. We got PyS-B (blue emitting product) with 60% yield, PyS-G (green emitting product) with 70% yield, PyS-Y (yellow emitting product) with 86% yield and PyS-R (red emitting product) with 65% yield; One important observation we noticed during purification is that, in the case of PyS-B we observed the sticky solid and the remaining cases are crystalline powder. All the isolated products of PyS were characterized by ^{1}H NMR, ^{13}C NMR and HRMS (Figure 5.1.1 to 5.1.9).
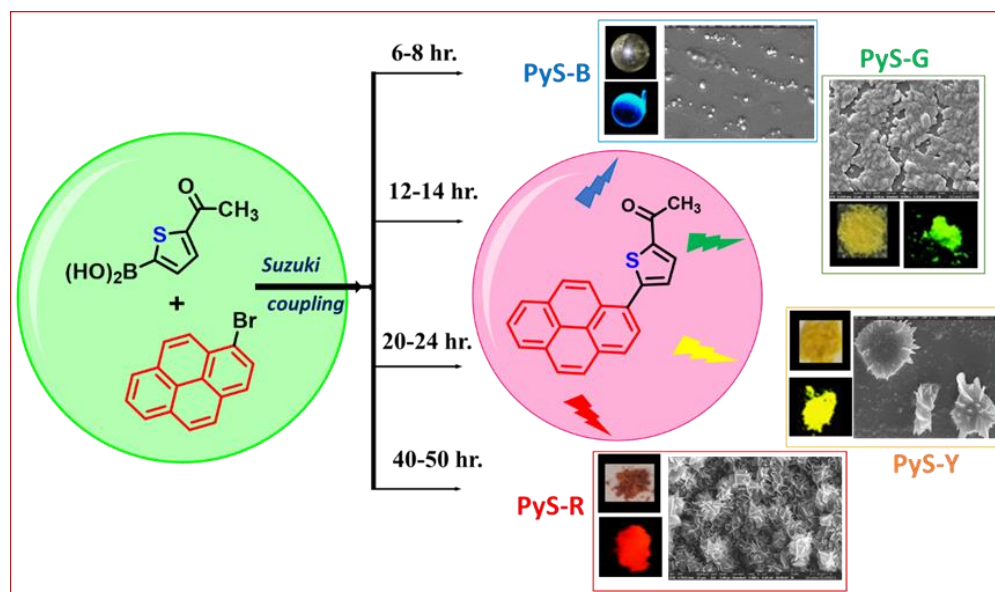
Scheme 5.1.1 Synthesis scheme for 1-(5-(pyren-1-yl) thiophen-2-yl) ethan-1-one (PyS) from 1-bromo pyrene and 5-acetyl thiophene-2-bronic acid via Suzuki coupling. The enclosed figures show the daylight colour and the fluorescent image of the isolated product at different time intervals under UV light excitation (365 nm) together with the corresponding FESEM image.

Table 5.1.1 Synthesis of PyS in the PyS-B, PyS-G, PyS-Y, and PyS-R forms at different reaction conditions.

Solvents	Base	Reaction time	Temperature	Yield (%)	Product emission
Ethanol, Toluene (1:2)	1. Na_2CO_3 2. K_2CO_3	6 to 50 hr	90-100^0 C	60 70 86 65	Blue(6-8 hrs) Green(12-16 hrs) Yellow(20-24 hrs) Red(40-50 hrs)
1,4-dioxane	1. Na_2CO_3 2. K_2CO_3	6 to 50 hr	90-100^0 C	50, 65 75, 57	Blue, Green, Yellow, Red
Dimethyl formamide	1. Na_2CO_3 2. K_2CO_3	6 to 50 hr	90-100^0 C	55, 70 80, 55	Blue, Green, Yellow, Red
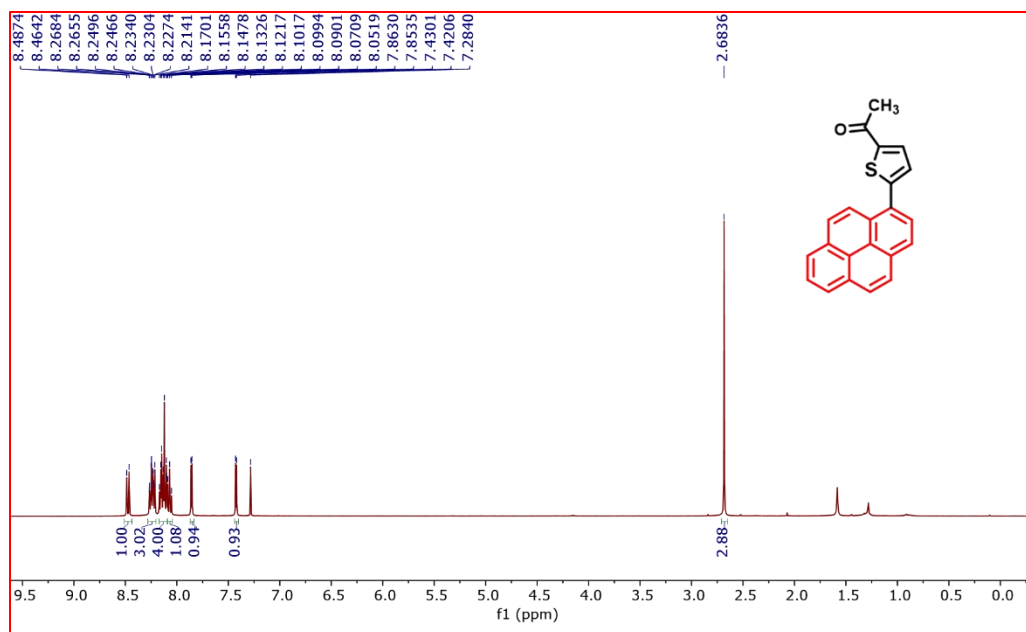
Figure 5.1.1 ^{1}H NMR spectra of PyS-Y
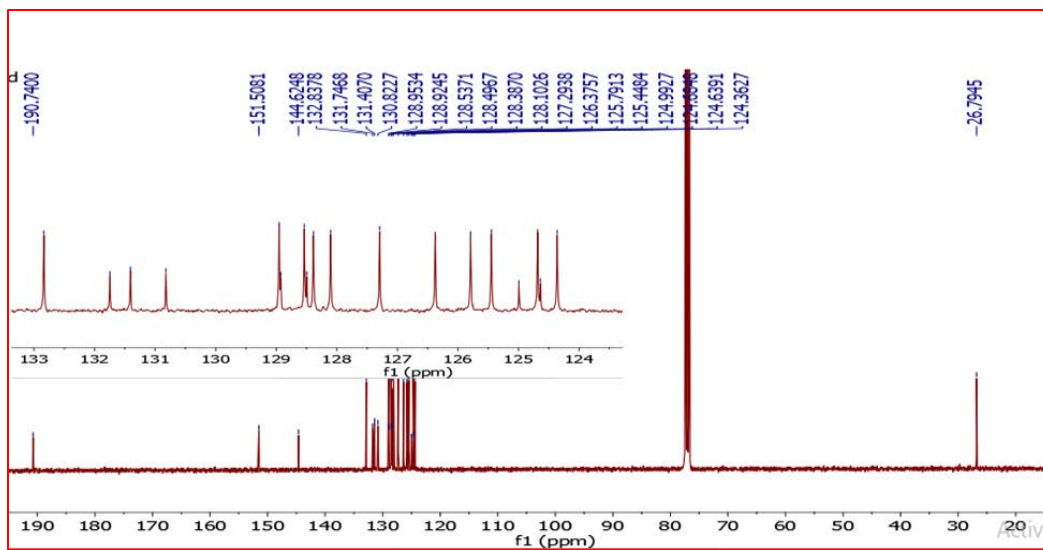
Figure 5.1.2 ^{13}C NMR of PyS-Y
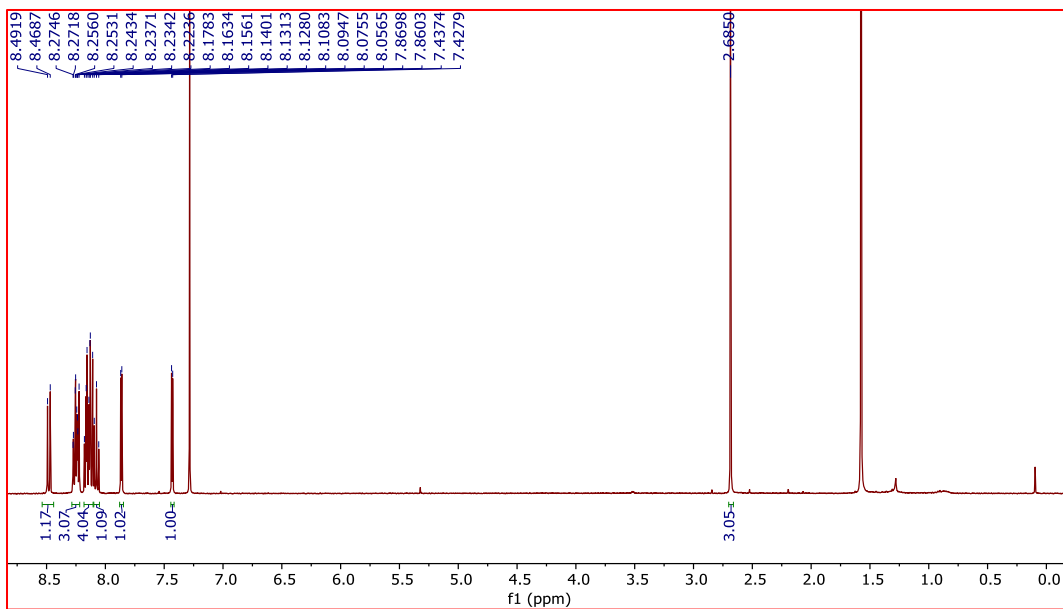
Figure 5.1.3 ¹H NMR spectra of PyS-B
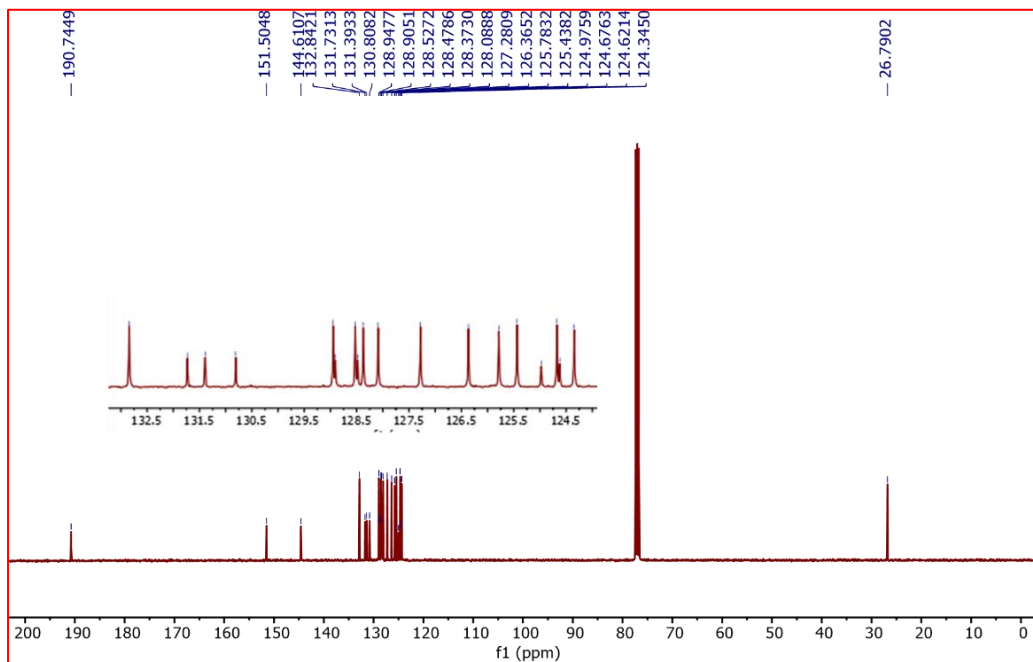
Figure 5.1.4 ¹³C NMR spectra of PyS-B
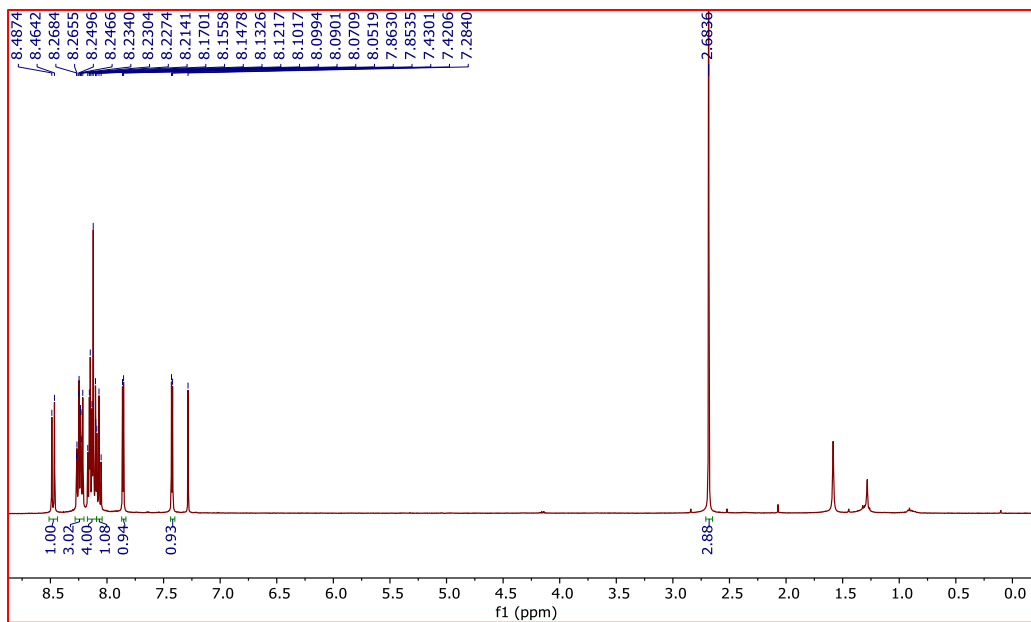
Figure 5.1.5 ^{1}H NMR spectra of PyS-G
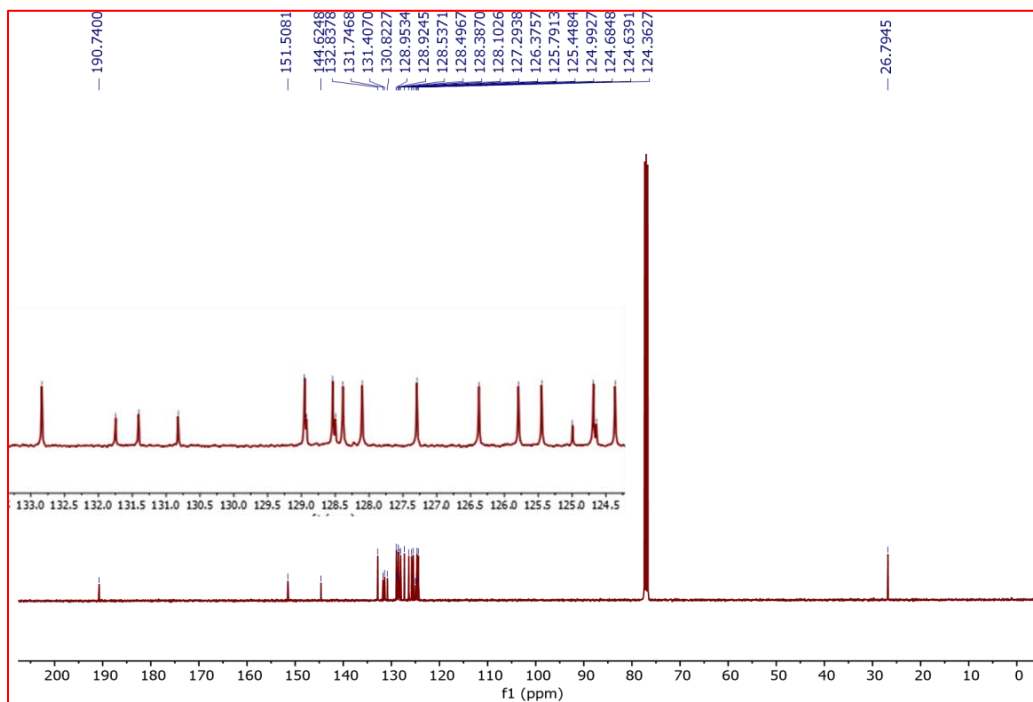
Figure 5.1.6 ^{13}C NMR spectra of PyS-G
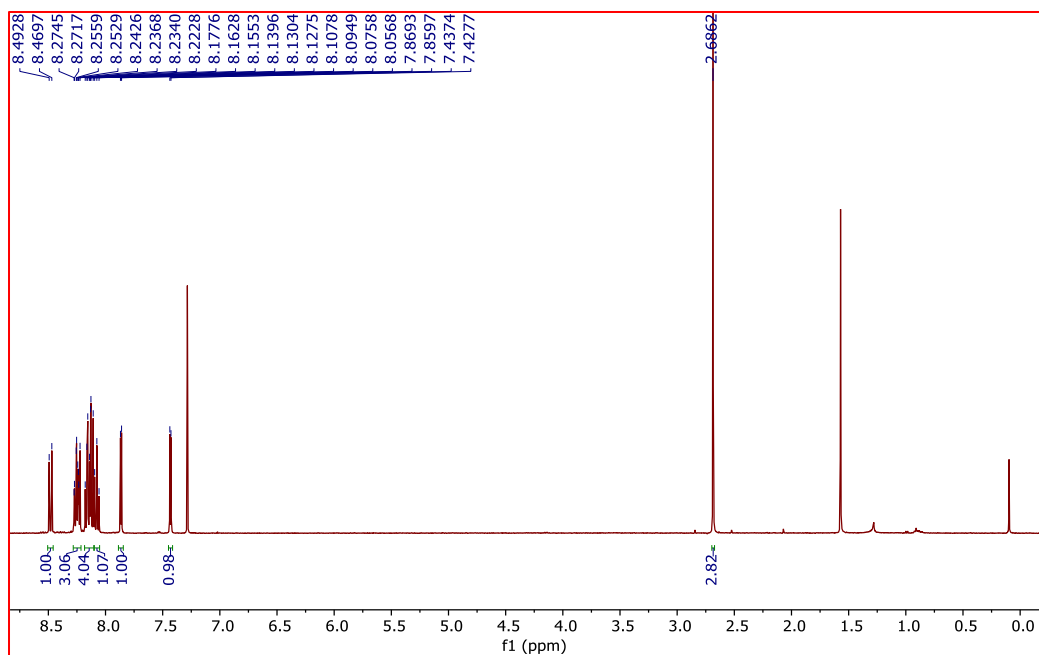
Figure 5.1.7 ^{1}H NMR spectra of PyS-R
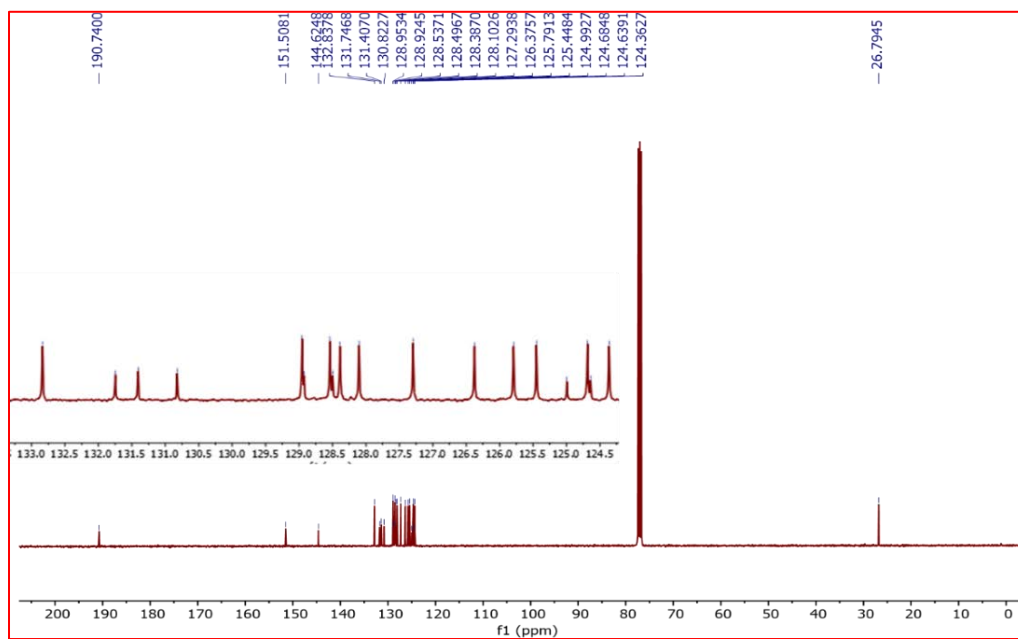
Figure 5.1.8 ^{13}C NMR spectra of PyS-R
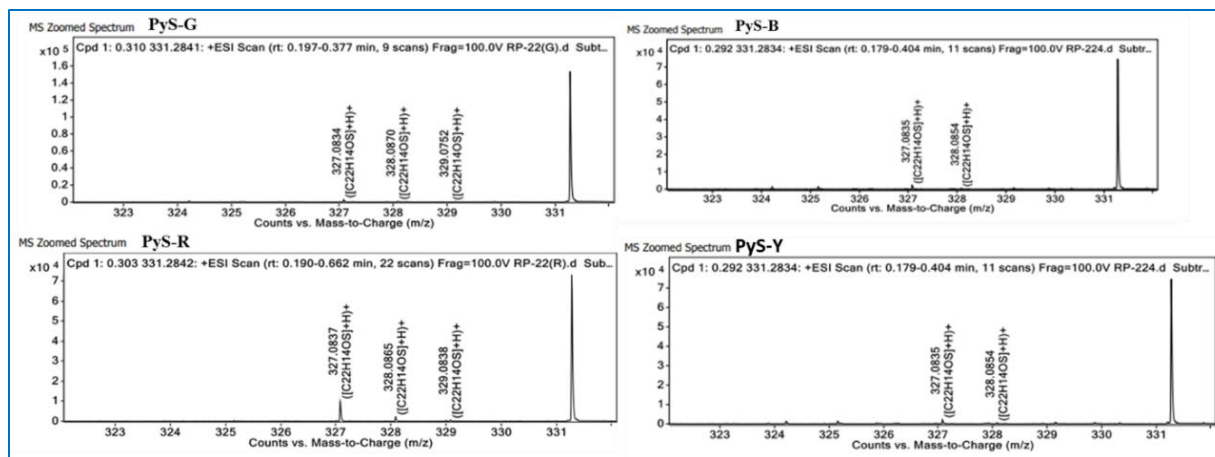
Figure 5.1.9 HRMS data of PyS (PyS-B, PyS-G, PyS-Y and PyS-R), we observed m/z at 327.0837 as a major peak apart from these at same molecular formula two small peaks are observed corresponding to the isotopic mass of the same compound

^{1}H and ^{13}C NMR and HRMS data of PyS-B

^{1}H NMR (400 MHz, Chloroform-*d*) δ 8.48 (d, *J* = 9.3 Hz, 1H), 8.30 – 8.20 (m, 3H), 8.20 – 8.09 (m, 4H), 8.08 (t, *J* = 7.6 Hz, 1H), 7.86 (d, *J* = 3.8 Hz, 1H), 7.43 (d, *J* = 3.9 Hz, 1H), 2.69 (s, 3H) (Fig 5.1.3). ^{13}C NMR (101 MHz, Chloroform-d) δ 190.74, 151.50, 144.61, 132.84, 131.73, 131.39, 130.81, 128.94, 128.91, 128.53, 128.48, 128.37, 128.09, 127.28, 126.37, 125.78, 125.44, 124.98, 124.68, 124.62, 124.35, 26.79. (Fig 5.1.4). LC-HRMS: found m/z: 327.0835 [M + H] $^+$, calculated m/z: 326.0765 (see Fig 5.1.9).

^{1}H and ^{13}C NMR and HRMS data of PyS-G

^{1}H NMR (400 MHz, Chloroform-*d*) δ 8.49 (d, *J* = 9.3 Hz, 1H), 8.30 – 8.20 (m, 3H), 8.20 – 8.09 (m, 4H), 8.08 (t, *J* = 7.6 Hz, 1H), 7.86 (d, *J* = 3.8 Hz, 1H), 7.43 (d, *J* = 3.9 Hz, 1H), 2.69 (s, 3H). (Fig 5.1.5). ^{13}C NMR (101 MHz, Chloroform-*d*) δ 190.74, 151.50, 144.62, 132.84, 131.75, 131.41, 130.82, 128.95, 128.92, 128.54, 128.50, 128.39, 128.10, 127.29, 126.38, 125.79, 125.44, 124.99, 124.68, 124.64, 124.36, 26.79. (Fig 5.1.6). LC-HRMS: found m/z: 327.0834 [M + H] $^+$, calculated m/z: 326.0765 (see Fig 5.1.9).

¹H and ¹³C NMR and HRMS data of PyS-Y

¹H NMR (400 MHz, Chloroform-*d*) δ 8.48 (d, *J* = 9.3 Hz, 1H), 8.29 – 8.19 (m, 3H), 8.19 – 8.08 (m, 4H), 8.07 (t, *J* = 7.6 Hz, 1H), 7.86 (d, *J* = 3.8 Hz, 1H), 7.43 (d, *J* = 3.8 Hz, 1H), 2.68 (s, 3H). (Fig 5.1.1). ¹³C NMR (101 MHz, Chloroform-*d*) δ 190.79, 151.50, 144.61, 132.84, 131.73, 131.39, 130.81, 128.95, 128.91, 128.53, 128.48, 128.37, 128.109, 127.28, 126.37, 125.78, 125.44, 124.98, 124.68, 124.642, 124.36, 26.79. (Fig 5.1.2). LC-HRMS: found m/z: 327.0835 [M + H] ⁺, calculated m/z: 326.0765 (see Fig 5.1.9).

¹H and ¹³C NMR and HRMS data of PyS-R

¹H NMR (400 MHz, Chloroform-*d*) δ 8.49 (d, *J* = 9.3 Hz, 1H), 8.30 – 8.20 (m, 3H), 8.20 – 8.09 (m, 4H), 8.08 (t, *J* = 7.6 Hz, 1H), 7.86 (d, *J* = 3.8 Hz, 1H), 7.43 (d, *J* = 3.9 Hz, 1H), 2.69 (s, 3H) (Fig 5.1.7). ¹³C NMR (101 MHz, Chloroform-*d*) δ 190.74, 151.51, 144.62, 132.84, 131.75, 131.40, 130.82, 128.95, 128.92, 128.54, 128.50, 128.39, 128.10, 127.29, 126.38, 125.79, 125.44, 124.99, 124.68, 124.64, 124.36, 26.79 (Fig 5.1.8). LC-HRMS: found m/z: 327.0837 [M + H] ⁺, calculated m/z: 326.0765 (see Fig 5.1.9).

5.1.2.2 Sample preparation

Glass coverslips were washed three times with methanol and acetone dried and used for making a thin film of isolated compounds. For UV visible and fluorescence spectra measurement in the solid state, thin films were prepared on glass coverslips. It was dissolved 2mg of pure samples of PyS (Blue, Green, Yellow and Red) in 1.0 ml of dichloromethane solution, then drop cast on glass coverslips. Dried the compounds coated thin film under vacuum at 50°C for 8.0 hr. These dried films were used to record the UV-vis spectroscopy, photoluminescence spectra measurement, and FESEM analysis. For HRTEM analysis, the sample was dissolved in ethanol followed by ultrasonication for 30 mins, and then drop cast on a copper grid. The copper grid was left for 24 hr. to make it dry. Then the sample was analyzed by using JEOL JEM 2100 PLUS High-Resolution TEM.

5.1.3 RESULTS AND DISCUSSION

The emission of PyS-Y under a 365 nm UV lamp showed a bright yellow colour. The most of the reported pyrene-derivatives indicate that these exhibited mechanoflorochromism (MFC) and polymorphism as a result of changes in molecular packing in the crystal structure.[5, 18, 48-50] So, we decided to study the effects of mechanical grinding on the newly synthesized derivative of pyrene-thiophene (PyS-Y). Many MFC materials transform from crystalline to amorphous under mechanical pressure due to the defects in the crystal packing and revert to their original structure when heating the ground product or after fuming it with solvents.[51-53] During mechanical grinding of PyS-Y with a mortar pestle, it was observed that a change in the emission colour from yellow (PyS-Y) to bright green (PyS-G) (Figure 5.1.10, a). The powder-XRD of PyS before (PyS-Y) and after (PyS-G) grinding reveals that the peak position of all peaks is identical, with just a few peaks disappearing in the ground form (PXRD, Figure 5.1.11). But the peak intensity is decreased noticeably. It was evident from the PXRD pattern that the crystallinity of PyS changes into a semicrystalline nature during mechanical grinding, but the few peaks that disappeared in ground form suggest that the molecular packing may alter.[54-56] On fuming the green emissive ground form (PyS-G) with different solvents (methanol, n-hexane, dichloromethane, or ethyl acetate) the product does not revert to its original form (PyS-Y). When the ground form (PyS-G) was dissolved in dichloromethane and the solvent was slowly evaporated in a rotavapor, the original yellow PyS-Y form was recuperated (PXRD, Figure 5.1.11).
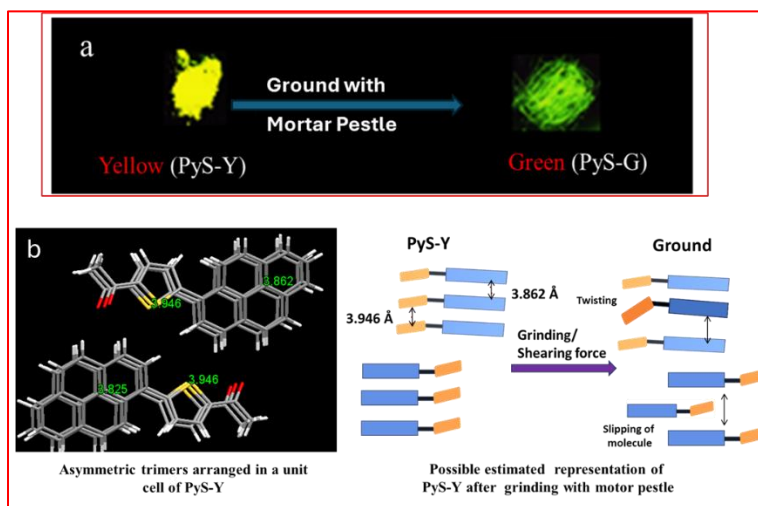
Figure 5.1.10 Images of products taken under a UV lamp (365 nm). **(a)** Product of normal Suzuki coupling obtained after 24 h (PyS-Y) and ground form of PyS-Y by using mortar pestle. **(b)** Asymmetric trimers arranged in unit cell and their possible deformation with external grinding. **(c)** Their possible deformation with external grinding force is shown by estimating representation to show effect of ring slipping and twisting
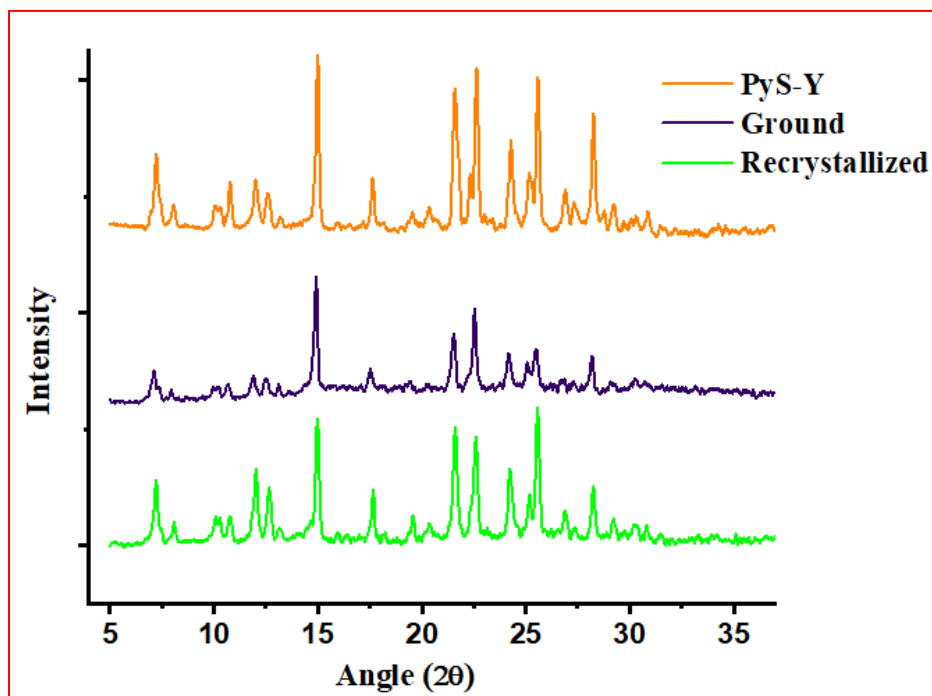
Figure 5.1.11 PXRD pattern of PyS-Y(Yellow), Ground form of PyS-Y and recrystallized form of PyS-Y in DCM, hexane

The single crystal structure of PyS-Y grown in DCM/hexane (9:1) by slow diffusion reveals that the twelve molecules present in the unit cell are grouped in four symmetry equivalent trimers with the molecules facing each other (Figure 5.1.12), allowing for effective π···π stacking interactions between their respective pyrene fragments (distances between pyrene planes ~3.8Å). As shown in the central part of figure 5.1.12, two of these trimers join to form a pair through lateral interactions, with these hexamers being the basic building block in the crystal structure. The crystal structure is composed by chains of these hexamers that run along the crystal's c direction (Figure 5.1.12 lower right part). The complete crystal structure is formed by multiple C-H…π interactions between molecules on neighbouring chains in two approximately perpendicular directions of the *a-b* plane in such a way that the orientation of the pyrene fragments in a chain is approximately perpendicular

to that in the four nearest-neighbour chains (Figure 5.1.12 right top part). The thiophene fragments of the molecules in each trimer are also stacked, but twisted with respect to the pyrene moieties, with the thiophene rings forming a dihedral angle of 41º – 48º with respect to the plane containing the pyrene fragment. The geometry of the PyS molecules in the crystal is very similar to that obtained from electronic structure calculations using Density Functional Theory (DFT) (Figure 5.1.13) where a dihedral angle of 48º between the thiophene and the pyrene fragments is found. PyS molecules are highly flexible, allowing for four different conformers by rotation around the C-C bonds joining the thiophene ring with either the pyrene fragment or with the acetyl group. The conformation found for PyS in the crystals (see Figure 5.1.12) is found to be the most stable one for the isolated molecule, although all four possible conformers differ in less than 1 kcal/mol. We have also evaluated the interconversion barriers between the four conformers, finding that it is extremely easy to rotate around the bond joining the thiophene and the pyrene fragments (1.1 kcal/mol) while rotation of the acetyl fragment is more difficult, with a barrier of 8.5 kcal/mol. From these data we can infer that in dilute solutions there should be a rapid interconversion between the two conformers that can be obtained by rotation around the thiophene-pyrene bond, while the most stable conformer is favoured in the early stages of the crystallization process when trimers are formed.
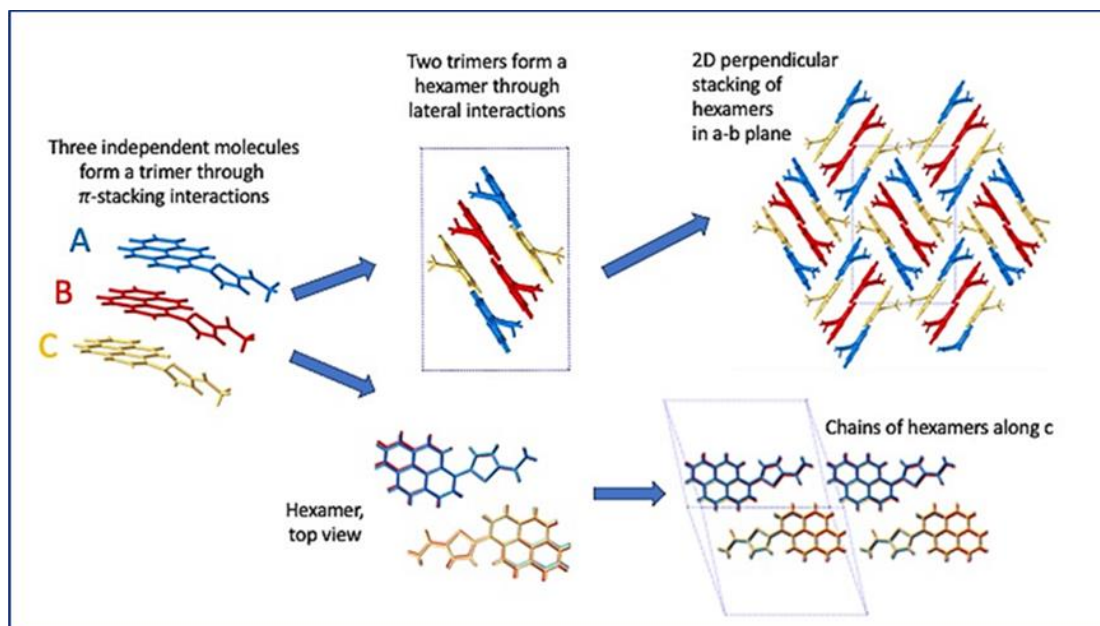
Figure 5.1.12. (a) Hierarchical analysis of the crystal structure of PyS-Y showing the formation of discrete trimeric and hexameric clusters, the formation of linear chains of hexamers along the crystal's *c* axis, and the formation of the final crystal structure as a packing of perpendicular chains in two directions of the *ab* planes.
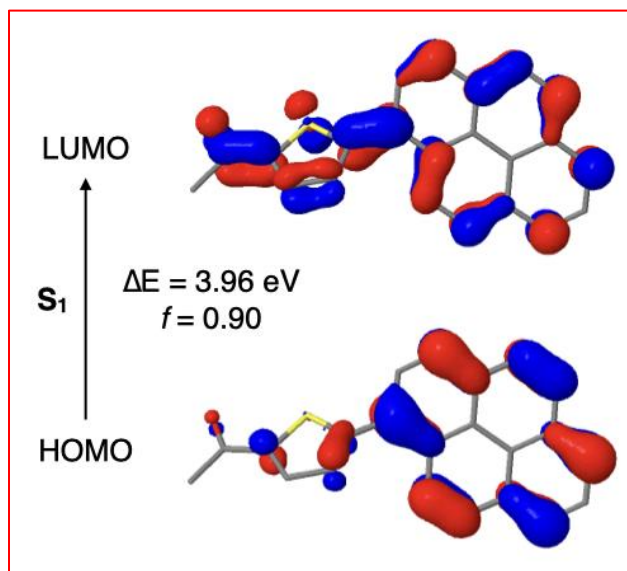
Figure 5.1.13 Frontier molecular orbitals responsible for the S_1 excited state of the lowest-energy conformer of the PyS molecule

As PyS-Y undergoes a hypsochromic shift from yellow to green during mechanical grinding, there may be a change in the π - π stacking between the pyrene rings as a result of thiophene ring twisting.[54] In PyS-Y, within a trimer weak $\pi...\pi$ stacking interactions (3.946 Å, 3.862 Å) are observed. After applying shearing force (grinding) there might be two possibilities either slipping of pyrene-thiophene moiety and displacing from the plane of pyrene-pyrene stacking, thus $\pi...\pi$ stacking interactions may reduce. On the other way, it was observed that pyrene thiophene is highly flexible so in the presence of shearing force there is a high chance of twisting the thiophene ring around pyrene thiophene single bond, which might be responsible for making pyrene-pyrene apart and stacking interaction may decrease (Figure 5.1.10). Conventional MFC materials can be reversed by fuming or heating, whereas PyS-G (ground form of PyS-Y) can only be reversed by dissolving in solvent and evaporating slowly, suggesting that both forms are stable. We observed that the PyS-G sample reverted to the original PyS-Y form by slow evaporation, indicating that the original PyS-Y form is more stable than the PyS-G one. To understand the structure of the

ground form, it was compared the Raman spectra of both forms noticed a peak at 1238.3 cm^{-1} is slightly shifted to a higher wavenumber (1239.3 cm^{-1}) in the PyS-G sample indicating a possible change in intermolecular interactions and short contacts (Figure 5.1.14).[57] A change in molecular packing could, however, not be confirmed since it is not possible to obtain a crystal structure for the ground PyS-G form.
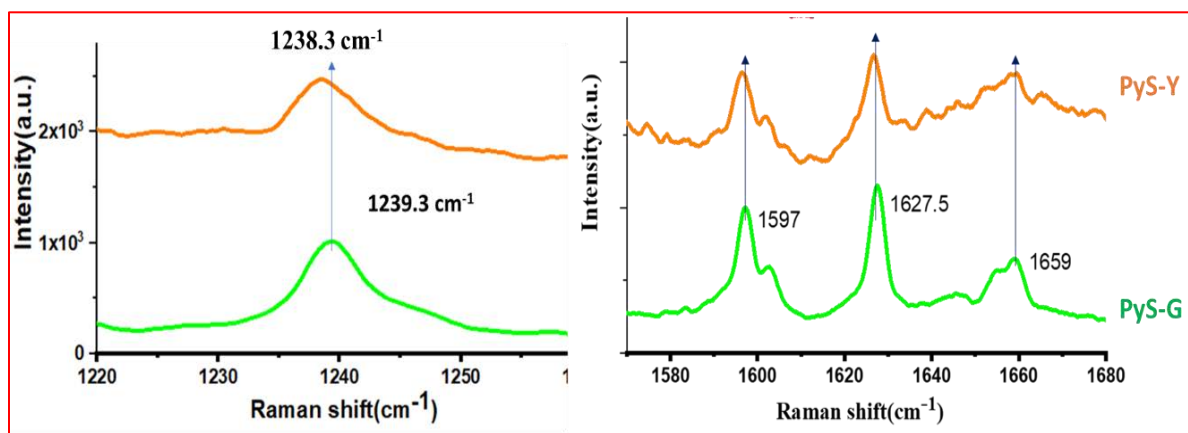
Figure 5.1.14 Raman analysis of PyS-G (ground form of PyS-Y) and PyS-Y. It was observed that the peak at 1239.3 cm^{-1} belongs to CH in-plane bending of the pyrene ring and that the peaks at 1597 cm^{-1} and 1627.5 cm^{-1} correspond to the C-C stretching for pyrene. The Raman frequency at 1659 cm^{-1} corresponds to the conjugated carbonyl C=O stretching frequency[58]

According to prior research, compounds such as PyS tend to exhibit polymorphism after recrystallization in various solvents owing to changes in molecular packing.[5] In order to explore the possibility of obtaining crystals for the PyS-G (ground form of PyS-Y), we tried a recrystallization using a slow diffusion technique in a different solvents (DCM/hexane (9:1), chloroform, toluene, MeOH). To our surprise, we observed the formation of aggregates of the crystals with a round shape, different from the needle-shaped crystals found for PyS-Y (Figure 5.1.15) in DCM/hexane (9:1). Under UV-visible light, a red emission was detected (~600 nm) for the circular aggregates of crystals which is labelled as PyS-R. To get a better understanding of the process of aggregate formation, we performed multiple reactions under identical conditions in ethanol/toluene (1:2), only varying the reaction time (checked up to 50 hours) and monitored the reaction progress using TLC. After 6-8 hrs it was obtained a new product (PyS-B) which was characterized by a blue emission (excitation by 365nm). A green emissive powder was isolated by extending the reaction time to 12-14 hrs. On extending the reaction time to 20-24 hrs the formation

of the original yellow-emitting PyS-Y product was observed. Finally, if the reaction time is increased above 40 hours, the isolated product corresponds to the orange-red emissive form, PyS-R.
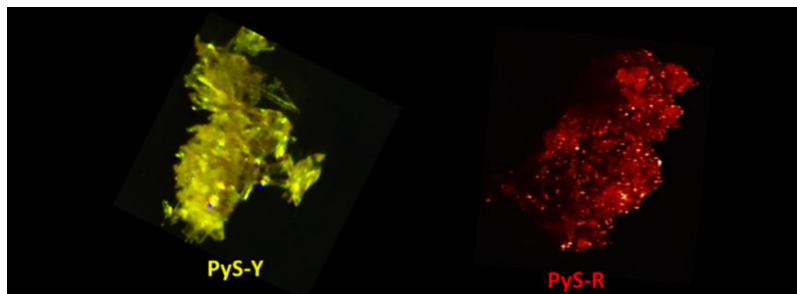
Figure 5.1.15 Fluorescence microscopic image of different coloured crystals of PyS (PyS-Y and PyS-R)
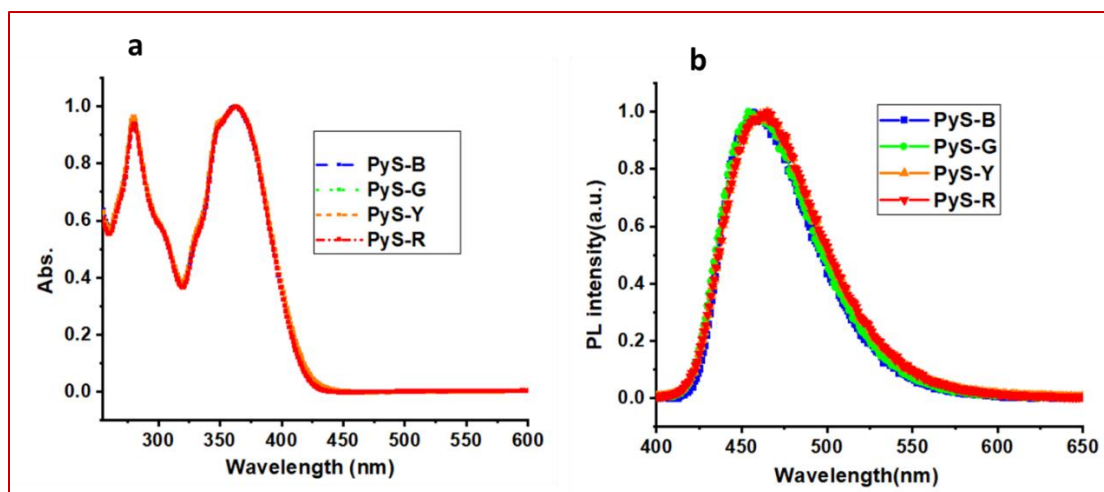
Figure 5.1.16 a) UV-visible spectra of PyS (obtained from blue, green, yellow, and red samples, respectively) in 10^{-5} M solutions of dichloromethane. (b) PL spectra of the same samples in the same solution

We have recorded ^{1}H and ^{13}C NMR spectra of all four forms of PyS in CDCl$_3$, observing similar chemical shift values for all of them (see experimental section), further analysed the HRMS analysis of PyS (PyS-B, PyS-G. PyS-Y and PyS-R) noticed similar m/z value for all cases (experimental section). To investigate the role of the solvent in the formation of the aggregates, we studied the same reaction with varying solvents such as 1,4 dioxane, and DMF instead of ethanol/toluene and found the same trends of forming the products (Table 5.1.1). We have been

able to grow single crystals of PyS in the green, yellow, and red forms in a DCM / hexane (9:1) mixture through the diffusion technique (PyS-Y, **CCDC**-2246684, PyS-G, **CCDC**-2246681, PyS-R, **CCDC**-2246692). We found that the molecular packing in all three crystal structures is practically the same (Table 5.1.2). If during the crystal growth solvent evaporates slowly, the product is transformed into the most stable form (PyS-R) as observed during the synthesis, which neglects a possible solvent effect since slow recrystallization always leads to the red emissive form irrespective of the solvent used. This fact hints that the change in emission colour should be associated with change in the aggregated states, as the dilute solution of all the compounds shows the same absorption and emission spectra (Figure 5.1.16)). We have compared the PXRD patterns of PyS (PyS-G, PyS-Y and PyS-R) powders (Figure 5.1.17), to similar PXRD patterns. Also, One of the PyS (PyS-R) powders with the simulated powder pattern (from single crystal data) observed that all the peaks matched in both forms (Figure 5.1.18). This observation neglects the possibility of polymorphs. Further, we compared the photophysical properties of PyS-Y, the ground form of PyS-Y(Ground) and PyS-G. In the case of PyS-Y absorbance peaks λ_{abs} at 336 nm, 380 nm and additionally, red-shifted absorption band at ~480 nm was observed. The same compound shows the emission spectrum with λ_{max}, 544nm @excitation 380nm. On grinding of PyS-Y with a mortar pestle, a green emissive compound was obtained which showed a red-shifted absorption (~380nm) and an emission maximum (λ_{em} ~500 nm). Although the emission profile and the maxima (λ_{max}, ~500) are almost matching with the green compound prepared from the solution, but a distinct absorbance difference is observed (Figure 5.1.19) in-ground form of PyS-Y (green) and synthesized green (PyS-G).
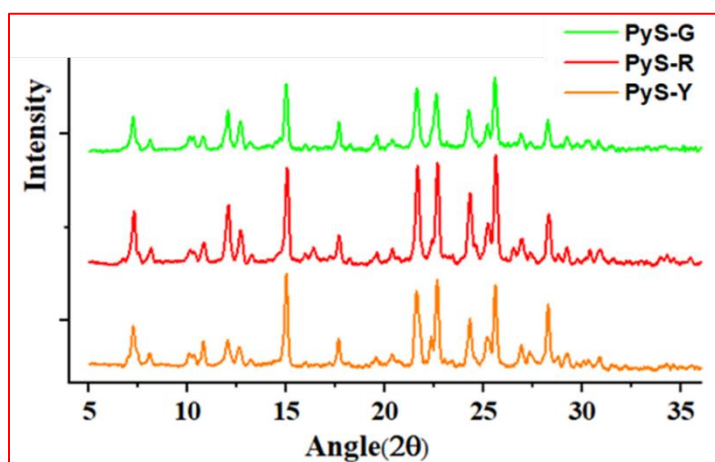
Figure 5.1.17 PXRD diagrams of PyS-G, PyS-Y and PyS-R samples

Table 5.1.2 Crystallographic data for PyS-G, PyS-Y and PyS-R

Crystal data of PyS-G

Identification code   PyS-G
Empirical formula $C_{22}H_{14}OS$
Formula weight   326.39
Temperature/K   298K
Space group   P21/n
a/Å   14.9740(5)
b/Å   21.4386(6)
c/Å   15.6550(6)
α/°   90
β/°   110.492(4)
γ/°   90
Volume/Å^3 4707.6(3)
Z   12
ρ_{calc}g/cm^3 1.382
μ/mm^{-1} 0.211
F(000)   2040.0

Crystal data of PyS-Y

Identification code   PyS-Y
Empirical formula $C_{22}H_{14}OS$
Formula weight   326.39
Temperature/K   298K
Space group   P21/n
a/Å   14.989(2)
b/Å   21.458(2)
c/Å   15.650(2)
α/°   90
β/°   110.322(16)
γ/°   90
Volume/Å^3 4720.3(3)
Z   12
ρ_{calc}g/cm^3 1.378
μ/mm^{-1} 0.210
F(000)   2040.0

Crystal data of Red emitting product

Identification code   PyS-R
Empirical formula $C_{22}H_{14}OS$
Formula weight   326.39
Temperature/K   298K
Space group   P21/n
a/Å   15.0076(6)
b/Å   21.4845(7)
c/Å   15.6667(6)
α/°   90
β/°   110.541(5)
γ/°   90
Volume/Å^3 4730.3(3)
Z   12
ρ_{calc}g/cm^3 1.375
μ/mm^{-1} 0.210
F(000)   2040.0

Figure 5.1.18 PXRD of PyS-R in powder and simulated form single crystal data
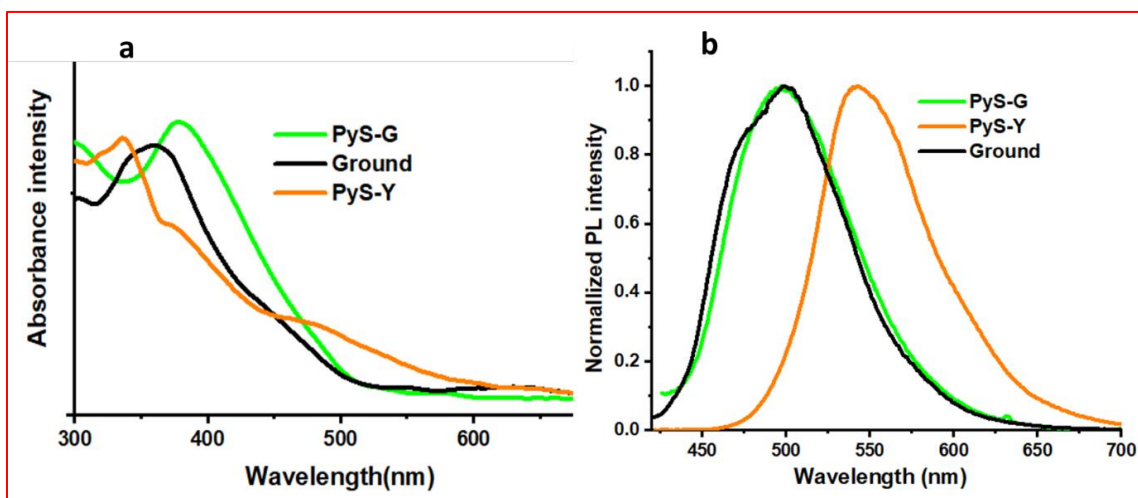
Figure 5.1.19 a) Absorption spectra of (PyS-Y), PyS-G and ground form of PyS-Y(Ground), (**b**) Emission spectra of pristine powder (PyS-Y), ground form of PyS-Y (Ground) and synthesized green emissive (PyS-G

In order to get a deeper understanding of the nature of the excited states involved in the emission, we have undertaken a computational study for the PyS molecule, and the trimers found in the crystal structure using Time-Dependent Density Functional Theory (see Figure 5.1.20). The

calculations reveal that the most stable conformer of the PyS molecule has a strongly absorbing first excited singlet state, S_1, with a vertical transition energy of 3.96 eV. This electronic state corresponds to a HOMO-to-LUMO transition with π-π* character centered on the pyrene moiety and a slight charge transfer character from the pyrene to the thiophene unit (see figure 5.1.13 for molecular orbitals). According to our results, the S_1 state is responsible for the lowest-energy band observed in the experimental UV/Vis absorption spectra in solution (Figure 5.1.16). We did not find any significant differences in the excited states of the remaining three conformers. To gain further insight into the optical properties in the solid state, we calculated the trimer of the crystal structure shown in Figure 5.1.12. According to our calculations, the vertical excitation energy of the brightest lowest-lying transition is 3.98 eV, which is very similar to that of the PyS monomer, suggesting that the excitation mainly corresponds to a local π-π* transition on each monomer. Inspection of the molecular orbitals involved in the transition indeed confirms the local nature of the excitation, with no strong net charge transfer between the neighbouring molecules.
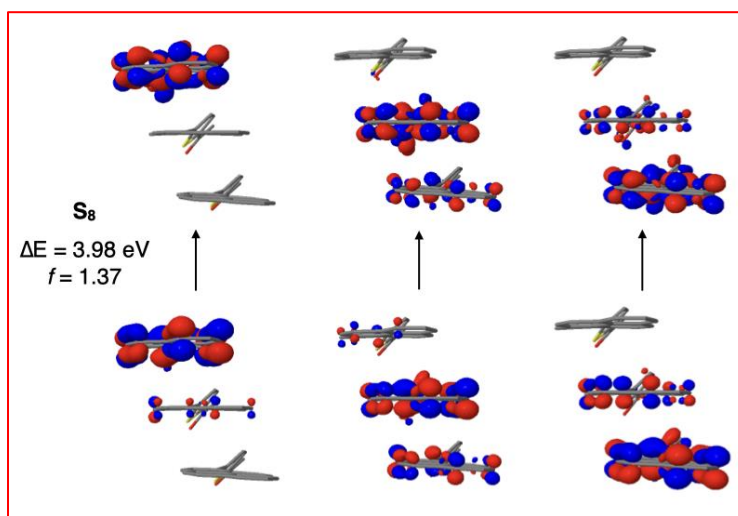
Figure 5.1.20 Main occupied-to-virtual molecular orbital contributions responsible for the brightest lowest-energy singlet excited state of the PyS trimer from the experimental crystal structure
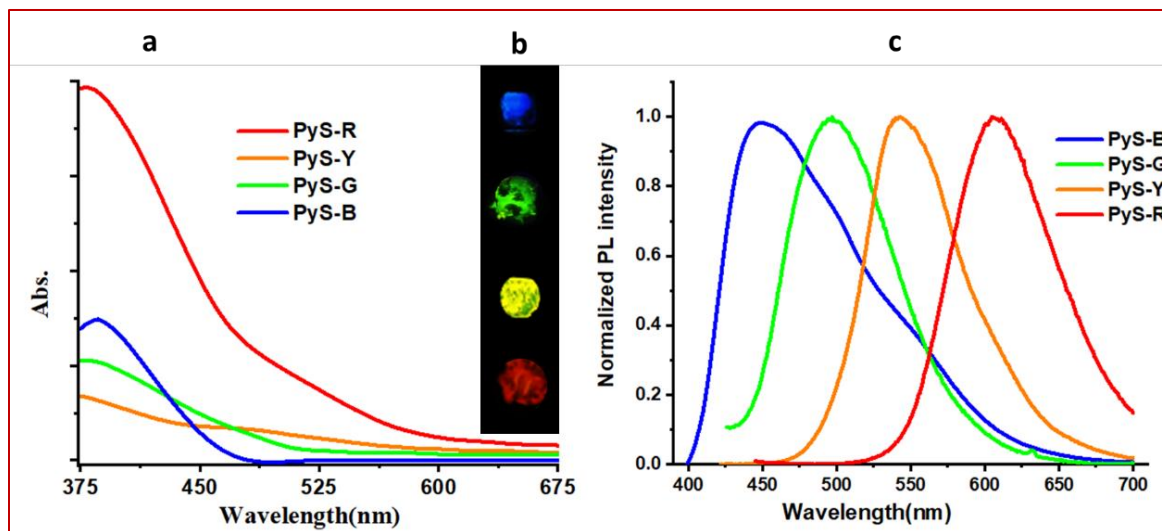
Figure 5.1.21 (a) UV-visible spectra of PyS (blue, green, yellow, and red) compounds in solid state. (b) The emission colour of PyS compounds (2mg/ml in DCM of different colour products deposited on glass coverslip by drop casting) under UV light (365 nm). (c) PL spectra of PyS (PyS-B, PyS-G, PyS-Y and PyS-R) compounds in solid state

To analyse the absorption and emission properties of all four forms, thin films were prepared in dichloromethane (2mg/ml) by the drop-casting technique on the surface of a glass coverslip. The films were dried in a vacuum at 50 ^{0}C for 8 h. The images of the dried films were taken under excitation by a UV lamp (365 nm) (Figure 5.1.21, b). UV absorption and photoluminescence (PL) spectra of dried films were recorded as shown in Figure 5.1.21. The absorption spectra showed a gradual and significant, red-shifted band edge absorption observed, their corresponding energy gap was calculated by using UV−VIS diffuse-reflectance spectroscopy (DRS). It was observed band gap energy for PyS-B, PyS-G, PyS-Y and PyS-R are 2.80 eV, 22.69 eV, 2.36 eV and 2.16 eV respectively (Figure 5.1.22). The bathochromically shifted emission peaks are observed at 450 nm, 498 nm, 543 nm, and 608 nm for PyS-B, PyS-G, PyS-Y and PyS-R, respectively.
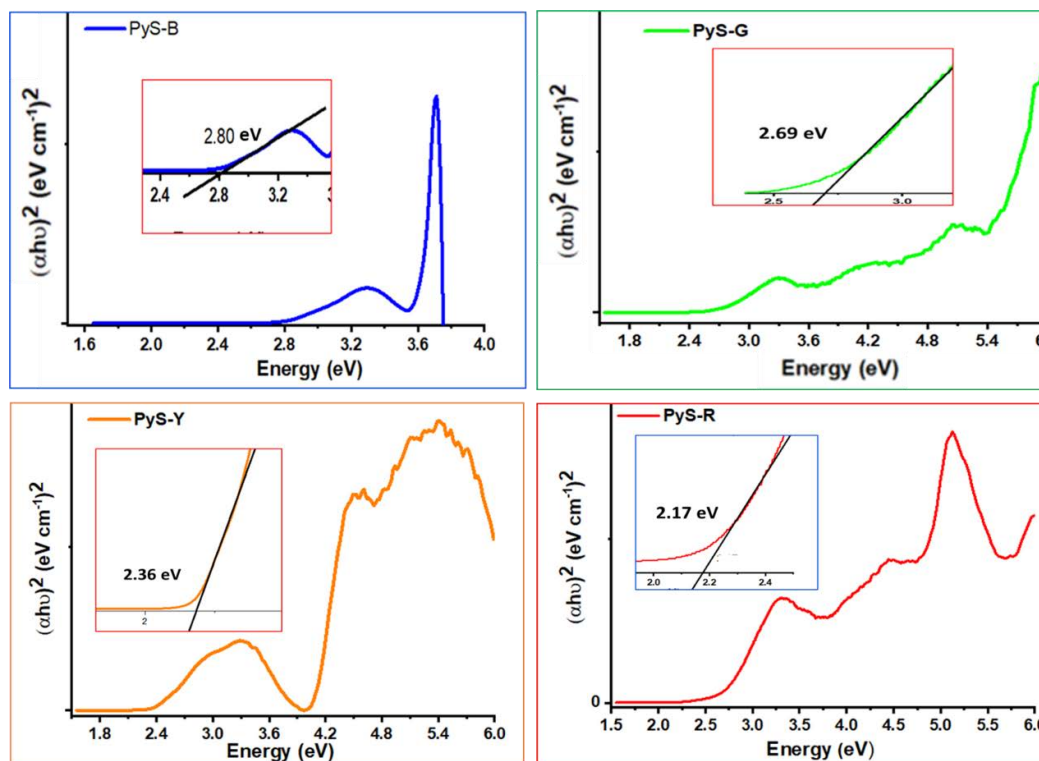
Figure 5.1.22 UV−vis DRS spectra of all forms of PyS (PyS-B, PyS-G, PyS-Y and PyS-R) samples (inset- determination of the optical band gap)

The measured excited state lifetime is triexponential for all the cases (Table 5.1.3). The average excited state lifetime is sequentially observed with increasing order with 1.0, 14.0, 16.0 and 18.0 ns for PyS-B, PyS-G, PyS-Y and PyS-R, respectively. The absorption, emission and lifetime data support the formation of J-aggregation. The crystal packing of PyS-R supports the head-to-tail arrangement, Figure 5.1.23. It is to be noted that the separation of the consecutive absorption, emission, and lifetime data (e.g., λ_{abs} (PyS-B) - λ_{abs} (PyS-G) and λ_{abs} (PyS-Y) - λ_{abs} (PyS-G) etc) is increased sequentially. The four isometric compounds were formed as a function of reaction time from the same reaction mixture. These facts convince us that the extent of J – aggregation increases across the sequentially obtained four compounds (PyS-B → PyS-G → PyS-Y → PyS-R).[59-63] Furthermore, we have performed concentration-dependent lifetime experiments for PyS-Y in an ethanol and toluene mixture (1:2) and observed that the excited state lifetime increases with increasing concentration (figure 5.1.24, d). The trend for this lifetime shows a similar trend as found for solid-state samples obtained with different reaction time. `
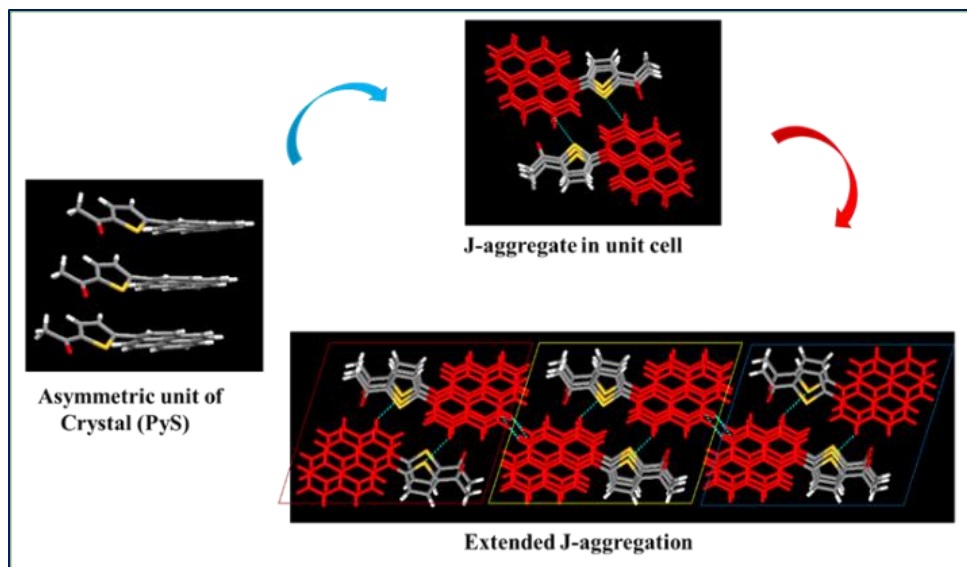
Figure 5.1.23 Representation of crystal packing of PyS showing the J-aggregation
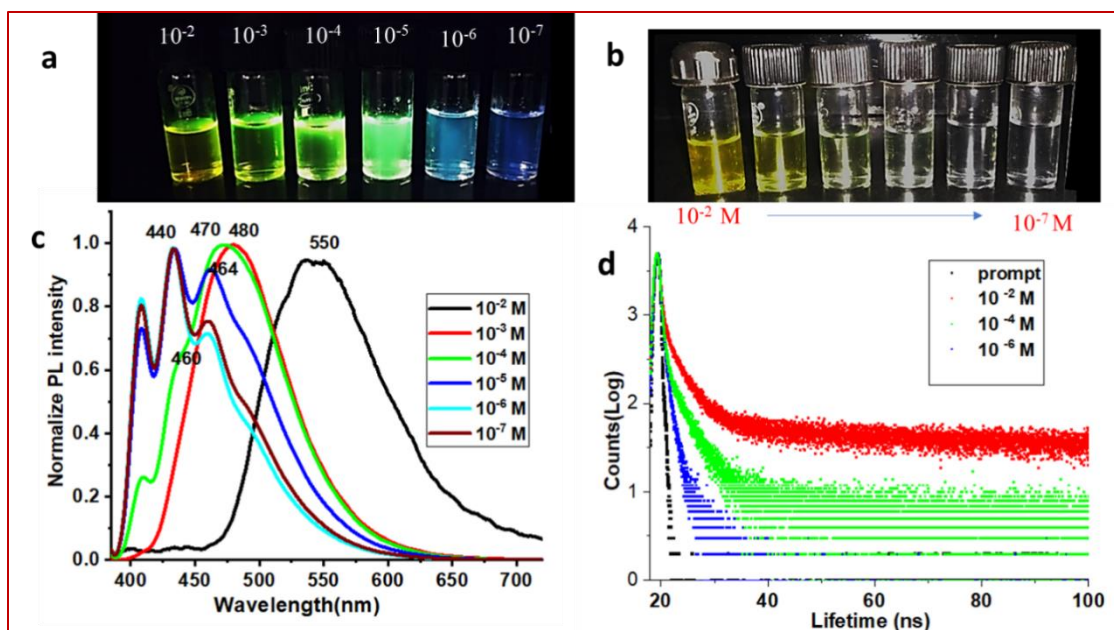
Figure 5.1.24 (a) Image of PyS-R solutions at different concentrations (from 10^{-2} M to 10^{-7} M from left to right) in toluene and ethanol (2:1) under excitation by a UV lamp (365 nm). (b) Daylight emission of PyS-R solutions at different concentrations. (c) PL spectra of PyS-R at the same concentrations as shown in the fluorescence image in (a). (d) Lifetime measurements of PyS-R in ethanol, toluene (1:2) solution at different concentrations (10^{-2} M (5 ns), 10^{-4} M (3 ns) and 10^{-6} M (1 ns))

Table 5.1.3 Solid state emission wavelength, quantum yield and excited state lifetime with components including the relative amplitude (a, b, and c in percentages) for the four different samples of PyS.

Entry	Λ_{em} (nm)	Φ_F (%)	τ1(ns), a (%)	τ2(ns), b(%)	τ3(ns), c(%)	$\langle\tau\rangle$ (ns)	$\chi2$
PyS-B	524	4.01	0.27, 55.87	0.54, 30.81	1.08, 13.32	1.0	1.16
PyS-G	583	7.9	0.48, 45.39	2.07, 35.57	5.63, 19.04	14	1.04
PyS-Y	590	11.8	0.55, 36.67	2.08, 42.93	6.59, 20.40	16	1.08
PyS-R	600	16.0	0.68, 29.54	2.09, 48.04	7.00, 22.42	18	1.18
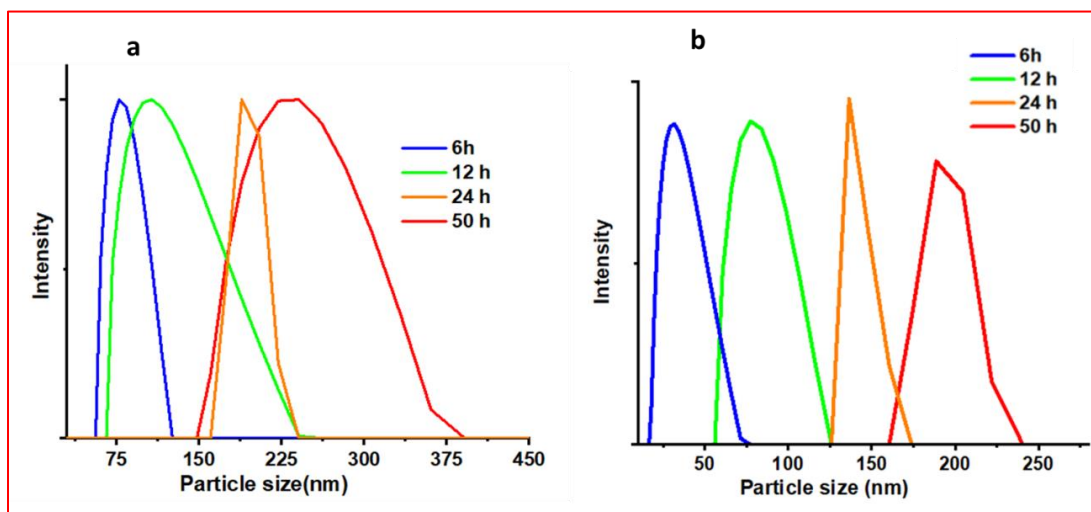
Figure 5.1.25 Particle size analysis from DLS measurement for PyS from the direct reaction mass (RM) collected at 6h, 12h, 24h and 50h time intervals and from the isolated pure products collected at the same time intervals (isolated pure compounds dissolved in Ethanol/Toluene (1:2) to record DLS)(average particle sizes found from the RM: @6h, 80 nm, @12h, 150 nm, @24h, 190 nm and @50h, 250 nm. (b) Average particle sizes from the isolated pure product: @6h, 32 nm, @15h, 82 nm, @24h, 140 nm and @50h product, 195 nm

Solid state emission wavelengths, quantum yields, and the excited state lifetimes of PyS in the four different forms are gathered in Table 5.1.3). We are eager to know the particle size (aggregates formed) of the species formed in the reaction mixture (just after preparing the compounds and before purification) during the course of the reaction at the specified time intervals (reaction time for the four products, 6th h; 12th h; 24th h and 50th h). The observed particle sizes with increasing

the reaction time increases i.e., 80, 150, 190 and 250nm, at 6th, 12th, 24th and 50th h, respectively. As all the compounds were isolated by column chromatography, the particle size may be affected during the purification process. Thus, it is required to check the sizes of these compounds obtained after purification. The isolated pure solid products were dissolved in the same solvent system used (during the reaction; ethanol/ toluene mixture) and then recorded the DLS measurement. We observed that the average particle sizes are 32, 82, 140 and 195 nm, respectively (figure 5.1.25). On comparing the sizes of these two sets, it is observed that the decrement of sizes about ~50 nm for the case of pure product, which is expected as de-aggregation might be occurring partly because of the treatment of the species during purifications. It is also observed that the increasing trend for the size of the aggregates remained the same with increasing reaction time.

This observation supports that the particles intact their aggregation behaviour even after the purification process. To understand the stability of the particles in solution, we have arbitrarily chosen two pure compounds (PyS-G and PyS-R), and these were separately dissolved in an ethanol/toluene mixture at varying times. On comparing the time-dependent emission spectra of this solution (up to 9th h of preparing the solution), it was observed that the maximum emission wavelength remained the same (figure 5.1.26).
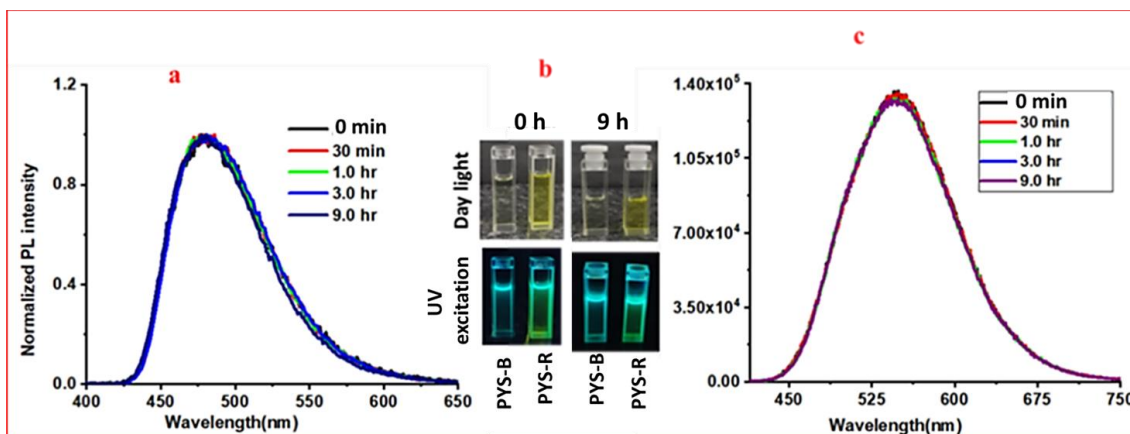
Figure 5.1.26 Fluorescence spectra of the isolated pure product of PyS-G(a) and PyS-R(c) in ethanol/toluene (1:2) 10^{-3} M with time; the recorded emission spectra of the red and green species at variable time. (b) It shows emission colours in daylight and Under UV excitation of 365 nm for initial (0 min) and after 9 h time (Insect image) for PyS-B and PyS-R

To analyse the morphology of all four isolated products, it was performed FESEM study (Figure 5.1.27) of all the PyS compounds. In the case of PyS-B, the particles are linearly arranged forming one-dimensional arrays (Figure 5.1.26, PyS-B). At the molecular level, it is observed from the

crystal packing arrangement (Figure 5.1.12 and Figure 5.1.28), a strong C-H…π interaction (2.82 Å) between the hydrogen atom on the thiophene ring with the pyrene fragment of a neighbouring molecule, and the other side, an interaction between the terminal methyl hydrogen atom of the acetyl group of one molecule with one of the hydrogen atoms on the pyrene fragment (2.365 Å) of another molecule, leading to the formation of linear chains of PyS parallel to the crystal *c* axis.
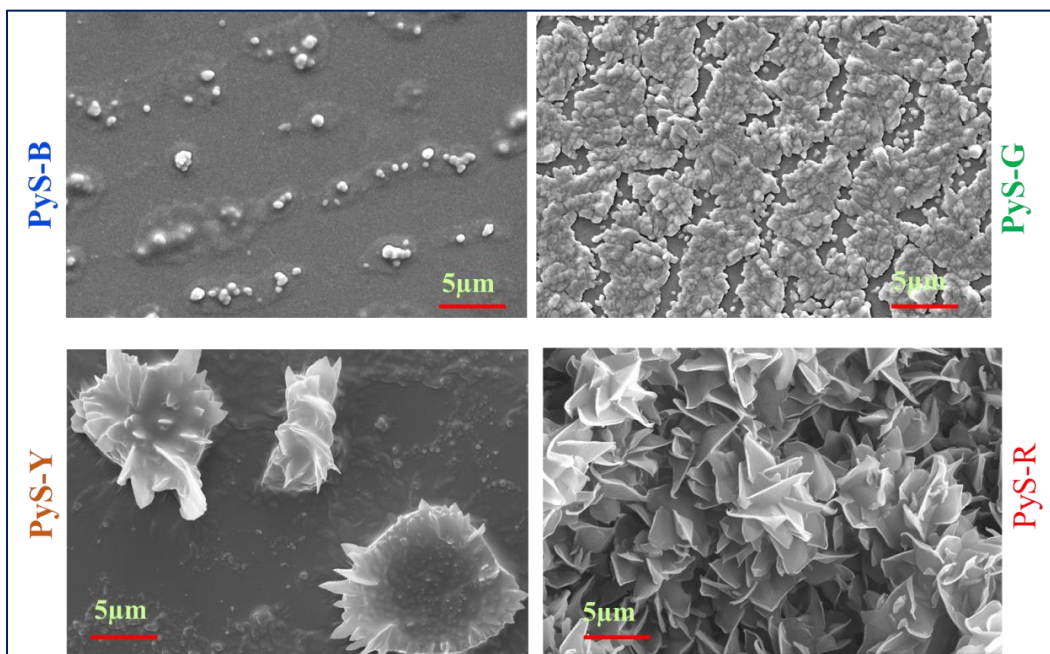
Figure 5.1.27 FESEM images of PyS-B, PyS-G, PyS-Y, and PyS-R samples
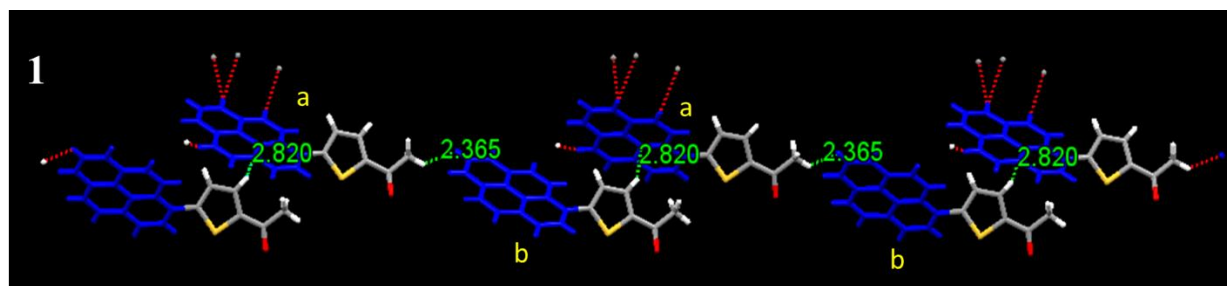
Figure 5.1.28 Crystal packing of PyS in the PyS-Y crystals, highlighting different interactions that might be involved in the morphological evolution of aggregates. In **1,** the formation of chains through the interaction of a thiophene ring hydrogen with pyrene π-electrons (C-H…π interactions, 2.820 Å) in a neighbouring molecule and interaction between the terminal methyl hydrogen of the acetyl group of one molecule with a hydrogen atom of the pyrene fragment (2.365 Å) of another molecule

The formation of discrete trimers and hexamers and their arrangement in linear chains through these interactions seem to be playing a significant role as the driving force towards the formation of the linear arrangements of particles observed from FESEM at the early stages of product formation (Figure 5.1.27, PyS-B). Moving towards PyS-G, the product obtained for reaction times between 12-14 h, the FESEM image (Figure 5.1.27, PyS-G) shows surface particles aligned in a more uniform two-dimensional sheet-type arrangement formed by gradual growing and coalescence of the one-dimensional aggregates found for shorter reaction times. In the case of PyS-Y, the product found for reaction times between 20-24 h, the FESEM image shows a morphology with discrete 3D flowers (Figure 5.1.27). The morphology for the final product, PyS-R, was found that of a closely packed, uniform, and well-ordered array of condensed flowers.
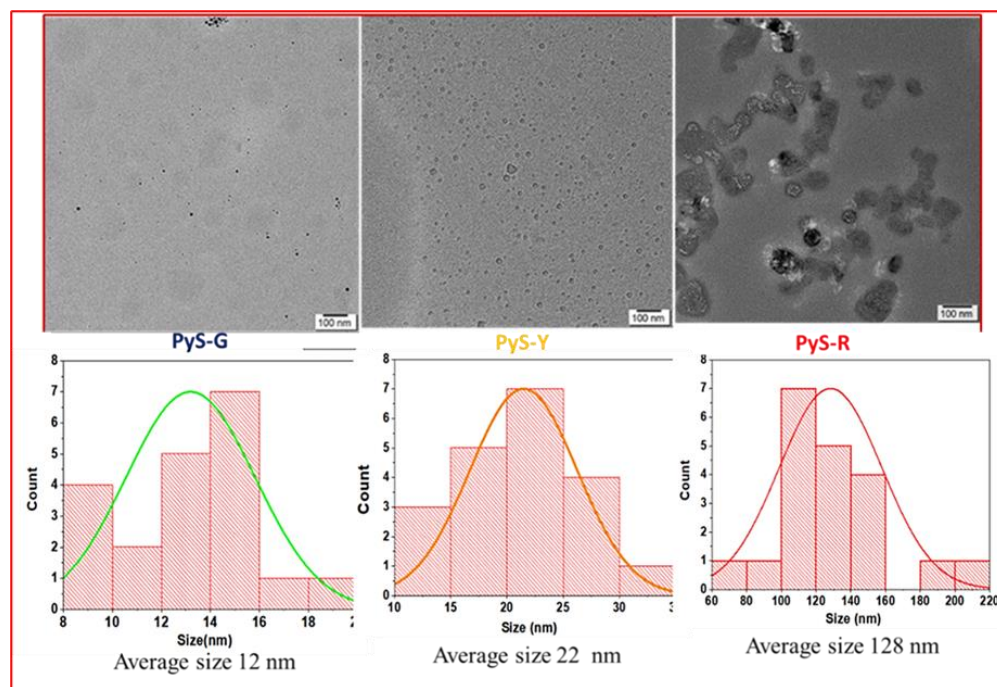
Figure 5.1.29 Average particle size and distribution from HRTEM images of PyS-G, PyS-Y, and PyS-R samples

To know the size of the particles in all three forms (PyS-G, PyS-Y, and PyS-R), we undertook an additional HRTEM analysis (Figure 5.1.29). The HRTEM study reveals the presence of spherical particles with an average particle size of ~12 nm for PyS-G and round particles with an average particle size of ~22 nm for PyS-Y. A densely packed array of aggregates with an average particle size of ~128 nm is observed for the PyS-R variety (Figure 5.1.29). From these observations, it is

concluded that with time, particles approach each other forming a closely packed aggregate. Further, to check the emission and the size of the aggregates formed in the solution, we have performed a concentration-dependent emission study and particle size analysis for a PyS-R sample dissolved in an ethanol/toluene (1:2) mixture.
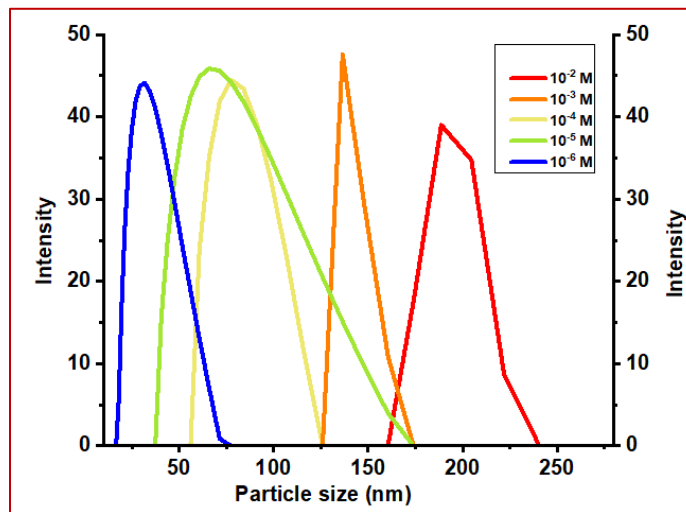
Figure 5.1.30 Particle size analysis of PyS-R in ethanol-toluene (1:2) solutions at different concentrations (10^{-2} M to 10^{-6} M)

This experiment shows that PyS-R exhibits a bathochromic concentration-dependent emission shift (Fig. 5.1.24, c) and that the particle size increases with increasing concentration (Figure 5.1.30). This study also convinces us that with increasing concentrations, bigger aggregates are formed in the solution resulting in a bathochromic emission shift.

5.1.4 CONCLUSION

Pyrene-thiophene containing simple organic compound was synthesized from a Suzuki coupling reaction. The initially blue emitting compound in a reaction mixture is sequentially transformed into three other emissive compounds (green, yellow, red), just simply allowing the reaction for a longer time. The observed colour tunability resulted from the growth of aggregates (nano to micro) with different morphologies and sizes, which were supported by FESEM and HRTEM analysis. It was found that the initially formed 1D particles slowly converted into a 2D sheet. This is further transformed into 3D hierarchical self-assembled flower-based architecture. On allowing the same reaction for a longer time (~40h), the morphology finally evolves into an array of condensed

flowery structures. It is well known that the inorganic quantum dots (e.g., Au, CdSe etc), contrary to the organic fluorophores exhibit size-dependent tunable emission. A similar property i,e, the size (and morphology) dependent tunable emission has also been observed by the organic fluorophore. This finding will open a new direction for obtaining controlled tunable emission in the visible range from a single organic fluorophore.

5.1.5 REFERENCES

1. Devi, P.; Thakur, A.; Chopra, S.; Kaur, N.; Kumar, P.; Singh, N.; Kumar, M.; Shivaprasad, S. M.; Nayak, M. K., Ultrasensitive and selective sensing of selenium using nitrogen-rich ligand interfaced carbon quantum dots. *ACS applied materials & interfaces* **2017,** *9* (15), 13448-13456.

2. Lu, W.; Jiao, Y.; Gao, Y.; Qiao, J.; Mozneb, M.; Shuang, S.; Dong, C.; Li, C.-z., Bright yellow fluorescent carbon dots as a multifunctional sensing platform for the label-free detection of fluoroquinolones and histidine. *ACS Applied Materials & Interfaces* **2018,** *10* (49), 42915-42924.

3. Wu, D.; Gong, W.; Yao, H.; Huang, L.; Lin, Z.; Ling, Q., Highly efficient solid-state emission of diphenylfumaronitriles with full-color AIE, and application in explosive sensing, data storage and WLEDs. *Dyes and Pigments* **2020,** *172*, 107829.

4. Feng, Q.; Wang, M.; Dong, B.; He, J.; Xu, C., Regulation of arrangements of pyrene fluorophores via solvates and cocrystals for fluorescence modulation. *Crystal growth & design* **2013,** *13* (10), 4418-4427.

5. Jiang, W.; Shen, Y.; Ge, Y.; Zhou, C.; Wen, Y.; Liu, H.; Liu, H.; Zhang, S.; Lu, P.; Yang, B., A single-molecule conformation modulating crystalline polymorph of a physical π–π pyrene dimer: blue and green emissions of a pyrene excimer. *Journal of Materials Chemistry C* **2020,** *8* (10), 3367-3373.

6. Yan, D.; Evans, D. G., Molecular crystalline materials with tunable luminescent properties: from polymorphs to multi-component solids. *Materials Horizons* **2014,** *1* (1), 46-57.

7. Lu, B.; Liu, S.; Yan, D., Recent advances in photofunctional polymorphs of molecular materials. *Chinese Chemical Letters* **2019,** *30* (11), 1908-1922.

8. Brittain, H. G., Polymorphism in pharmaceutical solids. *Drugs and the pharmaceutical sciences* **1999,** *95*, 183-226.

9. Jones, J. D., Putting knowledge of plant disease resistance genes to work. *Current opinion in plant biology* **2001,** *4* (4), 281-287.

10. Poornima, R.; Prasad, K. N.; Yathindra, H.; Jois, S. N., Influence of pranic agriculture on morphological traits, chlorophyll content and genetic polymorphism of ridge gourd (Luffa acutangula L. Roxb.) assessed by RAPD marker analysis. *AGRIVITA, Journal of Agricultural Science* **2020,** *42* (3), 521-532.

11. Susca, A.; Stea, G.; Perrone, G., Rapid polymerase chain reaction (PCR)-single-stranded conformational polymorphism (SSCP) screening method for the identification of Aspergillus section Nigri species by the detection of calmodulin nucleotide variations. *Food Additives and Contaminants* **2007,** *24* (10), 1148-1153.

12. Salih, A.; Larkum, A.; Cox, G.; Kühl, M.; Hoegh-Guldberg, O., Fluorescent pigments in corals are photoprotective. *Nature* **2000,** *408* (6814), 850-853.

13. Ma, Y. J.; Xiao, G.; Fang, X.; Chen, T.; Yan, D., Leveraging Crystalline and Amorphous States of a Metal-Organic Complex for Transformation of the Photosalient Effect and Positive-Negative Photochromism. *Angewandte Chemie* **2023,** *135* (11), e202217054.

14. Ito, S., Luminescent polymorphic crystals: mechanoresponsive and multicolor-emissive properties. *CrystEngComm* **2022,** *24* (6), 1112-1126.

15. Ito, S.; Nagai, S.; Ubukata, T.; Tachikawa, T., Multi-color mechanochromic luminescence of three polymorphic crystals of a donor–acceptor-type benzothiadiazole derivative. *CrystEngComm* **2021,** *23* (34), 5899-5907.

16. Huang, R.; Wang, C.; Tan, D.; Wang, K.; Zou, B.; Shao, Y.; Liu, T.; Peng, H.; Liu, X.; Fang, Y., Single-Fluorophore-Based Organic Crystals with Distinct Conformers Enabling Wide-Range Excitation-Dependent Emissions. *Angewandte Chemie International Edition* **2022,** *61* (41), e202211106.

17. Zheng, C.; Zang, Q.; Nie, H.; Huang, W.; Zhao, Z.; Qin, A.; Hu, R.; Tang, B. Z., Fluorescence visualization of crystal formation and transformation processes of organic luminogens with crystallization-induced emission characteristics. *Materials Chemistry Frontiers* **2018,** *2* (1), 180-188.

18. Tchoń, D.; Trzybiński, D.; Wrona-Piotrowicz, A.; Makal, A., Polymorphism and resulting luminescence properties of 1-acetylpyrene. *CrystEngComm* **2019,** *21* (38), 5845-5852.

19.   Biesen, L.; Müller, T. J. J., Solid-state emissive biphenylene bridged bisaroyl-S,N-ketene acetals as distinct aggregation-induced enhanced emitters and fluorometric probes. *Aggregate* **2021,** *2* (5), e105.

20.   Wang, Y.; Zhang, G.; Zhang, W.; Wang, X.; Wu, Y.; Liang, T.; Hao, X.; Fu, H.; Zhao, Y.; Zhang, D., Tuning the Solid State Emission of the Carbazole and Cyano-Substituted Tetraphenylethylene by Co-Crystallization with Solvents. *Small* **2016,** *12* (47), 6554-6561.

21.   Zhou, Z.; Ushakova, E. V.; Liu, E.; Bao, X.; Li, D.; Zhou, D.; Tan, Z.; Qu, S.; Rogach, A. L., A co-crystallization induced surface modification strategy with cyanuric acid modulates the bandgap emission of carbon dots. *Nanoscale* **2020,** *12* (20), 10987-10993.

22.   Sohi, T. H. H.; Maass, F.; Czekelius, C.; Suta, M.; Vasylyeva, V., Co-crystallization of organic chromophore roseolumiflavin and effect on its optical characteristics. *CrystEngComm* **2022,** *24* (41), 7315-7325.

23.   Saito, D.; Ogawa, T.; Yoshida, M.; Takayama, J.; Hiura, S.; Murayama, A.; Kobayashi, A.; Kato, M., Intense Red-Blue Luminescence Based on Superfine Control of Metal–Metal Interactions for Self-Assembled Platinum (II) Complexes. *Angewandte Chemie International Edition* **2020,** *59* (42), 18723-18730.

24.   Philp, D.; Stoddart, J. F., Self-assembly in natural and unnatural systems. *Angewandte Chemie International Edition in English* **1996,** *35* (11), 1154-1196.

25.   Whitesides, G. M.; Grzybowski, B., Self-assembly at all scales. *Science* **2002,** *295* (5564), 2418-2421.

26.   Nie, F.; Zhou, B.; Wang, K.-Z.; Yan, D., Highly tunable ultralong room-temperature phosphorescence from ionic supramolecular adhesives for multifunctional applications. *Chemical Engineering Journal* **2022,** *430*, 133084.

27.   Yan, D.; Bučar, D.-K.; Delori, A.; Patel, B.; Lloyd, G. O.; Jones, W.; Duan, X., Ultrasound-Assisted Construction of Halogen-Bonded Nanosized Cocrystals That Exhibit Thermosensitive Luminescence. *Chemistry – A European Journal* **2013,** *19* (25), 8213-8219.

28.   Zhong, H.; Li, L.; Zhu, S.; Wang, Y., Controllable self-assembly of thiophene-based π-conjugated molecule and further construction of pillar[5]arene-based host-guest white-light emission system. *Frontiers in Chemistry* **2022,** *10*.

29.   Li, H.; Wu, J.; Li, H.; Xu, Y.; Zheng, J.; Shi, Q.; Kang, H.; Zhao, S.; Zhang, L.; Wang, R., Designing π-conjugated polypyrene nanoflowers formed with meso-and microporous nanosheets

for high-performance anode of potassium ion batteries. *Chemical Engineering Journal* **2022,** *430*, 132704.

30.   Bhongale, C. J.; Chang, C.-W.; Diau, E. W.-G.; Hsu, C.-S.; Dong, Y.; Tang, B.-Z., Formation of nanostructures of hexaphenylsilole with enhanced color-tunable emissions. *Chemical physics letters* **2006,** *419* (4-6), 444-449.

31.   Li, N.; Liu, Y. Y.; Li, Y.; Zhuang, J. B.; Cui, R. R.; Gong, Q.; Zhao, N.; Tang, B. Z., Fine tuning of emission behavior, self-assembly, anion sensing, and mitochondria targeting of pyridinium-functionalized tetraphenylethene by alkyl chain engineering. *ACS applied materials & interfaces* **2018,** *10* (28), 24249-24257.

32.   Kazlauskas, K.; Miasojedovas, A.; Dobrovolskas, D.; Arbačiauskienė, E.; Getautis, V.; Šačkus, A.; Juršėnas, S., Self-assembled nanoparticles of p-phenylenediacetonitrile derivatives with fluorescence turn-on. *Journal of Nanoparticle Research* **2012,** *14*, 1-13.

33.   Boles, M. A.; Engel, M.; Talapin, D. V., Self-assembly of colloidal nanocrystals: From intricate structures to functional materials. *Chemical reviews* **2016,** *116* (18), 11220-11289.

34.   Jana, A.; Bai, L.; Li, X.; Ågren, H.; Zhao, Y., Morphology tuning of self-assembled perylene monoimide from nanoparticles to colloidosomes with enhanced excimeric NIR emission for bioimaging. *ACS Applied Materials & Interfaces* **2016,** *8* (3), 2336-2347.

35.   Gulyani, A.; Dey, N.; Bhattacharya, S., Tunable Emission from Fluorescent Organic Nanoparticles in Water: Insight into the Nature of Self-Assembly and Photoswitching. *Chemistry– A European Journal* **2018,** *24* (11), 2643-2652.

36.   Hou, J.-T.; Kwon, N.; Wang, S.; Wang, B.; He, X.; Yoon, J.; Shen, J., Sulfur-based fluorescent probes for HOCl: Mechanisms, design, and applications. *Coordination Chemistry Reviews* **2022,** *450*, 214232.

37.   Han, B.; Yan, Q.; Xin, Z.; Liu, Q.; Li, D.; Wang, J.; He, G., Color-tunable and bright nonconjugated fluorescent polymer dots and fast photodegradation of dyes under visible light. *Aggregate* **2022,** *3* (2), e147.

38.   Huang, G.; Li, Q.; Li, L.; Wang, E., Development of novel polymeric nanoagents and their potential in cancer diagnosis and therapy. *Frontiers in Chemistry* **2022,** *10*, 1569.

39.   Xu, Z.; Zhang, Z.; Jin, X.; Liao, Q.; Fu, H., Polymorph-Dependent Green, Yellow, and Red Emissions of Organic Crystals for Laser Applications. *Chemistry–An Asian Journal* **2017,** *12* (23), 2985-2990.

40.   Zhang, Z.; Xu, B.; Su, J.; Shen, L.; Xie, Y.; Tian, H., Color-Tunable Solid-State Emission of 2, 2′-Biindenyl-Based Fluorophores. *Angewandte Chemie International Edition* **2011,** *50* (49), 11654-11657.

41.   Liu, J.; Zhang, H.; Gong, H.; Zhang, X.; Wang, Y.; Jin, X., Polyethylene/polypropylene bicomponent spunbond air filtration materials containing magnesium stearate for efficient fine particle capture. *ACS applied materials & interfaces* **2019,** *11* (43), 40592-40601.

42.   Zhang, W.; Li, Y.; Zhang, H.; Zhou, X.; Zhong, X., Facile synthesis of highly luminescent Mn-doped ZnS nanocrystals. *Inorganic Chemistry* **2011,** *50* (20), 10432-10438.

43.   Xiao, L.; Sun, H., Novel properties and applications of carbon nanodots. *Nanoscale Horizons* **2018,** *3* (6), 565-597.

44.   Wang, L.; Li, W.; Yin, L.; Liu, Y.; Guo, H.; Lai, J.; Han, Y.; Li, G.; Li, M.; Zhang, J.; Vajtai, R.; Ajayan, P. M.; Wu, M., Full-color fluorescent carbon quantum dots. *Science Advances 6* (40), eabb6772.

45.   Makkar, M.; Viswanatha, R., Frontier challenges in doping quantum dots: synthesis and characterization. *RSC advances* **2018,** *8* (39), 22103-22112.

46.   Hardman, R., A toxicologic review of quantum dots: toxicity depends on physicochemical and environmental factors. *Environmental health perspectives* **2006,** *114* (2), 165-172.

47.   Turkoglu, G.; Cinar, M. E.; Ozturk, T., Thiophene-based organic semiconductors. *Sulfur Chemistry* **2019**, 79-123.

48.   Morris, W. A.; Butler, T.; Kolpaczynska, M.; Fraser, C. L., Stimuli responsive furan and thiophene substituted difluoroboron β-diketonate materials. *Materials chemistry frontiers* **2017,** *1* (1), 158-166.

49.   Zhang, R.; Wang, M.; Sun, H.; Khan, A.; Usman, R.; Wang, S.; Gu, X.; Wang, J.; Xu, C., Effect of configurational isomerism and polymorphism on chalcone fluorescent properties. *New Journal of Chemistry* **2016,** *40* (7), 6441-6450.

50.   Nirmala, M.; Vadivel, R.; Chellappan, S.; Malecki, J. G.; Ramamurthy, P., Water-Soluble Pyrene-Adorned Imidazolium Salts with Multicolor Solid-State Fluorescence: Synthesis, Structure, Photophysical Properties, and Application on the Detection of Latent Fingerprints. *ACS omega* **2021,** *6* (15), 10318-10332.

51.   Ikeya, M.; Katada, G.; Ito, S., Tunable mechanochromic luminescence of 2-alkyl-4-(pyren-1-yl) thiophenes: controlling the self-recovering properties and the range of chromism. *Chemical Communications* **2019,** *55* (82), 12296-12299.

52.   Cavallini, M.; Brucale, M.; Gentili, D.; Liscio, F.; Maini, L.; Favaretto, L.; Manet, I.; Zambianchi, M.; Melucci, M., Polymorph Separation by Ordered Patterning. *Molecules* **2022,** *27*.

53.   Li, W.; Yang, P.-P.; Wang, L.; Wang, H., Bis-pyrene based reversibly multi-responsive fluorescence switches. *Journal of Materials Chemistry C* **2015,** *3* (15), 3783-3789.

54.   Liu, H.; Gu, Y.; Dai, Y.; Wang, K.; Zhang, S.; Chen, G.; Zou, B.; Yang, B., Pressure-induced blue-shifted and enhanced emission: a cooperative effect between aggregation-induced emission and energy-transfer suppression. *Journal of the American Chemical Society* **2020,** *142* (3), 1153-1158.

55.   Tang, Y.; Tang, B. Z., *Aggregation-Induced Emission*. Springer: 2022.

56.   Liao, R.; Wang, X.; Peng, L.; Sun, H.; Huang, W., Achieving Organic Smart Fluorophores by Controlling the Balance between Intermolecular Interactions and External Stimuli. *ACS Applied Materials & Interfaces* **2021,** *13* (23), 27491-27499.

57.   Wang, Y.; Wang, L.; Zheng, H.; Li, K.; Andrzejewski, M.; Hattori, T.; Sano-Furukawa, A.; Katrusiak, A.; Meng, Y.; Liao, F., Phase transitions and polymerization of C6H6–C6F6 cocrystal under extreme conditions. *The Journal of Physical Chemistry C* **2016,** *120* (51), 29510-29519.

58.   Xie, Y.; Wang, X.; Han, X.; Xue, X.; Ji, W.; Qi, Z.; Liu, J.; Zhao, B.; Ozaki, Y., Sensing of polycyclic aromatic hydrocarbons with cyclodextrin inclusion complexes on silver nanoparticles by surface-enhanced Raman scattering. *Analyst* **2010,** *135* (6), 1389-1394.

59.   Zhang, Y.; Mollick, S.; Tricarico, M.; Ye, J.; Sherman, D. A.; Tan, J.-C., Turn-on fluorescence chemical sensing through transformation of self-trapped exciton states at room temperature. *ACS sensors* **2022,** *7* (8), 2338-2344.

60.   Yu, F.; Wang, M.; Sun, H.; Shan, Y.; Du, M.; Khan, A.; Usman, R.; Zhang, W.; Shan, H.; Xu, C., Tuning the solid-state fluorescence of chalcone crystals via molecular coplanarity and J-aggregate formation. *RSC advances* **2017,** *7* (14), 8491-8503.

61.   Xiong, T.; Zhang, Y.; Donà, L.; Gutiérrez, M.; Moslein, A. F.; Babal, A. S.; Amin, N.; Civalleri, B.; Tan, J.-C., Tunable fluorescein-encapsulated zeolitic imidazolate framework-8 nanoparticles for solid-state lighting. *ACS Applied Nano Materials* **2021,** *4* (10), 10321-10333.

62.	Más-Montoya, M.; Janssen, R. A., The effect of H-and J-aggregation on the photophysical and photovoltaic properties of small thiophene–pyridine–DPP molecules for bulk-heterojunction solar cells. *Advanced Functional Materials* **2017,** *27* (16), 1605779.

63.	Dimitriev, O. P.; Piryatinski, Y. P.; Slominskii, Y. L., Excimer emission in J-aggregates. *The journal of physical chemistry letters* **2018,** *9* (9), 2138-2143.

Chapter 5. Pyrene-thiophene Based Molecules for Stimuli-responsive Probes

Part B. 5.2 Precise Molecular Design for Twisted Pyrene-Thiophene Based Mechanofluorochromic Probes with Large Stokes' Shift and Feasibility Study Towards Security Ink and Re-writable Papers

5.2.1 INTRODUCTION

Mechanofluorochromic (MFC) materials are a class of smart stimuli-responsive materials in which the emission properties of the material change or respond upon the application of force/pressure, etc.[1] Organic mechanofluorochromic (MFC) materials (that change their emission under anisotropic and isotropic pressure) have attracted a great attention in recent years due to their promising applications in sensing pressure, storage devices, security inks, three-dimensional (3D) printing, etc.[2-5] Stimuli responsive materials with tunable emission and reversible switching are highly demanding for different applications, such as security encryption devices, deformation detectors, fluorescent probes, switches, and optoelectronic [6] The process of protein folding and unfolding, as well as the movement of cells, can be influenced by pressure in biology.[7] Due to the influence of the aggregation-caused quenching (ACQ) effect, most conventional organic chromophores exhibit weakened or even totally quenched emission in the aggregated state, which limits the development and application of mechanochromic luminescent materials to a greater extent.[8-9]

A new opportunity to overcome the ACQ problem and develop durable solid-state luminescent materials is presented through the generation of aggregation-induced emission (AIE) compounds.[10] Compounds possessing AIE properties are usually observed that the molecules having twisted geometry. This attribute allows for efficient emission in the aggregated state by preventing the close stacking of molecules. Moreover, the strongly twisted structure often results in a loose packing arrangement of molecules in the crystals, which makes

them sensitive to pressure stimulation. Stimuli-responsive organic materials with aggregation-induced emission (AIE) characteristics would be an interesting platform to explore the structure-property relationship for future designing MFC compounds. In several reports, it was observed that AIE active organic compounds exhibit distinct responses in emission properties upon mechanical grinding (anisotropic) and hydrostatic pressure (isotropic).[1] The isotropic force is applied uniformly by the diamond anvil cell (DAC). The mechanochromic luminescence performance of AIEgens can be explained as a synergetic processes associated with changing of molecular conformations, molecular packing forms, and intermolecular interactions.[11] In general, the photophysical properties of AIEgens will be affected by weak intermolecular interactions (such as C–H…π, C–H…O, and C–H…N hydrogen bonds), molecular packing and conformational change in the solid state.[6,12] The majority of mechanochromic luminescent materials have loose and metastable packing, which are believed to be critical factors in achieving structural transformation and pressure-dependent multicolor emissions. After grinding or compressing physically, these weak intermolecular interactions are altered, resulting in the variation of the stacking mode and the molecular conformation, and finally causing the emission color change.[13-15]

In 2012, Tian *et al.* [16] first reported mechanochromic luminescence of a 9,10-distyrylanthracene (DSA) derivative 9,10-bis[(E)-2-(pyridin-2-yl)vinyl]anthracene(BP2VA). This molecule showed extraordinary luminescence properties: grinding and applying external pressure changing the photoluminescence (PL) of BP2VA powder from green to red color. With the external pressure increasing from 0 to 8 GPa, the emission of BP2VA powder showed a gradual redshift from green (with a maximum at 528 nm) to red (with a maximum at 652 nm) distinctly, which is the greatest shift in mechanofluorochromic effect. In 2016, Zou *et al.*[17] reported the polymorphs, B-phase and G-phase, prepared from a cyano-substituted distyrylbenzene (CN-DSB), the molecular conformation changes under the hydrostatic pressure of 0.75 GPa from a highly twisted shape to a flat shape under external stimulation (color changes from blue to green). In 2019, Liu *et al.*[18] reported the mechanofluorochromism of the powder and single crystal of two compounds, photoacid-spiropyran(PASP) and tetraphenylethene-decorated photoacid-spiropyran(PASPTPE), under grinding and hydrostatic pressure. Both PASP and PASPTPE exhibited the mechanofluorochromic property under anisotropic grinding and isotropic atmospheric pressure color change from orange to red. Further contribution to MFC materials, including carbon nanodots, metal organic framework (MOF), covalent organic framework (COF), etc.[19-22]

Majority of high contrast solid-state MFC materials have tetraphenyl ethylene(TPE),[23-25] triphenylamine (TPA),[26-28] anthracene,[29-31] carbazole, phenothiazine, stilbene, spiropyrans etc. as their core structural unit.[32-37] Pyrene is a highly planar and conjugated molecule. Hence, it is prone to form a dimer structure due to strong π- π stacking at the aggregated state.[38-39] In 2020, Xiong *et al.*[12] synthesized (4-(phenothiazin-10-yl)phenyl)(pyren-1-yl)-methanone (Py–BP–PTZ), which exhibits AIEE, polymorphism, and mechanochromic properties. It shows gradual red-shifted emission under high pressure by DAC, the planar pyrene derivative changes emission mainly due to planarization under high pressure and change of molecular packing mode with changing intermolecular interactions. Very recently (2024), Eldhose *et al.*[40] reported MFC property of AIE active pyrene-based compounds and investigated the molecular packing and luminescence behaviour. Careful investigation of the crystal structures demonstrated abundant and intense intermolecular interactions, such as C-H…π and C-H…N hydrogen bonds, contributing to the remarkable mechanochromic luminescence performance of these compounds. Pyrene based molecules are enriched in optical properties because of a highly electron rich polyaromatic system. Some of the pyrene based materials with high contrast solid state emission are reported, still there are several challenges such as, poor yield pyrene based twisted compounds,[41-42] to control morphological modulation for changing emission, unclear chemical structure–MFC property relationships etc.[43-44]

In 2017, our group (Pasha *et al.*) reported an AIE active salicylaldehyde-based Schiff base which exhibited a reversible change of emission color gradually with applying pressure slowly.[45] The reported molecule (shown below) has twisted D-A-type features with ICT characteristics.
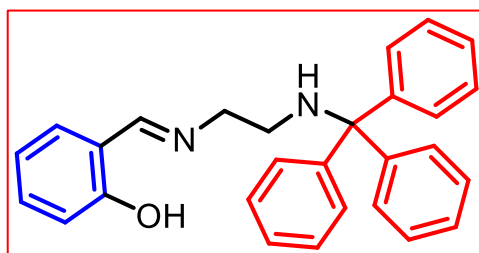
After analyzing the packing of the crystal structure, it was found that two molecules form a pair aligned in an opposite manner with a definite weak interaction across the two molecules. Each of the pairs are connected axially forming a long linear chain, and these chains are connected horizontally through intermolecular interactions resulting in a molecular sheet type of pattern. To determine the molecular structure which is responsible for demonstrating a

particular way of molecular arrangement described above, more study is required with consideration of appropriate molecular structure. Recently, the pyrene and acyl-thiophene connected a D-A type molecule [1-(5-(pyren-1-yl) thiophen-2-yl) ethan-1-one (PySY)] has been synthesized [46] and the observed dihedral angle is ~48° (pyrene and thiophene plane). The compound was found to be sensitive to shearing force (by grinding) with hypsochromic emission shifting (yellow to green). But it does not respond to mechanofluorochrism with applying pressure. To make the present compound sensitive towards pressure imposed mechanofluorochrism to mimic our previous work,[46] a four unit conjugated spacer attached to the thiophene side (of pyridine-acyl substituted thiophene) along with a photoactive species connected terminally. Here, two compounds (PySS and PySP) have been synthesized, studied their MFC property, and checked the feasibility in the data encryption-decryption and security ink.

5.2.2 EXPERIMENTAL SECTION

5.2.2.1 Synthesis of PySS and PySP and characterization

The synthetic scheme of pyrene thiophene-based compounds is summarized in scheme 5.2.1. Initially, 1-(5-(Pyren-1-yl)thiazol-2-yl)ethan-1-one (PyS) was synthesized by using an earlier method reported by our group.[46] For the second step, compound (PySS), PyS (0.3 gm, 0.92 mmol) in ethanol (4 ml) was stirred for 30 min at 50 ^{0}C and cooled to (10-15) ^{0}C, then to a clear solution of reaction mass NaOH (10% aq. solution, 1ml) was added slowly and further stirred the reaction mass for 10-15 min then added thiophene-2-aldehyde (0.155 gm, 1.38 mmol). Then the reaction mass was stirred for 10-12 hr at 40-50 °C. Slowly cooled the reaction mass temperature to RT, then water (3 ml) was added which resulted in precipitate formation, filtered the reaction mass, washed with chilled ethanol, and dried the obtained product for 12 hr. under vacuum. A dried product (350 mg, 90 % yield) was obtained. A similar process was followed to synthesize PySP. The synthesized compound was characterized by NMR and HRMS (Figure 5.2.1 to 5.2.9)
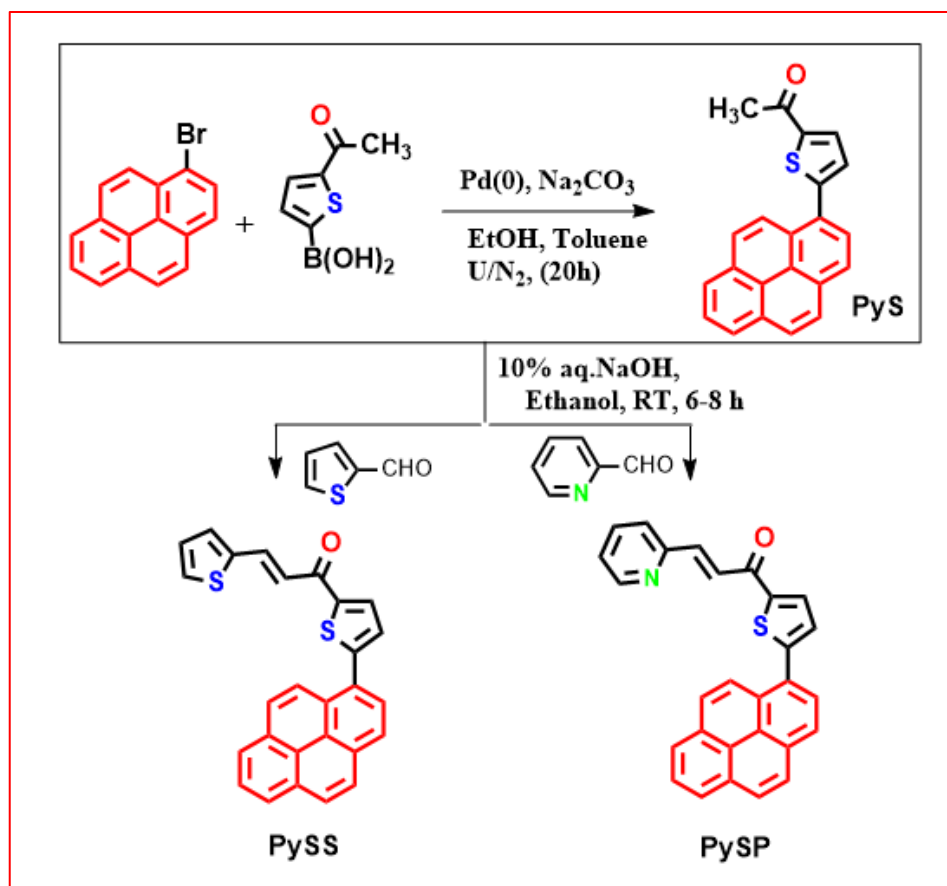
Scheme 5.2.1. Synthetic scheme for the compounds (PySS and PySP)

PyS (1-(5-(Pyren-1-yl) thiazol-2-yl) ethan-1-one)

^{1}H NMR (400 MHz, Chloroform-*d*) δ 8.48 (d, *J* = 9.3 Hz, 1H), 8.29 – 8.19 (m, 3H), 8.19 – 8.08 (m, 4H), 8.07 (t, *J* = 7.6 Hz, 1H), 7.86 (d, *J* = 3.8 Hz, 1H), 7.43 (d, *J* = 3.8 Hz, 1H), 2.68 (s, 3H). (see Fig 5.2.1).

^{13}C NMR (100 MHz, Chloroform-*d*) δ/ppm: 190.72, 151.54, 132.72, 131.77, 131.43, 130.85, 128.97, 128.91, 128.52, 128.37, 128.08, 127.28, 126.35, 125.76, 125.43, 124.65, 124.36, 26.74 (see Fig 5.2.2).

LC-HRMS (ESI): found m/z: 327.0837 [M + H] $^+$. calculated m/z: 326.0835 (see Fig 5.2.7).

PySS ((E)-1-(5-(pyren-1-yl) thiophen-2-yl)-3-(thiophen-2-yl) prop-2-en-1-one)

^{1}H NMR (400 MHz, Chloroform-*d*) δ 8.52 (d, *J* = 9.3 Hz, 1H), 8.25 (td, *J* = 7.9, 2.7 Hz, 3H), 8.15 (dd, *J* = 9.7, 7.2, 2.9 Hz, 4H), 8.12 – 8.03 (m, 2H), 8.01 (d, *J* = 3.9 Hz, 1H), 7.48 (dd, *J* =

4.4, 2.1 Hz, 2H), 7.43 (d, *J* = 3.6 Hz, 1H), 7.34 (d, *J* = 15.3 Hz, 1H), 7.15 (dd, *J* = 5.0, 3.6 Hz, 1H). (see Fig 5.2.3).

¹³C NMR (101 MHz, Chloroform-*d*) δ/ppm: 181.46, 151.62, 145.68, 140.29, 136.43, 132.21, 132.09, 131.76, 131.42, 130.85, 129.11, 128.93, 128.90, 128.60, 128.56, 128.44, 128.38, 128.15, 127.31, 126.36, 125.78, 125.45, 125.02, 124.71, 124.66, 124.43, 120.35 (see Fig 5.2.4).

LC-HRMS: found m/z: 421.0715 [M + H] ⁺, calculated m/z: 420.0643 (see Fig 5.2.8).

PySP (E)-1-(5-(pyren-1-yl)thiophen-2-yl)-3-(pyridin-2-yl)prop-2-en-1-one

¹H NMR (400 MHz, Chloroform-*d*) δ 8.75 (dt, *J* = 4.6, 1.5 Hz, 1H), 8.54 (d, *J* = 9.3 Hz, 1H), 8.29 – 8.21 (m, 3H), 8.20 – 8.10 (m, 5H), 8.13 – 8.03 (m, 2H), 7.90 (d, *J* = 15.1 Hz, 1H), 7.79 (td, *J* = 7.7, 1.8 Hz, 1H), 7.57 – 7.51 (m, 1H), 7.50 (d, *J* = 3.8 Hz, 1H), 7.35 (ddd, *J* = 7.6, 4.7, 1.2 Hz, 1H), (see Fig 5.2.5).

¹³C NMR (101 MHz, Chloroform-*d*) δ 182.13, 153.12, 152.26, 150.24, 145.72, 142.02, 136.98, 132.98, 131.79, 131.42, 130.85, 129.21, 128.91, 128.59, 128.57, 128.41, 128.16, 127.31, 126.38, 125.80, 125.76, 125.48, 125.16, 125.03, 124.73, 124.66, 124.52, 124.44 (see Fig 5.2.6).

LC-HRMS: found m/z: 416.1131 [M + H] ⁺, calculated m/z: 415.1031 (see Fig 5.2.9)**.**
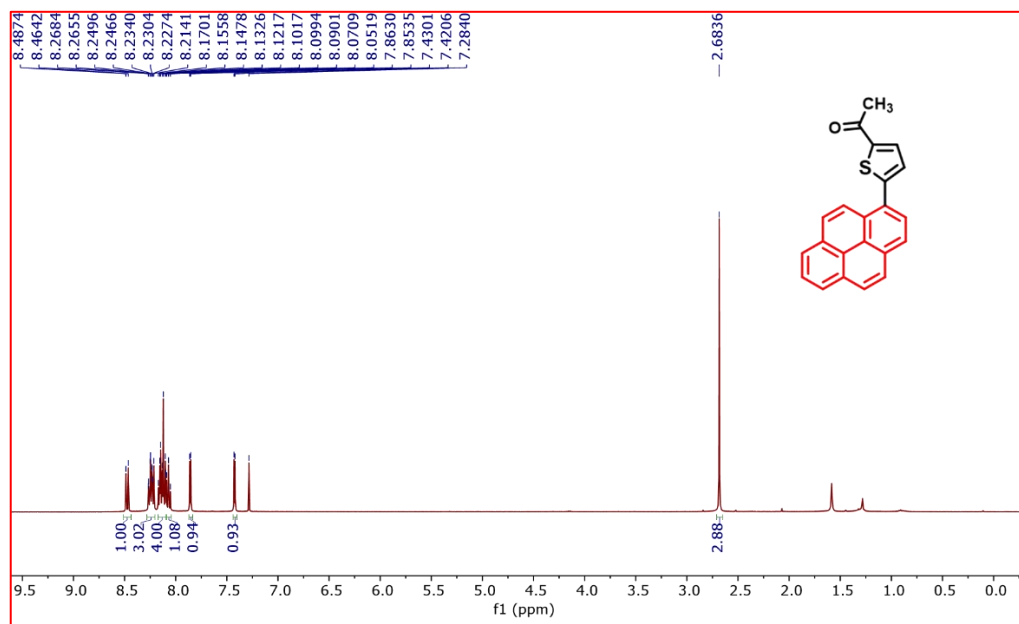
Figure 5.2.1 ¹H NMR spectra of PyS
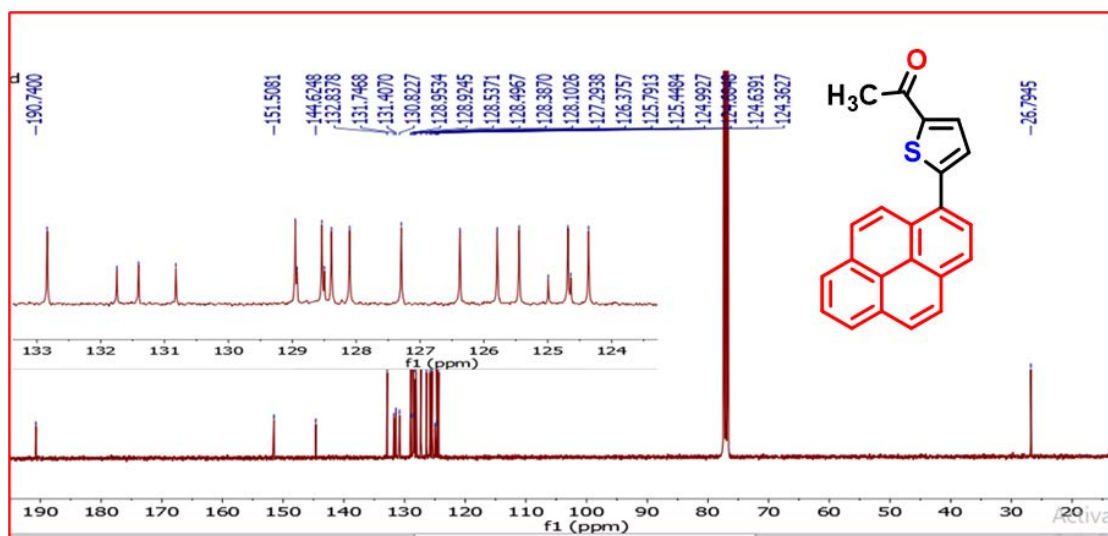
Figure 5.2.2 ^{13}C NMR spectra of PyS
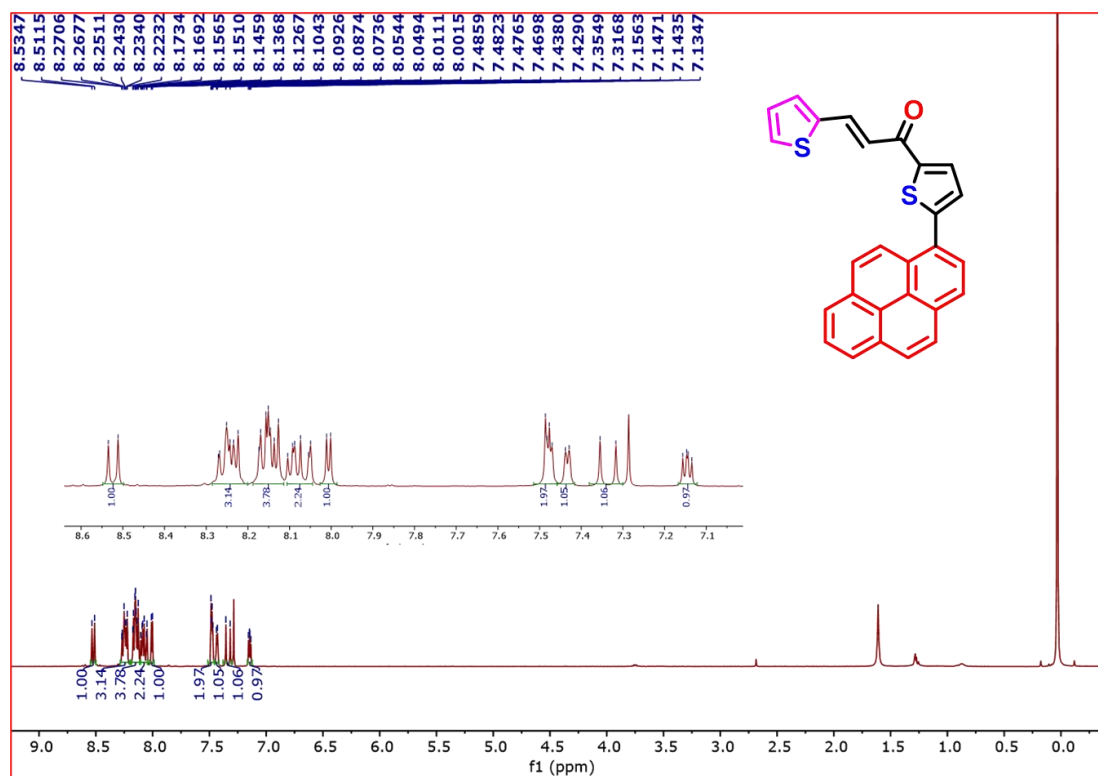
Figure 5.2.3 ^{1}H NMR of PySS
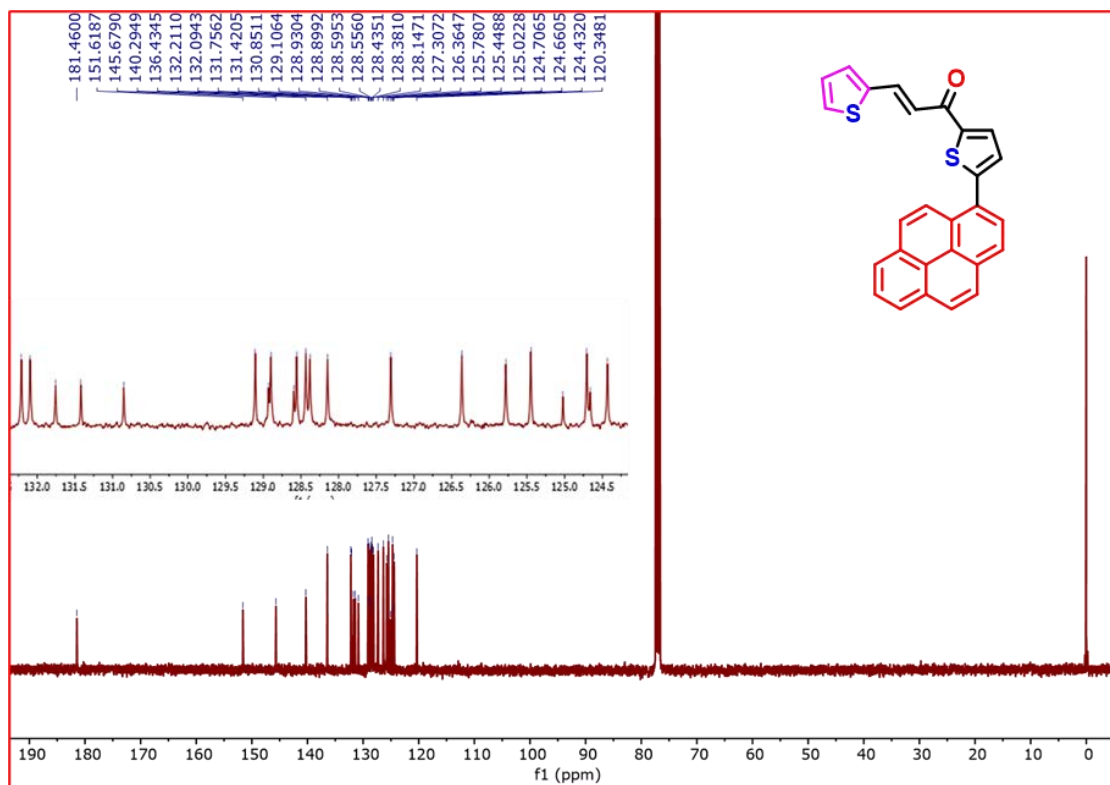
Figure 5.2.4 ^{13}C NMR of PySS
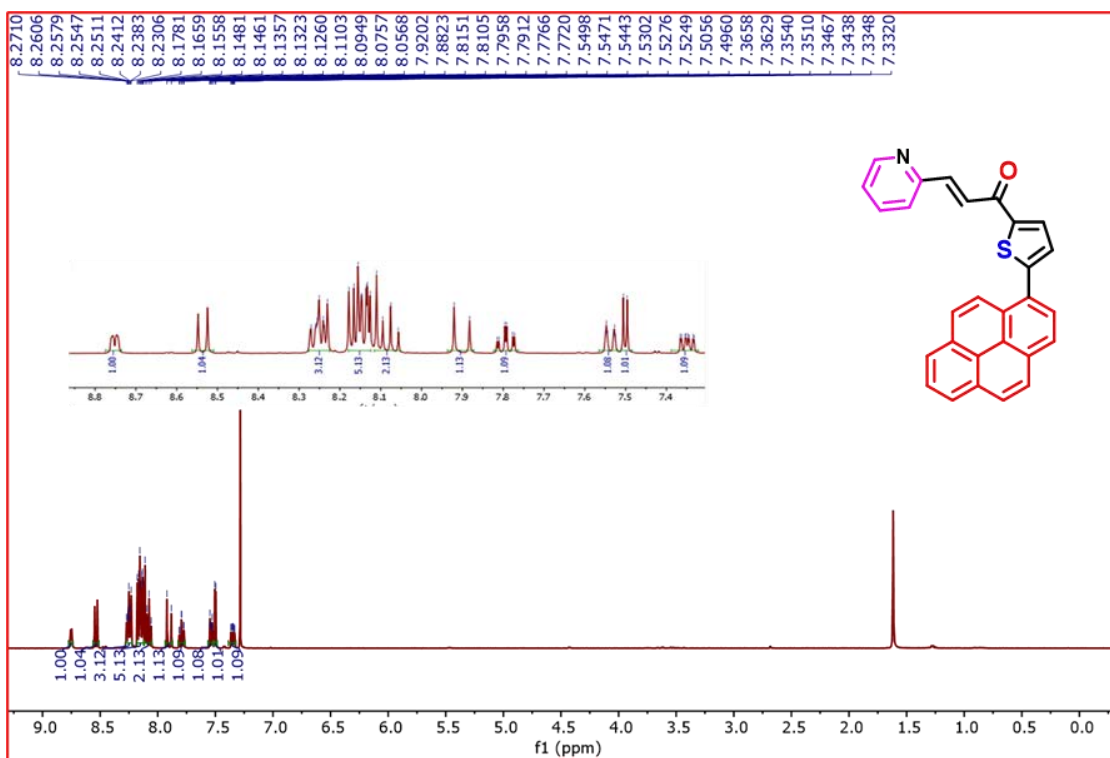
Figure 5.2.5 ^{1}H NMR spectra of PySP
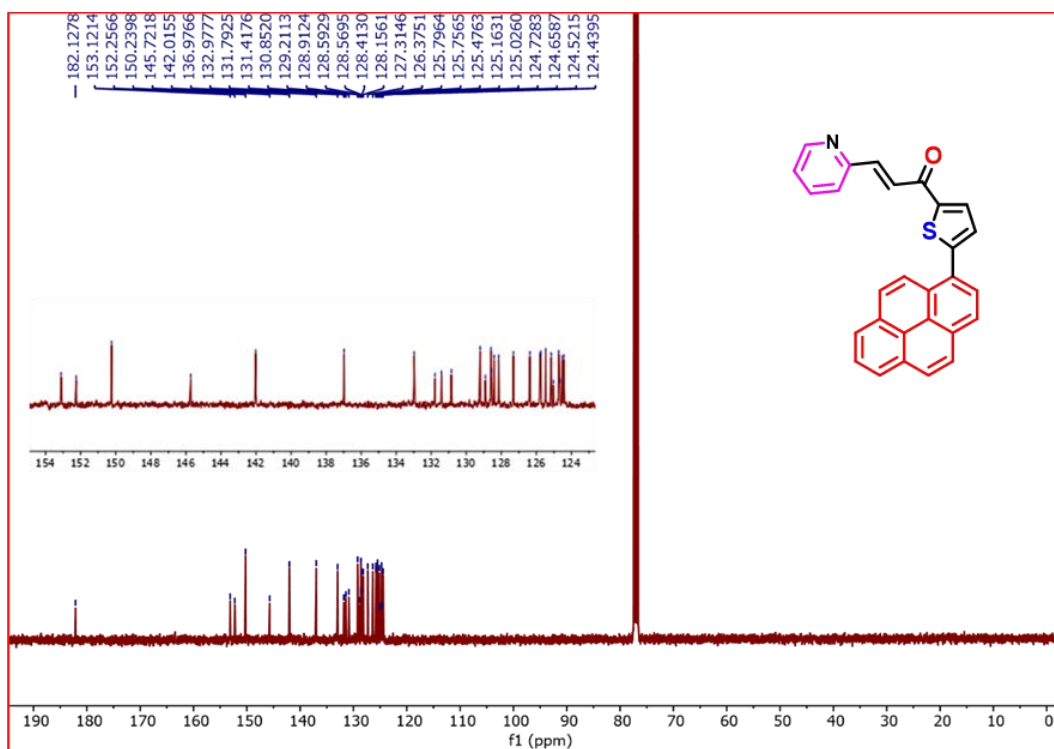
Figure 5.2.6 ^{13}C NMR spectra of PySP
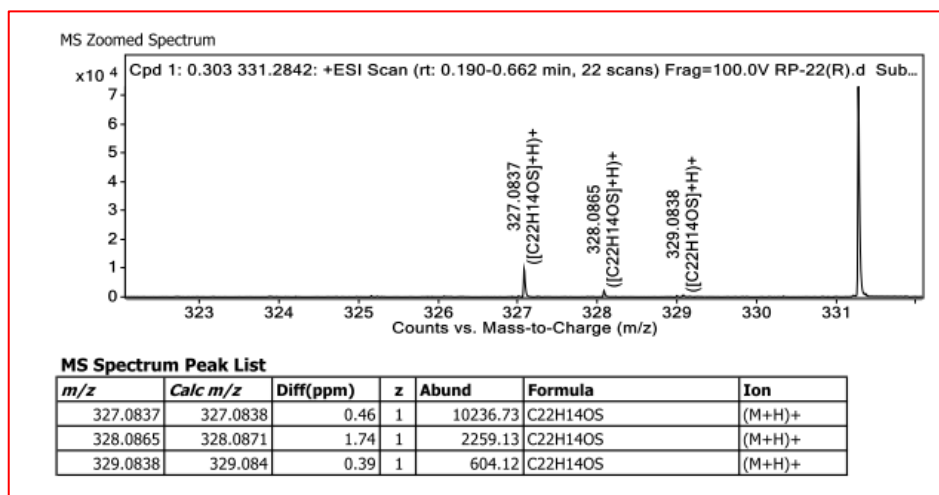
Figure 5.2.7 HRMS data of PyS
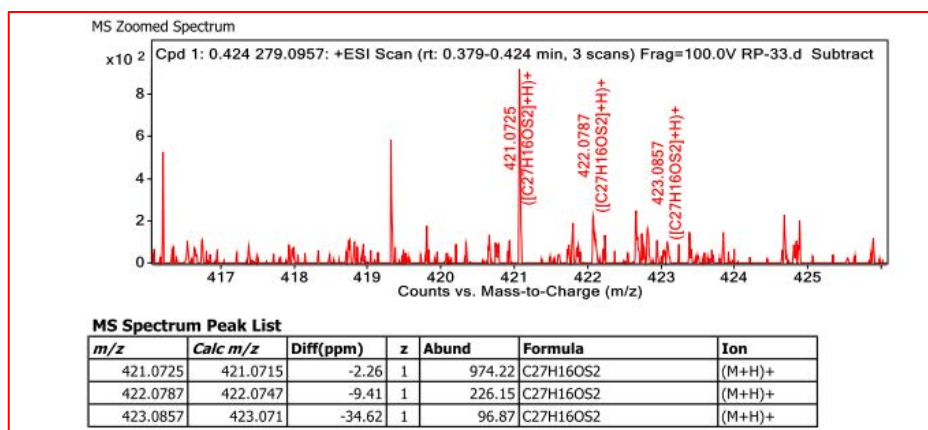
Figure 5.2.8 HRMS data of PySS
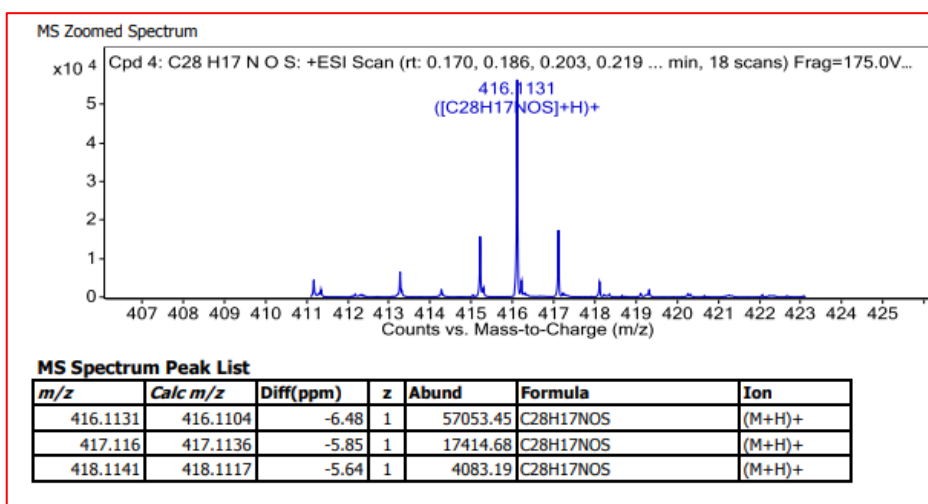
Figure 5.2.9 HRMS data of PySP

5.2.3 RESULTS AND DISCUSSION

The UV-VIS absorption spectra of synthesized compounds (PySS and PySP) were recorded in THF (10 µM) solution. It shows absorption peaks at two major regions, intense and sharp peaks observed at ~230-260 nm and broad vibronic peaks at ~300-400 nm (Figure 5.2.10). The intense absorption peak at 242 nm corresponds to the $\pi - \pi^*$ transition of pyrene moieties in both compounds.[48] Absorption band in the long-wavelength region can be attributed to a π–π^* transition with a charge transfer (CT) character that belongs to the push-pull chalcone π-system.[47-50] Solid state absorption of PySS and PySP were recorded; PySS shows a broad absorption tailing up to 600 nm and PySP case absorption tail up to 560 nm. (Figure 5.2.11). Emission spectra of the powder sample of both the compounds were recorded at excitation,

(λ_{max} =400 nm), and the corresponding emission peak were observed at 510 nm for PySS and 531 nm for PySP (Figure 5.2.10). In the dilute solution of THF (10^{-4} M), emission maxima were observed at 509 nm and 520 nm for PySS and PySP, respectively (Figure 5.2.10).
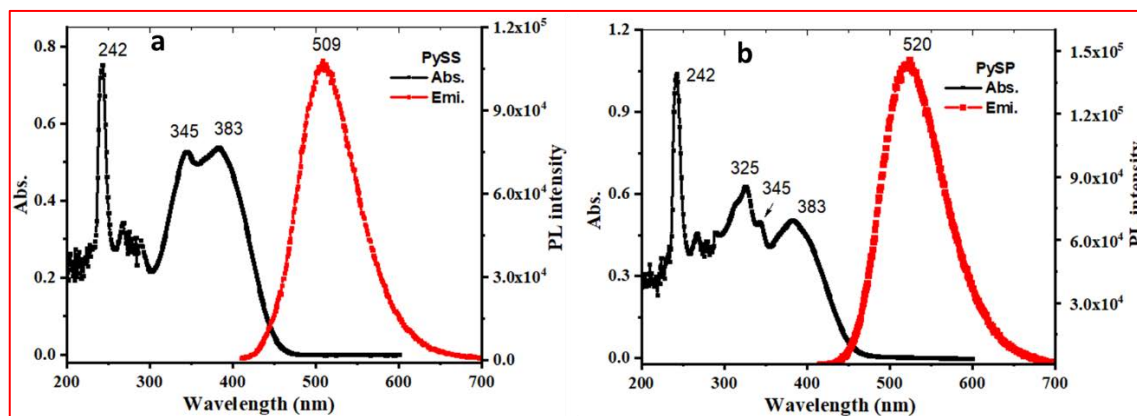
Figure 5.2.10. Absorption spectra (black line) with 10 µM concentration and emission (red line) with a concentration of 100 µM of (a) PySS (b) PySP in THF
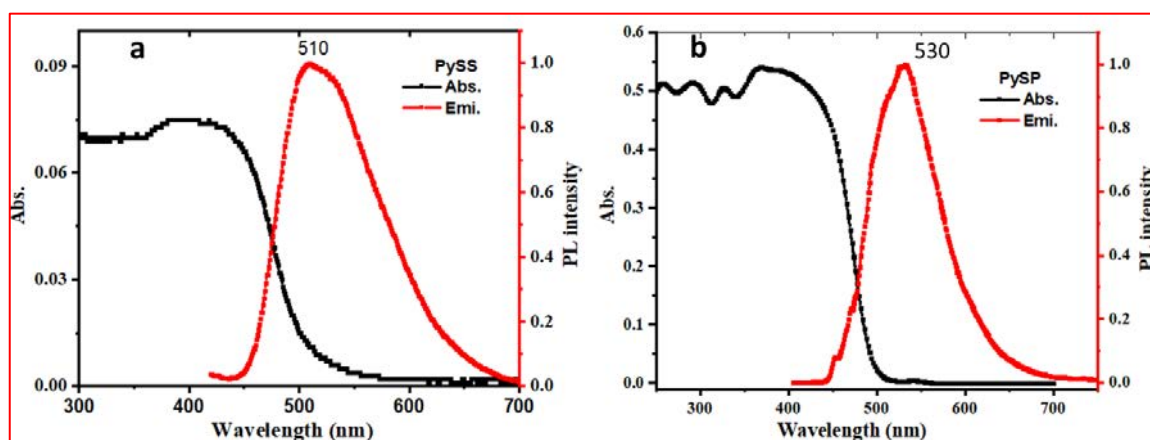
Figure 5.2.11 (a) Absorption spectra (black line) and emission (red line) in solid state of (a) PySS (b) PySP, respectively.

The solvatochromic properties of PySS and PySP were investigated with UV-VIS absorption and photoluminescence (PL) spectroscopy in different solvents with varying polarities (Figure 5.2.12 and 5.2.13), and the corresponding data are summarized in Table 5.2.1 and 5.2.2. It was observed in both cases (PySS and PySP) with increasing polarity of the solvent, and continuous shifting of emission bands.
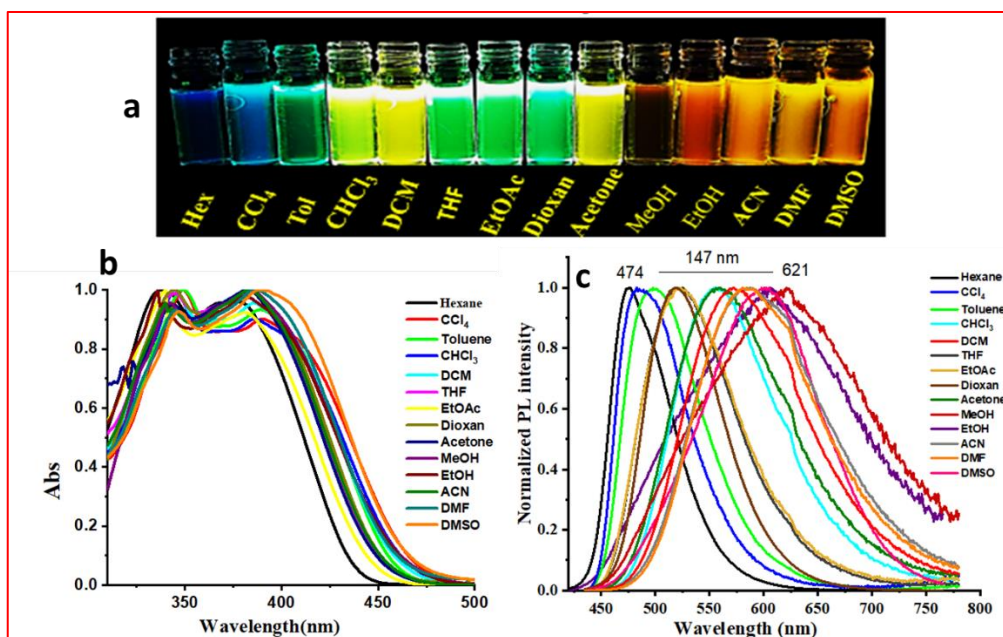
Figure 5.2.12 (a) Image of PySS in different solvents taken under 365 nm UV light excitation. (b) UV-visible spectrum of PySS in different solvents in wide ranges of polarities. (c) PL spectra of PySS in the same solvents used in absorption spectra.
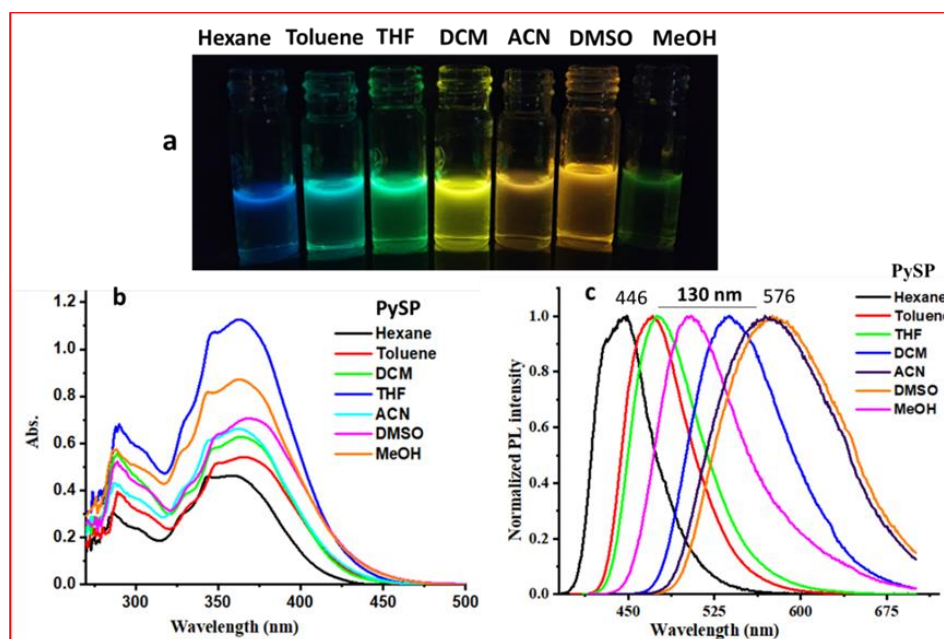
Figure 5.2.13 (a) Image of PySP in different solvents taken under 365 nm UV light excitation, (b) UV-visible spectrum of PySP in different solvents in wide ranges of polarities. (c) PL spectra of PySP in the same solvents used in absorption spectra.

Table 5.2.1 Photophysical properties (absorption and emission) in different solvents (PySS)

S.NO.	Solvents	Absorption $\lambda_{max.}$ (nm)	Emission $\lambda_{max.}$ (nm)	Stokes shift (cm^{-1})
1	Hexane	379	474	5288
2	Carbon tetrachloride	389	486	5132
3	Toluene	389	490	5299
4	Chloroform	386	557	7953
5	Dichloromethane	385	571	8461
6	Tetrahydrofuran	384	522	6885
7	Ethyl acetate	381	521	7053
8	1,4-dioxan	383	521	6916
9	Acetone	382	556	8192
10	Methanol	383	621	10007
11	Ethanol	382	605	9649
12	Acetonitrile	383	588	9103
13	N,N'-dimethyl formamide	386	586	8842
14	Dimethyl sulfoxide	388	602	9162

Table 5.2.2 Photophysical properties (absorption and emission) in different solvents (PySP)

S.NO.	Solvents	Absorption $\lambda_{max.}$ (nm)	Emission $\lambda_{max.}$ (nm)	Stokes shift (cm^{-1})
1	Hexane	358	446	5511
2	Toluene	366	470	6046
3	Tetrahydrofuran	363	476	6540
4	Dichloromethane	364	537	8850
5	Methanol	364	502	7552
6	Acetonitrile	363	570	10004
7	Dimethyl sulfoxide	369	576	9739

To better understand the solvatochromic behavior, the relationship between the solvent polarity parameter (Δf) and the Stokes' shift (Δv) based on the Lippert–Mataga equation was investigated. As shown in Figure 5.2.14 a, PySS displays a linear dependence of Δv on Δf, which suggests that solvents with strong polarity are able to stabilize the excited state via the reorientation of the solvent molecules,[51] resulting in a lowered energy of the system and the bathochromically shifted emission maximum. In the case of PySP (Figure 5.2.14 b), relatively more deviation was observed from the linearity. The protic polar solvent (MeOH) deviates more because of the presence of a pyridine ring, the nitrogen possibly forms a hydrogen bond with MeOH.
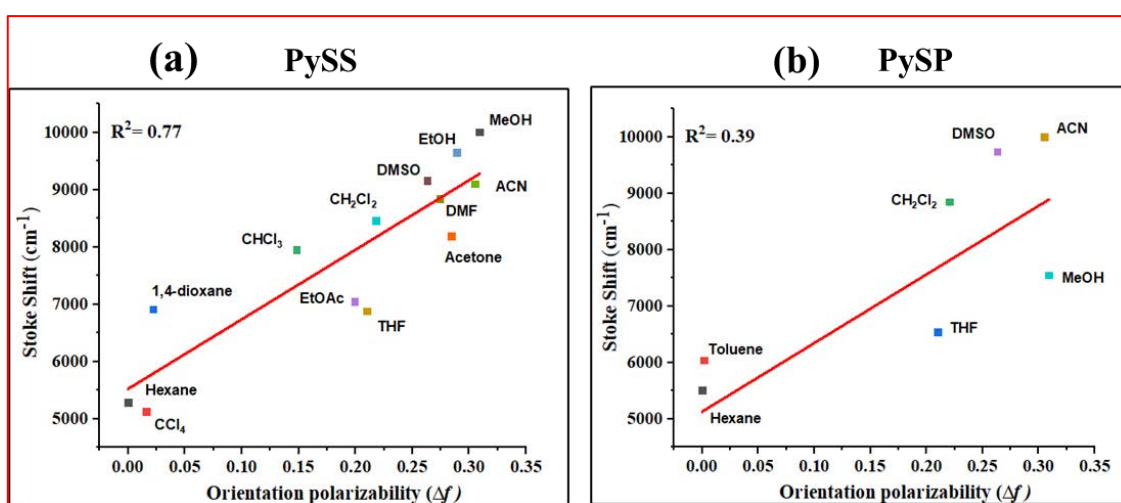
Figure 5.2.14 Lippert–Mataga representation of orientation polarizability of PySS (a) and PySP (b) dissolved in different solvents

From the literature, we found that solvatochromic properties were observed mainly because of ICT (Intramolecular charge transfer) and TICT (twisted intramolecular charge transfer) character of molecules.[49]. Here, we observed PySS and PySP are highly sensitive towards the solvent polarity (for PySS ~ 147 nm shifting from hexane to methanol and in case of PySP ~130 nm red shift from hexane to DMSO (Figure5.2.12, and 5.2.13)). The mechanism for the blue to orange-red emission of this pyrene–thiophene dyes were studied. The formation of excimer and intramolecular charge transfer (ICT) are two possibilities that can account for the emission changes. Pyrene has a rigid planar system; it tends to form an excimer at high concentrations.[52-53]. The packing diagram of PySS (Figure 5.2.35) clearly shows the absence of any pyrene-pyrene interaction, thus excluding the possibility of formation of any excimer. However, the packing diagram of PySP (Figure 5.2.36) shows the weak pyrene-pyrene interaction which indicates the possibility of formation of excimer. To examine whether an

excimer was formed in this system, the PL spectra of PySP in DCM solution with increasing concentrations (10^{-2} to 10^{-6} M) were recorded (Figure 5.2.15). However, no clear peak shifting was observed, indicating that no excimer was formed.
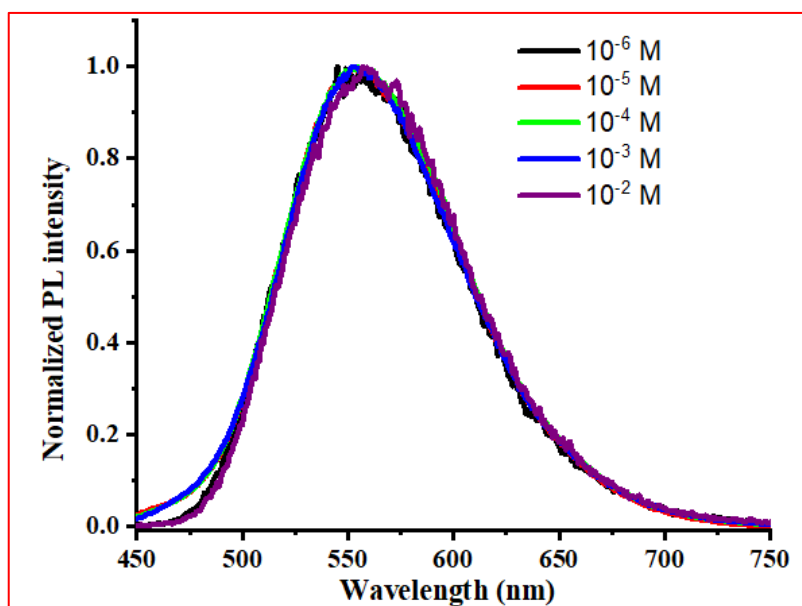
Figure 5.2.15 The normalized PL spectra of PySP in DCM solution with concentration from 1×10^{-6} M to 1×10^{-2} M

Therefore, it is speculated that the lowest emitting state consists of ICT characters for PySS and PySP. To verify this fact, theoretical calculations of pyrene thiophene in its optimized lowest energy gas phase were performed using the Gaussian 16 package. The frontier orbital plots of HOMO and LUMO are shown in Figure 5.2.16. The HOMO of PySS was mainly distributed on pyrene and immediately connected to thiophene moiety, whereas the LUMO of PySS was majorly shifted towards the second thiophene through π-electron bridge. In the case of PySP, it was observed that the HOMO is entirely located on the pyridine side and LUMO is distributed throughout the molecule. Since the distribution of HOMO and LUMO were located in the donor-acceptor system, this emission will be more consistent with that of the ICT character.
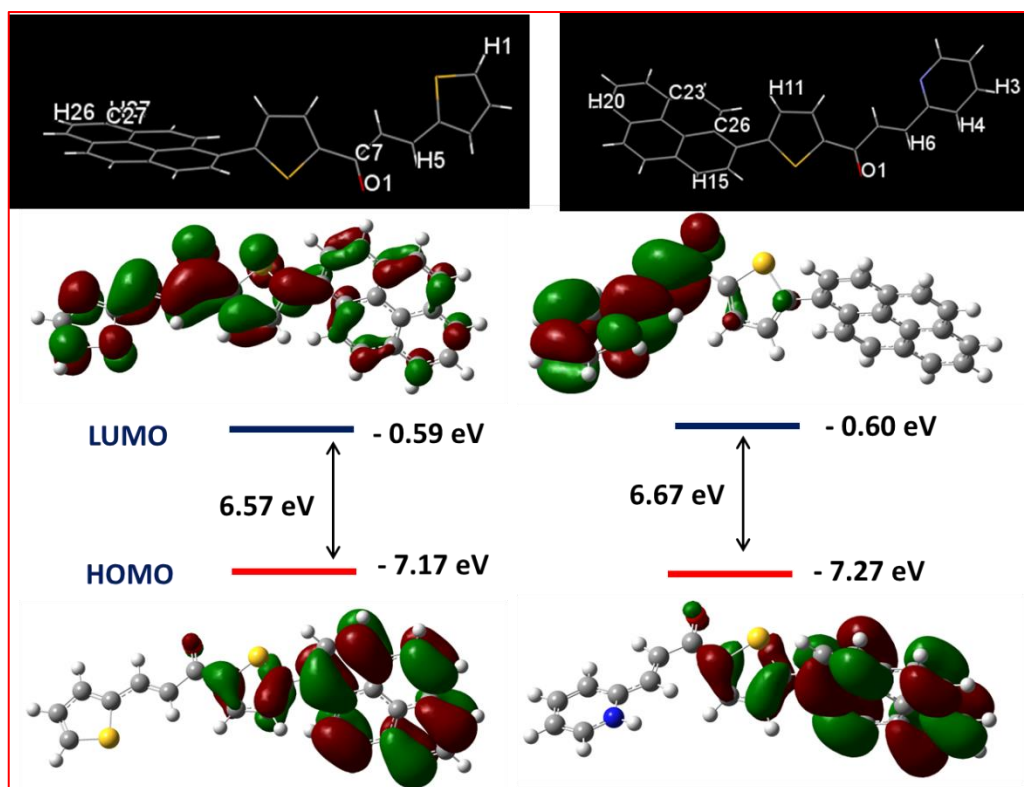
Figure 5.2.16 The spatial electron distributions of HOMOs and LUMOs of PySS (left) and PySP (right) which were calculated using the ωB97X-D/6-311++G (d, P) by Gaussian 16 package

It was observed from the optimized structures that the dihedral angle between the pyrene and attached thiophene for both molecules was in the range of 50-52°. The observed twisted structure hints the possibility of the 'Aggregation-induced Enhanced Emission' (AIEE) behaviour of PySS and PySP. To check the AIEE behavior, it was prepared a 100 μM tetrahydrofuran solution of PySS and PySP as a stock solution. Prepared the AIEE solution by varying different water fractions (v/v %) from 0% to 90% (details given in the experimental section). In the case of PySS (Figure 5.2.17), the PL intensity slightly decreases with redshifted emission observed till 60% water fraction (f_w), and then a sudden rise of PL intensity was observed. In the case of PySP (Figure 5.2.18), PL intensity decreases up to 40% water then slightly increments up to 70% water fraction, and then a sharp increment is observed. The extended molecular conjugations for exciton movements typically elucidate the redshifted emission upon aggregation.[54-55] From the single crystal analysis (Figure 5.2.19), From the single crystal analysis (Figure 5.2.31 and 5.2.32), PySS and PySP have many intermolecular interactions and short contacts (Table 5.2.4) between the neighbouring molecules. Those contacts will restrict the rotational motion of molecules, facilitating the excited state molecules to be relaxed in a radiative pathway.
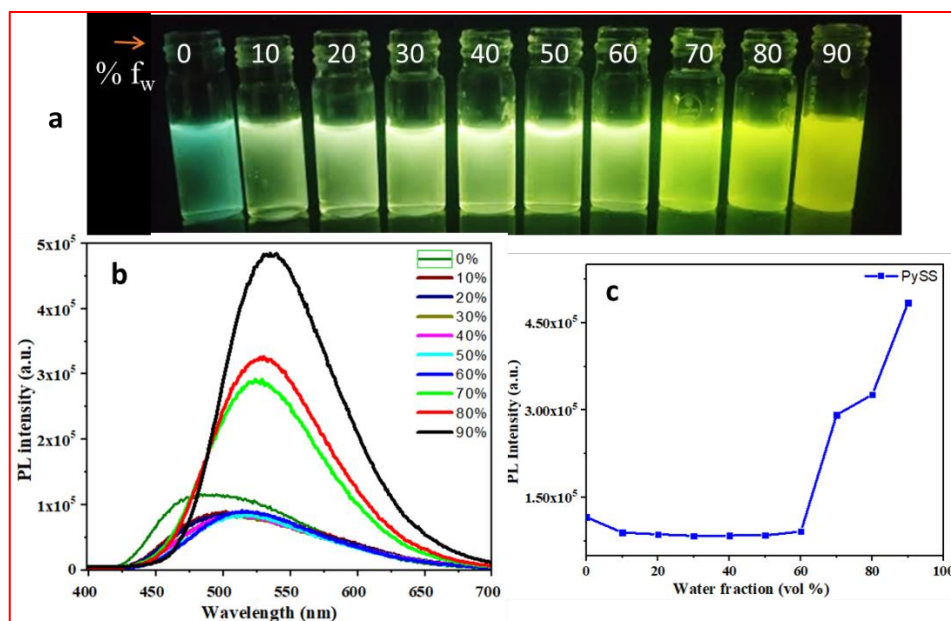
Figure 5.2.17. Aggregation-induced Emission study of PySS. (a) The image was taken at water percentage (f_w = 0 % to f_w = 90 %) for PySS under a 365 nm UV excitation. (b) Emission spectra of PySS, (λ_{ex} = 400 nm) at different f_w in 100 μM in THF. (c) Line plot of PL intensity versus volume of water fraction
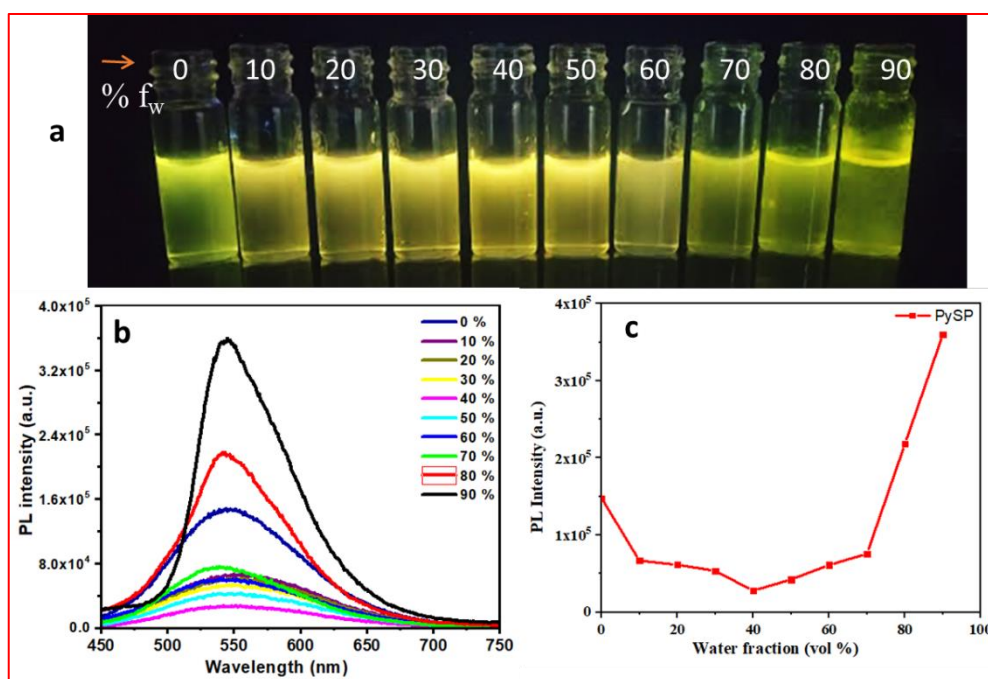
Figure 5.2.18 Aggregation-induced Emission study of PySP. (a) The image was taken at water percentage (f_w = 0 % to f_w = 90 %) for PySP under a 365 nm UV excitation. (b) Emission spectra of PySP, (λ_{ex} = 400 nm), at different f_w in 100 μM in THF. (c) Line plot of intensity versus volume of water fraction
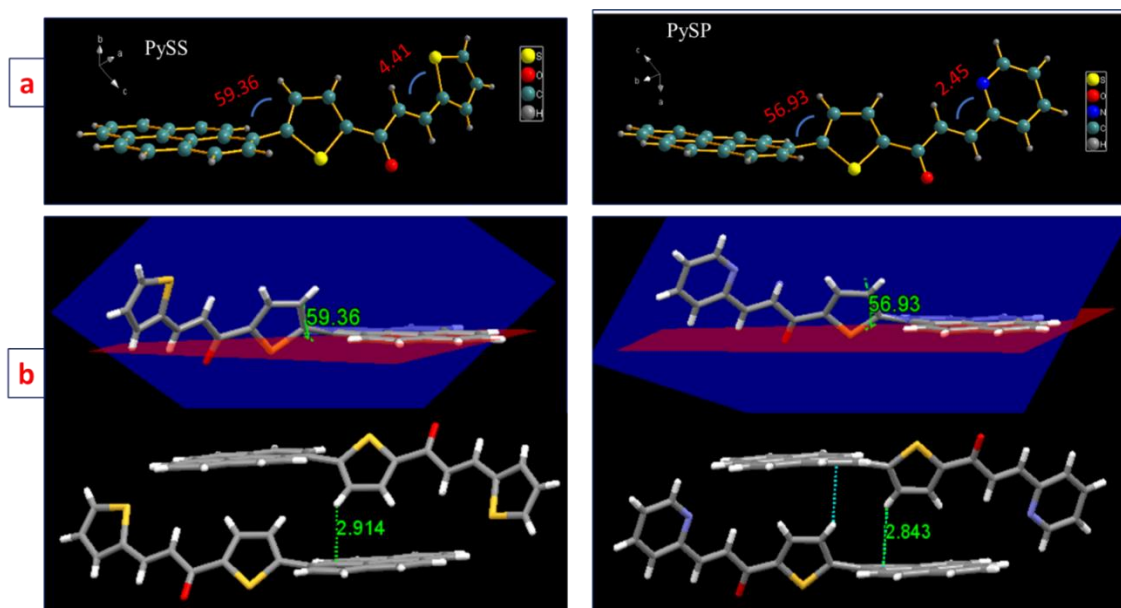
Figure 5.2.19 (a) The asymmetric unit of PySS and PySP with dihedral angles. (b) The angle between the thiophene plane and the pyrene plane is more than 55° in both cases. The unit cell contains two molecules lying in antiparallel orientation. Two molecules are interacted through C-H…π interactions (PySS-2.914 Å, and for PySP two identical short contacts of 2.843 Å)

Single-crystal X-ray structures were investigated to comprehend solid-state AIEE, and MFC behavior for these fluorophores. Single crystal structure of PySS and PySP were grown in DCM/Hexane system by slow diffusion process (CCDC- for PySS- **2349027** and for PySP- **2349045**). In the crystal structure of PySS, pyrene, and thiophene are in different planes having a dihedral angle of 59.36°, and the unit cell consists of two molecules facing opposite to each other (see left side of Figure 5.2.19). Similarly, in the case of PySP, pyrene, and thiophene planes are different with a dihedral angle of 56.93°, and unit cell molecules are facing opposite to each other (right side of Figure 5.2.19). The angle between the plane of two thiophene rings in the case of PySS are at 23.54° and the plane of thiophene and pyridine rings in the case of PySP are at 20.45°.

5.2.3.1 Mechanofluorochromic properties of PySS and PySP

Initially, the solid-state emission properties of both compounds were recorded in powder form. Interestingly, both molecules were emissive in the solid state with a reasonably high quantum yield: compound {λ_{max}, absolute quantum yield (% Φ_f)}: PySS (510 nm, 24.13); PySP (531 nm, 19.01). The MFC features of these molecules were studied by grinding (using a mortar

pestle) and by applying a hydraulic press (using a hydraulic pallet press). After grinding, PySS and PySP show a large bathochromic emission shift of 50 nm for the case of PySS (Figure 5.2.20, a) and 54 nm for the case of PySP (Figure 2.2.21, a). The reversibility of the after phase of PySS and PySP, without putting any stimuli at ambient temperature. The original emission of both the compounds is returned within 1 hr (Figure 5.2.20 and 5.2.22). As no external stimuli were required to bring them to their original state, the compounds can be used as self-reversible MFC materials.[56] Interestingly, the MFC behavior of PySS and PySP were reversible on fumigation with methanol vapor/heating at 70-80°C for 1-2 min, and the same platform can be reused more than five times (Figure. 5.2.21 and 5.2.23). These compounds are highly sensitive to a shearing force, a clear change of emission could be observed by simply rubbing with a metal spatula. Another efficient feature of PySS and PySP is their responsiveness towards hydraulic pressure (compressive pressure). Pristine sample of PySS and PySP, after applying hydraulic pressure of 12.5 tons showed bathochromically shifted emission with 68 nm emission shifting (PySS case Figure 5.2.20, b) and 64 nm (PySP case, Figure 5.2.22, b), respectively.
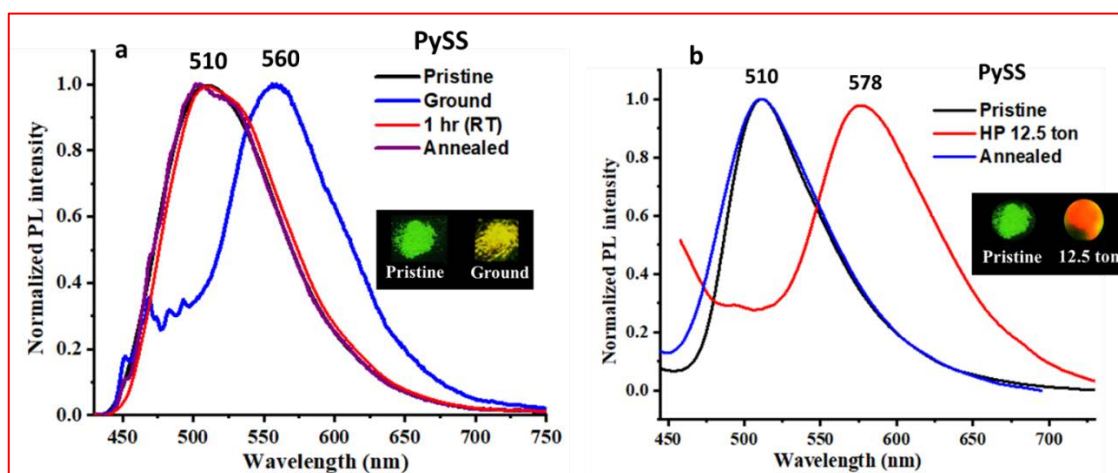
Figure 5.2.20 (a) PL spectra of PySS in pristine form and after grinding with the help of mortar pestle; 1hr (RT) indicates ground sample kept for 1 hr at rt and then recorded the emission. (b) PL spectra of PySS after applying a hydraulic press (HP) of 12.5 tons and heating at 70-80 °C for 1-2 minutes (annealed sample)
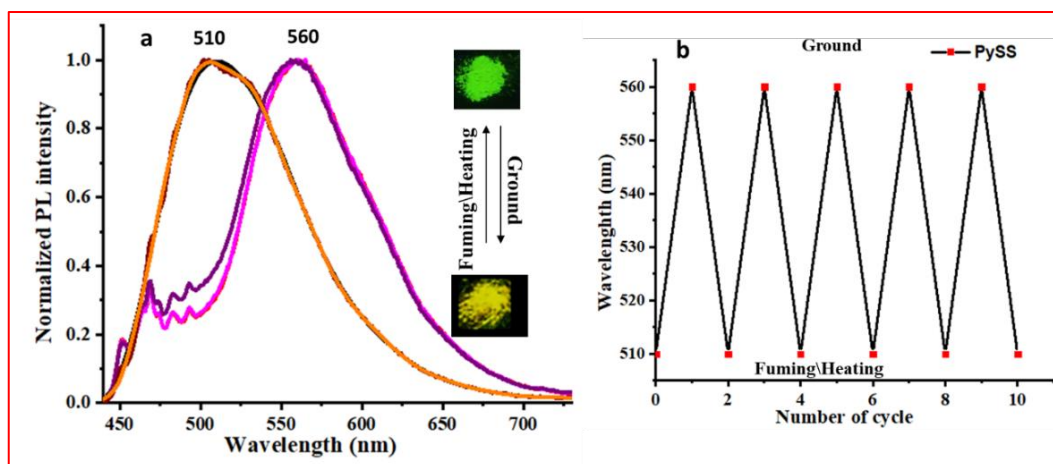
Figure 5.2.21 (a) PL spectra of PySS in pristine form and after grinding. (b) Recoverability of emission property of a ground sample of PySS after solvent (methanol fuming for 2 min) fumigation and heating (70-80 °C for 2 min), (inset figure shows the emission color of pristine and ground sample under UV (365 nm) excitation)
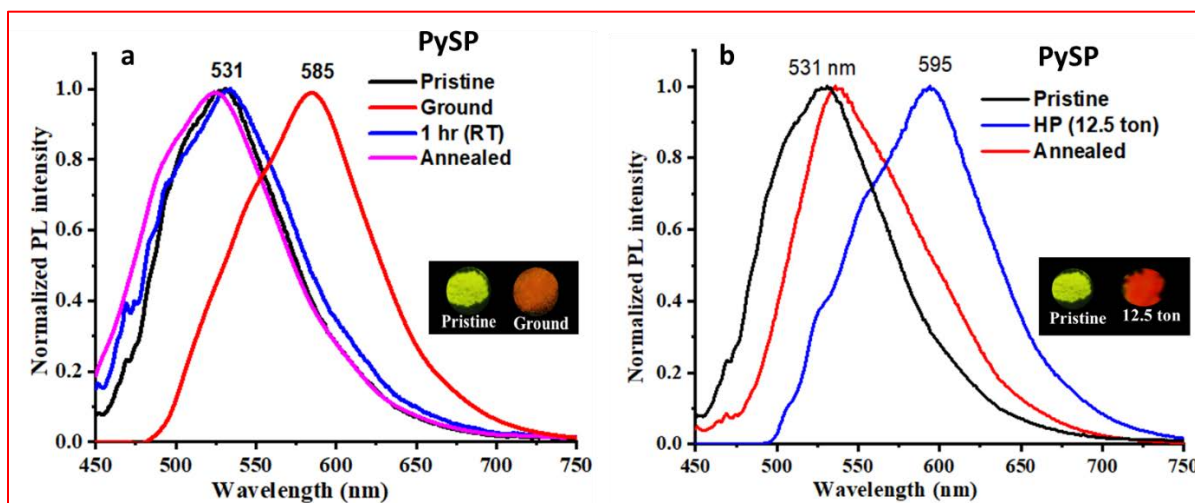
Figure 5.2.22 (a) PL spectra of PySP in pristine form and after grinding with the help of mortar pestle. 1hr (RT) indicates ground sample kept for 1 hr at rt and recorded the emission. (b) PL spectra of PySP after applying a hydraulic press (HP) of 12.5 tons and heating at 70-80 °C for 1-2 min (annealed sample)
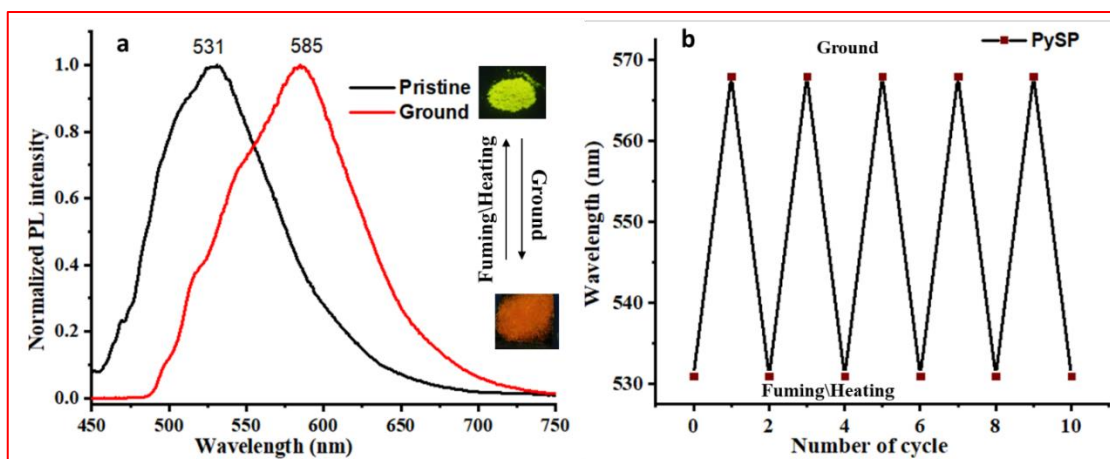
Figure 5.2.23 (a) PL spectra of PySP in pristine form and ground form. (b) Recoverability of emission property of a ground sample of PySP after solvent (methanol fuming for 2 min) fumigation and heating (70-80 °C for 2 min). (The inset figure shows the emission color of pristine and ground samples under UV (365 nm) excitation)
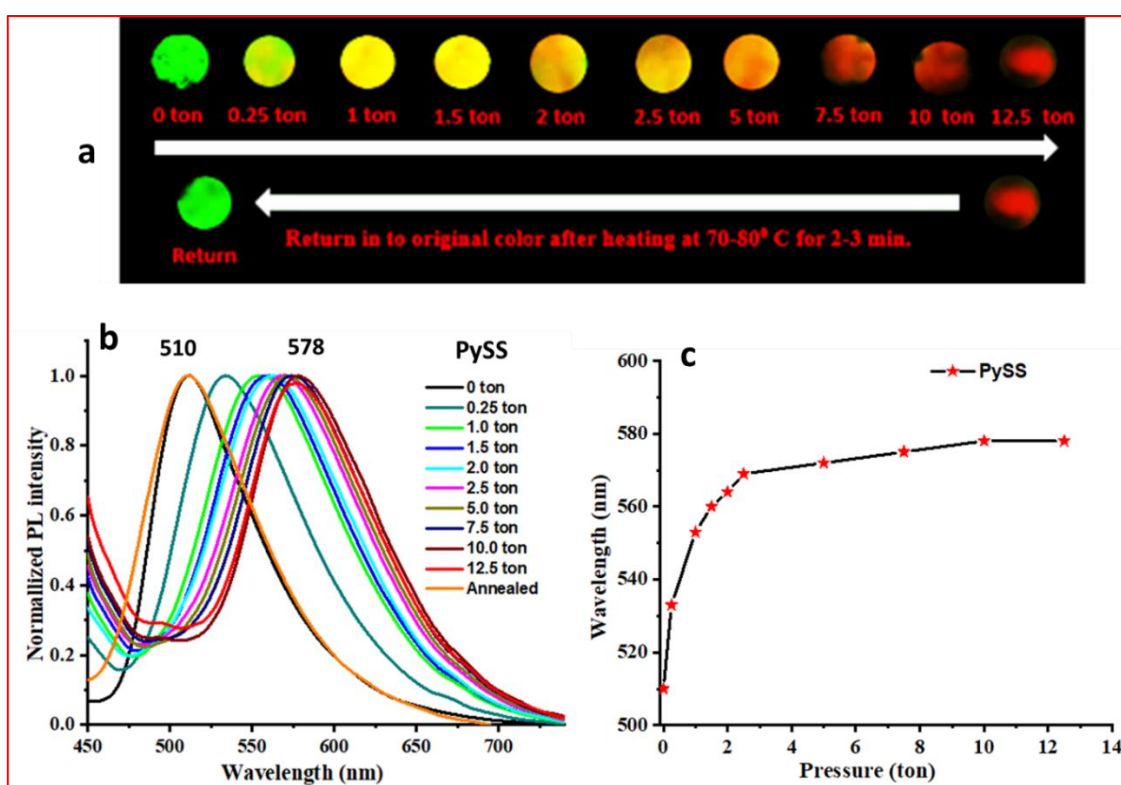
Figure 5.2.24 PL properties of PySS under different hydraulic pressure. (a) Emission images of PySS were taken under UV excitation (365 nm) with increasing pressure and after releasing pressure. (b) Normalized PL spectra of PySS at different amounts of pressure. (c) Plotted change in wavelength at different amounts of pressure

It was interestingly observed that slowly increasing compressive force (by hydraulic press) from 0 to 12.5 tons, the original green emission of PySS is gradually transformed through variable intermediate emission colors (yellow, yellow-orange, orange) and finally changed to orange-red (λ_{max} = 510 nm→ 578 nm). It slowly reverts into the pristine form after releasing pressure within 24 hr at ambient conditions and returns within 2-3 mins with heating at 60-70 $^{\circ}$C. (Figure 5.2.24). We have shown the images to describe the recovery process with heating (Figure 5.2.25 a) and without any external trigger (Figure 5.2.25 b). It was observed that with gradually increasing pressure (0 to 12.5 tons applied for 2 min each), emission wavelength increases uniformly and continuously (Figure 5.2.24, c). It was recorded the solid-state UV-VIS absorption spectra at different pressures (0 to 12.5 tons) and observed that by increasing pressure the absorption at ~445 nm gradually decreased and a new red-shifted peak observed at ~505 nm (Figure 5.2.26), indicating molecules become coplanar followed by increasing intermolecular interactions during the compression process.[57]
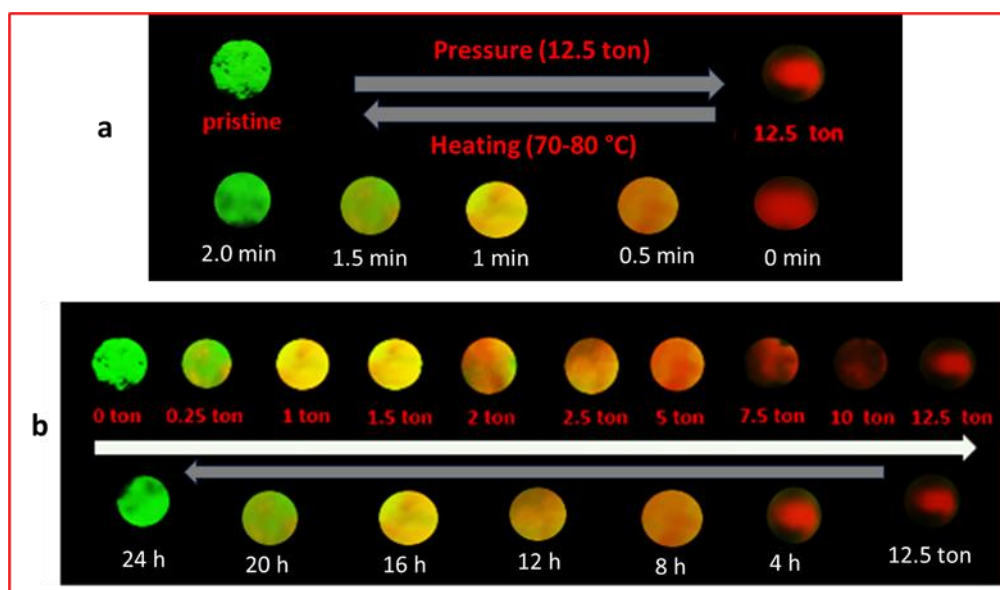
Figure 5.2.25. Emission images of PySS were taken under UV excitation (365 nm) with increasing amounts of hydraulic pressure and after releasing pressure with time. (a) shows images of the recovery process with heating (70-80 °C) at different times and (b) images of the recovery process with time without applying any external triggers up to 24 hr
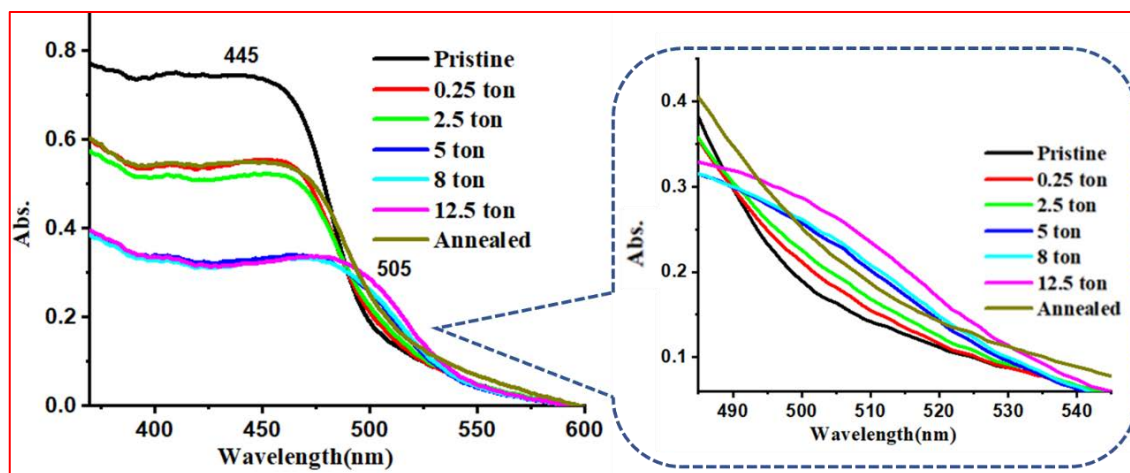
Figure 5.2.26 Solid state absorbance of PySS in pristine form and with gradually increasing hydraulic pressure and the absorbance spectrum after releasing pressure and after annealing at 70-80 °C for 2 min

Table 5.2.3 Quantum yields (Φ), and fluorescence lifetime (τ) of PySS and PySP samples before and after external stimuli.

Important parameters	Quantum yield (Φ_f) ,%		Lifetime $<\tau>$, ns	
	PySS	**PySP**	**PySS**	**PySP**
Pristine	24.13	19.01	0.29	0.28
Ground	28.5	22.31	0.57	0.58
Press (12.5 ton)	13.03	9.45	0.93	0.94

Table 5.2.4 non-covalent interactions present in crystal packing of PySS and PySP

S.NO.	Type of interaction	PySS	PySP
1	H-bonding	H26...O1 = 2.685 Å, H5...O1 = 2.597 Å,	O1...H6 = 2.579 Å O1...H4 = 2.645 Å
2	Inequivalent short contacts	C7...H27 = 2.883 Å C27...H1 = 2.796 Å	H3...H20 = 2.329 Å C26...H11 = 2.843 Å C23...H15 = 3.367 Å

The lifetime study and absolute quantum yield measurement of the pristine sample, ground sample, and compressed (12.5 tons) sample were recorded for PySS and PySP (Table 5.2.3). It was found that the excited state lifetime increases after mechanical grinding and compressive force for both compounds (Figure 5.2.27). The quantum efficiency (QY) of both compounds is increased after grinding, while QY decreases after compressive (12.5 tons) force (Table 5.2.3). The powder XRD diffractograms of pristine powder of PySS and PySP exhibited many sharp and strong scattered peaks, supporting good crystallinity with ordered molecular packing (Figure 5.2.28). However, the ground powder showed less intensity with some of the peaks disappearing implying it the less crystalline or semi-crystalline in nature. From the DSC, the PySS shows the melting point at 190.5 °C and 191.5 °C for the pristine and ground phases, respectively (Figure 5.2.29). Similarly, PySP shows a melting temperature at 207.9 °C and 208.7 °C (Figure 5.2.30), for pristine and ground samples, respectively. After having DSC data of the ground form of both compounds, we did not observe any phase transition which might be because of the highly reversible nature of the ground form of compounds. It was recorded the melting point of both compounds, melting range (188 - 192 °C) for PySS and (207 - 210 °C) for PySP. The compounds (PySS and PySP) were filled in melting capillaries and captured the emission before and after melting under UV (365 nm) excitation (Figure 5.2.31). After melting the bathochromic emission shifting for both compounds was observed, which supports the phase transition results in bathochromic emission shifting.[17] TGA analysis of PySS and PySP showed both compounds are thermally stable up to ~320 °C (Figure 5.2.32). As already discussed in photophysical properties, synthesized molecules show ICT characteristics. The new emission band which is gradually red-shifted with pressure originated from the ICT state.[58] This is also evident from the change in UV-VIS spectra of PySS with increasing pressure (Figure 5.2.26). We also performed the Raman spectra of PySS with different amounts of hydraulic press (Figure 5.2.33), there is no significant change found in the spectra, only it was observed that the peak intensity reduced at higher pressure. It means that there might be a possibility that, at high pressure intermolecular distance decreases, thus the molecules approach closer upon compression leading to the $\pi - \pi$ stacking interactions.[59] It was recorded the FESEM image of both samples (Figure 5.2.34). The pristine form shows a rod and sheet type morphology, and after applying shearing force (ground form) shows non-uniform micro-ranged particles formed.
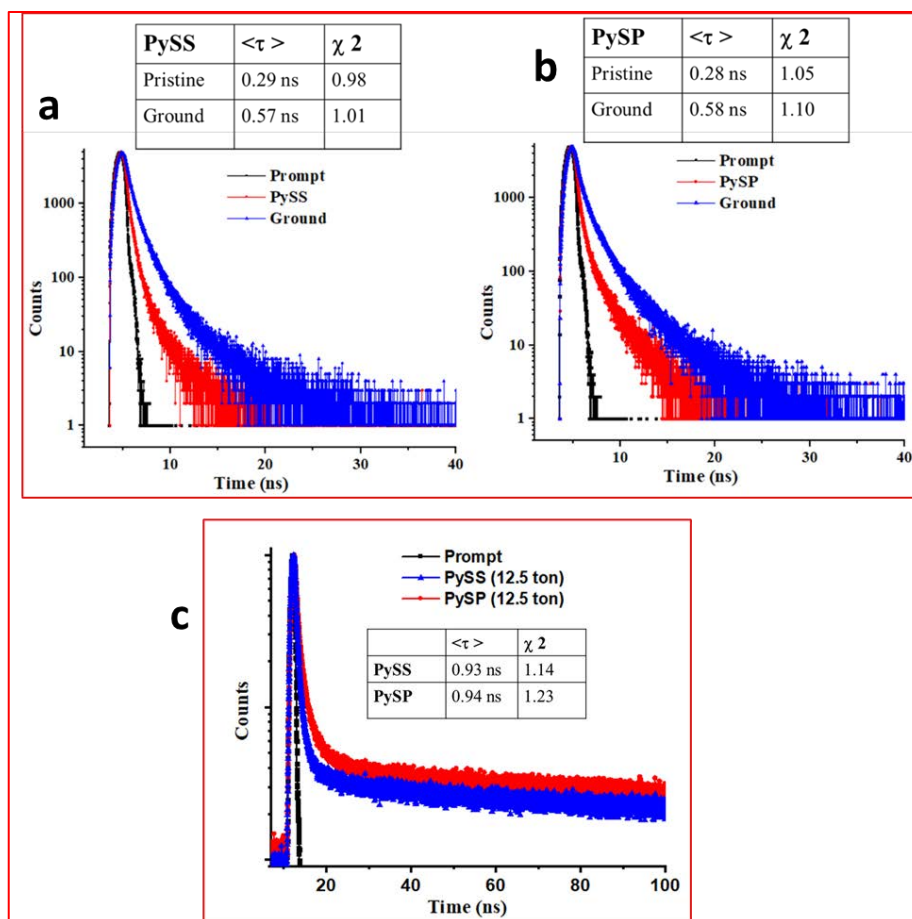
Figure 5.2.27 Lifetime plot of PySS in pristine and ground form (a), PySP in pristine and ground form (b), and after applying compressive force (12.5 ton) for PySS and PySP (c), inset table shows the average lifetime with fitting parameter.
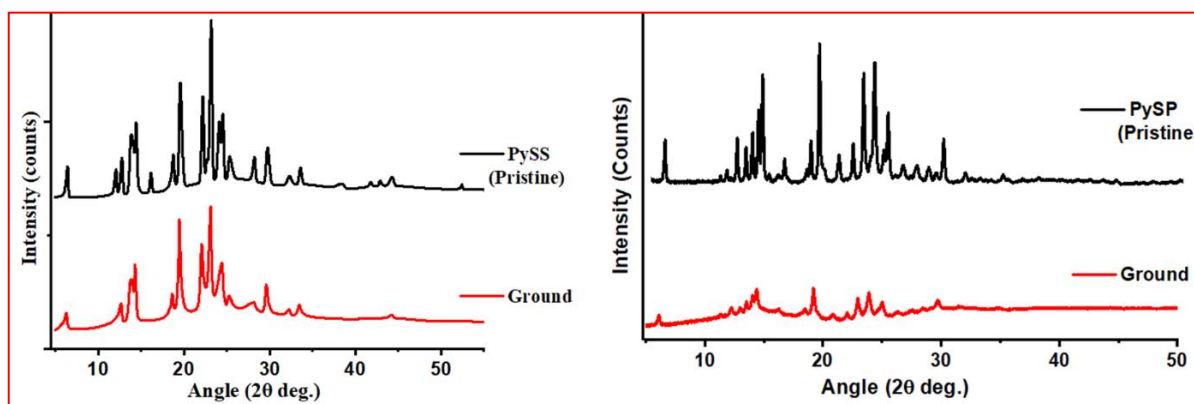
Figure 5.2.28 PXRD data of PySS and PySP in pristine and ground form
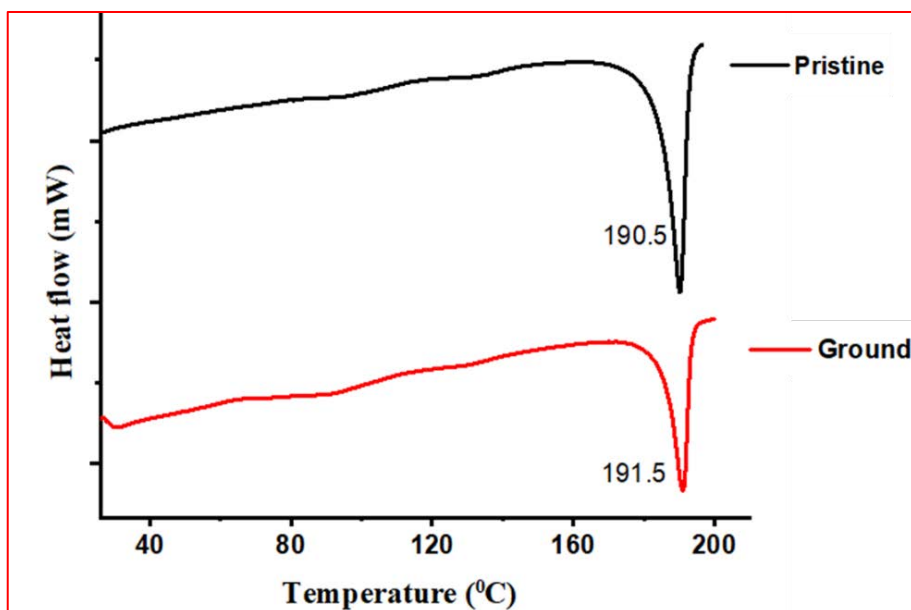
Figure 5.2.29 DSC analysis of PySS in pristine form and ground form, melting point observed at 190.5 °C for pristine sample and 191.5 °C for ground sample
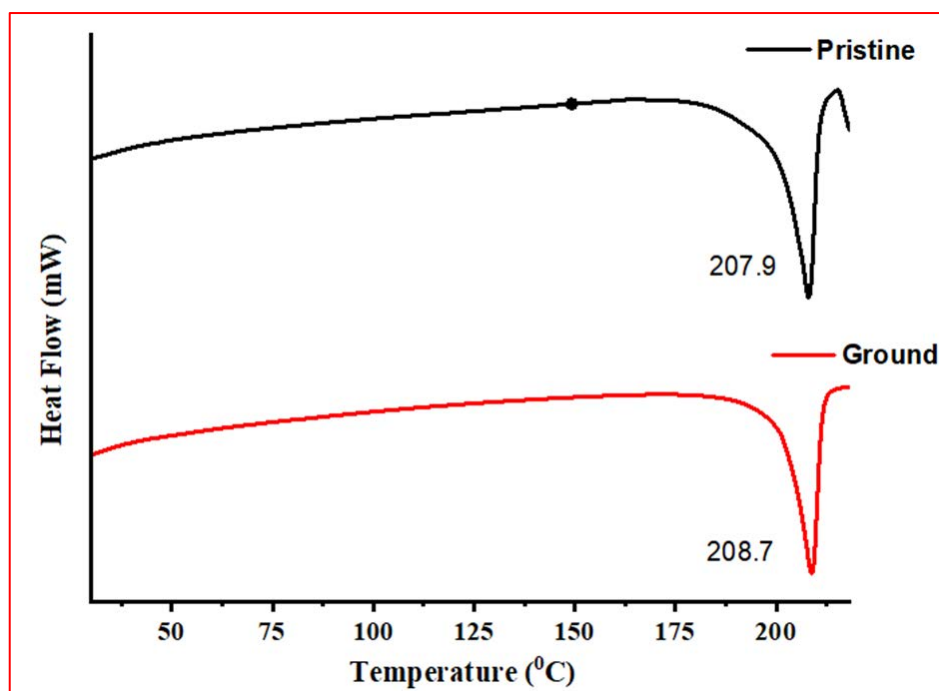
Figure 5.2.30 DSC of PySP in pristine form and ground form, melting point observed at 207.9 °C for pristine sample and 208.7 °C for ground sample
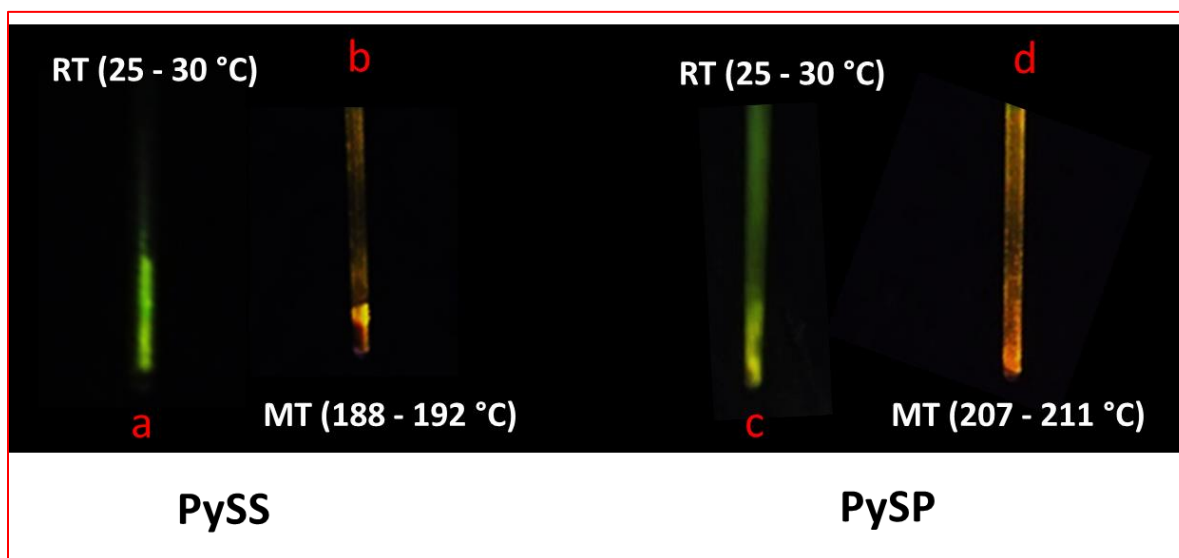
Figure 5.2.31 Filled the compounds (PySS and PySP) in melting capillaries and captured the emission at RT and after melting under UV (365 nm) excitation. a and c represent the image of compound filled in capillary at room temperature (RT) and b and d represent the capillary image at melting temperature (MT)
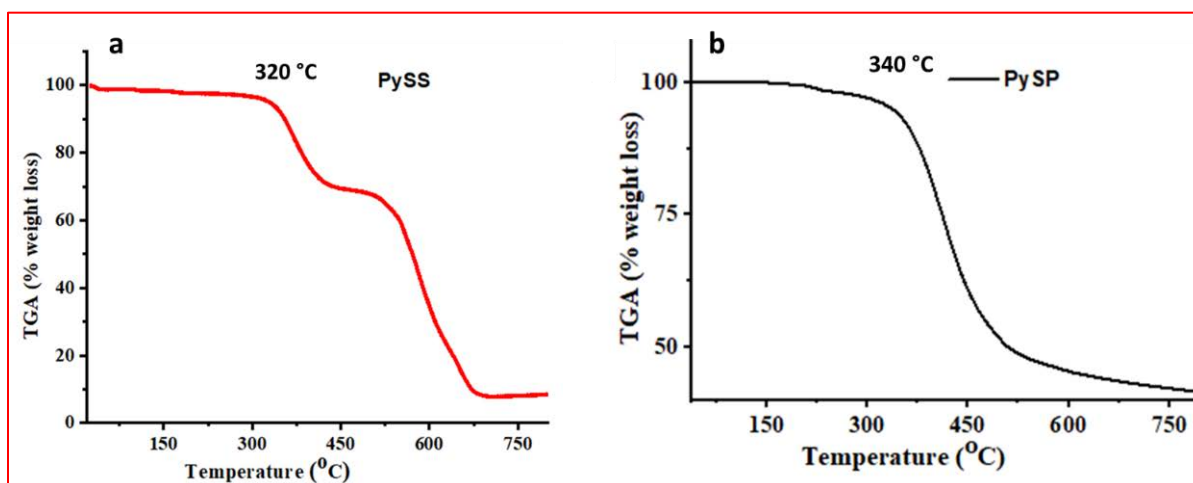
Figure 5.2.32 TGA analysis, a) thermogravimetric analysis of PySS, and b) thermogravimetric analysis of PySP
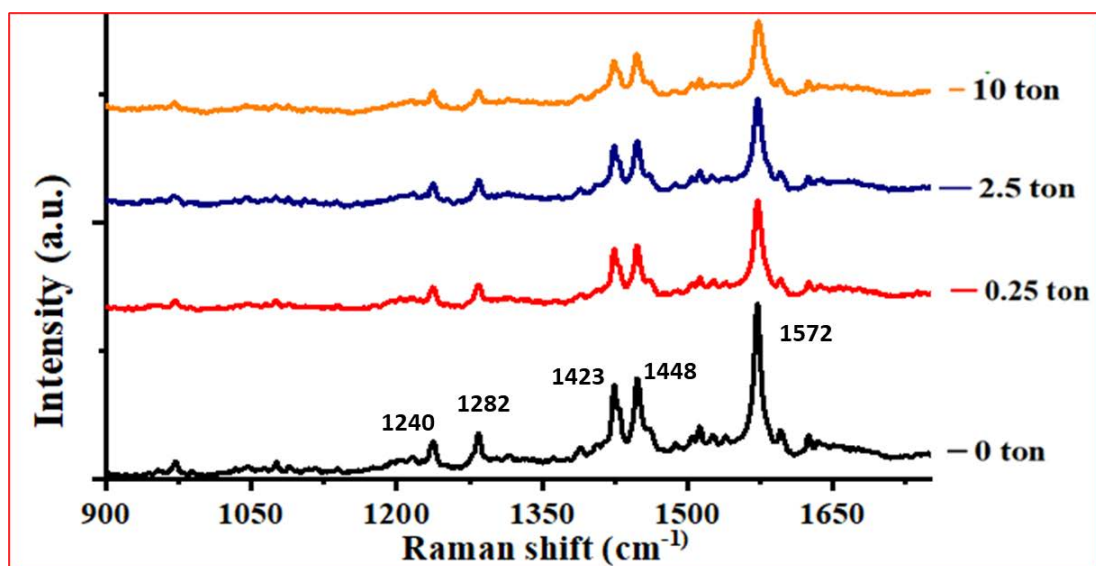
Figure 5.2.33 Raman analysis of PySS with increasing hydraulic pressure from 0 to 10 tons. It was observed that the peak at 1240 and 1282 cm^{-1} belongs to CH in-plane bending of the pyrene ring and that the peaks at 1423 cm^{-1} and 1448 cm^{-1} correspond to the C-C stretching for pyrene. The Raman frequency at 1572 cm^{-1} corresponds to the conjugated carbonyl (C=O) stretching frequency[60]
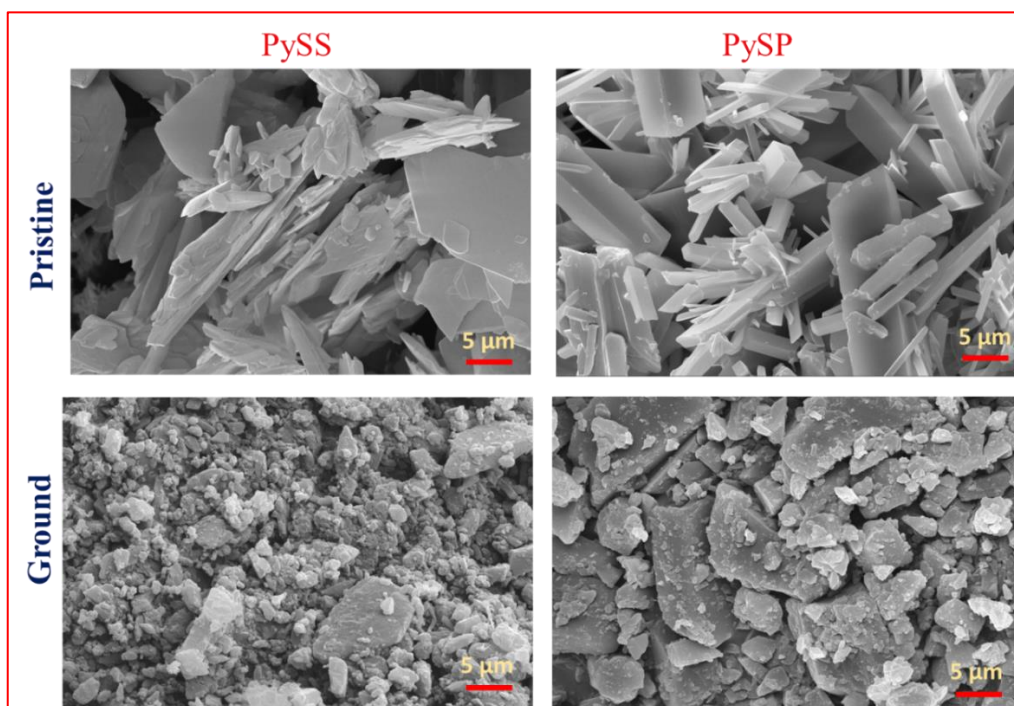
Figure 5.2.34 FESEM analysis of pristine phase and ground phase of PySS (left) and PySP (right)

It was investigated the mechanism behind the different luminescent behaviors of PySS and PySP by applying different external triggers (axial force using a hydraulic press and shearing force). The packing diagram shows that two molecules are arranged in an anti-parallel orientation, forming a molecular pair with two symmetrical interactions (Figure 5.2.19). This molecular pair further extended to a long-range one-dimensional chain-type arrangement. In the case of PySS, two molecules connected through π -electrons of pyrene ring with H of thiophene (C27...H1 = 2.796 Å) forming a molecular pair, and it is further extended through H-bonded interaction (H26...O1 = 2.685 Å) to another molecular pair in a one-dimensional fashion. These molecular pairs are extended to one direction linearly and form a one-dimensional chain (Figure 5.2.30, a). Each of these one-dimensional chains is interacting sidewise to the neighbouring parallel chain held with a total of four different interactions (Figure 5.2.35, b, and Table 5.2.4). Similarly, for the case of PySP (Figure 5.2.31, a) two molecules connected through C-H…π interaction (C26...H11 = 2.843 Å) and further extended linearly through the hydrogen of pyrene with pyridine ring hydrogen (H3...H20 = 2.329 Å) and forming a one-dimensional chain. This one-dimensional chain is further connected sidewise to neighbouring parallel chains through a total of three different interactions (Figure 5.2.36, b and Table 5.2.4). From the crystal packing, it was observed that planar pyrene rings are separated with twisted thiophene and pyridine; it is speculated that with applying high pressure, the twisted form is gradually planarized, thus the separated molecules approaching each other leading to the π-π interactions across the pyrene units and thiophene units of different molecules. A similar kind of molecular packing was observed for AIE active salicylaldehyde-based Schiff base reported by our group[45], that was also giving reversible MFC properties under compressive force (hydraulic press).

It is noted that in both the cases (PySS and PySP), MFC properties were reversible under the application of shearing force, which is in contradictory to the earlier report of our group,[45] where emission change by shearing force is not reversible. It was observed that in the case of shearing force emission properties are reversible within 1.0 hr at ambient conditions. Surprisingly, in the case of compressive force reversibility process takes longer time (more than 24 hr. in ambient condition). As pyrene is rigid polyaromatic system, in case of shearing force there is less possibilities that planarization of pyrene molecules. From the crystal packing, it is speculated that molecular pairs which help to form a regular arrangement of crystal will be intact under shearing force. So, after releasing pressure the ground sample recovers its original emission. On the other hand, it was observed from the crystal packing that flat pyrene

rings are arranged in such a way that with the application of axial force (hydraulic press), planarization of the molecule increases, which enhances the π–π stacking interactions between pyrene molecules, ultimately resulting in a decrease in emission intensity with red-shift.[43] The reason behind the slow returning the emission of the compressed sample (orange-red) towards the original emission (green) might be under the application of high pressure (axial force) pyrene molecules are stabilized by strong π–π stacking interactions.
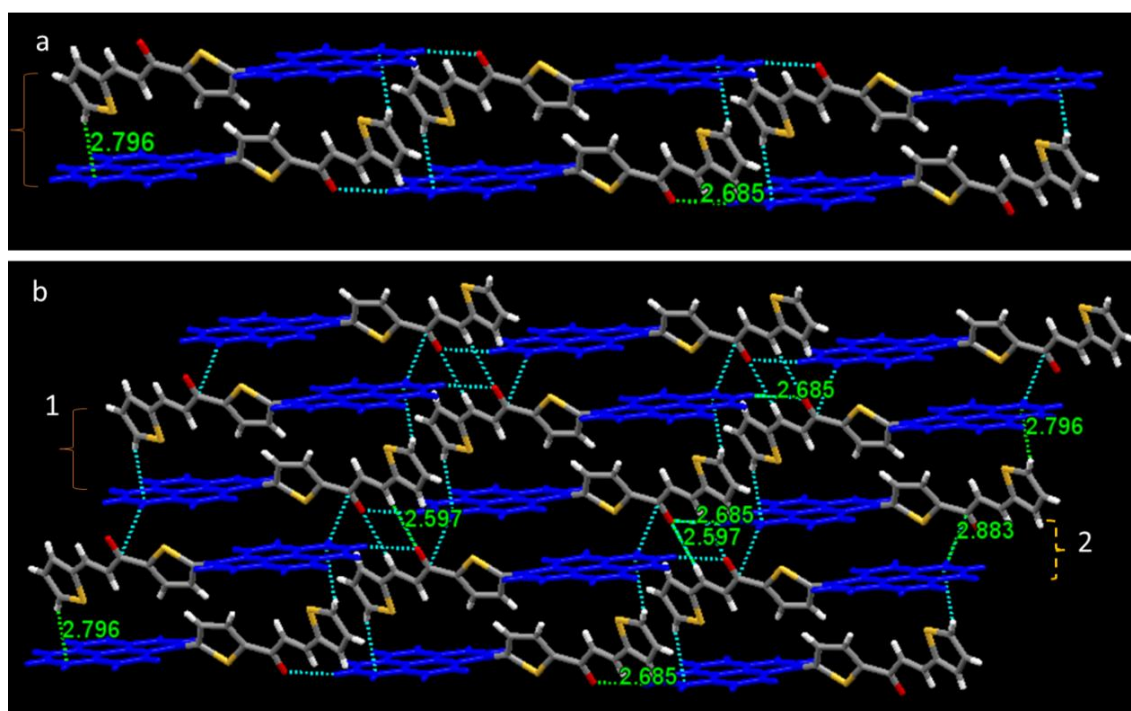
Figure 5.2.35 (a) Crystal packing of PySS showing molecules faces opposite to each other and extended in one direction. (b) Crystal packing of PySS with intermolecular interactions between molecules
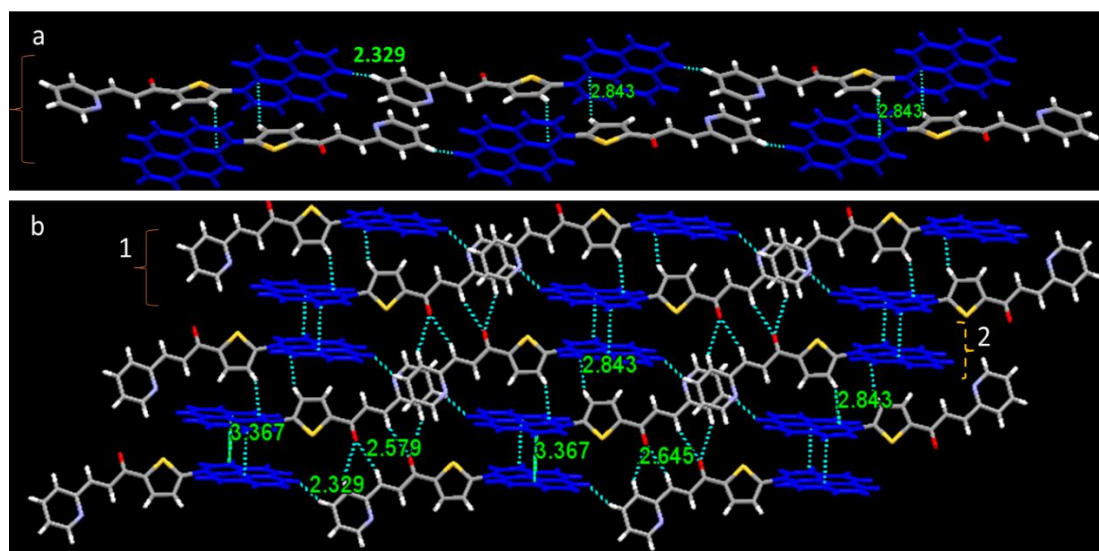
Figure 5.2.36 (a) Crystal packing of PySS showing interactions and short contacts between molecules and (b) Crystal packing of PySP with intermolecular interactions between molecules

5.2.3.2 Feasibility study for the application of PySS for reversible data storage and VOCs

The reversible color-switching features of PySS and PySP offer a promising reusable secured platform for anticounterfeiting applications. An economical paper strip-based device is fabricated by dispersing green emitting solid (PySS) on a Whatman filter paper, demonstrated in security writing and piezo patterning applications.[54] A needle spatula was used to write on the paper, after writing the emission color changes from green to yellow (Figure 5.2.37) which happens because of the stress airing from the MFC property. This phenomenon is reversible, after heating/fuming with MeOH its emission color returned to the original form (green emission). It may be useful in security data storage applications. Interestingly, if we expose the DCM vapor into the paper film of PySS, it converts its emission color from green to bright yellow. On the compound-coated filter paper it was written R with DCM and exposed to MeOH vapor; its emission color returns to its original emission (figure 5.2.37, b). This way reversible MFC properties of the probe could be useful for a rewritable paper and sensing of volatile organic compounds.
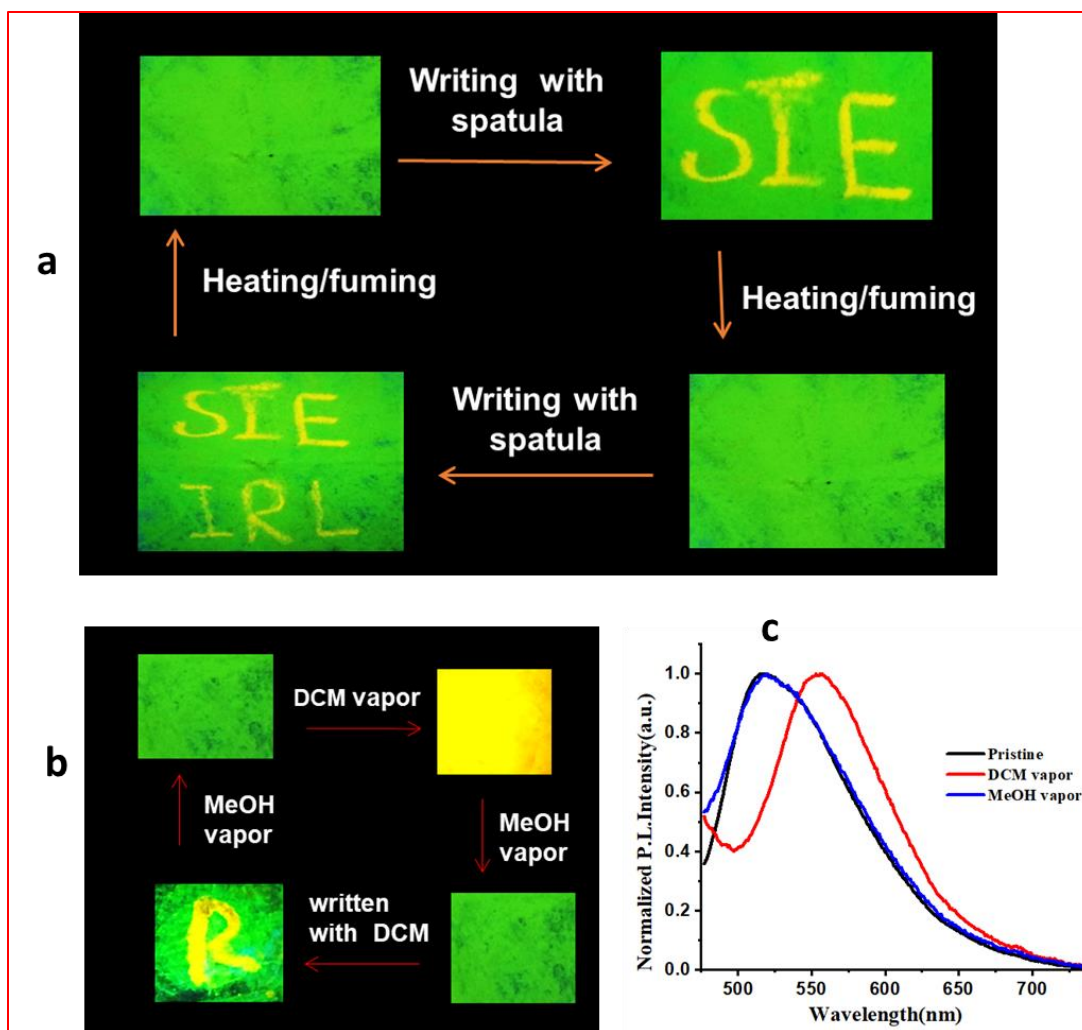
Figure 5.2.37 PySS used for stress sensing and VOC sensors. (a) Images of PySS taken under excitation of UV light (375nm), initially green emission after written with spatula (written S I E) convert it to yellow then heating (70-80°C) /fuming with methanol return to original state and repeated the process. (b) Images of PySS under UV (365 nm) excitation (green emission) and after exposed with DCM yellow emission) then after methanol fumigation return to original (green) emission. (c) Normalized PL spectra of PySS, black line initial emission, red line after DCM vapor exposer and blue line is return with MeOH vapor

5.2.4 CONCLUSION

It has been strategically designed and synthesized pyrene-thiophene based high-contrast MFC materials (PySS and PySP) which are sensitive to both grinding and compressive force. Further, PySS and PySP were found to be responsive towards solvent polarity with a large stoke shift (147 nm and 130 nm). Interestingly, PySS gives tunable color change by slowly increasing the hydraulic force (compressive) which is reversible in nature. By solvent fumigation or heating it could be reconverted into the original emission within 2 min for grinding and compressive force. The sensitive MFC properties have been employed to demonstrate for security ink and

data storage devices. The shape and the electronic properties of the present compounds showed head-tail pair followed by linear chain that leading to sheet and layer-based structure that is supported from the SCXRD study. The present study and the earlier studies[45] support the following arrangement of the molecules in the crystal would be responsible for the resulting the highly sensitive and tunable emission by compressive force. Certainly, this work will inspire further designing of compounds that will result in more precise and controllable reversible tunable emission color.

5.2.5 REFERENCES

1.   Kachwal, V.; Laskar, I. R., Mechanofluorochromism with Aggregation-Induced Emission (AIE) Characteristics: A Perspective Applying Isotropic and Anisotropic Force. *Topics in Current Chemistry* **2021,** *379* (4), 28.

2.   Hong, Y.; Meng, L.; Chen, S.; Leung, C. W. T.; Da, L.-T.; Faisal, M.; Silva, D.-A.; Liu, J.; Lam, J. W. Y.; Huang, X., Monitoring and inhibition of insulin fibrillation by a small organic fluorogen with aggregation-induced emission characteristics. *Journal of the American Chemical Society* **2012,** *134* (3), 1680-1689.

3.   Chen, M.; Chen, R.; Shi, Y.; Wang, J.; Cheng, Y.; Li, Y.; Gao, X.; Yan, Y.; Sun, J. Z.; Qin, A., Malonitrile-functionalized tetraphenylpyrazine: aggregation-induced emission, ratiometric detection of hydrogen sulfide, and mechanochromism. *Advanced Functional Materials* **2018,** *28* (6), 1704689.

4.   Wang, H.; Ji, X.; Page, Z. A.; Sessler, J. L., Fluorescent materials-based information storage. *Materials Chemistry Frontiers* **2020,** *4* (4), 1024-1039.

5.   Li, A.; Ma, Z.; Wu, J.; Li, P.; Wang, H.; Geng, Y.; Xu, S.; Yang, B.; Zhang, H.; Cui, H., Pressure-Induced Wide-Range Reversible Emission Shift of Triphenylamine-Substituted Anthracene via Hybridized Local and Charge Transfer (HLCT) Excited State. *Advanced Optical Materials* **2018,** *6* (3), 1700647.

6.   Sun, Y.; Lei, Z.; Ma, H., Twisted aggregation-induced emission luminogens (AIEgens) contribute to mechanochromism materials: a review. *Journal of Materials Chemistry C* **2022,** *10* (40), 14834-14867.

7.   Bustamante, C.; Alexander, L.; Maciuba, K.; Kaiser, C. M., Single-Molecule Studies of Protein Folding with Optical Tweezers. *Annual Review of Biochemistry* **2020,** *89* (Volume 89, 2020), 443-470.

8.   Hong, Y.; Lam, J. W.; Tang, B. Z., Aggregation-induced emission. *Chemical Society Reviews* **2011,** *40* (11), 5361-5388.

9.   Zhao, Z.; He, B.; Tang, B. Z., Aggregation-induced emission of siloles. *Chemical Science* **2015,** *6* (10), 5347-5365.

10.   Tang, B. Z.; Zhan, X.; Yu, G.; Lee, P. P. S.; Liu, Y.; Zhu, D., Efficient blue emission from siloles. *Journal of Materials Chemistry* **2001,** *11* (12), 2974-2978.

11.   Yuan, W. Z.; Tan, Y.; Gong, Y.; Lu, P.; Lam, J. W. Y.; Shen, X. Y.; Feng, C.; Sung, H. H. Y.; Lu, Y.; Williams, I. D.; Sun, J. Z.; Zhang, Y.; Tang, B. Z., Synergy between Twisted Conformation and Effective Intermolecular Interactions: Strategy for Efficient Mechanochromic Luminogens with High Contrast. *Advanced Materials* **2013,** *25* (20), 2837-2843.

12.   Xiong, Y.; Huang, J.; Liu, Y.; Xiao, B.; Xu, B.; Zhao, Z.; Tang, B. Z., High-contrast luminescence dependent on polymorphism and mechanochromism of AIE-active (4-(phenothiazin-10-yl) phenyl)(pyren-1-yl) methanone. *Journal of Materials Chemistry C* **2020,** *8* (7), 2460-2466.

13.   Li, C.; Luo, X.; Zhao, W.; Li, C.; Liu, Z.; Bo, Z.; Dong, Y.; Dong, Y. Q.; Tang, B. Z., Switching the emission of tetrakis(4-methoxyphenyl)ethylene among three colors in the solid state. *New Journal of Chemistry* **2013,** *37* (6), 1696-1699.

14.   Galer, P.; Korošec, R. C.; Vidmar, M.; Šket, B., Crystal Structures and Emission Properties of the BF2 Complex 1-Phenyl-3-(3,5-dimethoxyphenyl)-propane-1,3-dione: Multiple Chromisms, Aggregation- or Crystallization-Induced Emission, and the Self-Assembly Effect. *Journal of the American Chemical Society* **2014,** *136* (20), 7383-7394.

15.   Chakraborty, M.; Chakravarty, M., Variation in solvato-, AIE-and mechano-fluorochromic behavior for furanyl and thiophenyl-substituted anthranyl π-conjugates: the role of tiny flanking donor groups. *Materials Advances* **2021,** *2* (19), 6418-6427.

16.   Dong, Y.; Xu, B.; Zhang, J.; Tan, X.; Wang, L.; Chen, J.; Lv, H.; Wen, S.; Li, B.; Ye, L.; Zou, B.; Tian, W., Piezochromic Luminescence Based on the Molecular Aggregation of 9,10-Bis((E)-2-(pyrid-2-yl)vinyl)anthracene. *Angewandte Chemie International Edition* **2012,** *51* (43), 10782-10785.

17.   Xu, Y.; Wang, K.; Zhang, Y.; Xie, Z.; Zou, B.; Ma, Y., Fluorescence mutation and structural evolution of a π-conjugated molecular crystal during phase transition. *Journal of Materials Chemistry C* **2016,** *4* (6), 1257-1262.

18.   Liu, L.; Su, X.; Yu, Q.; Guo, H.; Wang, K.; Yu, B.; Li, M.; Zou, B.; Liu, Y.; Xiao-An Zhang, S., Photoacid-spiropyran exhibits different mechanofluorochromism before and after

modification of tetraphenylethene under grinding and hydrostatic pressure. *The Journal of Physical Chemistry C* **2019,** *123* (41), 25366-25372.

19.   Li, J.; Yuan, S.; Qin, J.-S.; Huang, L.; Bose, R.; Pang, J.; Zhang, P.; Xiao, Z.; Tan, K.; Malko, A. V.; Cagin, T.; Zhou, H.-C., Fluorescence Enhancement in the Solid State by Isolating Perylene Fluorophores in Metal–Organic Frameworks. *ACS Applied Materials & Interfaces* **2020,** *12* (23), 26727-26732.

20.   Li, X.; Gao, Q.; Wang, J.; Chen, Y.; Chen, Z.-H.; Xu, H.-S.; Tang, W.; Leng, K.; Ning, G.-H.; Wu, J.; Xu, Q.-H.; Quek, S. Y.; Lu, Y.; Loh, K. P., Tuneable near white-emissive two-dimensional covalent organic frameworks. *Nature Communications* **2018,** *9* (1), 2335.

21.   Wang, X.; Zhang, J.; Mao, X.; Liu, Y.; Li, R.; Bai, J.; Zhang, J.; Redshaw, C.; Feng, X.; Tang, B. Z., Intermolecular Hydrogen-Bond-Assisted Solid-State Dual-Emission Molecules with Mechanical Force-Induced Enhanced Emission. *The Journal of Organic Chemistry* **2022,** *87* (13), 8503-8514.

22.   Liu, C.; Xiao, G.; Yang, M.; Zou, B.; Zhang, Z.-L.; Pang, D.-W., Mechanofluorochromic Carbon Nanodots: Controllable Pressure-Triggered Blue- and Red-Shifted Photoluminescence. *Angewandte Chemie International Edition* **2018,** *57* (7), 1893-1897.

23.   Mei, J.; Hong, Y.; Lam, J. W. Y.; Qin, A.; Tang, Y.; Tang, B. Z., Aggregation-Induced Emission: The Whole Is More Brilliant than the Parts. *Advanced Materials* **2014,** *26* (31), 5429-5479.

24.   Valeur, B., Molecular Fluorescence. In *Encyclopedia of Applied Physics*, 2009; pp 477-531.

25.   Xiong, J.; Wang, K.; Yao, Z.; Zou, B.; Xu, J.; Bu, X.-H., Multi-Stimuli-Responsive Fluorescence Switching from a Pyridine-Functionalized Tetraphenylethene AIEgen. *ACS Applied Materials & Interfaces* **2018,** *10* (6), 5819-5827.

26.   Yang, W.; Li, C.; Zhang, M.; Zhou, W.; Xue, R.; Liu, H.; Li, Y., Aggregation-induced emission and intermolecular charge transfer effect in triphenylamine fluorophores containing diphenylhydrazone structures. *Physical Chemistry Chemical Physics* **2016,** *18* (40), 28052-28060.

27.   Jia, J.; Zhao, H., Structure-dependent reversible mechanochromism of D-π-A triphenylamine derivatives. *Tetrahedron Letters* **2019,** *60* (3), 252-259.

28.   Fang, M.; Yang, J.; Liao, Q.; Gong, Y.; Xie, Z.; Chi, Z.; Peng, Q.; Li, Q.; Li, Z., Triphenylamine   derivatives: different   molecular   packing   and   the   corresponding

mechanoluminescent or mechanochromism property. *Journal of Materials Chemistry C* **2017,** *5* (38), 9879-9885.

29.   Yoshizawa, M.; Klosterman, J. K., Molecular architectures of multi-anthracene assemblies. *Chemical Society Reviews* **2014,** *43* (6), 1885-1898.

30.   Sun, B.; Yang, X.; Ma, L.; Niu, C.; Wang, F.; Na, N.; Wen, J.; Ouyang, J., Design and Application of Anthracene Derivative with Aggregation-Induced Emission Charateristics for Visualization and Monitoring of Erythropoietin Unfolding. *Langmuir* **2013,** *29* (6), 1956-1962.

31.   Zhao, J.; Chi, Z.; Yang, Z.; Mao, Z.; Zhang, Y.; Ubba, E.; Chi, Z., Recent progress in the mechanofluorochromism of distyrylanthracene derivatives with aggregation-induced emission. *Materials Chemistry Frontiers* **2018,** *2* (9), 1595-1608.

32.   Gu, Y.; Wang, K.; Dai, Y.; Xiao, G.; Ma, Y.; Qiao, Y.; Zou, B., Pressure-Induced Emission Enhancement of Carbazole: The Restriction of Intramolecular Vibration. *The Journal of Physical Chemistry Letters* **2017,** *8* (17), 4191-4196.

33.   Mei, X.; Wei, K.; Wen, G.; Liu, Z.; Lin, Z.; Zhou, Z.; Huang, L.; Yang, E.; Ling, Q., Carbazole-based diphenyl maleimides: Multi-functional smart fluorescent materials for data process and sensing for pressure, explosive and pH. *Dyes and Pigments* **2016,** *133*, 345-353.

34.   Takeda, Y.; Mizuno, H.; Okada, Y.; Okazaki, M.; Minakata, S.; Penfold, T.; Fukuhara, G., Hydrostatic Pressure-Controlled Ratiometric Luminescence Responses of a Dibenzo[a,j]phenazine-Cored Mechanoluminophore. *ChemPhotoChem* **2019,** *3* (12), 1203-1211.

35.   Yang, Y.; Li, A.; Ma, Z.; Liu, J.; Xu, W.; Ma, Z.; Jia, X., Dibenzo[a,c]phenazine-phenothiazine dyad: AIEE, polymorphism, distinctive mechanochromism, high sensitivity to pressure. *Dyes and Pigments* **2020,** *181*, 108575.

36.   Ghosh, S.; Bhambri, H.; Singh, A. K.; Mandal, S. K.; Roy, L.; Addy, P. S., A convenient route to a vinylogous dicyano aryl based AIEgen with switchable mechanochromic luminescence properties. *Chemical Communications* **2023,** *59* (30), 4463-4466.

37.   Meng, X.; Qi, G.; Li, X.; Wang, Z.; Wang, K.; Zou, B.; Ma, Y., Spiropyran-based multi-colored switching tuned by pressure and mechanical grinding. *Journal of Materials Chemistry C* **2016,** *4* (32), 7584-7588.

38.   Robertson, J. M.; White, J., 72. The crystal structure of pyrene. A quantitative X-ray investigation. *Journal of the Chemical Society (Resumed)* **1947**, 358-368.

39.   Fang, M.; Yang, J.; Li, Z., Light emission of organic luminogens: Generation, mechanism and application. *Progress in Materials Science* **2022,** *125*, 100914.

40.   Varghese, E. V.; Yao, C.-Y.; Chen, C.-H., Investigation of Mechanochromic Luminescence of Pyrene-based Aggregation-Induced Emission Luminogens: Correlation between Molecular Packing and Luminescence Behavior. *Chemistry – An Asian Journal* **2024,** *19* (1), e202300910.

41.   Islam, M. M.; Hu, Z.; Wang, Q.; Redshaw, C.; Feng, X., Pyrene-based aggregation-induced emission luminogens and their applications. *Materials Chemistry Frontiers* **2019,** *3* (5), 762-781.

42.   Sonar, P.; Soh, M. S.; Cheng, Y. H.; Henssler, J. T.; Sellinger, A., 1, 3, 6, 8-tetrasubstituted pyrenes: solution-processable materials for application in organic electronics. *Organic Letters* **2010,** *12* (15), 3292-3295.

43.   Xiong, Y.; Huang, J.; Liu, Y.; Xiao, B.; Xu, B.; Zhao, Z.; Tang, B. Z., High-contrast luminescence dependent on polymorphism and mechanochromism of AIE-active (4-(phenothiazin-10-yl)phenyl)(pyren-1-yl)methanone. *Journal of Materials Chemistry C* **2020,** *8* (7), 2460-2466.

44.   Feng, X.; Wang, X.; Redshaw, C.; Tang, B. Z., Aggregation behaviour of pyrene-based luminescent materials, from molecular design and optical properties to application. *Chemical Society Reviews* **2023**.

45.   Pasha, S. S.; Yadav, H. R.; Choudhury, A. R.; Laskar, I. R., Synthesis of an aggregation-induced emission (AIE) active salicylaldehyde based Schiff base: study of mechanoluminescence and sensitive Zn (ii) sensing. *Journal of materials chemistry C* **2017,** *5* (37), 9651-9658.

46.   Bhatta, R. P.; Kachwal, V.; Climent, C.; Joshi, M.; Alemany, P.; Choudhury, A. R.; Laskar, I. R., Tunable emission in the visible range from a single organic fluorophore through time-controlled morphological evolution. *Journal of Materials Chemistry C* **2023,** *11* (33), 11399-11408.

47.   Gong, Y.-B.; Zhang, P.; Gu, Y.-r.; Wang, J.-Q.; Han, M.-M.; Chen, C.; Zhan, X.-J.; Xie, Z.-L.; Zou, B.; Peng, Q.; Chi, Z.-G.; Li, Z., The Influence of Molecular Packing on the Emissive Behavior of Pyrene Derivatives: Mechanoluminescence and Mechanochromism. *Advanced Optical Materials* **2018,** *6* (16), 1800198.

48.   Varghese, E. V.; Yao, C. Y.; Chen, C. H., Investigation of Mechanochromic Luminescence of Pyrene-based Aggregation-Induced Emission Luminogens: Correlation between Molecular Packing and Luminescence Behavior. *Chemistry–An Asian Journal* **2024,** *19* (1), e202300910.

49.   Yang, S.-W.; Elangovan, A.; Hwang, K.-C.; Ho, T.-I., Electronic polarization reversal and excited state intramolecular charge transfer in donor/acceptor ethynylpyrenes. *The Journal of Physical Chemistry B* **2005,** *109* (35), 16628-16635.

50.   D'Aléo, A.; Karapetyan, A.; Heresanu, V.; Giorgi, M.; Fages, F., Tuning solid-state emission properties of pyrene-containing chalcone derivatives. *Tetrahedron* **2015,** *71* (15), 2255-2259.

51.   Huang, Z.; Tang, F.; He, F.; Kong, L.; Huang, J.; Yang, J.; Ding, A., Pyrene and triphenylamine substituted cyanostyrene and cyanostilbene derivatives with dual-state emission for high-contrast mechanofluorochromism and cell imaging. *Organic Chemistry Frontiers* **2022,** *9* (19), 5118-5124.

52.   Zhao, Z.; Chen, S.; Lam, J. W. Y.; Wang, Z.; Lu, P.; Mahtab, F.; Sung, H. H. Y.; Williams, I. D.; Ma, Y.; Kwok, H. S.; Tang, B. Z., Pyrene-substituted ethenes: aggregation-enhanced excimer emission and highly efficient electroluminescence. *Journal of Materials Chemistry* **2011,** *21* (20), 7210-7216.

53.   Kim, Y.; Bouffard, J.; Kooi, S. E.; Swager, T. M., Highly Emissive Conjugated Polymer Excimers. *Journal of the American Chemical Society* **2005,** *127* (39), 13726-13731.

54.   Chakraborty, M.; Chakravarty, M., Varied optical features and mechanofluorochromism in dicyanovinyl-vs. cyanoacrylicacid-linked twisted π-conjugates: A potential reusable platform for security applications. *Materials Today Chemistry* **2024,** *35*, 101836.

55.   Niu, G.; Zheng, X.; Zhao, Z.; Zhang, H.; Wang, J.; He, X.; Chen, Y.; Shi, X.; Ma, C.; Kwok, R. T. K.; Lam, J. W. Y.; Sung, H. H. Y.; Williams, I. D.; Wong, K. S.; Wang, P.; Tang, B. Z., Functionalized Acrylonitriles with Aggregation-Induced Emission: Structure Tuning by Simple Reaction-Condition Variation, Efficient Red Emission, and Two-Photon Bioimaging. *Journal of the American Chemical Society* **2019,** *141* (38), 15111-15120.

56.   Hariharan, P. S.; Prasad, V. K.; Nandi, S.; Anoop, A.; Moon, D.; Anthony, S. P., Molecular engineering of triphenylamine based aggregation enhanced emissive fluorophore: structure-dependent mechanochromism and self-reversible fluorescence switching. *Crystal Growth & Design* **2017,** *17* (1), 146-155.

57.   Wang, X.; Liu, Q.; Yan, H.; Liu, Z.; Yao, M.; Zhang, Q.; Gong, S.; He, W., Piezochromic luminescence behaviors of two new benzothiazole–enamido boron difluoride complexes: intra- and inter-molecular effects induced by hydrostatic compression. *Chemical Communications* **2015,** *51* (35), 7497-7500.

58.   Qi, Q.; Qian, J.; Tan, X.; Zhang, J.; Wang, L.; Xu, B.; Zou, B.; Tian, W., Remarkable Turn-On and Color-Tuned Piezochromic Luminescence: Mechanically Switching Intramolecular Charge Transfer in Molecular Crystals. *Advanced Functional Materials* **2015,** *25* (26), 4005-4010.

59.   Li, A.; Li, P.; Geng, Y.; Xu, S.; Zhang, H.; Cui, H.; Xu, W., Investigation of supramolecular interaction in 4, 4′-bipyridine crystal by hydrostatic pressure spectroscopies. *Spectrochimica Acta Part A: Molecular and Biomolecular Spectroscopy* **2018,** *202*, 70-75.

60.   Xie, Y.; Wang, X.; Han, X.; Xue, X.; Ji, W.; Qi, Z.; Liu, J.; Zhao, B.; Ozaki, Y., Sensing of polycyclic aromatic hydrocarbons with cyclodextrin inclusion complexes on silver nanoparticles by surface-enhanced Raman scattering. *Analyst* **2010,** *135* (6), 1389-1394.

Chapter-6

CONCLUSIONS AND FUTURE SCOPE
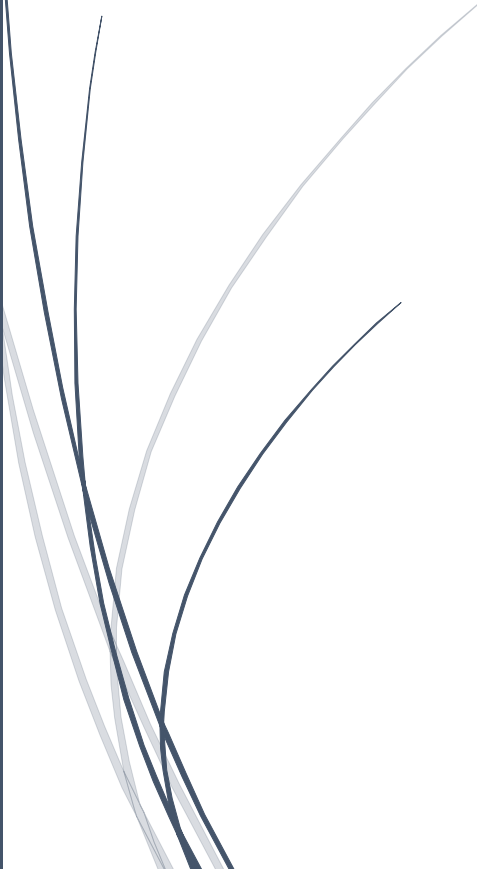
Chapter 6. Conclusion and Future Scope

6.1 Primary focus of the thesis:

I. Development of Aggregation-induced Emission (AIE) active fluorescent organic molecules and Aggregation-induced Phosphorescent Emission (AIPE) active Ir(III) for sensitive and selective detection of TNT explosive.

II. The development of pyrene-thiophene-based AIE active stimuli-responsive probes for mechanofluorochromic (MFC) materials with tunable emission color and its application towards rewritable papers, security ink, VOC sensors, etc.

The following things are proposed as future scope-

6.2 Design and synthesis of new AIE-active pyrene-triazine based compounds for improved TNT vapor sensing applications

In the field of explosive sensing (particularly for TNT), it was developed a pyrene triazine containing efficient molecules. Synthesized probe molecules could be able to detect TNT from water bodies at lower ppt levels, and it is also able to detect TNT vapor at ppb level (<10 ppb). The surface morphology of the material is one of the important parameters for analyte sensing in the vapor phase. The film morphology by FESEM images reported that the aggregated nano-rod type horizontally aligned morphology observed for the cases of PyTr and VinTr, while a vertically grown flowery and highly condensed nano-rod based morphology observed for PyTrDA would be responsible for the excellent results obtained for TNT detection. Further, to improve the quantum efficiency, the probe molecules can be modified by incorporating more twisted rings to improve sensitivity. Introducing more twisted rotors could also help to improve surface morphology for TNT vapor adsorption. Adding active functionality in basic pyrene-triazine core molecules (Figure 6.1- P1, P2, P3, and P4) will further improve the sensitivity of TNT vapor detection.
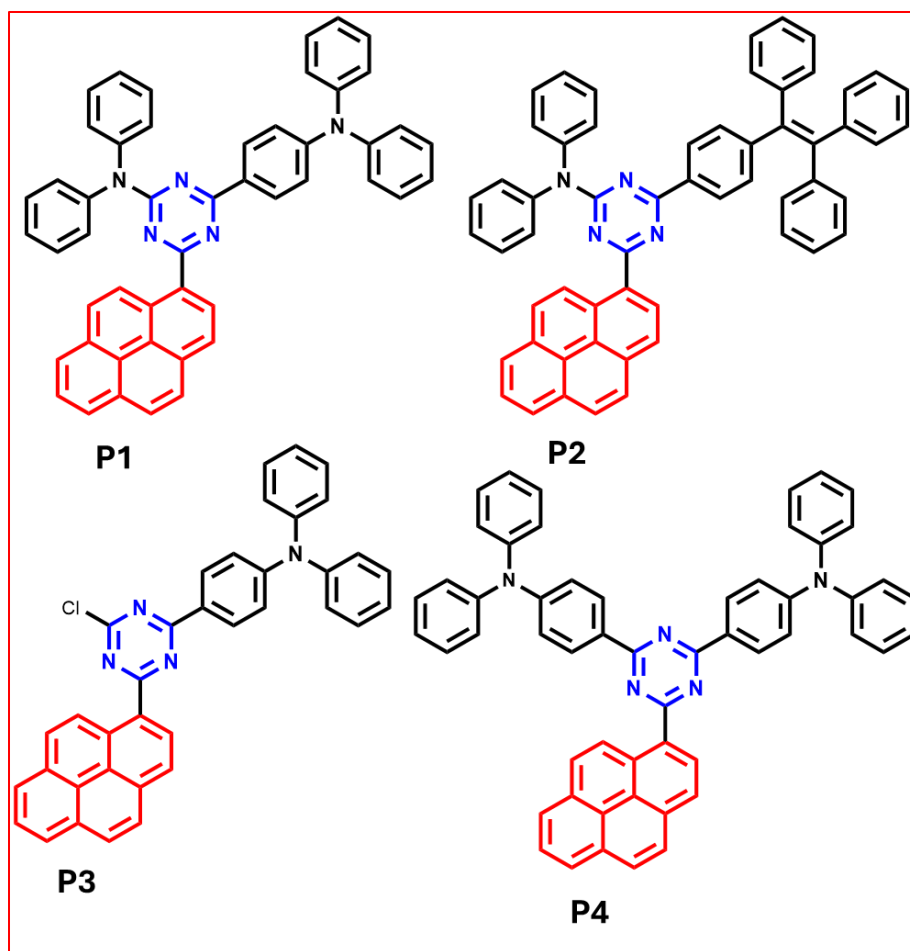
Figure 6.1 Chemical structure of modified PyTr series for TNT sensing

6.3 Design and synthesis of new AIE-active pyrene-thiophene based compounds for mechanofluorochromism (MFC)

In mechanofluorochromic (MFC) materials, it was developed a certain design strategy to get the reversible MFC property of pyrene-thiophene containing molecules. To make the present compound sensitive towards pressure-imposed mechanofluorochrism to mimic our previous work, a four-unit conjugated spacer attached to the thiophene side (of pyridine-acyl substituted thiophene) along with some photoactive species connected terminally. In the same direction to make molecules more sensitive and reversible to imposed pressure (Figure 6.2), terminal substituents can be altered with TPA, TPE, naphthalene, anthracene, and pyrene (structure P5).

Additionally, in the same molecule (PySP), alkylation with varying chain lengths along with Incorporating hetero atoms (N, O, carbonyl, S, etc) optimally to create weak interactions could be one of the ways to improve reversibility under compressive force. (structure P6)
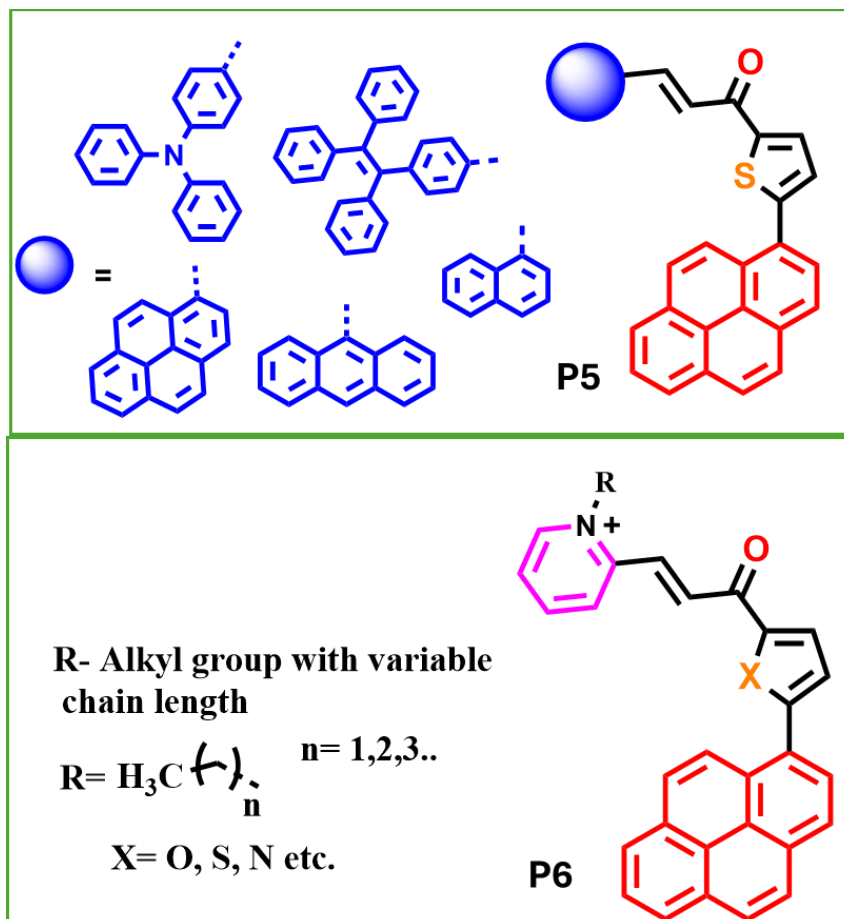

Figure 6.2 Chemical structure of modified pyrene-thiophene series for MCF materials

Appendices

List of Publications and Patents [A-1]

➡ Pyrene-based AIEE-active Vertically Grown Luminescent Material for Selective and Sensitive Detection of TNT Vapor. **Ramprasad Bhatt**, Ajeet Singh, Priya Bhandari, Tirupati Chander Sharma, Pramod Soni, Anindya Datta and Inamur Rahaman Laskar. *J. Phys. Chem. C, 2024*, https://doi.org/10.1021/acs.jpcc.4c04823.

➡ Precise Molecular Design for Twisted Pyrene-Thiophene-Based Mechanofluorochromic Probe with Large Stokes Shift and Feasibility Study Towards Security Ink and Re-writable Papers. Ram Prasad Bhatt, Sumit, Vishal Kachwal, Vandana Vishwakarma, Angshuman Roy Choudhury and Inamur Rahaman Laskar. *J. Mater. Chem. C, 2024*, 12, 12906-12918.

➡ Enhanced TNT Vapor Sensing Through PMMA-mediated AIPE-Active Monocyclometalated Iridium(III) Complex: A Leap Towards Real-Time Monitoring. **Ramprasad Bhatt**, Annu Agarwal, Vishal Kachwa, Pramod C. Raichure, and Inamur Rahaman Laskar. *Analyst*, **2024, 149, 2445-2458**.

➡ Controlling the sensitivity and selectivity for detecting nitro-based explosives by modulating the electronic substituents on the ligand of the AIPE-active cyclometalated iridium(III) complex. Annu Agarwal, **Ramprasad Bhatt**, Vishal Kachwal and Inamur Rahaman Laskar. *Dalton Trans., 2023, 52, 14182-14193.*

➡ Tunable emission in the visible range from a single organic fluorophore through time-controlled morphological evolution. **Ramprasad Bhatt**, Vishal Kachwal, Clàudia Climent, Mayank Joshi, Pere Alemany, A. Roy Choudhury and Inamur Rahaman Laskar. *J. Mater. Chem. C*, **2023, 11, 11399-11408.**

➡ Multi-Stimuli Distinct Responsive D-A Based Fluorogen Oligomeric Tool and Efficient Detection of TNT Vapor. Pramod C. Raichure, **Ramprasad Bhatt**, Vishal Kachwal, Tirupati Chander Sharma, and Inamur Rahaman Laskar (My role: - synthesis synthesis and explosive sensing applications). *New J. Chem., 2022, 46, 6560-6569*.

➡️ A selenium-coordinated palladium(II) *trans*-dichloride molecular rotor as a catalyst for site-selective annulation of 2-arylimidazo[1,2-*a*]pyridines Neha Meena, Shobha Sharma, **Ramprasad Bhatt**, Vikki N. Shinde, Anurag Prakash Sunda, Nattamai Bhuvanesh, Anil Kumar and Hemant Joshi. (My role- Catalyst design synthesis and characterization). *Chem. Commun.*, **2020, 56, 10223-10226.**

➡️ Palladium complexes of chalcogenoethanamine (S/Se) bidentate ligands: Applications in the catalytic arylation of C-H and O-H bonds. **Ramprasad Bhatt**, AlpeshK. Sharma, Himanshi, Nattamai Bhuvanesh, Hemant Joshi**. *Polyhedron,* 2020, 185, 114597.**

➡️ Palladium Complexes of Thio/Seleno-Ether Containing N-Heterocyclic Carbenes: Efficient and Reusable Catalyst for Regioselective C-H Bond Arylation." **Ramprasad Bhatt**, Nattamai Bhuvanesh, Kamal Nayan Sharma, and Hemant Joshi. *European Journal of Inorganic Chemistry,* **2020, 6, 532-540.**

Papers communicated: *List of papers under review process*

1. Pyrene- thiophene containing AIEE-active Probes, Effect of Terminal Substituent with Molecular Packing and Mechanofluorochromic (MFC) Properties. **Ramprasad Bhatt,** Nancy Punia, and Inamur Rahaman Laskar (under preparation).

2. Multi-stimuli Responsive Pyrene-containing D-A-D Based Solid-state Emitters for Efficient Detection of nitro-explosive and Acid vapor. **Ramprasad Bhatt,** Annu, Bharat Kaushik and Inamur Rahaman Laskar (under preparation).

Information about patents

"Pyrene-triazine based luminescent compounds for TNT sensing and method for preparation thereof" (**Indian Patent Filed, Application No. 202411039635**)

List of Oral / Poster Presented in Conferences / Workshops [A-2]

Papers presented in conferences/symposia/….

1.'Enhanced TNT Vapor Sensing Through PMMA-mediated AIPE-Active Monocyclometalated Iridium(III) Complex: A Leap Towards Real-Time Monitoring' in an **International Conference on 'Luminescent Materials: From Fundamental to Applications (IClMFA-2024)'** held at the department of chemistry, Guru Nanak Dev University, India during December 15-16, 2024.

2. Presented our collaborative research work with TBRL-DRDO Gov. of India and Department of EEE BITS Pilani entitled "Solid state luminescent material for selective detection of TNT vapor" on **Atal Innovation Mission, NITI Aayog National Technology Week 2023 at Pragati Maidan, Delhi**.

List of conferences attended, presented posters, etc.

1. "17th DAE-BRNS Biennial Trombay Symposium on Radiation & Photochemistry (TSRP-2024)" organized by BARC Mumbai on 7-11 Jan 2024 (**Best Poster award**).

2. "International Conference on Frontiers at the Chemistry-Allied Sciences Interface (FCASI-2023)" organized by the Department of Chemistry, University of Rajasthan, Jaipur, India from April 20-21, 2023 (**Poster**).

3. "International Conference on 'Aggregation-induced Emission' from Fundamental to Applications' (ICAIEFA 2022), organized by the Department of Chemistry, BITS Pilani University on 16th-18th Dec 2022. (**Poster**).

4. workshop on 'Applications of FTIR and 2D NMR in Pharmaceutical Research' on Dec. 3, 2022, held at BITS Pilani, Pilani Campus, India.

5. Participated in the National Workshop on 'Software and Applications of Single Crystal X-ray Diffraction' from 29-31 August 2019. The Gujarat Council on Science and Technology **(GUJCOST)**, govt. of Gujarat sponsored this workshop.

BRIEF BIOGRAPHY OF THE CANDIDATE [A-3]

Mr. Ram Prasad Bhatta is currently a Ph.D. scholar at BITS Pilani, Pilani campus, Rajasthan. He graduated with a Master of Science (MSc) in organic chemistry from Mukand Lal National College (Affiliated with Kurukshetra University), Yamuna Nagar, Haryana (India) in 2016. Thereafter, he joined as a research associate trainee at the Chemical research division (Micro Labs Limited), Bengaluru, Karnataka, and worked as a research associate for 2.5 years. Then for six months he worked as a JRF to design, synthesis, and utilization of catalyst for different chemical transformations at BITS Pilani, Pilani campus. He started his Ph.D. studies at the Department of Chemistry, BITS Pilani, in September 2019. He has been working on the development of solid state-smart luminescent molecules for different applications. His professional experience includes strategic design and synthesis of luminescent materials for nitro-aromatic explosives sensing, mechanoflorochromism, tunable emission, aggregation-induced emission (AIE)-active mono- cyclometalated iridium metal complex for detection of explosive vapors etc. He has published seven research articles in peer-reviewed international journals and presented papers at six conferences/symposiums to date. Using all the resources available to do cutting-edge research to benefit humanity is his passion.

Appendices

BRIEF BIOGRAPHY OF THE SUPERVISOR [A-4]

Currently, **Prof. Inamur Rahaman Laskar** has been employed as a Professor at the Department of Chemistry, Birla Institute of Technology & Science, Pilani Campus, Pilani, Rajasthan, India. He received his Ph.D. in inorganic chemistry from the Indian Association for the Cultivation of Science (IACS), Kolkata, India, in 2000. From September 1999 to July 2001, he worked as a Lecturer at Ananda Mohan College, a Kolkata, India that is affiliated with the University of Calcutta. During July 2001 and March 2006, he worked as a Postdoctoral Associate at NTHU and NCTU, Taiwan, ROC. Further, he worked on JSPS post-doctoral research fellow at Kochi University in Japan during April 2006 and March 2008. In August 2008, he joined the BITS Pilani Department of Chemistry as Assistant Professor. His research interest includes designing and synthesizing of 'Aggregation-induced Emission' active compounds with heavy (iridium(III), platinum(II)) metals / small organic molecules/ conjugated polymers based compounds covering the wavelength from visible range to Near Infrared (NIR) emission with tunable optical properties. The synthesized materials are targeted in bio-imaging, theranostics, mechanofluorochromism, OLEDs / PLEDs, sensing of important analytes such as explosives from vapor phase, VOCs, biologically important analytes, biomolecules and toxic molecules, designing and synthesis of TADF molecules etc. The mechanism exploration in each of the cases with the help of computational study is his further interest.

Currently, seven Ph.D. students are working under his supervision. He received funding from various funding agencies from the Government of India: Indian Council of Medical Research, DRDO, Department of Biotechnology (DBT), Council of Scientific & Industrial Research, Department of Science and Technology, and SERB.